The Effect of Long-Term Thermal Cycling on the Microcracking Behavior and Dimensional Stability of Composite Materials

Timothy L. Brown

Dissertation submitted to the Faculty of the Virginia Polytechnic Institute and State University in partial fulfillment of the requirements for the degree of
Doctor of Philosophy
in
Engineering Mechanics

Michael W. Hyer (Chair)
Scott L. Hendricks
John J. Lesko
Brian J. Love
Kenneth L. Reifsnider

December 1,1997
Blacksburg, Virginia

Keywords: Graphite-Epoxy, Cyanate Ester, Coefficient of Thermal Expansion, Stiffness, Thermal Fatigue, Cryogenic, Fizeau Interferometry, Space, Shear Lag

The Effect of Long-Term Thermal Cycling on the Microcracking Behavior and Dimensional Stability of Composite Materials

Timothy L. Brown

(ABSTRACT)

The effect of thermal-cycling-induced microcracking in fiber-reinforced polymer matrix composites is studied. Specific attention is focused on microcrack density as a function of the number of thermal cycles, and the effect of microcracking on the dimensional stability of composite materials. Changes in laminate coefficient of thermal expansion (CTE) and laminate stiffness are of primary concern. Included in the study are materials containing four different Thornel fiber types: a PAN-based T50 fiber and three pitch-based fibers, P55, P75, and P120. The fiber stiffnesses range from 55 Msi to 120 Msi. The fiber CTE's range from $-0.50x10^{-6}$/°F to $-0.80x10^{-6}$/°F. Also included are three matrix types: Fiberite's 934 epoxy, Amoco's ERL1962 toughened epoxy, and YLA's RS3 cyanate ester. The lamination sequences of the materials considered include a cross-ply configuration, $[0/90]_{2s}$, and two quasi-isotropic configurations, $[0/+45/-45/90]_s$ and $[0/+45/90/-45]_s$. The layer thickness of the materials range from a nominal 0.001 in. to 0.005 in. In addition to the variety of materials considered, three different thermal cycling temperature ranges are considered. These temperature ranges are ±250°F, ±150°F, and ±50°F. The combination of these material and geometric parameters and temperature ranges, combined with thermal cycling to thousands of cycles, makes this one of the most comprehensive studies of thermal-cycling-induced microcracking to date.

Experimental comparisons are presented by examining the effect of layer thickness, fiber type, matrix type, and thermal cycling temperature range on microcracking and its influence on the laminates. Results regarding layer thickness effects indicate that thin-layer laminates microcrack more severely than identical laminates with thick layers. For some specimens in this study, the number of microcracks in thin-layer specimens exceeds that in thick-layer specimens by more than a factor of two. Despite the higher number of microcracks in the thin-layer specimens, small changes in CTE after thousands of cycles indicate that the thin-layer specimens are relatively unaffected by the presence of these cracks compared to the thick-layer specimens. Results regarding fiber type indicate that the number of microcracks and the change in CTE after thousands of cycles in the specimens containing PAN-based fibers are less than in the specimens containing comparable stiffness pitch-based fibers. Results for specimens containing the different

pitch-based fibers indicate that after thousands of cycles, the number of microcracks in the specimens does not depend on the modulus or CTE of the fiber. The change in *laminate* CTE does, however, depend highly on the stiffness and CTE of the fiber. Fibers with higher stiffness and more negative CTE exhibit the lowest change in laminate CTE as a result of thermal cycling. The overall CTE of these specimens is, however, more negative as a result of the more negative CTE of the fiber. Results regarding matrix type based on the ±250°F temperature range indicate that the RS3 cyanate ester resin system exhibits the greatest resistance to microcracking and the least change in CTE, particularly for cycles numbering 3000 and less. Extrapolations to higher numbers of cycles indicate, however, that the margin of increased performance is expected to decrease with additional thermal cycling. Results regarding thermal cycling temperature range depend on the matrix type considered and the layer thickness of the specimens. For the ERL1962 resin system, microcrack saturation is expected to occur in all specimens, regardless of the temperature range to which the specimens are exposed. By contrast, the RS3 resin system demonstrates a threshold effect such that cycled to less severe temperature ranges, microcracking does not occur. For the RS3 specimens with 0.005 in. layer thickness, no microcracking or changes in CTE are observed in specimens cycled between ±150°F or ±50°F. For the RS3 specimens with 0.002 in. layer thickness, no microcracking or changes in CTE are observed in specimens cycled between ±50°F. Results regarding laminate stiffness indicate negligible change in laminate stiffness due to thermal cycling for the materials and geometries considered in this investigation. The study includes X-ray examination of the specimens, showing that cracks observed at the edge of the specimens penetrate the entire width of the specimen. Glass transition temperatures of the specimens are measured, showing that resin chemistry is not altered as a result of thermal cycling.

Results are also presented based on a one-dimensional shear lag analysis developed in the literature. The analysis requires material property information that is difficult to obtain experimentally. Using limited data from the present investigation, material properties associated with the analysis are modified to obtain reasonable agreement with measured microcrack densities. Based on these derived material properties, the analysis generally overpredicts the change in laminate CTE. Predicted changes in laminate stiffness show reasonable correlation with experimentally measured values.

ACKNOWLEDGEMENTS

The author would like to gratefully acknowledge Professor Michael W. Hyer for his dedication to this project. I have worked with him for over seven years in my graduate education and his unending drive and dedication to the field of composite materials never ceases to amaze me. I am also grateful for the technical support of my Ph.D. committee members, Profs. Scott L. Hendricks, John J. Lesko, Brian J. Love, and Kenneth L. Reifsnider. I would like to thank Profs. Ron G. Kander and Don H. Morris, who served on my committee during the preliminary stages of my degree but had to withdraw in the end due to scheduling conflicts.

The technical support and advice I received during my residency at NASA Langley Research Center is gratefully acknowledged. Specifically, I would like to thank Dr. Stephen Tompkins, Dr. David Bowles, Dr. Wallace Vaughn, Dr. Howard Maahs, Craig Ohlhorst, and James Shen. Additional technical support was provided by Teresa O'Neil, Craig Leggette, Ron Penner, and Sandy Branham, to whom I am also grateful. A special thanks is given to Ashley Predith who helped tremendously with some of the experimental testing phases of this work.

I would also like to acknowledge Prof. Hugh McManus of M.I.T. for his help and advice with the analysis portion of the project. He was very willing to share his analysis code with me, for which I am most grateful.

Finally, I would like to thank my wife, Dr. Nicole L. Breivik, for her support throughout the completion of this degree. The final preparation of this dissertation coincided with the arrival of our son, Patrick Steven Brown, born on Oct. 17, 1997. I would like to thank my parents, Peter and Carol Brown, for their help and support during this momentous time in our lives.

This work was funded by the Environmental Interactions Branch of NASA Langley Research Center through the NASA-Virginia Tech Composites Program, grants NAG-1-343 and NAG-1-1912.

TABLE OF CONTENTS

LIST OF TABLES

LIST OF FIGURES

1. INTRODUCTION

This investigation considers the development of thermally-induced microcracking in fiber-reinforced composite materials and the effect these microcracks have on the dimensional stability of the materials. Dimensional stability refers to the ability of a material or structure to retain its shape over time, irrespective of environmental changes with time. Applications involving dimensionally stable structures such as those for space are typically stiffness-driven, rather than strength-driven designs. As a result, it is critical that the materials and structures retain their stiffness over time. It is also critical that the materials and structures retain their thermal expansion behavior, ideally zero thermal expansion, over time. The current investigation considers a variety of material and geometric parameters in order to increase the understanding of how composites microcrack and the effect this microcracking has on the stiffness and the thermal expansion behavior of these materials. This investigation ties together experimental results from previous work in this same area. Some of the results presented have been previously published and some of the same materials that were used in these earlier studies have been included in this study to investigate even longer-term thermal cycling effects. The combination of past experimental results with new experimental results makes the present investigation one of the most comprehensive studies to date of thermally-induced microcracking. Additionally, an analytical approach, developed by another investigator, predicting the evolution of microcracking and its effect on stiffness and thermal expansion is considered in this study.

1.1 BACKGROUND

Microcracking is a damage phenomenon which affects a wide variety of composites. As used here, microcracks, or transverse matrix cracks, are defined as *intra*laminar cracks which propagate in two directions: inplane and out-of-plane relative to the *x-y* plane of the laminate illustrated in Figure 1.1. Inplane, the cracks propagate parallel to the direction of the fiber, i.e., in the 1-direction of the principal material coordinate system for that layer (see Figure 1.1), and may extend through the entire length and width of the laminate. Out-of-plane, the cracks propagate through the thickness of an individual layer. The layers adjacent to the cracking layer typically arrest the out-of-plane propagation of the crack due to the change in fiber orientation. This arresting behavior allows the laminate to remain intact overall. Note that only the upper half of the laminate shown in Figure 1.1 is depicted as damaged. This is done purely for clarity and the laminate is typically damaged throughout.

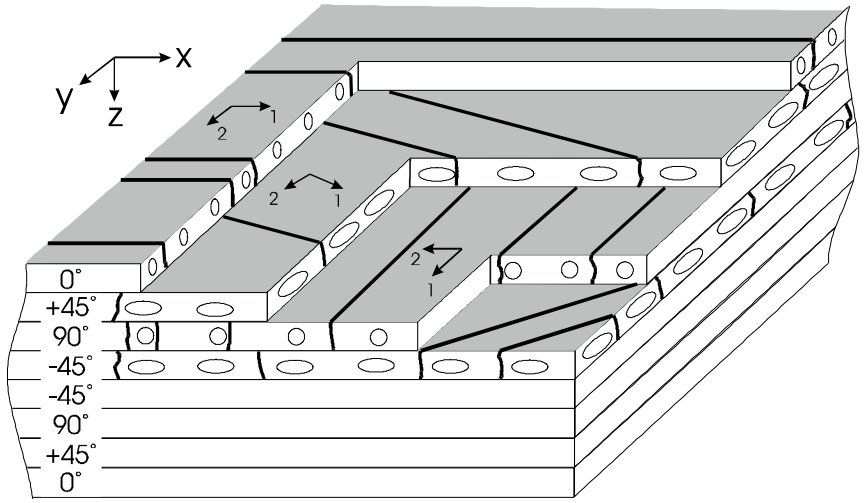

Figure 1.1. Microcracks present in a $[0/+45/90/-45]_s$ quasi-isotropic laminate.

Microcracks, as defined here, were first studied and modeled in the 1970's in the context of cross-ply laminates subjected to inplane tensile loading. Microcracks formed due to this type of loading were, and still are, well known to be one of the first forms of damage in composite laminates. The term ‘first ply failure’ often refers to the transverse matrix failure resulting in a microcrack. For mechanical loading, microcracks themselves are not usually detrimental to the laminate's performance. They do, however, often serve as initiators to delamination and eventual failure of the laminate.

It is also well known that residual thermal stresses, that is, stresses present in the laminate as a result of cooling the laminate from cure temperature to operating temperature, are sufficient to cause microcracking. The residual thermal stresses are the result of the mismatch in thermal expansion coefficients between the fiber and the matrix, and between the individual layers resulting from the various fiber orientations used in the laminate. In a strictly thermal loading application, such as those encountered by structures for use in space, the presence of microcracks can alter the stiffness and thermal expansion properties of the laminate, resulting in final properties which are unacceptable [1]. Many investigators have realized the importance of thermal stresses. As a result, much of their work done in understanding microcracking has included thermal effects either as a post-curing phenomenon or as a principal loading parameter, as in the case of applications for space.

1.2 OVERVIEW

The current investigation deals strictly with the thermal loading problem, and specifically, thermal conditions which might be encountered in space during orbit around the earth. This involves cyclic thermal conditions with temperature extremes ranging from −250°F to +250°F. The exact temperature extremes can depend on the type of orbit and the thermal control features included in the spacecraft. To simulate this effect, different cycling temperature ranges will be considered in this investigation.

Another characteristic of orbiting spacecraft is the duration of flight. A typical orbital spacecraft may spend years in space exposed to tens of thousands of thermal cycles. As a result, the current work will focus on long-term thermal exposure. For the experimental phase of this research, an accelerated thermal cycling profile will be used. Practical time limits restrict the investigation to a few thousand cycles, with the hope that information can be extrapolated to even higher numbers of cycles.

Finally, the above thermal loading conditions will be applied to a variety of composite material systems. The goal is to combine previous and current results to form a diverse material database which furthers the understanding of how various material and geometric factors affect thermally-induced microcracking. These material and geometric factors include: fiber type, matrix type, stacking sequence, and layer thickness.

An experimental approach is used in this investigation to gain empirical information related to the above mentioned issues. As a secondary approach, an existing analysis [2, 3, 4] will be used in an attempt to predict thermally-induced microcracking behavior. This analysis will be used to provide additional insight into many aspects of the experimental results obtained in this investigation.

The remainder of this chapter provides a review of past work that has been done in the area of microcracking. A large percentage of this work deals with microcracking in terms of mechanical loading, whether it be static or fatigue loading. More recently, however, with the increasing application of composites in dimensionally critical applications for space, more investigations dealing with thermal loading have appeared in the literature. To gain a better overall understanding, both loading cases must be considered.

The next sections begin with a review of much of the experimental work done in the area of microcracking. The remaining sections consider much of the analytical work. Some of the analytical work reviewed here provides the basis for the existing analysis addressed in the current investigation.

1.3 PAST EXPERIMENTAL CHARACTERIZATION

1.3.1 Microcrack Density Results

This section discusses past results dealing with mechanically-induced and thermally-induced microcracking.

1.3.1.1 Fiber Modulus Trends

Knouff et al. [5] thermally cycled quasi-isotropic laminates to 500 cycles between –250°F and +250°F. Five different fiber types were considered, ranging in stiffness from 57 Msi to 120 Msi. The matrix was an epoxy-cyanate blend known as ERL1939-3. It was found that although it depended on the ply angle, the maximum microcrack density did not vary significantly with fiber type. Fiber type did, however, have a significant effect on the rate of microcracking. Hyperbolic functions were used to describe the microcrack density as a function of the number of thermal cycles, leading to final microcrack density and microcracking rate parameters to describe each material.

McManus et al. [2] present limited microcrack density data on a variety of composites, including a T50/ERL1962, P55/ERL1962, P75/ERL1962, P100/ERL1962, and P120/ERL1962 in both $[0/90]_{2s}$ and $[0/\pm45/90]_s$ configurations. The materials were cycled 50 times between –250°F and +250°F. In general, the microcrack densities were seen to increase with increases in fiber stiffness.

1.3.1.2 Matrix Trends

Sykes et al. [6] considered the effect of low earth orbit (LEO) and geosynchronous earth orbit (GEO) on a variety of thermosetting and thermoplastic composites. Two of interest were the T300/934 brittle epoxy system and T300/BP907, a single phase toughened epoxy resin system. All laminates considered were quasi-isotropic with a lay-up of $[0/\pm45/90]_s$. The LEO and GEO temperature ranges were both represented by extremes of +200°F and –238°F. The GEO specimens also received a dose of 10^{10} rads of radiation to simulate 30 years in orbit. All specimens were cycled 500 times in a nitrogen atmosphere at atmospheric pressure. Specimens were characterized by microcrack density, laminate stiffness, and glass transition temperature. The 934 system cracked significantly due to thermal cycling alone. The BP907 system did not. However, including radiation effects caused the BP907 system to crack far more than the 934 system. Post-cycled stiffness reflected these trends, with small losses in stiffness for the 934 system after cycling and radiation/cycling. The BP907 system had small losses in stiffness after

thermal cycling and large losses in stiffness after radiation/cycling. Glass transition temperatures were seen to decrease slightly for the 934 system after radiation/cycling exposure, but not after thermal cycling alone. Little effect on glass transition temperature was observed in the BP907 system. The conclusion made is that increased matrix toughness may not lead to improved durability in the space environment.

Rawal et al. [7] investigated a number of composite materials, including organic matrix and metal matrix composites. These composites were subjected to 10,000 thermal cycles between −150°F and +150°F. Microcrack densities were recorded in P75/ERL1962 $[0/+45/90/-45]_s$ and $[\pm 30/0_4]_s$ specimens. Microcrack densities of 18 and 6 cracks per in., respectively, were recorded for the two laminates prior to thermal cycling. After 10,000 cycles, increases in microcrack density of 2 and 4 cracks per in., respectively, were reported for the two specimen configurations. Similarly small increases in microcrack density were reported for P75/PEEK specimens, which had initial microcrack densities of 41 and 21 cracks per in. for $[0/\pm 45/90]_s$ and $[\pm 30/0_4]_s$ specimens, respectively.

1.3.1.3 Ply Thickness Trends

Adams et al. [8] studied the effect of layer thickness and adjacent layer constraints on thermally-induced microcracking in cross-ply laminates. Static cooling to −250°F and thermal cycling tests from −250°F to +250°F were conducted to monitor the increase in the number of microcracks in the specimens. It was found that for static cooling tests, the temperature reduction required to initiate cracking decreased as the thickness of the 90° layer decreased. For cyclic testing, the microcrack densities were higher in those laminates with thinner 90° layers.

Tompkins et al. [9] considered three different cross-ply laminates subjected to 1500 thermal cycles from −250°F to +250°F. The three laminates were a $[0/90]_{2s}$ with 0.005 in. thick layers (thick layer/thick laminate), a $[0/90]_{10s}$ with 0.001 in. thick layers having the same overall laminate thickness as the first laminate (thin-layer/thick-laminate), and a $[0/90]_{2s}$ with 0.001 in. thick layers (thin-layer/thin-laminate). The first laminate was referred to as a low interply restraint laminate, whereas the second and third laminates were referred to as high interply restraint laminates, referring to the combined restraining effect of the thin layers and the nearby plies adjacent to the cracking layers. A delay in the onset of microcracking was observed in the thin-layer/thin-laminate, with a noticeable increase in microcrack density occurring only after 1000 cycles. The thin-layer/thick-laminate cracked early, after only 200 cycles, and had final microcrack densities exceeding the thick-layer/thick-laminate by almost a factor of two. Despite the higher microcrack

densities in the thin-layer/thick-laminate, the coefficient of thermal expansion changed little compared to the thick-layer/thick-laminate.

1.3.2 Property Degradation Results

This section discusses past results dealing with property degradation as a result of microcracking. Both mechanically-induced and thermally-induced microcracks are considered here. The two material properties of concern are laminate coefficient of thermal expansion (CTE) and laminate stiffness.

1.3.2.1 Coefficient of Thermal Expansion Trends

The effect of fiber modulus on thermal cycling induced microcracking behavior and the effect on laminate CTE were investigated for quasi-isotropic laminates by Knouff et al. [10]. The materials were cycled up to 500 times between −250°F and +250°F. Microcrack densities and CTE's were reported at various cycling intervals. Laminate CTE's were seen to decrease as a function of the number of thermal cycles. The decrease in CTE's was seen to be more dramatic in the lower modulus T50, P55, and P75 material systems, as opposed to the higher modulus P100 and P120 systems. In all cases the matrix was an epoxy-cyanate blend. Rate parameters were calculated for the reduction in CTE's as a function of thermal cycles and compared to microcracking rate parameters from their previous work [5]. In general, the microcracking and CTE reduction rate parameters for all materials considered followed similar trends with the exception of the P100 material system.

As mentioned previously, Tompkins et al. [9] observed changes in CTE that depended on the thickness of the layers in the laminate. Laminates with relatively thin layers exhibited small changes in CTE compared to laminates with relatively thick layers. This behavior was observed despite the higher number of microcracks present in the laminates with thin layers.

1.3.2.2 Stiffness Loss Trends

Sykes et al. [6] compared stiffness losses in materials exposed to two simulated earth orbit environments. A variety of fiber and thermosetting as well as thermoplastic matrix combinations were used. Each of these materials was exposed to thermal cycling alone as well as thermal cycling and radiation exposure. It was observed that stiffness losses were minimal due to thermal cycling exposure alone. In fact, stiffness increases were observed in some of the materials, probably due to manufacturing variations. Those materials exposed to thermal cycling as well as radiation were seen to exhibit significant reductions in stiffness.

Bowles and Shen [11] cycled P75/934 cross-ply laminates for up to 250 thermal cycles between −250°F and +250°F. Microcrack densities were observed in the 90° layers to be approximately 50 cracks per in. after 250 cycles. Room temperature stiffness losses after 250 cycles were seen to be approximately 10 percent of the original room temperature stiffness.

Highsmith and Reifsnider [12] investigated the loss in laminate stiffness due to mechanically-induced microcracking. They performed quasi-static and tension-tension fatigue loadings of four different laminate configurations: $[0/90_3]_s$, $[90_3/0]_s$, $[0/90]_s$, and $[0/\pm45]_s$. All laminates were made from a 1003 Scotchply glass-fiber-reinforced plastic. For quasi-static loading of the $[0/90_3]_s$ and $[90_3/0]_s$ specimens, stiffness was observed to decrease as microcrack density increased. Stiffness decreases of 45 percent and 37 percent, respectively, were observed for the $[0/90_3]_s$ and $[90_3/0]_s$ specimens. Fatigue loadings using a stress ratio of R=0.1 resulted in decreases in stiffness of approximately 15 percent for the $[0/90]_s$ specimens compared to approximately 12 percent for the $[0/\pm45]_s$ specimens. Again, for the fatigue loadings, stiffness was observed to decrease in close relation to increases in microcrack density. It was concluded that microcracks were directly responsible for the loss in stiffness in the specimens and that the magnitude of the stiffness loss was directly proportional to the number of microcracks in the specimens.

1.4 PAST ANALYTICAL CHARACTERIZATION

In general, models dealing with microcracking deal with the problem in two stages. The first stage deals with prediction of microcrack initiation due to static mechanical or static thermal loading, and microcrack progression with mechanical or thermal loading cycles. The goal of this first stage is typically to predict the distance (spacing) between the microcracks, or more commonly, the inverse of the distance between microcracks, the microcrack density, ρ (microcracks per unit length). Once the microcrack density as a function of loading (mechanical or thermal) is known, the second stage of modeling follows - the prediction of damaged laminate properties, i.e., stiffness and coefficient of thermal expansion as a function of microcrack density. In some cases, the prediction of damaged properties is a direct extension of the model, e.g., the shear lag and variational models. In other cases, a new model is developed explicitly for the purpose of property determination, e.g., the continuum damage mechanics model. There are, however, exceptions to the two-stage procedure. Some models do not base degraded property predictions on microcrack spacing, but rather, predict property variations directly, and may or may not predict microcrack spacing at all. All of the models will be reviewed in some detail in this chapter, and the identifying characteristics of each will be outlined.

Microcracking models which predict crack initiation and/or crack progression can be divided into two distinct categories:

1) strength models
2) fracture mechanics models

These two types of models will be discussed separately. Before this is done, the methods used to determine the stress state in the laminate will be examined. Only after the state of stress, and strain in some cases, is known, can these crack prediction models be applied.

1.4.1 Modeling the State of Stress

The section briefly describes many of the methods which have been used by investigators in approximating the stress state in composite laminates subject to either mechanical and/or thermal loads. As will be seen, a substantial effort has been placed on this aspect of modeling. The majority of the models to date have been concerned with microcracking in cross-ply laminates, primarily because this is the first type of laminate in which microcracking was observed, but also because approximating the stress state in cross-ply laminates is far easier than for more general laminates. As a result, some of the approximate stress analyses are valid for cross-ply laminates only, and cannot be extended to more general laminates.

1.4.1.1 Shear Lag Theory

One important model used by many investigators is the one-dimensional shear lag model. The basic premise behind the one-dimensional shear lag model is that of a plane-strain model, whereby only inplane displacements are considered and are assumed to be uniform throughout the thickness of the layer. Governing equations are then formulated based on simple one-dimensional equilibrium. The final condition is that the shear stress present between any two layers is assumed to be proportional to the relative displacement between those two layers.

One of the first microcracking models was developed by Garrett and Bailey [13] who used a one-dimensional shear lag analysis to investigate transverse matrix cracking in cross-ply laminates subjected to mechanical loading. To the authors knowledge, they were the first to apply the shear lag concept to the transverse ply cracking phenomenon. The shear lag concept had been previously applied to composite fracture by Hedgepeth [14], but in conjunction with fiber breakage in unidirectional composites. Applied to unidirectional composites, the idea is that when the stiff tensile-load-bearing members, the fibers, undergo fracture, they transfer their load to a neighboring unfractured fiber through a compliant shear transfer zone, the matrix. Due to this shear transfer, the tensile stress in the broken fiber varies from zero at the point of breakage to its

original value at some distance from the break. This distance is sometimes referred to as the ineffective length of the fiber. Garrett and Bailey apply this concept to transverse matrix cracking. Here, the weaker 90° plies fracture and transfer load via shear to the adjacent stiffer 0° plies. The shear transfer takes place in a negligibly small region between the plies, typically considered to be a resin rich area. The shear lag concept, as applied to the transverse matrix cracking, is illustrated in Figure 1.2. In solving for the stress state surrounding the matrix crack, a second order differential equation governs the increased stress, $\Delta\sigma$, carried by the surrounding unbroken 0° plies. This governing equation is given by

$$\frac{d^2\Delta\sigma}{dy^2} = \phi\Delta\sigma$$

where (1.1)

$$\phi = \frac{E_c G_t (b+d)}{E_1 E_t b d^2} \quad .$$

The general solution is given by

$$\Delta\sigma = \Delta\sigma_o \exp(-\phi^{1/2} y). \qquad (1.2)$$

In Equation 1.2, y=0 is at the location of the crack, and E_1, E_c, and G_t are the extensional moduli of the 0° ply and the composite, and the inplane shear modulus of the cracking ply, respectively. Note that the increase in normal stress in the adjacent 0° plies decays exponentially from the crack as more and more stress is transferred into the cracking ply via shear stresses. The variation in stress around the microcrack is a function only of the material properties of the laminate and the thickness of the plies. As will be seen in other shear lag models, additional terms are sometimes included in the formulation which must be empirically determined. These additional terms can be considered as weighting factors which serve to improve the accuracy of the model.

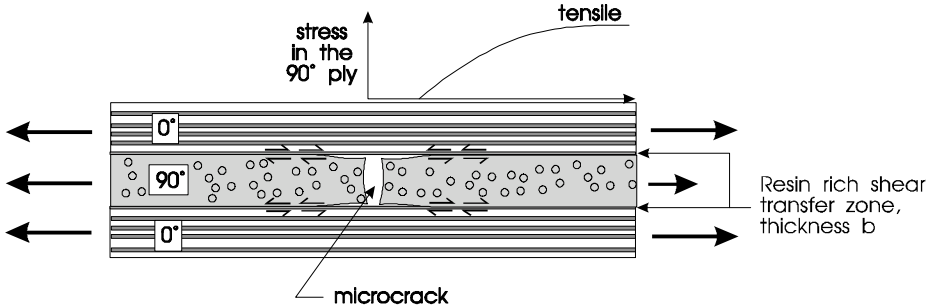

Figure 1.2. Shear lag concept in a cross-ply [0/90/0] composite laminate.

Highsmith and Reifsnider [15] investigate the stress state predicted by shear lag theory on a series of cross-ply and quasi-isotropic graphite-epoxy laminates subjected to mechanical loading. This model stems from the one presented earlier by Reifsnider [16] which investigated the microcrack saturation density of a laminate subjected to unidirectional mechanical loading. The thickness of the shear transfer region is not neglected in their model, but rather it is included as an additional parameter which is experimentally determined. Results from the shear lag model are shown to overpredict the inplane normal stresses away from the crack compared to finite-difference results for the same laminates. The distance, however, from the crack at which stable normal stress is regained is shown to correlate fairly well with finite-difference results. The shear lag model predicts that the stress state in the 90° plies away from the crack is a strong function of the layup. Namely, the distance from the crack at which stable stress is regained for a $[0/\pm45/90]_s$ laminate is greater than the distance for a $[0/90/\pm45]_s$ laminate. This suggests a difference in 90° ply constraint for the two laminates. This constraint concept is one originally discussed by Flaggs and Kural [17] and will be discussed later in the failure prediction section. Highsmith and Reifsnider predict that, loaded to the same level, the $[0/90/\pm45]_s$ laminate should ultimately have a higher microcrack density since a larger volume of the material is subjected to increased stress levels. Highsmith and Reifsnider also introduce the terminology characteristic damage state (CDS) to represent the saturated microcrack density just prior to ultimate failure of the laminate.

Laws and Dvorak [18] also use a one-dimensional shear lag model, but include residual thermal stresses in addition to mechanical stresses in the equilibrium formulation. They introduce the concept of a non-dimensional shear lag parameter, ξ, which is calculated from material and geometric parameters, including the critical strain energy release rate of the material and the first ply failure stress. They are concerned with microcrack progression rather than initiation, therefore, they develop expressions for the stress state between two cracks which are assumed to initially exist.

McManus et al. [2] and Park [3] use one-dimensional shear lag models to predict the effect of thermal loading on the microcracking behavior of composite materials. These authors are the first to deal specifically with thermal loading, neglecting mechanical loading entirely. Both models use a shear lag formulation identical in form to that used by Laws and Dvorak [18]. In the model by McManus et al., only cross-ply laminates are considered and Park extends the methodology to consider more general laminates as well. In Park's model, all layers above and below the cracking layer are smeared to appear as a single layer above and a single layer below the cracking layer. Maddocks and McManus later extend this general model to include combined thermomechanical loading [4].

Flaggs [19] extends the idea of the shear lag model to deal with out-of-plane stress components in addition to the inplane component considered in the conventional one-dimensional shear lag model. Flaggs refers to this model as a two-dimensional shear lag model. The two-dimensional shear lag model accounts for the redistribution of inplane normal stresses around the microcrack, as well as through-the-thickness shear stresses. The resulting governing system of equations are two coupled second order ordinary differential equations. Solving the system of equations, Flaggs goes on to deal with only the inplane portion of the problem when applying the failure criterion to determine the formation of microcracks.

Lim and Hong [20] improve upon a derivation by Fukunaga et al. [21] for unidirectional loading of cross-ply laminates including residual thermal effects. The model is a variation of the one-dimensional shear lag model which incorporates a separate shear transfer region between the layers, similar to that by Highsmith and Reifsnider [15], but possessing its own unique material properties. This model is most appropriately referred to as quasi-two-dimensional, including limited inplane displacements in the non-loading direction due to Poisson effects. Unlike the model by Fukunaga et al., the model by Lim and Hong satisfies boundary conditions as the crack spacing becomes small. The stress approximation includes a parameter similar to the shear lag parameter of Laws and Dvorak [18], which is a function of the material and geometric properties of the individual layers. Now, however, this parameter includes separate material properties for the additional shear transfer zone between the plies.

Lee and Daniel [22] developed what they refer to as a ‘simplified shear lag analysis’ for uniaxial tensile loading of symmetric cross-ply composites. The model includes residual thermal stresses in its formulation. This model is later extended to biaxial inplane tensile loading by Tsai, Daniel, and Lee [23]. The model uses a shear lag parameter, H, in Reference [22], which is later referred to as an interlaminar shear stiffness in Reference [23], to describe the variation in stresses around an existing microcrack. Unlike classical one-dimensional shear lag models, the simplified shear lag model includes interlaminar shear stresses and allows for inplane displacements which are a parabolic function of the through-the-thickness coordinate. However, the out-of-plane displacement is neglected. In addition, in order to solve the governing equations, the parabolic inplane displacements are eventually averaged through the thickness of each ply, negating the benefit gained by the previous parabolic distribution assumption. The uniaxial loading case results in a single ordinary differential equation which is solved to determine the axial stress in the cracked ply, which is then used to also determine the stress in the uncracked ply. The biaxial loading case results in a system of partial differential equations in terms of the displacements in the two directions. In the biaxial loading case, the notation follows that used in classical

lamination theory which is well suited to the averaged quantities used in the analysis. Thomas and Wetherhold [24] later extend this theory to general symmetric laminates.

1.4.1.2 Variational Approach

Nairn [25] presents a variational model, the theory behind which was originally outlined by Hashin [26], to predict microcracking in a cross-ply laminate subject to mechanical loads and taking into account residual thermal stresses. Nairn provides an argument against the use of a shear lag model by stating that the shear lag concept, originally developed for unidirectional composites, works well in that type of application, where the stiffness of the fibers is much greater than that of the matrix. In the microcracking problem, however, the stiffness of the transverse ply undergoing cracking is comparable to the stiffness of the matrix. This, according to Nairn, is a fundamental violation of the shear lag requirement. In the variational technique, the stress state in the uncracked laminate, σ_{xo}, is said to vary with spatial location by some unknown function, ψ, once cracks develop in the laminate. The stress state defined between two existing cracks is therefore given by the following relations:

$$\sigma_x^{(1)} = \sigma_{xo}^{(1)} - \psi_1(x) \quad \textit{and} \quad \sigma_x^{(2)} = \sigma_{xo}^{(2)} - \psi_2(x), \tag{1.3}$$

where the superscripts 1 and 2 indicate the cracking layer (90°) and adjacent layer (0°), respectively, and just like in shear lag theory, the inplane normal stress components do not vary in the thickness direction. In the above equation the *x* direction is the inplane longitudinal loading direction. The variational model does, however, include the through-the-thickness normal and shear stresses which are neglected in the one-dimensional shear lag model. By substituting the expressions for stress into equilibrium and by applying boundary and interface conditions, as well as the principle of minimum complementary energy, the complete thermoelastic stress state is determined by finding the functions $\psi_1(x)$ and $\psi_2(x)$ which produce the minimum value of complementary energy. This analysis, despite its more accurate solution compared to shear lag theory, is limited to simple cross-ply laminates.

Varna and Berglund [27] present another variational model which follows very closely that derived by Nairn [25] and again which is only applicable to cross-ply laminates. The only difference in the model by Varna and Berglund is that additional terms in the stress formulation are included to account for through-the-thickness variations in the inplane normal stress. In actuality, however, the final stress state derived for the 90° plies does not depend on the through-the-thickness coordinate, leaving an improvement only in the 0° layer stress predictions.

1.4.1.3 Other Methods for Determining the State of Stress

Sriram and Armanios [28] develop what they refer to as a shear deformation model, which is similar in principle to a shear lag model, but deals with through-the-thickness averaged laminate quantities such as those used in classical lamination theory. The model as presented is limited to mechanical loads, but incorporation of thermal loading would require little effort. Microcracking is limited to symmetric laminates only and in the 90° plies only. The plies to either side of the cracking 90° plies, however, can be of any orientation. The 90° plies can also be located anywhere throughout the laminate, as long as the laminate remains symmetric. The model should probably be referred to as quasi-two-dimensional, since it takes into account the through-the-thickness shear effects, but restricts the through-the-thickness displacement to be zero. This, as pointed out by the authors, does result in an unrealistic shear stress along the crack face, and one which physically cannot exist. As with some of the other models, the calculated stress state is derived for a laminate with a pre-existing crack, and hence, the crack initiation problem is ignored. The resulting boundary conditions from the presence of the crack are used to solve the governing equilibrium equations.

Nuismer and Tan [29] and Tan and Nuismer [30] present an approximate elasticity solution to predict the stress state in a symmetric microcracked laminate. The analysis is valid for general ply orientations, but the cracking is assumed to exist only in the 90° plies, which must be located at the midplane of the laminate. The model is valid for mechanical loading, be it inplane normal or shear, as well as thermal or moisture effects. By defining average quantities through a lamina thickness, including average equations of equilibrium, the problem is reduced to solving a single ordinary differential equation for interfacial shear stress.

Allen and Lee [31] use a different approach, referred to as the Internal State Variable (ISV) approach. The ISVs are defined, for instance, to be the volume-averaged value of the diadic product between the displacement vectors and the unit normals to the internal traction-free surfaces of microcracks. In the ISV approach, a randomly cracked cross-ply laminate is replaced by a representative 90° ply segment with a statistically averaged volume, bounded on two sides by microcracks and above and below by layer interfaces. The resulting displacement in the representative segment becomes independent of stacking sequence. Finally, the segment is handled as an equivalent undamaged homogeneous material with degraded stiffness and strength as functions of the applied stress or strain. To evaluate the stress state in the representative segment, displacements are assumed in three dimensions in terms of internal state variables, and strains are then calculated and substituted into constitutive relations to obtain the thermomechanical stress state. This analysis is extended to more general laminates with off-axis

plies and subjected to inplane tensile and shear loading. Results are presented for general laminates subjected to monotonic loading and cross-ply laminates subjected to monotonic and cyclic loading.

1.4.2 Modeling the Development of Microcracks

Once the stress state in the laminate has been defined, the next step is typically to model the development and accumulation of microcracks. This is done in a variety of ways, many of which are discussed in this section.

1.4.2.1 Strength Models

The static strength based models are conceptually simple to understand. They rely on failure criteria of some type to determine when the matrix fails and a microcrack occurs. The failure criteria used range from a simple maximum stress failure criterion [13], to a combined stress criterion such as that proposed by Hashin [32] and implemented by Flaggs [19]. These failure criteria typically deal with both crack initiation and crack progression. In a cross-ply laminate, for instance, the crack initiation occurs when the stress in the 90° ply exceeds the failure stress, i.e., σ_{2u} or Y_t, for the first time. Crack progression is dealt with in a systematic way by modifying the stress state in the adjacent 0° plies each time a new crack occurs in the 90° ply. The cracking process continues in the 90° plies until the additional stress in the 0° plies becomes large enough to cause failure in those plies, and hence failure of the laminate. Similar techniques are used for more general laminates as well.

A significant phenomenon related to strength failure criterion, that of in-situ lamina failure properties, was first observed by Aveston and Kelley [33] and Parvizi et al. [34] who at the time were investigating in-situ first failure strains and the constraining effect of the 0° plies surrounding the cracking 90° plies in cross-ply laminates. The phenomenon of in-situ lamina strength was later investigated by Flaggs and Kural [17]. Flaggs and Kural also observed this apparent constraining effect in a variety of laminates, i.e., $[0_2/90_n]_s$, $[\pm 30/90_n]_s$, and $[\pm 60/90_n]_s$, subjected to mechanical loading. Basically, the plies adjacent to the cracking 90° plies have a constraining effect which influences the stress at which failure, i.e., microcracking, occurs in the 90° plies. Flaggs and Kural employ a fracture mechanics approach based on stresses determined from classical lamination theory to predict the onset of microcracking. They demonstrate that the in-situ strength is a function of lamina thickness as reported by earlier investigators [33, 34] and also the orientation of the plies adjacent to the cracking plies. The observed *in-situ* strength of the 90° plies was observed to be as much as 2.5 times that of the transverse unidirectional tensile

strengths. Flaggs and Kural go on to use a two-parameter Weibull statistical distribution to describe the lamina strength as a function of the material volume being stressed. The conventional approach is used, whereby the scale and shape parameters describing the distribution are assumed to be material constants. They conclude that this assumption does not adequately describe the observed in-situ strength behavior. They do find, however, that if one of the parameters is allowed to be a function of the stiffness of the adjacent plies, excellent correlation can be obtained. This, they point out, may not be a valid application of the Weibull distribution. They conclude by stating that in-situ strength has not been adequately described in the context of a general strength theory.

Garrett and Bailey [13] use the maximum stress failure criterion to predict when the first crack will occur, as well as subsequent crack formation due to monotonically increasing load. They assume that the cracks first form midway along the length of the specimen, followed by cracks at both ends of the specimen, and then midway between existing cracks from then on. From this they can determine a crack spacing as a function of applied load. This is a relationship whereby continuous increases in load result in the formation of discrete cracks and hence discrete reductions in the crack spacing, giving a stairstep appearance to the graphical relationship between load and laminate strain. Microcracks continue to form until the stress transferred to the adjacent 0° plies is sufficient to cause failure in the 0° plies. In equation form, this final failure occurs when

$$\sigma_{lu} b \geq \sigma_{tu} d + \sigma'_1 b, \qquad (1.4)$$

where σ_{lu} and σ_{tu} are the strength of the 0° and 90° plies, respectively. The stress σ'_1 is the additional local stress placed on the longitudinal plies as a result of the microcrack formation. Finally, b and d are the thicknesses of the longitudinal and transverse plies, respectively.

Allen and Lee [31] use their ISV approach to predict monotonic matrix cracking based on a maximum stress type failure criterion. They do so in a somewhat different sequence than done by other authors. Allen and Lee formulate a damaged stiffness in their representative segment and use this stiffness to calculate the stress in the segment. It is this value of stress that is used to predict, by way of the maximum stress failure criterion, when a new crack forms in the laminate. Microcrack density results are presented for the monotonic mechanical loading of cross-ply laminates and compared to experimental data from previous authors. In general, good correlation is seen between analysis and experiment for the limited data presented. Other authors using a simple maximum stress failure criterion include Lee and Daniel [22] and Tsai, Daniel, and Lee [23].

Fukunaga et al. [21] assume that the strength of a unidirectional lamina follows a two-parameter Weibull cumulative distribution function. A failure probability for the 90° ply is established for a given stress which accounts for the nonuniformity of the stress distribution due to pre-existing cracks. Hence, their failure criterion predicts the formation of an additional crack between two existing cracks. To simplify calculations, they assume that a new crack forms halfway between two existing cracks at a 50% failure probability. They obtain a relation which predicts crack spacing versus stress in the 90° ply.

As seen in the above references, many of the strength models proposed to date have employed a simple maximum stress failure criterion to determine the onset of microcracking and perhaps the progression of microcracking. These models ignore the in-situ strength effect pointed out by many authors. There are some authors, especially recently, who try to better deal with the issue of in-situ strength by employing modified failure criteria. Still others choose to ignore the strength issue by cleverly removing strength from the failure prediction.

Reifsnider [16] avoids the issue of microcrack initiation and development by concentrating on the final damaged state which, as mentioned earlier, is referred to as the characteristic damage state. It is assumed that a microcrack initially develops, but no attempt is made to predict when it occurs. Instead, the shear lag model is used to characterize the inplane normal stress away from the location of the existing crack. The critical assumption that is made is that the second crack, adjacent to the first, will form when the normalized inplane normal stress reaches a value of 1.0, i.e., the value at which the first crack occurred. By normalizing quantities, the strength of the ply never enters the analysis. And since the normalized inplane normal stress between these existing cracks is always below 1.0, no new cracks form between the original and the newly predicted crack. As a result, the spacing between these cracks is proposed to be the saturation spacing of the laminate. The analysis is extended to both cross-ply laminates as well as quasi-isotropic laminates, showing fairly good correlation between analysis and experimental results. The analysis also demonstrates the correct trend for varying ply thicknesses, i.e., the saturation spacing is greater (lesser microcrack density) for thicker plies. For the graphite-epoxy material system studied, a single value for the shear layer thickness, b, was used. This value was determined from experimental results. This parameter can be used to adjust the results to fit data from other material systems, as seen by the different value for glass-epoxy used in the later work by Highsmith and Reifsnider [15]. Burr and Sikarskie [35] have successfully used this idea to model microcracking in woven glass-epoxy composites. Their analysis matches experimental results very well.

An example of a model employing a modified failure criterion is the one by Chang and Lessard [36], which modifies observed behavior witnessed by previous researchers. Chang and Lessard note that previous researchers have pointed out that in-situ transverse tensile strengths tend to vary roughly as one over the square root of the number of consecutive (clustered) plies. To account for the fiber orientations of the layers adjacent to the cracking layer, Chang and Lessard introduce the failure criterion

$$Y_t = Y_t^o \left(1 + A \frac{\sin(\Delta\theta)}{N^B} \right), \qquad (1.5)$$

where Y_t is the transverse strength of the laminate, $\Delta\theta$ is the minimum ply angle change between the ply under consideration and its neighboring plies, N is the number of consecutive (clustered) plies of the same orientation, Y_t^o is the transverse strength of a $[90_n]_s$ laminate ($n \geq 6$), and A and B are material parameters determined from experiment. By varying the material parameters, Chang and Lessard match experimental data reasonably well.

1.4.2.2 Fracture Mechanics Models

The fracture mechanics models analyze microcracking from an energy viewpoint. It is postulated that the microcrack will form when it is both mechanistically possible and energetically favorable [37]. The mechanistic possibility is typically argued as being a result of the stress singularity due to fiber/matrix debonds which serve as the crack initiation site [19, 38, 39]. Thus the question of microcrack formation is reduced to determining when it is energetically favorable for the crack to occur. The crack formation becomes energetically favorable when the strain energy release rate from forming a new crack exceeds some critical value. This critical value is referred to as the mode I critical strain energy release rate, G_{Ic}. This critical release rate is a material property related to the fracture toughness of a given material.

Laws and Dvorak [18] calculate the work done in generating a new crack as well as the increase in strain energy resulting from the crack. A formula is derived for the shear lag parameter, ξ, based on experimentally determined values of G_{Ic} and the first ply failure stress. The model predicts progressive transverse cracking based on statistical principles. There are three statistical choices used to predict the location of new crack formation between two existing cracks: 1) guaranteed to occur at the midpoint between the two cracks - for this a closed-form solution is obtained, 2) randomly between the two cracks, and 3) the probability density function is proportional to the stress in the 90° ply. Comparisons are made between the analysis and experimental data from Highsmith and Reifsnider [15]. By varying the critical strain energy

release rate and/or the choice of probability distribution for the location of the next crack forming, qualitatively correct predictions of microcrack progression are seen. Much better correlation is seen when compared to the graphite-epoxy material systems of Wang [40].

Nairn [25] uses a procedure very similar to that of Laws and Dvorak [18], including the choice of probability distribution for the formation of a new crack between two existing cracks. The expression for critical strain energy release rate obtained by Nairn is independent of the sign of the thermal stresses, a mistake according to Varna and Berglund [27]. Sriram and Armanios [28], although they have not included crack predictions in their model, leave this for future work and claim to follow the methodology employed by Nairn.

McManus et al. [2] use an energy-based model to predict cracking due to monotonic and cyclic thermal loading of cross-ply composite laminates. Much of the formulation is borrowed from Laws and Dvorak [18]. The model uses a shear lag theory and one-dimensional equilibrium considerations to develop the critical strain energy release rate due to crack formation in a simple cross-ply laminate. Cracking is assumed to take place in 90° degree plies only. The critical strain energy release rate and shear lag parameter are calculated for the monotonic loading case by fitting the model predictions to experimental monotonic cooling data for P75/934 graphite-epoxy laminates. The analysis is extended to thermal cycling by developing ratios between the static and cycling tests using a modified approach of Petitpas et al. [41]. A relation is derived for $G_{IC}(N)$ based on $G_{IC}(0)$, where the N represents the number of thermal cycles and the (0) represents the static case. McManus et al. present parametric results to indicate the sensitivity of microcrack density for monotonic cooling and thermal cycling to such parameters as G_{IC} and ply thickness. Park [3] extends this model for more general laminates. The trends seen in experiment are qualitatively predicted by the analysis, but in general, accurate quantitative predictions are not seen with this model.

Varna and Berglund [27] develop a fracture criterion based on energy principles. They compare their criterion to the one obtained by Laws and Dvorak (shear lag), and to the one obtained by Hashin by variational principles (actually it is one obtained by Nairn, but then corrected by Varna). This provides an excellent opportunity to compare the three fracture criteria. Varna and Berglund's criterion is as follows:

$$(\varepsilon_o + \varepsilon_T)^2 E_T d \left[\frac{4\alpha}{\alpha^2 + \beta^2} \left(1 + \frac{E_T d}{E_L b} \right) - \langle\ \rangle_{\alpha,\beta} \right] = G_{IC}(L)$$

where Reference 27

$\langle\ \rangle_{\alpha,\beta}$

is given in the paper and is responsible for the minimum value of complementary energy. The *L* and *T* refer to the longitudinal, i.e., 0°, and transverse, i.e., 90°, directions. The thickness of the cracking layer and adjacent layer are 2*d* and *b*, respectively. The expression by Laws and Dvorak is given by:

$$(\varepsilon_o + \varepsilon_T)^2 E_T d \sqrt{\frac{E_T}{dG/d_o}\left(1 + \frac{E_T d}{E_L b}\right)} = G_{IC}(L) \qquad \text{Reference 18}$$

and the corrected version of Nairn's, which Varna and Berglund refer to as Hashin's, is given by:

$$(\varepsilon_o + \varepsilon_T)^2 E_T d \sqrt{\frac{E_T}{C_v}\left(1 + \frac{E_T d}{E_T b}\right)} = G_{IC}(L) \qquad \text{Reference 25 - corrected}$$

where $C_\nu = f(E,G,d,b,\nu)$. Varna and Berglund present comparisons with previously obtained experimental data for cross-ply laminates. They show that for increasing 0° layer to 90° layer ratios, their model better predicts the crack initiation strain than Hashin's model. As the number of 90° plies increases, the two are virtually indistinguishable. For thin 90° plies, Hashin's model is said to be showing too weak a constraint effect from the adjacent 0° plies. Varna and Berglund's model predicts lower initiation strains and provides reasons as to why. In general, many of their statements are directed at ply thickness effects and more specifically, the ratio of 0° plies to 90° plies.

Lim and Hong [20] use a cracking criterion to predict the onset of microcracking. By using an existing stress analysis between equally spaced cracks which were assumed to already exist, they assume that the region between two of the existing cracks is an uncracked laminate of infinite length. The cracking criterion in mathematical form is

$$\frac{d}{da}(W - U) \geq 2dG_{Ic} \qquad (1.6)$$

where *W* is the work done by the external load, *U* is the stored elastic strain energy in the laminate, G_{IC} is the critical strain energy release rate in the fiber direction, and *a* is the growth of a transverse crack. This criterion is based upon the assumption of the growth of the transverse crack spanning the entire thickness of the 90° layer in the direction normal to the applied stress and parallel to the direction of the fiber. Instead of this crack growth criterion, however, they adopt the criterion used by Bailey et al. [37] and Flaggs [19].

Flaggs [19] develops a mixed mode strain energy release rate fracture criterion. This idea stems from the mixed mode 'tensile matrix' failure criteria of Hashin [32] which assumes that

microcrack formation is a function of both the inplane normal stresses and the inplane shear stresses. Flaggs cites references of experimental evidence supporting this mixed-mode failure source. This paper deals with the microcracking on the first ply failure level, attempting to determine the lamina strain at which microcracking initiates. Analytical predictions of initiation strains are compared to the experimental results of Flaggs and Kural [17] for $[0_2/90_n]_s$, $[\pm30/90_n]_s$ and $[\pm60/90_n]_s$ graphite-epoxy laminates. By varying a critical parameter of the failure model, excellent correlation is seen between analysis and experiment.

Nuismer and Tan [29] and Tan and Nuismer [30] develop expressions for energy stored and released by forming a new crack between two existing cracks. The new crack is assumed to occur halfway between the existing cracks. The applied inplane loading is in the form of an average extensional strain, including residual thermal strains. By allowing the crack spacing to approach infinity, they derive the first ply failure stresses and strains. The authors bring up the point that in a perfectly homogeneous material, the cracking occurs in a discrete stepwise fashion, so that a plot of strain versus crack density or a stress versus crack density appears stair-like. It should be noted that this behavior was also predicted by Garrett and Bailey [13]. Tan and Nuismer also note that a composite is not perfectly homogeneous and for that reason, the behavior should be 'smoother', with some cracks occurring at random times, helping to make the stress versus crack density relationship smoother. For the perfectly homogeneous material, they claim that a range of stress versus crack density would be better suited to accurately show behavior. Comparisons are made between the current model and other predictions. Comparing to the experimental work of Flaggs and Kural [17], both models predict the first ply failure strains for $[0_2/90_n]_s$ and $[\pm30/90_n]_s$ laminates reasonably well, with the second model [30] showing slight improvements over the first [29]. Tan and Nuismer also compare their predictions to the two-dimensional shear lag theory of Flaggs [19], showing similar results to Flaggs' for in-situ predictions. One major advantage to this theory is that only basic material properties such as moduli, Poisson's ratio, thermal expansion coefficients, and specific fracture energy are needed. It is stated that the model will be later improved to include cracking plies other than the central 90° plies.

1.4.3 Modeling Property Variations due to Microcracking

One of the primary reasons for understanding microcracking behavior has been to predict how this damage phenomenon affects the laminate response. One of the oldest and simplest techniques for analyzing the influence of microcracks is referred to as the ply discount method. In this technique, typically, the transverse modulus, E_2, and inplane shear modulus, G_{12}, of the

cracking ply are reduced to zero. For thermal applications, the transverse CTE, α_2, of the cracking ply is also reduced to zero. This technique is very conservative and can significantly overestimate the change in laminate stiffness and CTE. For this reason, a number of other models have been proposed. Many of the models previously discussed, e.g., shear lag models, which were used to predict microcrack formation are also used to predict these material property variations due to microcracking. In other cases, such as the continuum damage mechanics models, the models have been developed explicitly to deal with property variations resulting from a prescribed microcrack density.

1.4.3.1 Shear Lag Models

Highsmith and Reifsnider [15] investigate the stiffness loss in glass-epoxy laminates which were selected specifically to experience large decreases in stiffness due to the presence of microcracks. The stiffness reduction is calculated directly from the shear lag analysis for a prescribed microcrack density as observed in experiment. For the $[0/90_3]_s$ laminate investigated, the shear lag analysis predicts the proper trend for stiffness loss, but in general underpredicts the magnitude of the stiffness loss (non-conservative). They also calculate the stiffness loss from the ply discount method whereby they reduce the transverse modulus, E_2, in the cracking plies to zero. This, as pointed out earlier, overpredicts the stiffness loss (conservative). They note that by varying the shear layer thickness, b, a closer approximation may be obtained.

1.4.3.2 Fracture Mechanics Models

The model of Laws and Dvorak [18] uses the displacements between two existing cracks derived from its fracture mechanics approach to derive an average laminate strain and an effective stress-strain relation for the cracked composite. Neglecting the permanent strain due to initial stresses, they obtain a laminate stiffness as a function of crack density. The laminate stiffness approaches the original uncracked laminate stiffness as the crack density approaches zero, and to the stiffness predicted by ply discount theory as the crack density approaches infinity. By adjusting the value for the critical strain energy release rate, they improve upon the loss of stiffness predictions of Highsmith and Reifsnider [15] for the $[0/90_3]_s$ glass-epoxy laminate.

McManus et al. [2] use the expression of Laws and Dvorak [18] for the damaged stiffness as a function of microcrack density. McManus et al. then go on to derive a simple knockdown factor for the damaged stiffness in the cracking ply only as a function of the undamaged material properties, shear lag parameter, and the microcrack density. They then use this knockdown factor to modify the constitutive relations from classical lamination theory. Specifically, they multiply

the knockdown factor times each of the reduced stiffnesses, excluding the longitudinal, Q_{11}, term. This is done for each layer undergoing cracking. The effective modulus of the damaged laminate is then calculated as a symmetric laminate property as defined in classical lamination theory. The effective coefficient of thermal expansion of the damaged laminate is calculated in the same manner. Some parametric studies are then performed by McManus et al., to better understand the dependence of microcrack density on property variations for a variety of P75/ERL1962 graphite-epoxy cross-ply laminates. Park [3] also uses this same methodology, but in the context of more general laminates. Predictions of stiffness loss and change in coefficient of thermal expansion are made for a variety of lamination sequences for a graphite-epoxy material system.

1.4.3.3 Continuum Damage Mechanics Models

Talreja [42] derives a damage tensor to predict the stiffness reduction due to microcracking in composite laminates subjected to mechanical loading. In this theory, the cracks are represented by vector components whose magnitudes are functions of the cracks per unit surface area, or microcrack density, and the average length and width of the crack, generally taken to be the width of the laminate and the thickness of the cracking ply, respectively. The damaged stiffness relationships are calculated by knowing material constants which are calculated from E_1, E_2, G_{12}, and ν_{12} of the undamaged laminate and of the damaged laminate at a known microcrack density, typically the saturation density. Talreja suggests the use of a cross-ply laminate configuration for determining the values of the unknown material constants. The predicted stiffness loss versus load shows very good correlation with the experimental results of Highsmith and Reifsnider [15] for the cross-ply glass-epoxy laminates for both static and fatigue loading. Even better predictions are seen when compared to the graphite-epoxy material of Kistner et al. [43], including that of the change in major Poisson's ratio in the highly constrained laminates. In addition, Talreja concludes that the ply discount method is unreliable for predicting minimum values for cracked laminates, particularly in the low constraint laminates. Talreja [44] later extends this work to include the effects of interlaminar cracking as well as intralaminar cracking. Talreja et al. [45] investigate the effect of laminates with differing matrix toughness. Experimentally, the Poisson's ratio is seen to vary differently for different matrix materials with the same density of microcracks. This is a phenomenon that is predicted fairly well by the continuum damage mechanics model.

1.4.3.4 Internal State Variable Models

Based on their model [31], Allen and Lee develop a modified constitutive theory based on the ISV approach. They derive a damage parameter which modifies the reduced stiffnesses from classical lamination theory, which can then in turn be used to calculate the damaged laminate stiffness. The damage parameter is a function of material properties and a prescribed crack spacing in the laminate. This theory can be applied to any general laminate with prescribed crack spacing in each layer. Alternatively, the damage parameters can be calculated from a limited experimental data set and applied through an alternative constitutive relation to a more general laminate. The authors claim that this theory provides an upper bound for stiffness loss, i.e., non-conservative. Predictions of stiffness loss are compared to previous experimental results for glass-epoxy and graphite-epoxy cross-ply laminates. Reasonable correlation is seen, with the theory demonstrating an upper bound to stiffness loss in most cases.

1.5 REMAINING CHAPTERS

This concludes the review of past work in the area of microcracking. The remaining chapters deal specifically with the experimental and analytical research performed as a part of the present investigation. Chapter 2 outlines the procedure and materials to be included in the experimental program. Chapter 3 presents the experimental results obtained as well as conclusions made based on these results. Chapter 4 presents the theory of the analysis to be used to predict and compare to the experimental results presented in Chapter 3. Also in Chapter 4 are comparisons between analytical predictions and experimental results. Finally, Chapter 5 presents a summary of important findings and conclusions, as well as recommendations for future work.

2. EXPERIMENTAL PROGRAM

The goal of the experimental phase of this study is to empirically characterize the effects of long-term thermal cycling in a variety of polymeric composite materials. The composite materials of interest for this work are those considered for dimensionally critical space applications, namely materials with a high stiffness and a low thermal expansion. The effect of thermal cycling on these two material properties is of primary concern here.

As was discussed in Chapter 1, previous authors have shown that a relatively low number of thermal cycles can produce microcracks in composite materials. These thermally-induced microcracks have been shown to produce significant changes in thermal expansion [9, 10, 11]. Similarly, mechanically-induced and thermally-induced microcracks have been shown to produce significant changes in stiffness [11, 15]. This investigation will focus on microcracks induced by long-term thermal cycling, i.e., thousands of cycles, and the effect of these microcracks on the stiffness and thermal expansion in the composite materials of interest.

The composite materials investigated in this study include graphite fibers which range from moderate stiffness (55Msi) to very high stiffness (120Msi). The fibers alone dominate the stiffness of the composite, while the interaction of fibers and matrix greatly affects the thermal expansion characteristics of the laminate. Three matrix materials are studied, including a widely used space-qualified epoxy, a more advanced toughened epoxy, and a cyanate ester, or polycyanate. From the literature [46] the cyanate ester resin appears to offer low moisture absorption characteristics as well as greater resistance to microcracking.

In addition to the variety of material types considered in this investigation, the effect of stacking sequence and layer thickness will be addressed. Previous authors [9] have shown for cross-ply laminates that thinner layers result in a more dimensionally stable composite. The current investigation will extend some of the previous work to a greater number of thermal cycles and for quasi-isotropic laminates to see if this behavior continues. To further the understanding of this phenomenon, the current work will also consider new materials and different layer thicknesses.

Finally, the current investigation will focus on an issue which has not been clearly addressed in the past - the issue of thermal cycling temperature range effects. This portion of the research has several interesting aspects. The obvious comparison to make first is the effect of geosynchronous earth orbit versus low earth orbit temperature ranges. Geosynchronous earth orbit (GEO) is typically characterized by temperature extremes of -250°F to +250°F, whereas low earth orbit (LEO) is characterized by -150°F to +150°F temperature extremes. In the same spirit,

a third temperature range with extremes of -50°F and +50°F will be considered. This third range will be referred to as the thermally controlled orbit, which could be achieved through the use of active thermal control or by the correct choice of coating material applied to the composite [47]. Information will be gathered relating the degree of damage induced by each of these thermal cycling temperature ranges. The concept of characteristic damage state suggested by some authors [15, 16] would imply that materials cycled at each of these three temperature ranges would, after some unknown number of cycles, reach the same level of damage. It is hoped that information will be gathered which can be used to prove or disprove this concept.

Overall, this investigation will provide additional insight into many aspects of thermally induced damage in composite materials. As mentioned previously, the focus will be on microcracking and its effect on laminate stiffness and thermal expansion. By combining all aspects mentioned above, a consistent database of information regarding dimensional stability of composites for space application will be developed.

2.1 MATERIAL SPECIFICATIONS

Four different Thornel fiber types are included in this investigation. Their nominal axial direction properties are summarized below in Table 2.1. In the case of the 55 Msi fibers, both a polyacrylonitrile-based (PAN) and a pitch-based fiber are considered. The PAN-based fibers are synthetic acrylic fiber derivatives with typically lower densities than pitch-based fibers. Pitch-based fibers are organic-based fibers created from crude oil, coal tar, or similar materials. The pitch-based fibers typically have the advantage of higher production rates than the PAN-based fibers [48].

Table 2.1 Axial Direction Fiber Properties[†]

Fiber	Fiber Precursor	Tensile Modulus (Msi)	Tensile Strength (Ksi)	Longitudinal CTE (με /°F)
T50	PAN	55	375	-0.50
P55	Pitch	55	275	-0.70
P75	Pitch	75	300	-0.75
P120	Pitch	122	325	-0.80

[†] Fiber data taken from Amoco Performance Products, Inc. product information bulletin.

The neat resin properties for the three resin systems included in this investigation are summarized in Table 2.2.

Table 2.2 Room Temperature Neat Resin Properties†

Resin Designation	Resin Type	CTE (με/°F)	Tensile Modulus (Ksi)	Tensile Strength (Ksi)	G_{IC} (in-lb/in^2)	T_g (°F)
Fiberite 934	Epoxy	28	600	4.0	0.23[2]	381
Amoco ERL1962[49]	Toughened Epoxy	24	540	9.6	0.8	320
YLA RS3	Cyanate Ester	31.5	388	12	1.76	490

† Neat resin data taken from product information bulletins, except where noted.

The fibers listed in Table 2.1 and the resins listed in Table 2.2 were supplied by vendors in prepreg form, i.e., the fibers had been preimpregnated with resin, and were ready for laminate assembly and curing. The following prepregs were supplied by Amoco Performance Products, Inc.: T50/ERL1962, P55/ERL1962, P75/ERL1962, and P120/ERL1962. P75/RS3 prepreg was supplied by YLA, Inc., and P75/934 prepreg was supplied by Fiberite, Inc. The T50, P55, P75, and P120 fibers supplied in the ERL1962 resin prepreg had each been surface treated using a proprietary technique and sized with epoxy-compatible Union Carbide series 300 coatings selected by Amoco. Surface treatment and sizing information for the P75 fibers supplied in the RS3 resin prepreg and the P75 fibers supplied in the 934 resin prepreg were unavailable.

The prepreg materials were cut and assembled into 12 in. square laminates and consolidated using manufacturer recommended autoclave cure processes. In general, the three resin systems require two hour cure times at 350°F. The specific recommended cure cycles are included for completeness. The manufacturer recommended cure cycle for the 934 resin system is as follows:

1) Apply 25 in. H_g vacuum, holding for 30 minutes.
2) Heat up at 2-5°F per minute to 250°F. Hold at 250°F for 15±5 minutes.
3) Apply 100 psig. Hold for 45±5 minutes.
4) Heat up at 2-5°F per minute to 350°F. Hold at 350°F for 120±15 minutes.
5) Cool down at 5°F per minute. Below 175°F, vent vacuum, release pressure, remove part.

The manufacturer recommended cure cycle for the ERL1962 resin system is as follows:

1) Apply 29 in. H_g vacuum, holding for 20 minutes.

2) Apply 85 psig.
3) Heat up at 3°F per minute to 248°F. Vent vacuum after reaching 248°F.
4) Hold at 248°F for 60 minutes.
5) Heat up at 3°F per minute to 355°F. Hold at 355°F for 120 minutes.
6) Cool down at 5°F per minute. Vent pressure.

The manufacturer recommended cure cycle for the RS3 resin system is as follows:

1) Apply vacuum.
2) Apply 45 to 80 psig.
3) Release vacuum.
4) Heat up at 2-8°F per minute to 350°F. Hold at 350°F for 120 minutes.
5) Cool part to room temperature. Cooling rate is unimportant.

The average room temperature lamina properties of the materials are shown below in Table 2.3. These properties were obtained at NASA Langley Research Center from in-house testing of unidirectional laminates. The individual property designations follow standard classical lamination theory naming conventions. In the case of G_{12}, values for several of the materials are estimated from similar materials. The fiber volume fraction, V_f, for each material is listed as well. To be discussed later is the fact that despite having these lamina properties, the properties of all the various specimens considered in this study are determined on a per specimen basis. This is due to variations in laminate thickness and fiber volume fraction in the cured laminates.

Table 2.3 Average Room Temperature Composite Lamina Properties[†]

Fiber/Matrix	V_f (%)	E_1 (Msi)	E_2 (Msi)	ν_{12}	G_{12} (Msi)	α_1 (με/°F)	α_2 (με/°F)	σ_{1u} (Ksi)	σ_{2u} (Ksi)
T50/ERL1962	55.9	28.4	1.04	0.270	0.630	-0.305	18.0	152	4.36
P55/ERL1962	59.9	25.1	1.00	0.340	0.700[*]	-0.385	15.3	101	3.25
P75/ERL1962	52.3	34.3	0.903	0.293	0.700[*]	-0.501	21.0	85.2	3.88
P120/ERL1962	54.8	58.5	0.865	0.280	0.700[*]	-0.675	15.6	110	2.89
P75/934	65.7	49.4	1.01	0.300[*]	0.700[*]	-0.652	16.7	164	2.55
P75/RS3	69.0	43.0	0.964	0.261	0.700[*]	-0.662	15.7	120	4.16

[†] Lamina property data taken from NASA Langley Research Center in-house test data.
[*] estimated

2.2 SPECIMEN DESIGNS CONSIDERED

A test matrix of the materials studied and testing parameters considered for this investigation is shown in Table 2.4. Specimen material designations, i.e., fiber type, matrix type, and laminate stacking sequence, are included above the table along with a temperature range designation, indicating the thermal cycling range various specimens will undergo. The columns of the table represent the combinations of fiber and matrix of the specimens. The rows of the table indicate the laminate stacking sequence and nominal thickness of a single layer within the specimens. Those tabular positions marked with a temperature range designation (G, L, or C) indicate which specimen designs are included in this investigation and what thermal cycling range they will experience. In general, three specimens are included for each combination of material and thermal cycling range. As can be seen from Table 2.4, comparisons between fiber type, matrix type, lamination sequence, cycling temperature range, and laminate thickness versus the number of thermal cycles can be made. More details of the individual specimens are included in Table 2.5.

Some of the specimens under consideration are reclaimed from previous unpublished and published [9] thermal cycling studies, and some were fabricated for the current study. In most cases the existing specimens had been cycled 500 times between −250°F and +250°F. The specimens from Reference [9] had been exposed to as many as 2000 thermal cycles. Microcrack densities and thermal expansion characteristics were measured for these specimens at various stages in their cycling history. These existing specimens will be exposed to higher numbers of cycles, along with the specimens created for the current study.

Table 2.4 Materials and Testing Parameters

Fiber Type:
T50 - PAN based/55 Msi modulus
P55 - pitch based/55 Msi modulus
P75 - pitch based/75 Msi modulus
P120 - pitch based/122 Msi modulus

Matrix Type:
ERL1962 - toughened epoxy
RS3 - cyanate ester
934 - epoxy

Laminate Stacking Sequence:
X - $[0/90]_{2S}$ (cross-ply)
Q1 - $[0/+45/-45/90]_{S}$ (quasi-isotropic)
Q2 - $[0/+45/90/-45]_{S}$ (quasi-isotropic)

Temperature Range (earth orbit):
G - ±250°F (geosynchronous earth orbit)
L - ±150°F (low earth orbit)
C - ±50°F (thermally controlled orbit)

		Material System (Fiber/Matrix)					
Lay-up	Layer Thick.	T50/ ERL1962	P55/ ERL1962	P75/ ERL1962	P120/ ERL1962	P75/ RS3	P75/ 934
X	5mil	G	G	G	G		
	2mil						
	1mil			G			
Q1	5mil	G	G	G	G		
	2mil						
	1mil						
Q2	5mil			G,L,C		G,L,C	G
	2mil					G,L,C	
	1mil			G			

(1mil=.001 in.)

Below in Table 2.5 the specimen designations and the specimen testing history are shown. The information from Table 2.4 is included in the first column of this table in the abbreviated form illustrated here:

I.II.III.IV,

where ‘I’ represents the fiber and matrix combination, ‘II’ represents the laminate stacking sequence (see Table 2.4), ‘III’ represents the nominal thickness of a single layer within the specimens (in mils), and ‘IV’ represents the thermal cycling range for the specimen, i.e., G, L, or

C (see Table 2.4). In some cases, a B is used in place of the G, L, or C. The B represents a baseline (BSL) stiffness specimen to measure initial, i.e., uncycled, laminate stiffness. The individual specimen designations shown in the second column will be used later in appendices when presenting specific specimen results. The third column represents the initial status of the specimens at the onset of this study. The 'G' refers to the ±250°F cycling range followed by the number of previous thermal cycles in parentheses. 'AF' represents an 'as-fabricated' uncycled specimen which either existed previously or was created for the current study. The remaining columns in Table 2.5 represent the testing history of the individual specimens as a function of the number of thermal cycles measured in thousands. A 'ρ' represents a microcrack density measurement taken at the indicated thermal cycle count. Similarly, an 'α' represents a thermal expansion measurement, and an 'E' represents a laminate stiffness measurement. As can be seen from the table, the experimental phase of this study is quite ambitious.

It should be noted that specimen series 75RS3 and 75R-A, both using the designation P75/RS3.Q2.5.G, are nominally the same. They were manufactured from different material lots and at different times. They have both been included in this study to provide evidence regarding manufacturing repeatability.

Table 2.5 Specimen Designations and Testing History

Test Matrix Designation	Specimen Designation	Initial Status	Specimen Thermal Cycle Count (x1000)					
			0	1.0	1.5	2.5	3.0	4.0
T50/ERL1962.X.5.B	J-1	AF	E					
T50/ERL1962.X.5.G	J-2	G(500)	ρ	ρ		ρ	ραE	
T50/ERL1962.X.5.G	J-3	G(500)	ρ	ρ		ρ	ραE	
T50/ERL1962.X.5.G	J-4	G(500)	ρ	ρ		ρ	ραE	
P55/ERL1962.X.5.B	O-1	G(5)	E					
P55/ERL1962.X.5.G	O-2	G(5)	ρ		ρ		ραE	
P55/ERL1962.X.5.G	O-3	G(500)	ρ	ρ		ρ	ραE	
P55/ERL1962.X.5.G	O-4	G(500)	ρ	ρ		ρ	ραE	
P75/ERL1962.X.5.B	H-1	AF	E					
P75/ERL1962.X.5.G	H-2	G(500)	ρ	ρ		ρ	ραE	
P75/ERL1962.X.5.G	H-3	G(500)	ρ	ρ		ρ	ραE	
P75/ERL1962.X.5.G	H-4	G(500)	ρ	ρ		ρ	ραE	
P120/ERL1962.X.5.G	Q-1	G(500)	ρ	ρ		ρ	ραE	

Test Matrix Designation	Specimen Designation	Initial Status	Specimen Thermal Cycle Count (x1000)					
			0	1.0	1.5	2.5	3.0	4.0
P120/ERL1962.X.5.G	Q-2	G(500)	ρ	ρ		ρ	ραE	
P120/ERL1962.X.5.G	Q-3	G(500)	ρ	ρ		ρ	ραE	
P120/ERL1962.X.5.B	Q-4	AF	E					
P75/ERL1962.X.1.B	UT8X-1	AF	E					
P75/ERL1962.X.1.G	UT8X-2	G(2022)	ρ	ρ		ρ	ραE	
P75/ERL1962.X.1.G	UT8X-4	G(1)	ρ		ρ		ραE	
P75/ERL1962.X.1.G	UT8X-5	G(2022)	ρ	ρ		ρ	ραE	
P75/ERL1962.X.1.G	UT8X-6	G(1)	E					
P75/ERL1962.X.1.B	UT8X-2A	AF	E					
P75/ERL1962.X.1.B	UT8X-4A	AF	E					
P75/ERL1962.X.1.B	UT8X-5A	AF	E					
T50/ERL1962.Q1.5.B	K-2	AF	E					
T50/ERL1962.Q1.5.G	K-3	G(500)	ρ	ρ		ρ	ραE	
T50/ERL1962.Q1.5.G	K-4	G(500)	ρ	ρ		ρ	ραE	
P55/ERL1962.Q1.5.G	P-1	G(500)	ρ	ρ		ρ	ραE	
P55/ERL1962.Q1.5.G	P-2	G(500)	ρ	ρ		ρ	ραE	
P55/ERL1962.Q1.5.G	P-3	G(500)	ρ	ρ		ρ	ραE	
P55/ERL1962.Q1.5.B	P-4	AF	E					
P75/ERL1962.Q1.5.G	I-1	G(500)	ρ	ρ		ρ	ραE	
P75/ERL1962.Q1.5.G	I-2	G(500)	ρ	ρ		ρ	ραE	
P75/ERL1962.Q1.5.G	I-3	G(500)	ρ	ρ		ρ	ραE	
P75/ERL1962.Q1.5.B	I-4	AF	E					
P120/ERL1962.Q1.5.G	R-1	G(500)	ρ	ρ		ρ	ραE	
P120/ERL1962.Q1.5.B	R-2	AF	E					
P120/ERL1962.Q1.5.G	R-3	G(500)	ρ	ρ		ρ	ραE	
P120/ERL1962.Q1.5.G	R-4	G(500)	ρ	ρ		ρ	ραE	
P75/ERL1962.Q2.5.G	6762-1	G(1)	ρ		ρ		ραE	
P75/ERL1962.Q2.5.G	6762-3	G(1)	ρ		ρ		ραE	
P75/ERL1962.Q2.5.G	6762-5	G(1)	ρ		ρ		ραE	
P75/ERL1962.Q2.5.L	6762-2	AF	ρ		ρ		ρ	ραE

Test Matrix Designation	Specimen Designation	Initial Status	Specimen Thermal Cycle Count (x1000)					
			0	1.0	1.5	2.5	3.0	4.0
P75/ERL1962.Q2.5.L	6762-4	AF	ρ		ρ		ρ	ραE
P75/ERL1962.Q2.5.L	6762-6	AF	ρ		ρ		ρ	ραE
P75/ERL1962.Q2.5.C	6762-7	AF	ρ		ρ		ρ	ραE
P75/ERL1962.Q2.5.C	6762-8	AF	ρ		ρ		ρ	ραE
P75/ERL1962.Q2.5.C	6762-9	AF	ρ		ρ		ρ	ραE
P75/ERL1962.Q2.5.B	6762-13	AF	E					
P75/ERL1962.Q2.5.B	6762-14	AF	E					
P75/ERL1962.Q2.5.B	6762-15	AF	E					
P75/ERL1962.Q2.5.B	6762-1A	AF	E					
P75/ERL1962.Q2.5.B	6762-5A	AF	E					
P75/ERL1962.Q2.5.B	6762-10A	AF	E					
P75/RS3.Q2.5.G	75RS3-1	AF	ρ		ρ		ραE	
P75/RS3.Q2.5.G	75RS3-2	AF	ρ		ρ		ραE	
P75/RS3.Q2.5.G	75RS3-3	AF	ρ		ρ		ραE	
P75/RS3.Q2.5.G	75R-A-41	G(1000)	ρ	ρ		ρ	ραE	
P75/RS3.Q2.5.G	75R-A-43	G(500)	ρ	ρ		ρ	ραE	
P75/RS3.Q2.5.G	75R-A-44	AF	ρ		ρ		ραE	
P75/RS3.Q2.5.L	75RS3-4	AF	ρ		ρ		ρ	ραE
P75/RS3.Q2.5.L	75RS3-5	AF	ρ		ρ		ρ	ραE
P75/RS3.Q2.5.L	75RS3-6	AF	ρ		ρ		ρ	ραE
P75/RS3.Q2.5.L	75R-A-36	AF	ρ		ρ		ρ	ραE
P75/RS3.Q2.5.L	75R-A-37	AF	ρ		ρ		ρ	ραE
P75/RS3.Q2.5.L	75R-A-45	AF	ρ		ρ		ρ	ραE
P75/RS3.Q2.5.C	75RS3-7	AF	ρ		ρ		ρ	ραE
P75/RS3.Q2.5.C	75RS3-8	AF	ρ		ρ		ρ	ραE
P75/RS3.Q2.5.C	75RS3-9	AF	ρ		ρ		ρ	ραE
P75/RS3.Q2.5.C	75R-A-38	AF	ρ		ρ		ρ	ραE
P75/RS3.Q2.5.C	75R-A-39	AF	ρ		ρ		ρ	ραE
P75/RS3.Q2.5.C	75R-A-46	AF	ρ		ρ		ρ	ραE
P75/RS3.Q2.5.B	75RS3-13	AF	E					

Test Matrix Designation	Specimen Designation	Initial Status	Specimen Thermal Cycle Count (x1000)					
			0	1.0	1.5	2.5	3.0	4.0
P75/RS3.Q2.5.B	75RS3-14	AF	E					
P75/RS3.Q2.5.B	75RS3-15	AF	E					
P75/RS3.Q2.5.B	75RS3-3A	AF	E					
P75/RS3.Q2.5.B	75RS3-8A	AF	E					
P75/RS3.Q2.5.B	75RS3-11A	AF	E					
P75/RS3.Q2.5.B	75R-A-40	AF	E					
P75/934.Q2.5.G	P734Q-2	G(1)	ρ		ρ		ραE	
P75/934.Q2.5.G	P734Q-3	G(1)	ρ		ρ		ραE	
P75/934.Q2.5.G	P734Q-4	G(1)	ρ		ρ		ραE	
P75/934.Q2.5.G	P734Q-5	G(1)	ρ		ρ		ραE	
P75/934.Q2.5.B	P734Q-6	AF	E					
P75/RS3.Q2.2.G	275RS3-01	AF	ρ		ρ		ραE	
P75/RS3.Q2.2.G	275RS3-02	AF	ρ		ρ		ραE	
P75/RS3.Q2.2.G	275RS3-03	AF	ρ		ρ		ραE	
P75/RS3.Q2.2.L	275RS3-04	AF	ρ		ρ		ρ	ραE
P75/RS3.Q2.2.L	275RS3-05	AF	ρ		ρ		ρ	ραE
P75/RS3.Q2.2.L	275RS3-06	AF	ρ		ρ		ρ	ραE
P75/RS3.Q2.2.C	275RS3-07	AF	ρ		ρ		ρ	ραE
P75/RS3.Q2.2.C	275RS3-08	AF	ρ		ρ		ρ	ραE
P75/RS3.Q2.2.C	275RS3-09	AF	ρ		ρ		ρ	ραE
P75/RS3.Q2.2.B	275RS3-13	AF	E					
P75/RS3.Q2.2.B	275RS3-14	AF	E					
P75/RS3.Q2.2.B	275RS3-15	AF	E					
P75/RS3.Q2.2.B	275RS3-1A	AF	E					
P75/RS3.Q2.2.B	275RS3-5A	AF	E					
P75/RS3.Q2.2.B	275RS3-11A	AF	E					
P75/ERL1962.Q2.1.G	UTQ-1	G(1500)	ρ		ρ		ραE	
P75/ERL1962.Q2.1.G	UTQ-2	G(1500)	ρ		ρ		ραE	
P75/ERL1962.Q2.1.G	UTQ-3	G(1500)	ρ		ρ		ραE	
P75/ERL1962.Q2.1.B	UTQ-3A	AF	E					

Test Matrix Designation	Specimen Designation	Initial Status	Specimen Thermal Cycle Count (x1000)					
			0	1.0	1.5	2.5	3.0	4.0
P75/ERL1962.Q2.1.B	UTQ-7A	AF	E					
P75/ERL1962.Q2.1.B	UTQ-9A	AF	E					

2.3 SPECIMEN GEOMETRY AND PREPARATION

The geometry of the specimens used in this investigation is dictated by the size requirements of the interferometer used to measure the thermal expansion behavior of the material. For convenience and necessity, this specimen geometry will be used for all aspects of the investigation: microcrack density characterization, thermal expansion characterization, and laminate stiffness characterization. The specimen geometry is shown in Figure 2.1. The specimens were each machined from 12 in. by 12 in. panels to approximately 3 in. long by 1 in. wide, with both ends of the specimen machined to a radius of approximately 1.5 in., with the center of curvature located at the geometric center of the specimen. More will be said later in section 2.6 of the need for radiusing of the ends of the specimen. The thickness of the specimens in this study range from approximately 0.040 in. to 0.008 in. In all cases, the specimens are machined from panels such that the 0° fibers in the top and bottom plies are oriented along the long axis of the specimen.

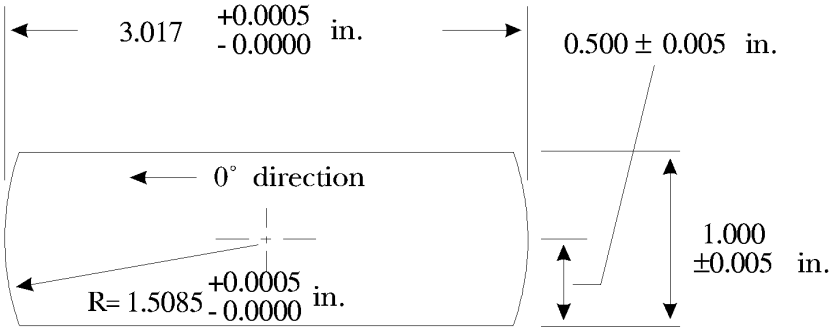

Figure 2.1. Specimen geometry.

After machining, all specimens are polished along one 3 in. long edge for visual inspection before and after thermal cycling events. To ensure uniformity of polish over the length of the specimen, specimens are mounted in a tool plate and machine polished. Polishing is performed by wet sanding the specimen edge using three successive polishing grades: 600 grit silicon carbide, 1200 grit silicon carbide, and a 0.05 micron colloidal alumina slurry.

Upon completion of polishing, all specimens are dried to constant weight in a vacuum oven maintained at 150°F. Drying may take anywhere from one to six weeks, depending on the moisture diffusion characteristics of the composite material. Except when the specimens are actively undergoing thermal cycling or testing, they are stored in a 150°F vacuum oven to minimize moisture uptake.

2.4 THERMAL CYCLING PROCEDURE

Two types of cycling chambers were used to expose the composite specimens to the three different thermal cycling ranges. A single chamber cycling apparatus was used for the ±50°F cycling range specimens in which the specimens remain in a single insulated chamber which is repeatedly cooled and heated with liquid nitrogen and electrical heating elements. For the ±150°F and ±250°F thermal cycling range specimens, a two-chamber shuttle system was used in which an insulated cold chamber and an insulated hot chamber are maintained at or near the temperature extremes of the desired thermal cycle and a carriage containing the specimens is shuttled back and forth between the two chambers. Both cycling apparatus are designed to prevent direct contact of liquid nitrogen with the specimens. In all cases, the specimens were exposed to fan-circulated air at atmospheric pressure during thermal cycling.

Thermocouples were attached to several specimens in the chamber as well as in the air surrounding the specimens. Cycle times were adjusted such that the specimens were at high and low temperature extremes for no less than five minutes. From an approximate heat transfer analysis, this time is estimated to be sufficient for thickest of the composite specimens to reach uniform temperature throughout the volume of the specimen (see Appendix A).

2.5 MICROCRACK CHARACTERIZATION

Microcrack characterization is performed by visually examining a polished edge of the specimen at magnifications ranging from 200X to 500X, and counting the number of microcracks per unit length. Microcracks are counted along a two-inch centered gage section in the three-inch long specimen and reported as a number of cracks per unit length, referred to as the microcrack density. In the case of the eight-layer cross-ply specimens, microcrack densities in the four 90° layers are counted, compared to microcrack densities counted in the six layers (two 90° layers, two +45° layers, and two –45° layers) in the quasi-isotropic specimens. It is noted that the double-thickness layer at the midplane of both the cross-ply and the quasi-isotropic specimens are considered as a single layer for microcrack characterization. Microcrack densities reported in Chapter 3 are averaged over this two inch gage length and between layers having the same

nominal thickness and the same fiber orientation. The three specimens of each specimen configuration are then averaged, with the high and low values representing a high and a low error range to this average value.

A photograph of a typical polished specimen edge is shown in Figure 2.2. The 0° layers in this $[0/+45/90/-45]_s$ specimen can clearly be seen at the top and bottom of the photograph. The 90° layers are seen as layers with fibers appearing circular in cross-section, whereas the 45° layers are seen as layers with fibers appearing elliptical in cross-section. The microcracks are clearly seen in the interior layers of the specimen, oriented at some angle to the thickness direction of the specimen. For cross-ply specimens, the orientation angle is typically 90 degrees (parallel to the thickness direction). For quasi-isotropic specimens, the orientation angle typically ranges from 90 degrees to approximately 45 degrees. Only cracks which propagate halfway or more through the thickness of a given layer are counted as a microcrack. In some cases, a coalition of fiber debonds exists which propagates halfway or more through a given layer. These coalitions, if they are verified to be continuous, are also counted as microcracks.

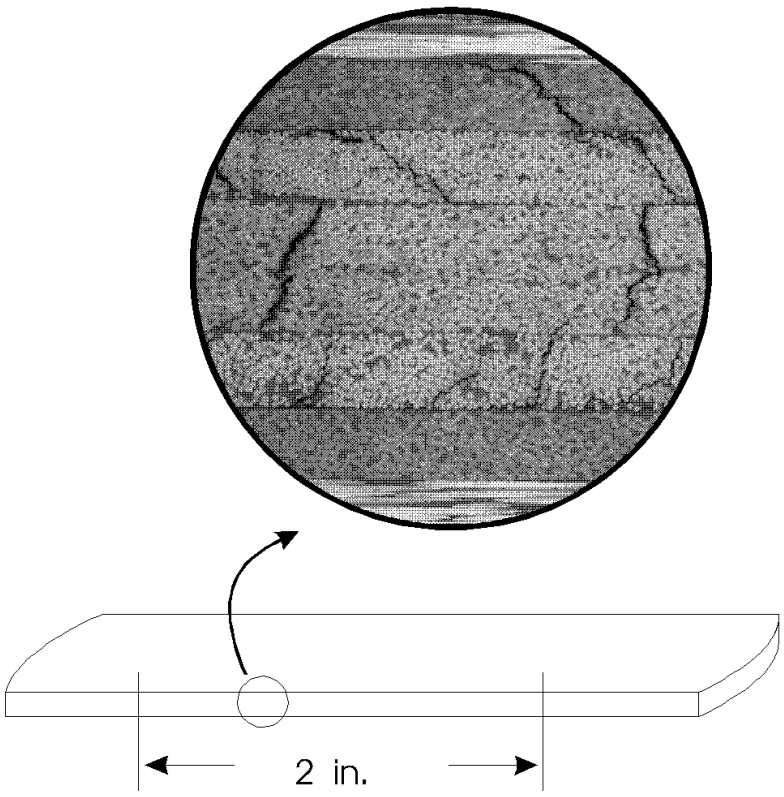

Figure 2.2. Microcrack characterization specimen.

In addition to the edge characterization, a representative specimen from each material series is selected for microcrack characterization using X-ray photography. The selected specimens are allowed to soak from 24 to 48 hours submerged in a dye penetrant solution that is absorbed into the cracks. X-ray radiation then is directed through the thickness of the specimen and onto a film plane below the specimen. Wherever a crack is present, the dye penetrant blocks the radiation from propagating through the specimen. The cracks can then be observed across the width of the specimen as dark lines on the film plane. This is a qualitative test which shows whether or not the cracks observed at the edge of the specimen propagate through the entire width of the specimen, or are confined only to the edge regions of the specimen. This procedure is performed only once and only *after* the completion of all thermal cycling, thermal expansion testing, and stiffness testing. In doing so, any effect of the dye penetrant solution on the thermal or mechanical performance of the composite is avoided.

2.6 THERMAL EXPANSION MEASUREMENTS

Thermal expansion measurements of the specimens are performed in a Priest (Fizeau-type) interferometer developed for high precision thermal strain measurements [50, 51] over a wide temperature range. Specific details of the interferometer can be found in Reference [50], with some of the key information included here.

The components of the interferometer are shown in Figure 2.3. They include the interferometer base and pedestal, two reference rods, a top optical flat, a specimen, a specimen support spring, and some other minor hardware to support the reference rods. The two reference rods and specimen are all mounted vertically in the interferometer to form the three legs of a tripod which supports the top flat. The specimen, as well as the reference rods, have been radiused on both ends to form discrete contact points at the interferometer base and discrete support points for the top flat. In the case of the reference rods, the radiusing forms a hemispherical dome on the rod ends. In the case of the specimen, the radiusing is present in two directions. The primary radiusing is machined as shown in Figure 2.1. A second radiusing, in the thickness direction, is achieved by hand sanding with a 600 grit sandpaper, such that the midplane of the specimen forms the support point for the top flat.

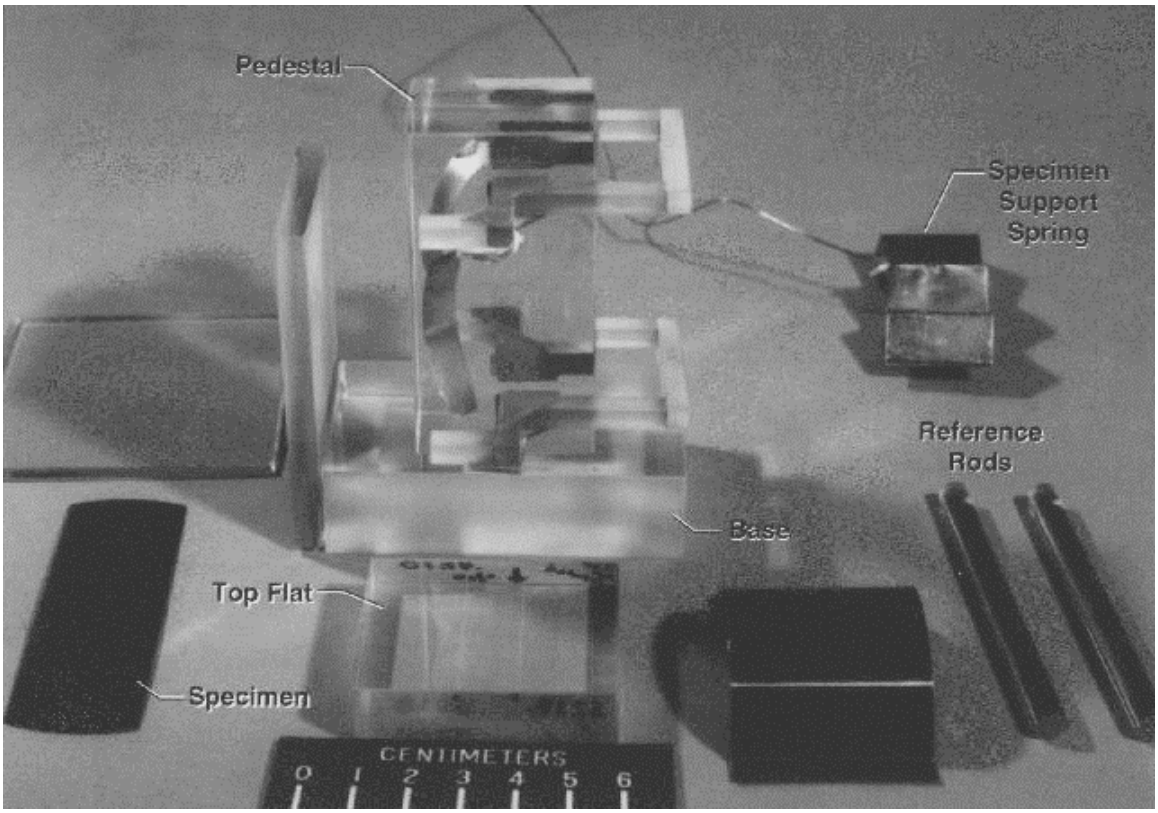

Figure 2.3. Photograph of the disassembled Priest interferometer.

The Priest interferometer operates on a two-beam interference principle. The incident beam in Figure 2.4 is a collimated Helium-Neon laser beam which travels through the top optical flat. As the beam reaches the bottom surface of the optical flat, approximately 40% of its intensity is reflected back through the flat due to a partially reflective coating on the underside of the flat. Approximately 60% of the incident beam intensity is transmitted through the flat to the mirrored top of the interferometer pedestal, where it is then reflected back up through the flat. As these two reflected beams re-emerge from the top flat, they diverge at some angle to one another, creating an interference pattern. This interference 'fringe' pattern can be directly related to the angle of the top flat relative to the top surface of the pedestal. As the interferometer assembly is heated and cooled inside an environmental chamber, the specimen and reference rods change length, which, in turn, change the angle of the top flat. By measuring the angle of the top flat using interference patterns, the relative strain between the specimen and the reference rods can be determined. To determine the absolute strain of the specimen, the relative strain measured from the interference patterns is added to the absolute strain of the reference rods as calculated from calibrated data for the given reference material.

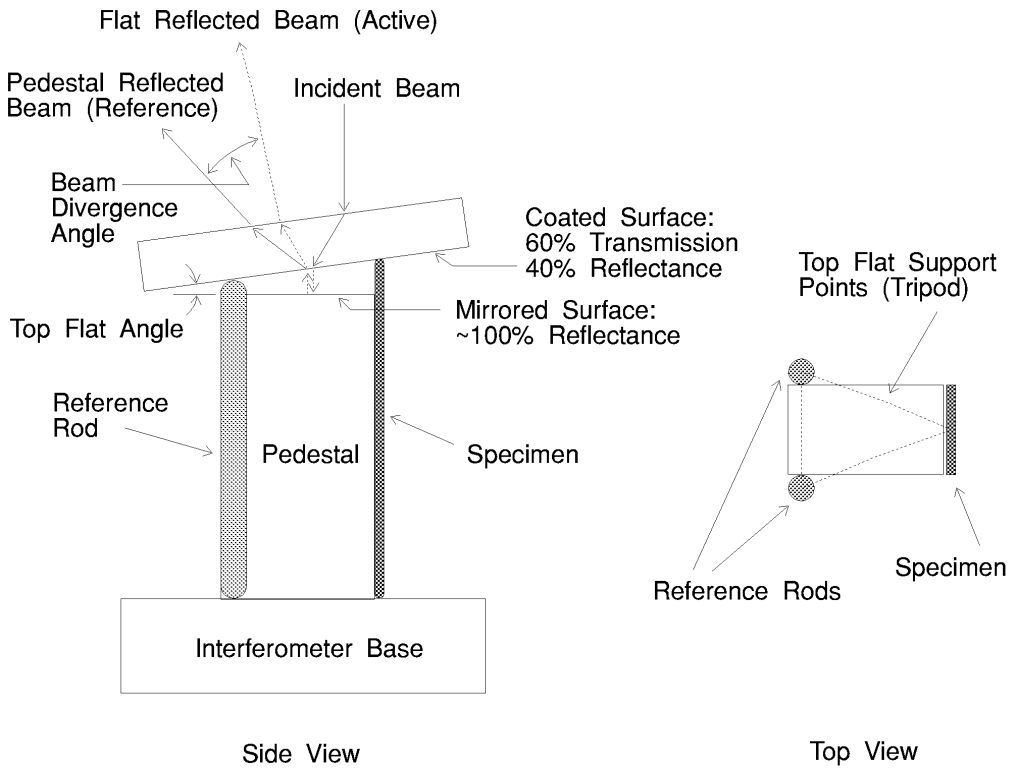

Figure 2.4. Priest interferometer measurement principles.

As alluded to previously, the entire interferometer assembly is placed in an environmental chamber which provides the heating and cooling function. The chamber itself is an insulated box with an access door, a top-located viewport through which the laser light travels, liquid nitrogen ports, and electrical resistance heaters together with a circulating fan to enhance cooling and heating. The practical temperature limits of the chamber are approximately -280°F to +300°F.

The thermal expansion tests follow a thermal profile which typically begins at room temperature, increases with time to the maximum prescribed temperature for the test (+150°F or +250°F), decreases with time to the minimum prescribed temperature (−150°F or −250°F), and then increases again to room temperature. In the case of the ±50°F temperature range, the profile decreases from room temperature to −50°F, and then increases to room temperature. Included in the temperature versus time profiles are a series of 45 minute temperature holds, typically spaced from 25 to 50 degrees apart, at which time the specimen and interferometer are allowed to reach a stable uniform temperature. At the end of each 45 minute temperature hold, an interference fringe image and temperature value are recorded for later reduction. Anywhere from 15 to 25 of these data records are taken in a given test. A curve fit to these discrete data points defines the thermal strain behavior of the specimen over the entire temperature range. The slope of this thermal strain

curve is, by definition, the coefficient of thermal expansion of the material. Both raw thermal strain data and coefficient of thermal expansion data are presented in an appendix for the materials in this study.

2.7 LAMINATE STIFFNESS MEASUREMENTS

The goal of the laminate stiffness measurements is to determine the tensile stiffness of the composite specimen without actually introducing any new microcracks into the specimen or catastrophically failing the specimen during testing. This is true for the uncycled and cycled specimens alike. For this reason, during stiffness testing the specimens are loaded to relatively low strain levels. Preliminary loading calculations based on classical lamination theory and the lamina properties from Table 2.3 are summarized below in Table 2.6 for the specimens included in this investigation. Maximum allowable loads are calculated based on the maximum stress criterion in the lamina 1 and 2 directions, i.e., the fiber and matrix failure modes. The maximum allowable test load is then calculated as 90% of the lower of the two failure loads. Theoretically, if the tensile load remains below that maximum allowable load, no microcracks should occur in the specimen. Realistically, however, maximum stress failure predictions, as with any failure prediction, are only indicators of real behavior. As a second measure, an average specimen failure strain based on the calculated laminate stiffness and the maximum allowable load is determined. This failure strain value is shown in the adjacent column. Strain values at maximum load are seen to range from approximately 0.2% to 0.5%. Previous work indicates that microcracking can be initiated for strain levels at or below 0.3% depending on the thickness of the cracking ply [17]. In most cases, this 0.3% strain limit was not exceeded.

Table 2.6 Tensile Stiffness Testing Loading Parameters

Spec. Series	Avg. C.S. Area ($in.^2$)	Avg. Layer Thick. (in.)	CLT Stiffness (Msi)	Matrix Failure Load (lbs.)	Fiber Failure Load (lbs.)	Failure Strain (in./in.)	Load Rate (lb./min.)	Max. Test Load[†] (lbs.)
275RS3	0.0189	0.0024	15.9	1761	814	0.00271	300	733
6762	0.0380	0.0048	12.32	2882	1175	0.00251	500	1500[‡]
75R-A	0.0385	0.0048	15.9	3521	1629	0.00266	500	1500[‡]
75RS3	0.0388	0.0049	15.9	3595	1663	0.00270	500	1500[‡]
H	0.0498	0.0062	17.64	4869	2168	0.00247	877	2631[‡]
I	0.0505	0.0063	12.32	3782	1542	0.00248	621	1863[‡]

Spec. Series	Avg. C.S. Area ($in.^2$)	Avg. Layer Thick. (in.)	CLT Stiffness (Msi)	Matrix Failure Load (lbs.)	Fiber Failure Load (lbs.)	Failure Strain (in./in.)	Load Rate (lb./min.)	Max. Test Load† (lbs.)
J	0.0424	0.0053	14.754	3016	3349	0.00482	625	1875‡
K	0.0424	0.0053	10.332	2293	2352	0.00524	439	1317‡
O	0.0428	0.0054	13.05	2831	2273	0.00407	559	1677‡
P	0.0435	0.0054	9.248	2222	1617	0.00402	402	1206‡
P734Q	0.0446	0.0056	17.38	4237	1892	0.00244	775	1703
Q	0.0428	0.0054	29.69	7386	2413	0.00190	1266	2172
R	0.0436	0.0055	20.36	5650	1688	0.00190	885	1519
UT8X	0.0104	0.0013	17.64	1020	455	0.00248	183	410
UTQ	0.01	0.0013	12.32	781	318	0.00258	123	286

† Maximum test load is calculated as 90% of the lower of the matrix and fiber failure mode loads.
‡ Fiber mode failure was not accounted for prior to testing.

The specimens are loaded in a screw driven load frame capable of low strain rate loading. Hydraulically actuated wedge grips are used, with special care taken in gripping the specimens to allow for minimal grip slippage, yet prevent damage due to excessive grip pressure. The gripping elements are illustrated in Figure 2.5. A 0.030 in. thick cellulose acetate plastic sheet is placed adjacent to the serrated grip surface along with a sheet of 180 grit silicon carbide Fabricut manufactured by 3M. This combination was tested and shown to prevent damage to the specimen and provide adequate friction to prevent excessive specimen slippage. The specimen is tested in load control to ensure that the desired loads are reached in the gage section of the specimen even if some grip slippage does occur. The specimens are tested at a load rate which translates into a near constant strain rate of approximately 0.001 in./in.·min. Strains in the specimen are measured with an extensometer over a one-inch gage length. The extensometer is attached directly to the specimen using small rubber bands which secure sharpened knife edges against the as-fabricated specimen surface. Two consecutive tests are made on each specimen to measure back-to-back stiffness, referred to here as front and back stiffness.

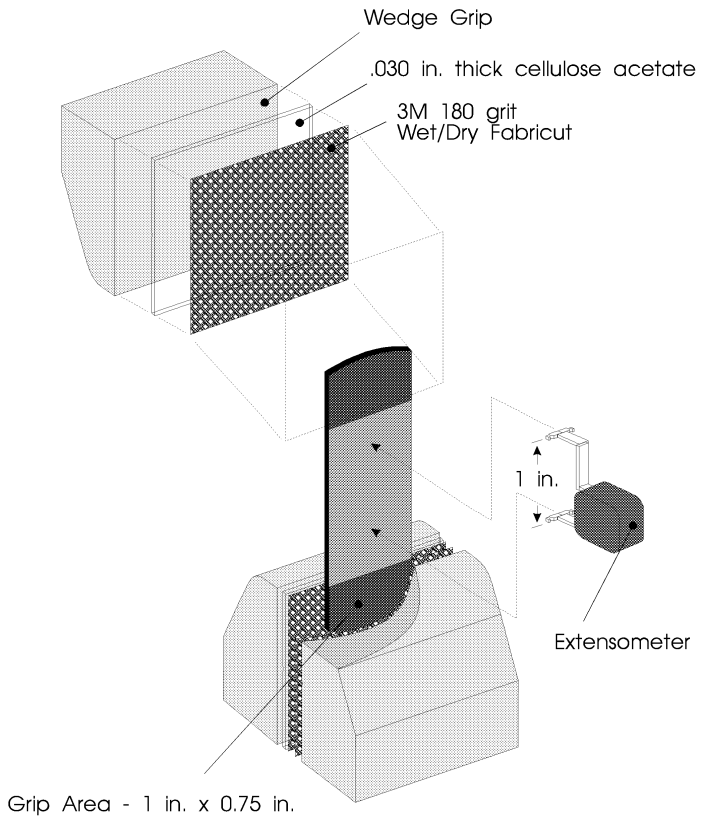

Figure 2.5. Tensile specimen gripping elements.

Calibration checks were performed on both an aluminum and a composite specimen to compare the accuracy of the extensometer-derived stiffness compared to the strain-gage-derived stiffness, and to determine the repeatability of the extensometer and strain gage measurements. Measurements Group, Inc. CEA-06-250UW-350 strain gages with a 0.3 in. gage length were mounted to the front and back on both the aluminum and composite calibration specimens for this purpose. Very good agreement was observed between the strain gage and extensometer readings.The results of the calibration tests are shown in Appendix B.

Laminate stiffness is calculated by performing a least squares linear regression on the stress-strain data from each test using strain values ranging from 0.10% up to the maximum strain in the test, usually between 0.25% and 0.30%. Average stress in the specimens is calculated based on the cross-sectional area of each specimen using the dimensions shown in Table 2.7. Front and back stiffnesses are calculated for each specimen. Average stiffness is reported for each specimen along with one standard deviation based on an assumed Gaussian distribution.

Table 2.7 Dimensions of Specimens Used for Stiffness Measurements

Test Matrix Designation	Specimen Designation	Specimen Width (in.) (Nominal/Actual)	Specimen Thickness (in.) (Nominal/Actual)
T50/ERL1962.X.5.B	J-1	1.0/1.0038	0.040/0.0422
T50/ERL1962.X.5.G	J-2	1.0/0.9668	0.040/0.0425
T50/ERL1962.X.5.G	J-3	1.0/0.9633	0.040/0.0424
T50/ERL1962.X.5.G	J-4	1.0/0.9618	0.040/0.0424
P55/ERL1962.X.5.B	O-1	1.0/0.9523	0.040/0.0428
P55/ERL1962.X.5.G	O-2	1.0/0.9570	0.040/0.0427
P55/ERL1962.X.5.G	O-3	1.0/0.9605	0.040/0.0428
P55/ERL1962.X.5.G	O-4	1.0/0.9588	0.040/0.0428
P75/ERL1962.X.5.B	H-1	1.0/1.0000	0.040/0.0498
P75/ERL1962.X.5.G	H-2	1.0/0.9655	0.040/0.0499
P75/ERL1962.X.5.G	H-3	1.0/0.9613	0.040/0.0496
P75/ERL1962.X.5.G	H-4	1.0/0.9698	0.040/0.0500
P120/ERL1962.X.5.G	Q-1	1.0/0.9738	0.040/0.0427
P120/ERL1962.X.5.G	Q-2	1.0/0.9615	0.040/0.0429
P120/ERL1962.X.5.G	Q-3	1.0/0.9738	0.040/0.0430
P120/ERL1962.X.5.B	Q-4	1.0/0.9858	0.040/0.0419
P75/ERL1962.X.1.B	UT8X-1	1.0/0.9943	0.008/0.0102
P75/ERL1962.X.1.G	UT8X-2	1.0/0.9943	0.008/0.0103
P75/ERL1962.X.1.G	UT8X-4	1.0/0.9945	0.008/0.0105
P75/ERL1962.X.1.G	UT8X-5	1.0/0.9928	0.008/0.0104
P75/ERL1962.X.1.B	UT8X-6	1.0/0.9923	0.008/0.0103
P75/ERL1962.X.1.B	UT8X-2A	1.0/1.0038	0.008/0.0108
P75/ERL1962.X.1.B	UT8X-4A	1.0/1.0050	0.008/0.0105
P75/ERL1962.X.1.B	UT8X-5A	1.0/1.0048	0.008/0.0105
T50/ERL1962.Q1.5.B	K-2	1.0/0.9730	0.040/0.0424
T50/ERL1962.Q1.5.G	K-3	1.0/0.9740	0.040/0.0427
T50/ERL1962.Q1.5.G	K-4	1.0/0.9733	0.040/0.0423
P55/ERL1962.Q1.5.G	P-1	1.0/0.9710	0.040/0.0431

Test Matrix Designation	Specimen Designation	Specimen Width (in.) (Nominal/Actual)	Specimen Thickness (in.) (Nominal/Actual)
P55/ERL1962.Q1.5.G	P-2	1.0/0.9568	0.040/0.0442
P55/ERL1962.Q1.5.G	P-3	1.0/0.9548	0.040/0.0432
P55/ERL1962.Q1.5.B	P-4	1.0/0.9858	0.040/0.0426
P75/ERL1962.Q1.5.G	I-1	1.0/0.9733	0.040/0.0508
P75/ERL1962.Q1.5.G	I-2	1.0/0.9585	0.040/0.0506
P75/ERL1962.Q1.5.G	I-3	1.0/0.9600	0.040/0.0502
P75/ERL1962.Q1.5.B	I-4	1.0/1.0040	0.040/0.0500
P120/ERL1962.Q1.5.G	R-1	1.0/0.9560	0.040/0.0439
P120/ERL1962.Q1.5.B	R-2	1.0/0.9860	0.040/0.0437
P120/ERL1962.Q1.5.G	R-3	1.0/0.9705	0.040/0.0436
P120/ERL1962.Q1.5.G	R-4	1.0/0.9698	0.040/0.0436
P75/ERL1962.Q2.5.G	6762-1	1.0/0.9730	0.040/0.0384
P75/ERL1962.Q2.5.G	6762-3	1.0/0.9590	0.040/0.0380
P75/ERL1962.Q2.5.G	6762-5	1.0/0.9583	0.040/0.0373
P75/ERL1962.Q2.5.L	6762-2	1.0/0.9705	0.040/0.0387
P75/ERL1962.Q2.5.L	6762-4	1.0/0.9708	0.040/0.0347
P75/ERL1962.Q2.5.L	6762-6	1.0/0.9778	0.040/0.0357
P75/ERL1962.Q2.5.C	6762-7	1.0/0.9663	0.040/0.0376
P75/ERL1962.Q2.5.C	6762-8	1.0/0.9650	0.040/0.0367
P75/ERL1962.Q2.5.C	6762-9	1.0/0.9675	0.040/0.0358
P75/ERL1962.Q2.5.B	6762-13	1.0/0.9748	0.040/0.0394
P75/ERL1962.Q2.5.B	6762-14	1.0/0.9708	0.040/0.0434
P75/ERL1962.Q2.5.B	6762-15	1.0/0.9698	0.040/0.0455
P75/ERL1962.Q2.5.B	6762-1A	1.0/1.0025	0.040/0.0429
P75/ERL1962.Q2.5.B	6762-5A	1.0/1.0045	0.040/0.0365
P75/ERL1962.Q2.5.B	6762-10A	1.0/1.0048	0.040/0.0430
P75/RS3.Q2.5.G	75RS3-1	1.0/0.9775	0.040/0.0387
P75/RS3.Q2.5.G	75RS3-2	1.0/0.9790	0.040/0.0388
P75/RS3.Q2.5.G	75RS3-3	1.0/0.9725	0.040/0.0387

Test Matrix Designation	Specimen Designation	Specimen Width (in.) (Nominal/Actual)	Specimen Thickness (in.) (Nominal/Actual)
P75/RS3.Q2.5.G	75R-A-41	1.0/0.9680	0.040/0.0381
P75/RS3.Q2.5.G	75R-A-43	1.0/0.9480	0.040/0.0382
P75/RS3.Q2.5.G	75R-A-44	1.0/0.9495	0.040/0.0389
P75/RS3.Q2.5.L	75RS3-4	1.0/0.9873	0.040/0.0388
P75/RS3.Q2.5.L	75RS3-5	1.0/.09878	0.040/0.0389
P75/RS3.Q2.5.L	75RS3-6	1.0/0.9893	0.040/0.0384
P75/RS3.Q2.5.L	75R-A-36	1.0/0.9748	0.040/0.0388
P75/RS3.Q2.5.L	75R-A-37	1.0/0.9755	0.040/0.0389
P75/RS3.Q2.5.L	75R-A-45	1.0/0.9533	0.040/0.0386
P75/RS3.Q2.5.C	75RS3-7	1.0/0.9710	0.040/0.0384
P75/RS3.Q2.5.C	75RS3-8	1.0/0.9780	0.040/0.0381
P75/RS3.Q2.5.C	75RS3-9	1.0/0.9758	0.040/0.0376
P75/RS3.Q2.5.C	75R-A-38	1.0/0.9735	0.040/0.0389
P75/RS3.Q2.5.C	75R-A-39	1.0/0.9690	0.040/0.0371
P75/RS3.Q2.5.C	75R-A-46	1.0/0.9508	0.040/0.0388
P75/RS3.Q2.5.B	75RS3-13	1.0/0.9795	0.040/0.0394
P75/RS3.Q2.5.B	75RS3-14	1.0/0.9838	0.040/0.0397
P75/RS3.Q2.5.B	75RS3-15	1.0/0.9760	0.040/0.0394
P75/RS3.Q2.5.B	75RS3-3A	1.0/1.0040	0.040/0.0396
P75/RS3.Q2.5.B	75RS3-8A	1.0/1.0058	0.040/0.0390
P75/RS3.Q2.5.B	75RS3-11A	1.0/1.0043	0.040/0.0394
P75/RS3.Q2.5.B	75R-A-40	1.0/0.9688	0.040/0.0379
P75/934.Q2.5.G	P734Q-2	1.0/0.9500	0.040/0.0449
P75/934.Q2.5.G	P734Q-3	1.0/0.9485	0.040/0.0447
P75/934.Q2.5.G	P734Q-4	1.0/0.9463	0.040/0.0442
P75/934.Q2.5.G	P734Q-5	1.0/0.9438	0.040/0.0428
P75/934.Q2.5.B	P734Q-6	1.0/0.9525	0.040/0.0395
P75/934.Q2.5.B	P734Q-3A	1.0/1.0033	0.040/0.0480
P75/934.Q2.5.B	P734Q-7A	1.0/1.0043	0.040/0.0402

Test Matrix Designation	Specimen Designation	Specimen Width (in.) (Nominal/Actual)	Specimen Thickness (in.) (Nominal/Actual)
P75/934.Q2.5.B	P734Q-12A	1.0/1.0053	0.040/0.0465
P75/RS3.Q2.2.G	275RS3-1	1.0/0.9638	0.016/0.0189
P75/RS3.Q2.2.G	275RS3-2	1.0/0.9650	0.016/0.0187
P75/RS3.Q2.2.G	275RS3-3	1.0/0.9670	0.016/0.0189
P75/RS3.Q2.2.L	275RS3-4	1.0/0.9683	0.016/0.0194
P75/RS3.Q2.2.L	275RS3-5	1.0/0.9680	0.016/0.0188
P75/RS3.Q2.2.L	275RS3-6	1.0/0.9680	0.016/0.0191
P75/RS3.Q2.2.C	275RS3-7	1.0/0.9638	0.016/0.0189
P75/RS3.Q2.2.C	275RS3-8	1.0/0.9665	0.016/0.0191
P75/RS3.Q2.2.C	275RS3-9	1.0/0.9633	0.016/0.0192
P75/RS3.Q2.2.B	275RS3-13	1.0/0.9620	0.016/0.0189
P75/RS3.Q2.2.B	275RS3-14	1.0/0.9625	0.016/0.0192
P75/RS3.Q2.2.B	275RS3-15	1.0/0.9600	0.016/0.0194
P75/RS3.Q2.2.B	275RS3-1A	1.0/0.9995	0.016/0.0193
P75/RS3.Q2.2.B	275RS3-5A	1.0/1.0038	0.016/0.0189
P75/RS3.Q2.2.B	275RS3-11A	1.0/1.0040	0.016/0.0190
P75/ERL1962.Q2.1.G	UTQ-1	1.0/0.9928	0.008/0.0105
P75/ERL1962.Q2.1.G	UTQ-2	1.0/0.9948	0.008/0.0107
P75/ERL1962.Q2.1.G	UTQ-3	1.0/0.9928	0.008/0.0105
P75/ERL1962.Q2.1.B	UTQ-3A	1.0/1.0045	0.008/0.0109
P75/ERL1962.Q2.1.B	UTQ-7A	1.0/1.0038	0.008/0.0110
P75/ERL1962.Q2.1.B	UTQ-9A	1.0/1.0038	0.008/0.0107

2.8 MATERIAL AGING CHARACTERIZATION

The thermal cycling and elevated temperature storage have combined to expose the specimens in this study to an extensive thermal history. The purpose of the material aging characterization is to determine if any significant changes occurred in the morphology of the specimens over their lifetime which may have affected their behavior. Particular interest centers on whether or not thermal history altered the glass transition temperature, T_g, of the specimens.

A change in T_g could account for an increased or a decreased resistance to microcracking, a change in the thermal expansion, or a change in the stiffness behavior of the material. Also, if the matrix is affected by thermal history, the degree of thermal cycling, i.e., ±50°F versus ±150°F versus ±250°F, may affect the matrix differently. To address the above mentioned issues, a differential scanning calorimeter (DSC) device is used to determine the T_g of the desired specimens. The T_g is taken to be the temperature at which one-half of the change in heat capacity in the specimen occurs. The T_g of various specimens will be compared to determine relative changes as a result of thermal history.

This concludes the description of the experimental procedures and materials tested as a part of this investigation. The following chapter summarizes the results from the procedures described here.

3. EXPERIMENTAL RESULTS

This chapter contains summaries of experimental results for all specimens in the test program. The first section briefly summarizes some of the details of the experimental measurements that were not included in Chapter 2. The remaining sections are arranged according to the four major material and loading variables from which empirical conclusions are made: layer thickness, fiber type, matrix type, and thermal cycling temperature range.

3.1 EXPERIMENTAL MEASUREMENTS

As described in Chapter 2, three experimental measurements are used to characterize behavior in the specimens before and after thermal cycling. These three measurements are: microcrack density, laminate thermal expansion coefficient, and laminate stiffness. A fourth measurement, glass transition temperature, is also used in some instances to assess the possibility of chemical changes taking place in the material due to thermal cycling. The following sections outline the specifics of each of these measurements.

3.1.1 Microcrack Density

Average microcrack densities as a function of the number of thermal cycles for each specimen series are presented in the following sections. Individual specimen data are contained in Appendix C. Because of the layer thickness effects that are yet to be discussed, it was found necessary to nondimensionalize the microcrack density when evaluating certain trends in the data. This nondimensionalization is achieved by multiplying the dimensional microcrack densities, in microcracks per unit length, by the layer thickness for that layer containing cracks. All layers within the specimen, with the exception of the centrally located double-thickness layer, are assumed to be of equal thickness and are calculated based on the measured total thickness of the specimen. Based on experimental observation of the specimen cross-sections, uniform layer thickness is a reasonable assumption. It is also useful to evaluate the trends in microcrack density by converting the experimentally measured microcrack densities into lineal values, i.e., those values measured in a local coordinate system aligned perpendicular to the fiber direction in a given layer. This would represent the 2-direction in a standard principal material coordinate system (see Figure 1.1). The lineal conversion only affects the +45° and –45° layers and is illustrated in Figure 3.1. Lineal values are calculated in these layers by dividing the measured microcrack densities, which could be recorded only from specimen edge views, by the cosine of forty-five degrees. The combination of the nondimensionalizing and the local coordinate system

effect results in what is referred to here as the 'nondimensional lineal microcrack density', represented by ρ'. The figures in all but Section 3.2 include this nondimensional lineal microcrack density, while the more typical dimensional crack density values, denoted by ρ, and as recorded by experimental observation, are summarized in tables.

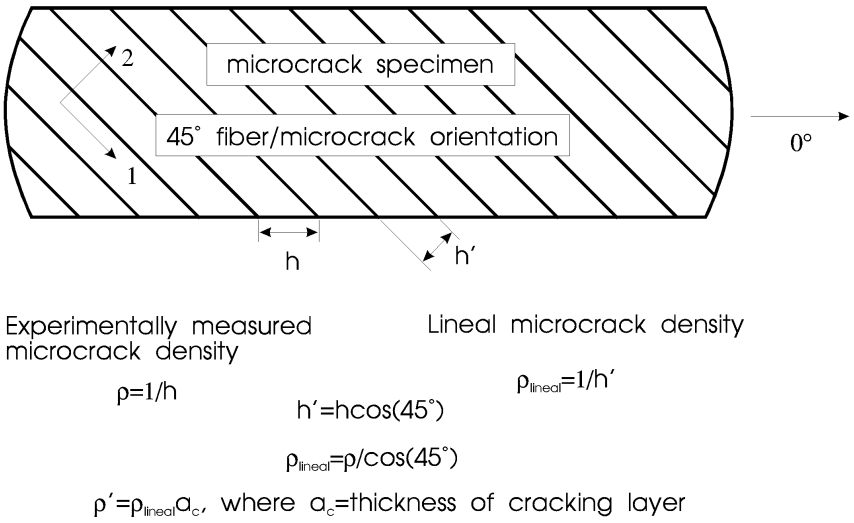

Figure 3.1. Definition of lineal microcrack density.

Microcrack densities are presented for all layer orientations other than 0°. In the case of cross-ply specimens, the 'o90' indicates the outer 90° layers whereas the 'c90' represents the central 90° layers, i.e., $[0/o90/0/c90]_s$. Microcrack densities for some of the layer orientations are not reported for less than 500 thermal cycles. In these cases, the specimens were obtained from a previous study that did not record microcrack densities in all layers.

Included after the figures and tabulated microcrack densities are specimen edge-view images of microcracking patterns for one representative specimen from each series. Specimen edge-views like these are used to characterize the microcrack density along the length of the specimen. In all cases, the images of cracking patterns are recorded at the maximum thermal cycle count for the given specimen series. In some cases, X-ray images from above the specimen surface looking down are also included to illustrate the extent of microcracking across the width of the specimen.

3.1.2 Laminate Thermal Expansion Coefficients

Average room temperature thermal expansion coefficients before and after thermal cycling are presented for each specimen series. The average coefficients are calculated from three specimens in general, except where noted. To calculate the coefficient of thermal expansion, the

procedure outlined in detail in Appendix D is followed. Briefly, the procedure consists of fitting a second or third order polynomial regression, depending on actual data, to the discrete thermal strain measurements obtained from the interferometric measuring system described in Chapter 2. The polynomial expression of thermal strain is then differentiated to obtain the equation for CTE as a continuous function of temperature. The room temperature CTE is evaluated by substituting a value of 77°F into this expression. For completeness, the experimental thermal strain data represented by polynomial relations fit to the strain data, and the CTE expressions as a function of temperature, are included for all specimens in Appendix D.

3.1.3 Laminate Stiffness

The third experimental measurement used to determine the effect of thermal cycling on the specimens is laminate stiffness. Both the uncycled and cycled average laminate tensile stiffness are presented for each of the material series. In all cases of thermally cycled specimens, stiffness testing is performed at the maximum thermal cycling count. Initial results from these tests indicated unacceptable scatter in the measured stiffness. Further investigation found this scatter to be attributed primarily to variations in fiber volume fraction among the individual specimens. As a result, fiber volume fraction for each specimen was measured after completion of testing. Individual specimen stiffness values were then normalized by their respective fiber volume fraction. Justification for this normalization is included in Appendix E, along with the normalized laminate stiffness results. The average stiffness values reported represent the average normalized stiffness for all of the specimens of that series, typically three specimens, except where noted. Error bars indicate one standard deviation from the mean based on an assumed Gaussian distribution. In a few cases only one specimen was available for testing so there are no error bars presented.

3.1.4 Glass Transition Temperature

When comparing the effect of matrix type and thermal cycling temperature range, a fourth experimental measurement, glass transition temperature (T_g), is used to determine the effect of thermal cycling on material behavior. The as-fabricated T_g as well as the post-cycled T_g are tabulated and presented for comparison.

3.2 EFFECT OF LAYER THICKNESS

Results are presented in this section for two independent specimen/material configurations. They include a P75/ERL1962 system in a cross-ply (X) configuration, i.e., $[0/90/0/90]_s$, and a

P75/RS3 in a quasi-isotropic (Q2) configuration, i.e., $[0/+45/90/-45]_s$. In the P75/ERL1962 configuration, comparisons are made between specimens with 0.005 in. and 0.001 in. nominal layer thickness. In the P75/RS3 configuration, comparisons are made between specimens with 0.005 in. and 0.002 in. nominal layer thickness. In all cases, the materials were subjected to thermal cycles ranging from -250°F to +250°F. The designations for the materials being compared are P75/ERL1962.X.*.G and P75/RS3.Q2.*.G, respectively, where the '*' is a symbol representing, in this case, the variation in layer thickness. The same symbol will be used later in this chapter to indicate variations in other parameters according to its location within the specimen designation.

3.2.1 Microcrack Density

It will be shown in this section that layer thickness has a considerable effect on the dimensional microcrack densities in specimens undergoing thermal cycling. Material series with varying layer thickness were manufactured specifically to determine if there is an effect. It is also true, however that, due to the manufacturing limitations, undesirable variability in layer thickness is present in some material series. This undesirable variability may mask trends in data that are used to compare other material and loading effects. This point will be discussed in more detail at the end of this section on layer thickness effects. Subsequent to that discussion, all remaining comparisons using microcrack density will do so using the nondimensional microcrack density.

It should be noted that recording microcrack densities experimentally in the 'ultra-thin' specimens with a 0.001 in. nominal layer thickness is extremely difficult. The microcracks often times do not clearly propagate halfway through the thickness of the layer, and therefore judgments have to be made. As a result, it was decided that accurate and consistent results were not attainable for the single 0.001 in. thick layers. As a minimum, however, microcrack densities were recorded in the double-thickness 90° layer at the midplane of the cross-ply specimens. It should also be noted that the damage might not manifest itself as clearly definable microcracks. Damage occurs in these ultra-thin specimens due to thermal cycling, but often in the form of fiber/matrix debonds. Changes in the specimen coefficient of thermal expansion are expected to be the only way to accurately record the degree of damage in these specimens.

The left-hand graphs in each of the figures that follow represent dimensional microcrack density versus the number of thermal cycles plotted on a linear scale. The right-hand graphs also represent dimensional microcrack density versus the number of thermal cycles, but the number of thermal cycles is presented on a log scale. The lines drawn through the data are linear

regressions, in the log scale, to the data and are shown with their defining equations. The slope of these lines can be viewed as microcracking rates. In order to prevent skewing of the microcracking rates, only non-zero microcrack densities are used in the right-hand figures. As will be seen later, this more accurately portrays the delayed initiation of microcracking in some specimens. It is noted that in some cases, the regressions are calculated based on limited data that are grouped closely together. Care should be taken when making conclusions about such data. This format for presenting microcrack densities will be repeated in later sections of this chapter.

Microcrack densities for the P75/ERL1962.X.*.G specimens are shown in Figure 3.2. As mentioned previously, data for the c90 layer only are compared since they are the only data available for the 0.001 in. layer thickness specimens. Also, due to scatter in the data among the 0.001 in. layer thickness specimens, only values from specimens UT8X-2 and 5 are included in the figures.

Remarkably different behavior is seen in Figure 3.2 for the 0.005 in. and 0.001 in. layer thickness specimens. Examining Figure 3.2 (a), in the 0.005 in. layer thickness specimens the microcrack density increases rapidly in the early stages of cycling and slowly approaches a seemingly asymptotic value, or microcrack saturation density. The 0.001 in. layer thickness specimens behave quite differently. A significant delay in the onset of microcracking is observed in these ultra-thin specimens. Once cracking does occur in these ultra-thin specimens, there appears to be a rather steady and large increase in the microcrack density. By 3000 cycles, the microcrack density in the 0.001 in. layer thickness specimens has exceeded that in the 0.005 in. layer thickness specimens. By 5000 cycles, the microcrack density in the thinner specimens is nearly twice that in the thicker specimens. There also appears to be no indication of the microcrack density in the thin ply specimens reaching an asymptotic value for the number of thermal cycles completed.

The microcracking rates shown in Figure 3.2(b) are also significantly different for the two specimens. The rate for the thicker 0.005 in. ply thickness specimen is lower than that of the 0.001 in. ply thickness specimen, as seen by the lower slope of the linear regression. This is somewhat misleading, however, in that the initial rate of cracking in the thick specimen is very high, as seen in Figure 3.2(a). The lower rate of cracking in the logarithmic plot is a result of the logarithmic scale that tends to expand the scale at low cycle numbers and compress the scale at high cycle numbers. It should be noted that the rate of cracking in the thin ply specimen is actually zero until nearly 2000 cycles. This would be indicated by a horizontal line in Figure 3.2(b). On the log scale, the rate of cracking is therefore bilinear for the thin ply specimen.

Although the microcracking rates in Figure 3.2(b) are of limited use in this instance, they will serve as a useful method for comparison later in this chapter. For this reason, this format will be adopted throughout the following sections.

Overall, the behavior observed in the 0.005 in. and 0.001 in. nominal layer thickness specimens is somewhat expected due to the preliminary results shown for these same specimens in reference [9]. The previous work ended cycling at approximately 2000 thermal cycles, but at that cycle count, a rapidly increasing microcrack density in the thinner specimens was observed. Analytical models which account for layer thickness also predict that laminates with thin layers will have microcrack densities that exceed those for the same laminates with thick layers [2].

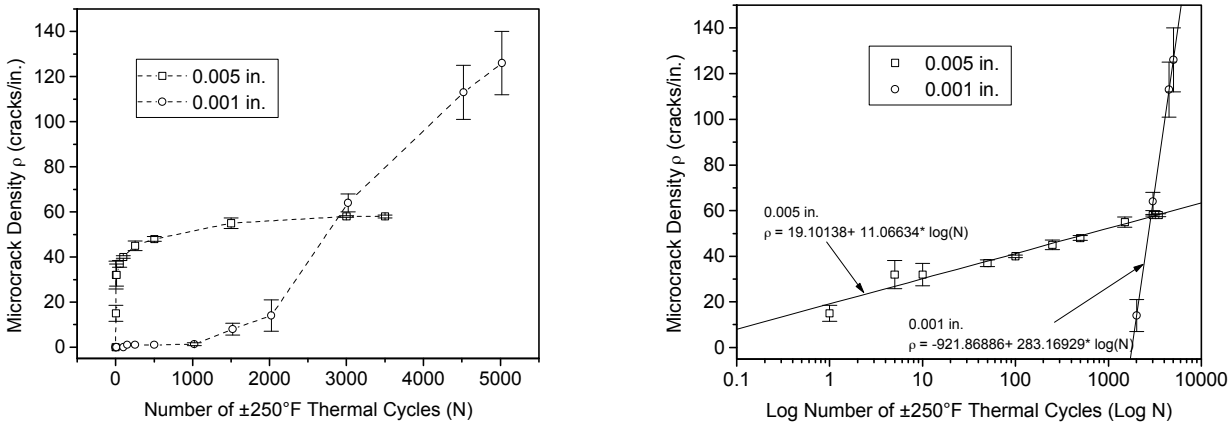

(a) (b)

Figure 3.2. Effect of layer thickness on microcrack density in the c90 layer in P75/ERL1962.X.*.G specimens.

Tabulated microcrack densities for the P75/ERL1962.X.*.G specimens are shown in Table 3.1. The tabulated values are reported in cracks per in., as recorded by experimental observation of the specimen edge. The first number represents the average, with the '+' and '-' representing the maximum deviation above and below average, respectively.

Table 3.1 Dimensional Microcrack Densities (in cracks/in.)
for P75/ERL1962.X.*.G Specimens

0.005 in.	Layer	0	1	5	10	50	100	250	500	1500	3000	3500
lyr. thick.	c90	0	15	32	32	37	40	45	48	55	58	58
Series		+0	+2	+5	+3	+1	+0	+2	+1	+3	+0	+1
H		-0	-4	-7	-6	-2	-1	-2	-1	-2	-0	-1

0.001 in.	Layer	1	1500	2022	2500	3000	3020	4520	5020
lyr. thick.	c90	0†	48†	14‡	80†	92†	64‡	113‡	126‡
Series		+0	+0	+7	+0	+0	+4	+12	+14
UT8X		-0	-0	-7	-0	-0	-4	-12	-14

† Specimen UT8X-4 only; ‡ Specimens UT8X-2 and UT8X-5 only

Edge-view photographs of the P75/ERL1962.X.*.G specimens containing microcracks are shown in Figure 3.3. The microcracks in the thicker 0.005 in. layer thickness specimens tend to be very clear and readily countable. Those cracks in the central double-thickness layer typically are observed to have larger crack opening displacements as well. In general, the microcracks propagate perpendicular to the thickness direction, indicating the lack of shear stresses in the cross-ply specimens. The microcracks in the thinner 0.001 in. layer thickness specimens are much more difficult to see. Rarely do they result in the large crack opening displacements observed in the thicker layer specimens. Often times, the microcracks in the thin-layer specimens are nothing more than a coalescence of fiber debonds which combine to form a continuous crack running more than halfway through the thickness of the layer. It should be noted that the microcracks observed with the microscope are much more readily seen than the photographs indicate, particularly in the case of the thin-layer specimens.

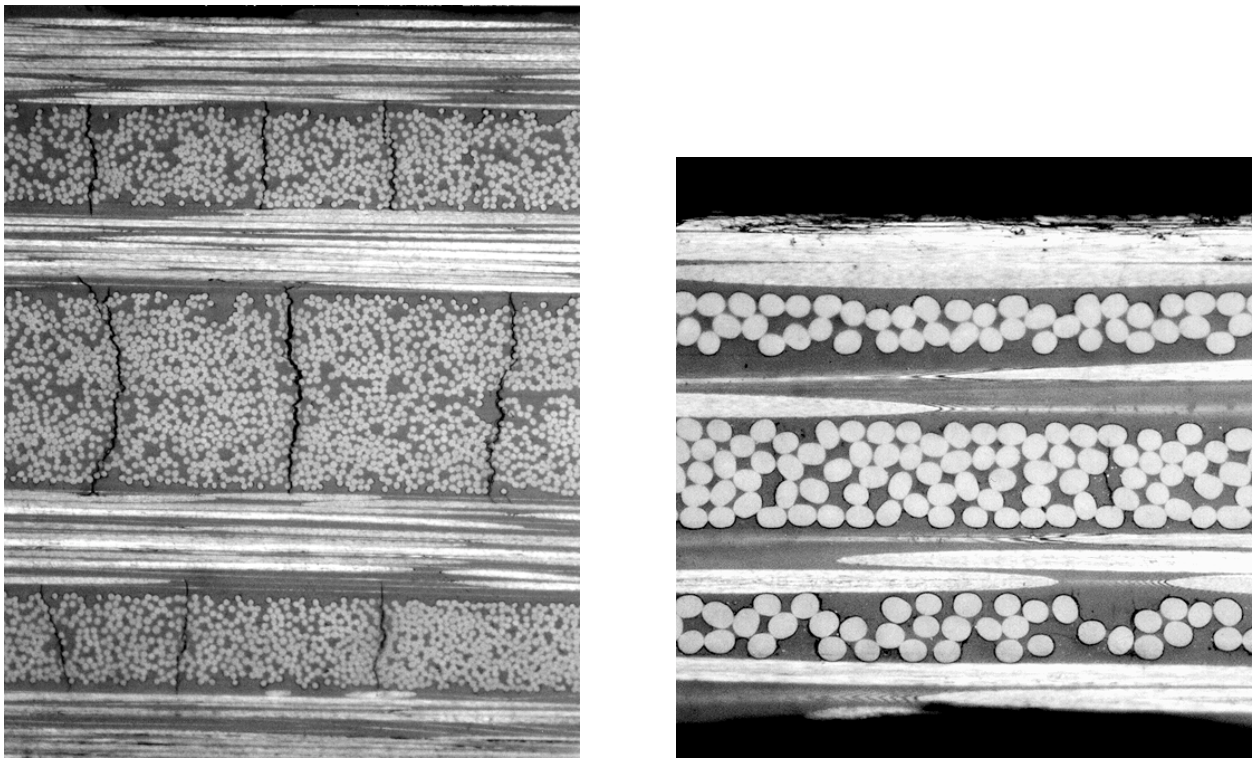

(a) H-2 (0.005 in. layer thickness) 3500 ±250°F cycles (100X)

(b) UT8X-2 (0.001 in. layer thickness) 5020 ±250°F cycles (400X)

Figure 3.3. Edge-view photographs of P75/ERL1962.X.*.G specimens containing microcracks.

X-ray photographs are shown in Figure 3.4 of specimens from the same material series and same thermal cycling history as those specimens shown in Figure 3.3. These X-rays are taken from above the top surface of the specimen looking down. The microcracks appear as dark lines as a result of the dye penetrant that wicks into the cracks and prevents the X-rays from penetrating the specimen completely. There are multiple cracking layers in all of the specimens considered in this study, and the X-rays detect cracks in all layers. This tends to make the microcracks appear unfocused due to 'overlapping' cracks from the multiple layers.

The microcracks observed in specimen H-3 shown in Figure 3.4(a), appear as horizontal and vertical lines in the figure, clearly identifying the cross-ply lamination sequence. If the microcracks did not propagate throughout the entire width of the specimen and were instead concentrated at the edges of the specimen, darker areas near the left and right edges of the specimen would be observed in the figure. The cracks instead appear to be continuous throughout the entire width of the specimen. The X-ray for specimen UT8X-5 in Figure 3.4(b) does not show the microcracks clearly. This may be in part due to the very small crack opening

mentioned earlier for these thin specimens. As a result, the cracks simply do not show up well. Those cracks that are characterized by a coalescence of fiber debonds would not be expected to show up due to the meandering nature of the crack through the thickness of the layer. It is encouraging, however, to observe the lack of discoloration of the X-ray near the specimen edges, indicating that the cracks present do not exist simply at the edges of the specimen.

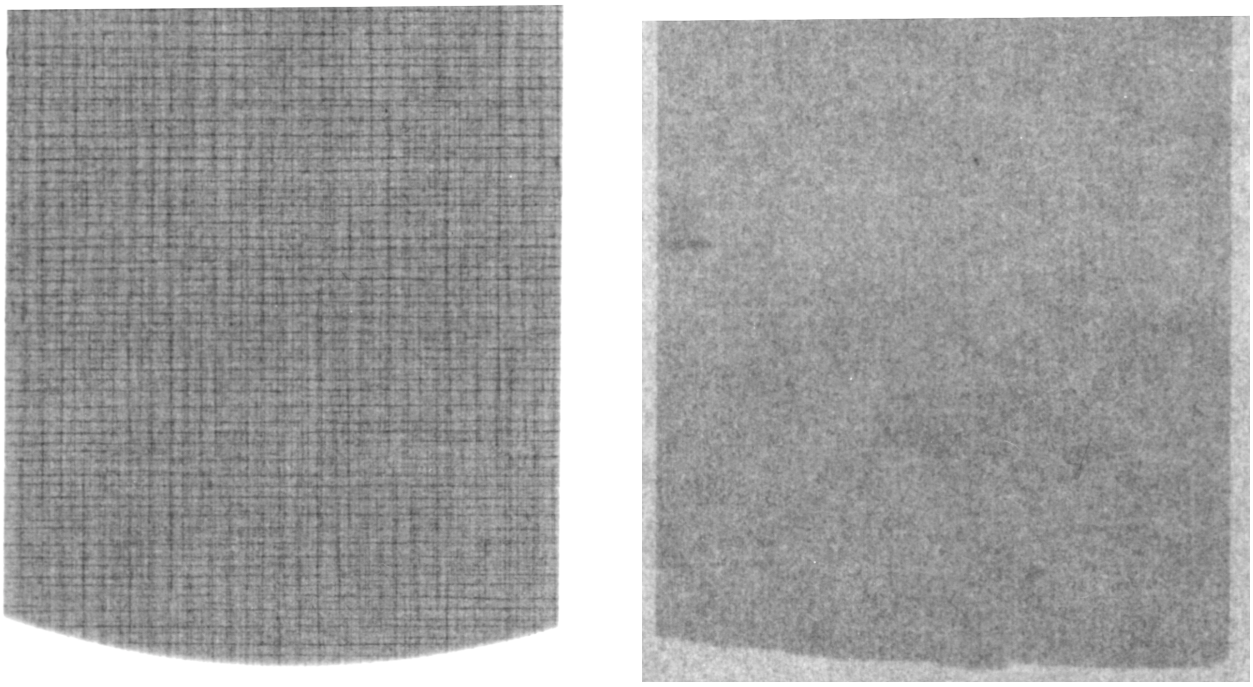

(a) H-3 (0.005 in. layer thickness) 3500 ±250°F cycles

(b) UT8X-5 (0.001 in. layer thickness) 5020 ±250°F cycles

Figure 3.4. X-ray photographs of P75/ERL1962.X.*.G specimens containing microcracks.

Microcrack densities for the P75/RS3.Q2.*.G specimens are presented next and are tabulated in Table 3.2. The two specimens compared are both P75/RS3 material and have the same quasi-isotropic lamination sequence. One of the specimens has a nominal layer thickness of 0.005 in. and the other has a 0.002 in. nominal layer thickness. It should be pointed out that after the initial record at 0 cycles, the next record of microcrack density for these materials is at 1500 cycles. For this reason, information about these materials below 1500 cycles will be surmised based on the empirical microcracking rates presented in the right-hand graphs of Figure 3.5.

The microcracking characteristics in the +45° layer in Figure 3.5 (a) and the −45° layer in (c) are similar in some ways to the behavior seen previously for the P75/ERL1962 cross-ply

specimens. Namely, from the right-hand graphs in the figures there is predicted to be a delay in the onset of microcracking in the specimen with 0.002 in. thick layers compared to the specimen with 0.005 in. thick layers. Once microcracking does begin in these thin-layer specimens, microcrack densities in the –45° layer are experimentally observed to increase at a rate which exceeds that for the thick-layer specimens. For the 3000 cycles completed on these specimens, the –45° layer crack density in the specimens with 0.002 in. thick layers exceed those in specimens with 0.005 in. thick layers by approximately 35%. In the +45° layer, crack densities in the thin-layer specimens are predicted to exceed those in thick-layer specimens after approximately 6000 cycles, according to empirical microcracking rates from the right-hand graph in Figure 3.5(a).

The behavior in the 90° layer illustrated in Figure 3.5 (b) appears to be somewhat contrary to the behavior described to this point. Empirical microcracking rates in the right-hand figure imply that the specimen with 0.002 in. thick layers would have to have an uncharacteristically high microcrack density (140 cracks/in.) after the first thermal cycle. This is particularly surprising considering the fact that, as indicated in Table 3.2, there are no microcracks present in the 90° layer prior to cycling. Note, however, that this implied behavior is based on an extrapolation from very limited data that is tightly clustered near 1000 cycles. It is likely, therefore, that this extrapolation is misleading. Despite this apparent contrary behavior, the 90° layer does follow the previous trend with the thinner specimens having significantly higher microcrack densities after thermal cycling to several thousand cycles. In fact, for the 3000 cycles completed, the average microcrack density in the 90° layer of the thinner specimens exceeds that in the thicker specimens by a factor of 2.4.

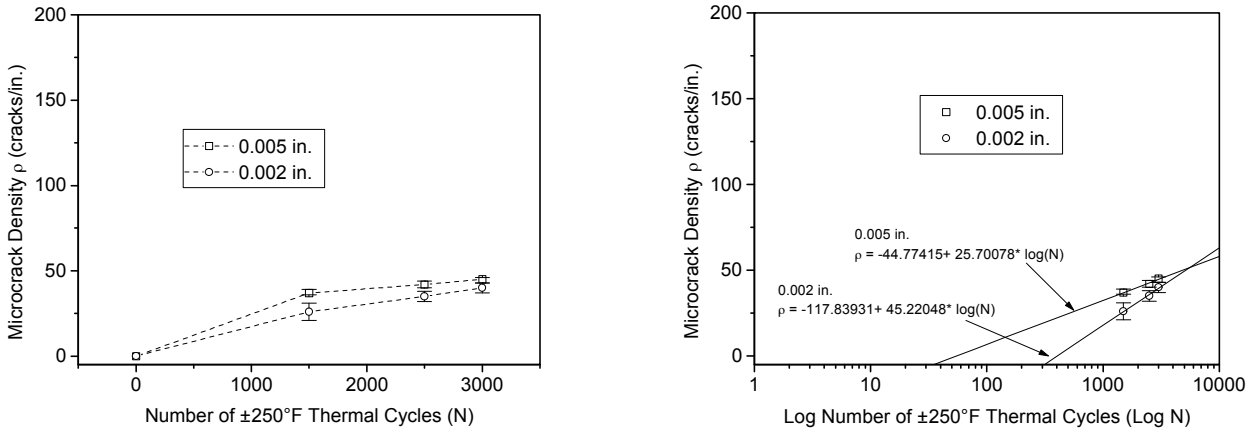

(a) +45° layer

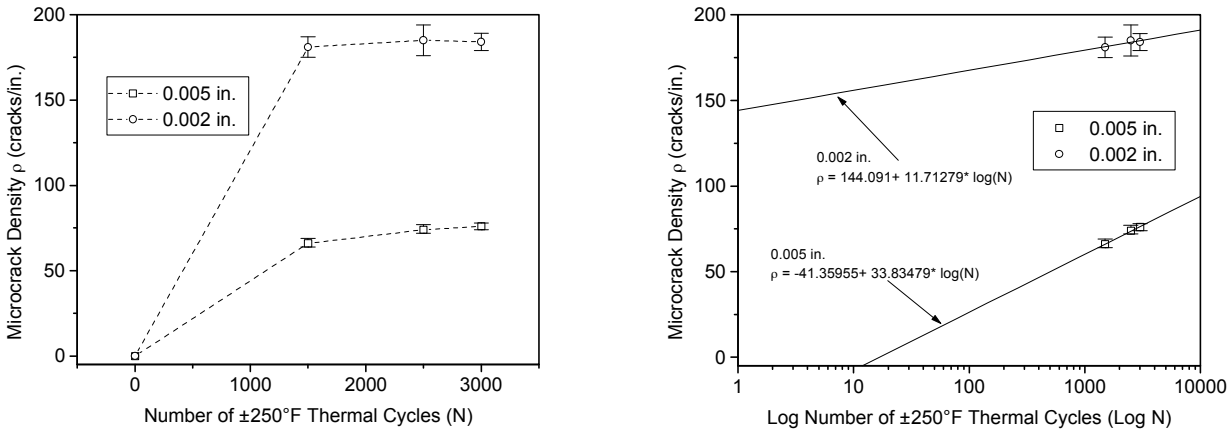

(b) 90° layer

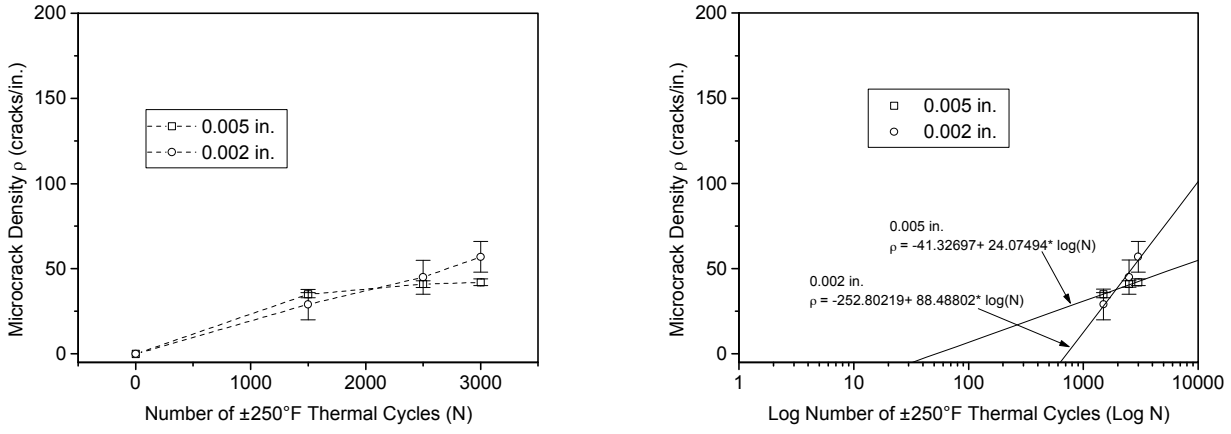

(c) –45° layer

Figure 3.5. Effect of layer thickness on microcrack density in P75/RS3.Q2.*.G specimens.

Table 3.2 Dimensional Microcrack Densities (in cracks/in.)
for P75/RS3.Q2.*.G Specimens

	Layer	0	1500	2500	3000
0.005 in. layer thickness Specimen Series 75RS3	45	0 +0 -0	37 +2 -1	42 +2 -2	45 +1 -2
	90	0 +0 -0	66 +3 -2	74 +3 -2	76 +2 -2
	-45	0 +0 -0	35 +1 -2	41 +2 -2	42 +2 -2

	Layer	0	1500	2500	3000
0.002 in. layer thickness Specimen Series 275RS3*	45	0 +0 -0	26 +5 -5	35 +3 -3	40 +3 -3
	90	0 +0 -0	181 +6 -6	185 +9 -9	184 +5 -5
	-45	0 +0 -0	29 +9 -9	45 +10 -10	57 +9 -9

* Specimens 275RS3-1 and 275RS3-2 only.

Edge-view photographs of P75/RS3.Q2.*.G specimens containing microcracks are shown in Figure 3.6. Note the magnification of the specimen containing 0.002 in. thick layers is twice that of the specimen with 0.005 in. thick layers. The significantly higher microcrack density in the 90° layer in the specimen containing 0.002 in. thick layers compared to the specimen with 0.005 in. thick layers can clearly be seen. The near-45° direction with which some of the microcracks propagate through the thickness of the layers implies the presence of through-the-thickness shear stresses in the quasi-isotropic specimens that were not present in the cross-ply specimens seen previously. Again, the cracks in the central double-thickness layers typically have larger crack opening displacements, as see in Figure 3.6 (a).

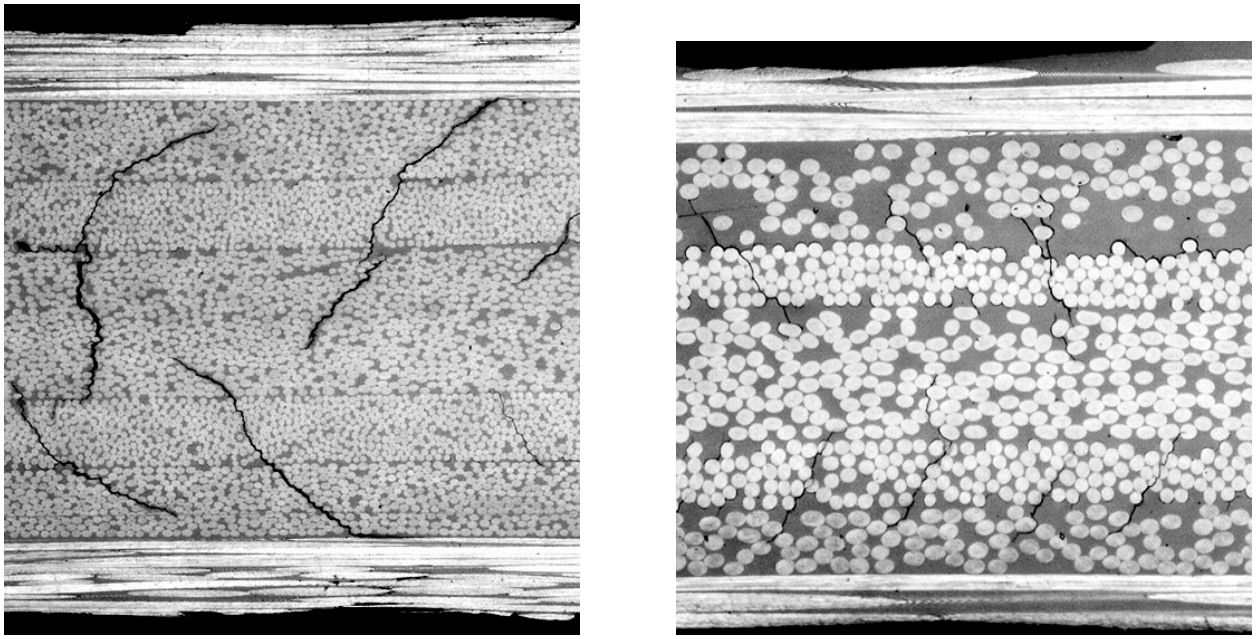

(a) 75RS3-2 (0.005 in. layer thickness) 3000 ±250°F cycles (100X)

(b) 275RS3-2 (0.002 in. layer thickness) 3000 ±250°F cycles (200X)

Figure 3.6. Edge-view photographs of P75/RS3.Q2.*.G specimens containing microcracks.

X-ray photographs of P75/RS3.Q2.*.G specimens are shown in Figure 3.7. Note the obvious presence of cracks oriented at 45° to the axial direction in the 0.005 in. layer thickness specimen in Figure 3.7(a). The clarity with which these cracks show up is attributed to the larger crack opening displacement of the cracks in this double-thickness layer at the midplane of the specimen. Note also that these cracks tend to propagate through the entire width of the specimen. Although most cracks are not clearly visible in either specimen, there are no obvious cracks confined only to the edges of the specimens, as indicated by the uniformity of grayness throughout the width of the specimens. It should also be noted that the 45° angle, or any angle other than vertical, with which most of the cracks in the quasi-isotropic specimens propagate through the thickness of a layer, makes viewing the cracks from above difficult.

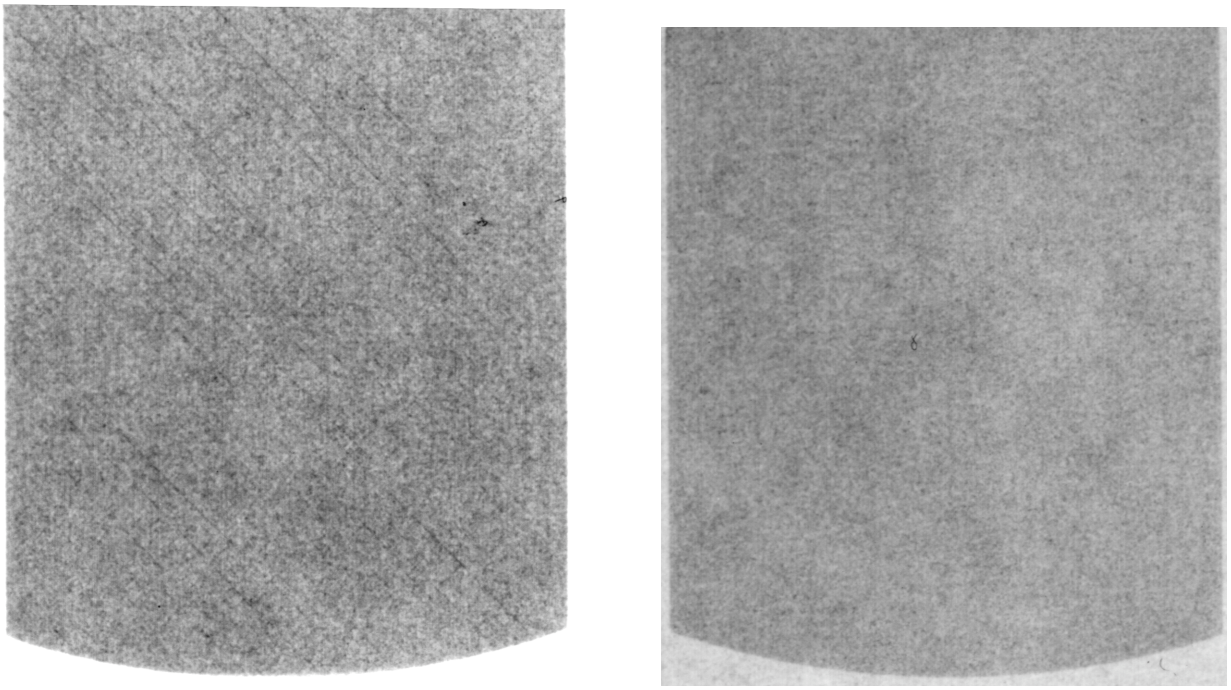

(a) 75RS3-1 (0.005 in. layer thickness) 3000 ±250°F cycles

275RS3-1 (0.002 in. layer thickness) 3000 ±250°F cycles

Figure 3.7. X-ray photographs of P75/RS3.Q2.*.G specimens containing microcracks.

Layer thickness has been shown in Figure 3.2 and Figure 3.5 to cause a dramatic effect on thermally-induced microcrack density, independent of material type and lamination sequence. Because of the inevitable variation in layer thickness from one material series to another due to manufacturing anomalies, a nondimensional microcrack density is now introduced in an attempt to isolate the layer thickness effect. In doing so, it is hoped that thickness variations will not affect trends observed in other parameters studied in this investigation, i.e., fiber type, matrix type, and thermal cycling range. The microcrack densities are nondimensionalized by multiplying the measured microcrack density by the layer thickness for the layer with the given crack density. This was explained earlier in section 3.1.1, along with the definition of lineal microcrack density. The nondimensional lineal microcrack densities for the same two specimen series presented in Figure 3.2, i.e., P75/ERL1962 $[0/90]_{2s}$ specimens with 0.005 in. and 0.002 in. thick layers, are now presented in Figure 3.8 as an example of the application of nondimensional microcrack density.

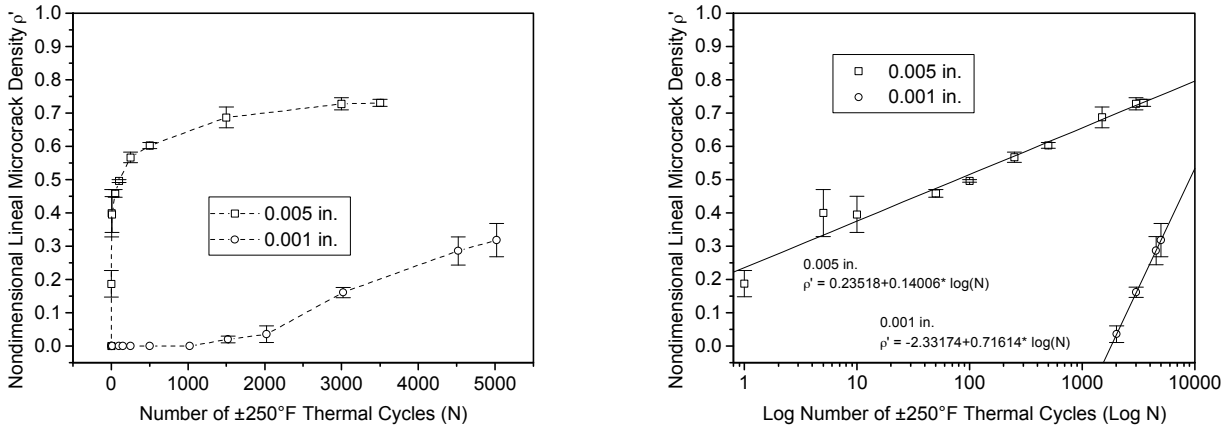

(a) (b)

Figure 3.8. Nondimensional lineal microcrack densities in the c90 layer in P75/ERL1962.X.*.G specimens.

Examining the nondimensional lineal microcrack densities in Figure 3.8, it is seen that the damage in the form of microcracking now appears to be greater in the specimen with 0.005 in. thick layers than in the specimen with 0.001 in. thick layers. This is an important point that will be later realized in the following section concerning the CTE's for these two specimens. It will be shown that the average room temperature CTE for the thinner specimen changes much less than that of the thicker specimen, indicating that volumetrically, the specimen with thick layers is 'damaged' to a greater extent. This trend is correctly indicated by the nondimensional microcrack density and incorrectly indicated by the dimensional microcrack density.

3.2.2 Laminate Thermal Expansion Behavior

This section examines the effect of layer thickness on room temperature laminate CTE. In addition to the P75/ERL1962.X.*.G and P75/RS3.Q2.*.G specimens examined in the previous section for microcrack density, the P75/ERL1962.Q2.*.G specimens are included in this section as well. Due to experimental difficulties, the ultra-thin P75/ERL1962.Q2.1.G specimens were not characterized using microcrack density. Recalling, the X and Q2 specimens from the P75/ERL1962 material compare specimens with 0.005 in. and 0.001 in. nominal layer thickness, whereas the Q2 specimens from P75/RS3 material compare specimens with 0.005 in. and 0.002 in. nominal layer thickness.

The average room temperature CTE's for the P75/ERL1962 cross-ply specimens are shown in Figure 3.9. Plus and minus one standard deviation from the average are indicated by the error bars in the figure. The change in CTE from the uncycled to the post-cycled state is indicated by Δ shown in the figures. As alluded to in the previous discussion of nondimensional microcrack

densities, the CTE of the specimens with 0.005 in. thick layers changes much more than for the specimens with 0.001 in. thick layers, i.e., -0.618 με/°F for the thick specimens compared to –0.083 με/°F for the thin specimens. From a dimensional stability viewpoint, the greater change in CTE implies far greater 'damage' in the thick-layer specimens. This characteristic qualitatively agrees with the trend shown previously by the nondimensional microcrack densities, but not the trend shown by the dimensional microcrack densities. For this reason, there appears to be some justification for nondimensionalizing the microcrack densities, particularly when identifying trends independent of layer thickness, i.e., fiber type, matrix type, and thermal cycling range.

Note in Figure 3.9 that the uncycled laminate CTE for the specimens with 0.005 in. thick layers is slightly more positive than the CTE for the specimens with 0.001 in. thick layers. All material properties being the same, the uncycled CTE's for the two specimens should be the same, regardless of layer thickness. As it turns out, due to variations in fiber volume fraction, the lamina properties are different for the two specimen series. Due to similar variations in fiber volume fraction, the actual lamina properties for all material series are somewhat different from the nominal properties listed in Table 2.3 and are summarized in Appendix F along with the explanation of how the lamina properties were calculated.

(a) 0.005 in. layer thickness (b) 0.001 in. layer thickness

Figure 3.9. Effect of layer thickness on room temperature CTE in P75/ERL1962.X.*.G specimens.

The average room temperature CTE's for the P75/ERL1962 quasi-isotropic specimens are shown in Figure 3.10. Although the uncycled and post-cycled CTE values are somewhat different from the cross-ply configuration of Figure 3.9, similar trends are observed when comparing the change in CTE for the thick-layer and thin-layer specimens. Once again, from a dimensional stability viewpoint, the thin-layer specimens appear to be significantly more stable.

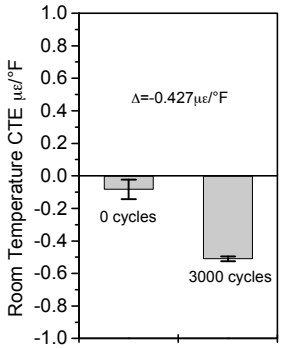

(a) 0.005 in. layer thickness

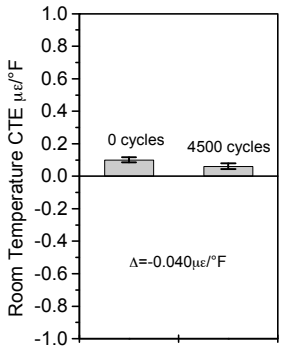

(b) 0.001 in. layer thickness

Figure 3.10. Effect of layer thickness on room temperature CTE in P75/ERL1962.Q2.*.G specimens.

The room temperature CTE data for the P75/RS3.Q2.*.G configuration specimens, shown in Figure 3.11, are contrary to that just shown for the P75/ERL1962.X.*.G and P75/ERL1962.Q2.*.G specimens. As seen in Figure 3.11 by the change in CTE from the uncycled to the post-cycled condition, the specimen with 0.002 in. nominal thickness layers appears to be affected more by thermal cycling than the specimen with 0.005 in. layers. After visual inspection of the specimens, it was noted that the specimens with 0.002 in. layers were noticeably warped along their length. It is possible that manufacturing problems related to fiber alignment and asymmetry in the lamination sequence are responsible for such warpage. Because the interferometer used to measure thermal expansion behavior requires flat specimens, the slight curvature of the specimen may have adversely affected the results for these particular specimens.

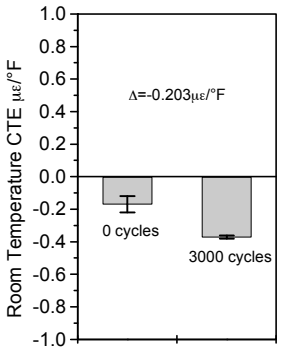

(a) 0.005 in. layer thickness

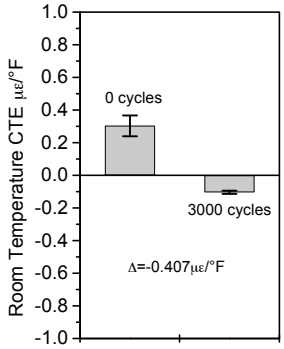

(b) 0.002 in. layer thickness

Figure 3.11. Effect of layer thickness on room temperature CTE in P75/RS3.Q2.*.G specimens.

3.2.3 Laminate Stiffness

Laminate stiffnesses, normalized by fiber volume fraction, for the P75/ERL1962.X.*.G, P75/ERL1962.Q2.*.G, and P75/RS3.Q2.*.G specimens are shown in Figure 3.12, Figure 3.13, and Figure 3.14, respectively. The average uncycled and post-cycled behavior is shown for each specimen series along with one standard deviation, indicated by the error bars, where applicable. In most cases, the average uncycled stiffness falls within one standard deviation of the average post-cycled stiffness. In some instances, the average post-cycled stiffness is seen to increase compared to the uncycled stiffness. Similar observations were noted in Reference [6] and were attributed to manufacturing variability, a likely explanation here as well. In the case of the P75/ERL1962.X.5.G specimens in Figure 3.12(a), only one specimen was available for uncycled stiffness. It is quite possible that given more specimens of this type, the average uncycled stiffness would again fall within the standard deviation of the post-cycled stiffness. The only instance in which a statistically significant change in stiffness is recorded occurs in the P75/ERL1962.Q2.5.G specimens, and in this case only a 4% decrease from cycled to post-cycled stiffness is observed. It is concluded that thermally-induced microcracking has virtually no effect on laminate stiffness in these specimens, and certainly there is no effect of thermal cycling on laminate stiffness due to variation in layer thickness.

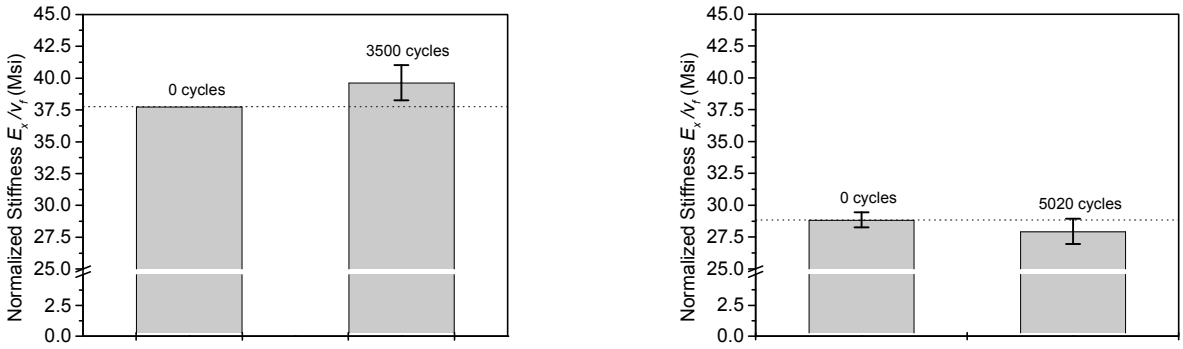

(a) 0.005 in. layer thickness (b) 0.001 in. layer thickness

Figure 3.12. Effect of layer thickness on normalized laminate stiffness in P75/ERL1962.X.*.G specimens.

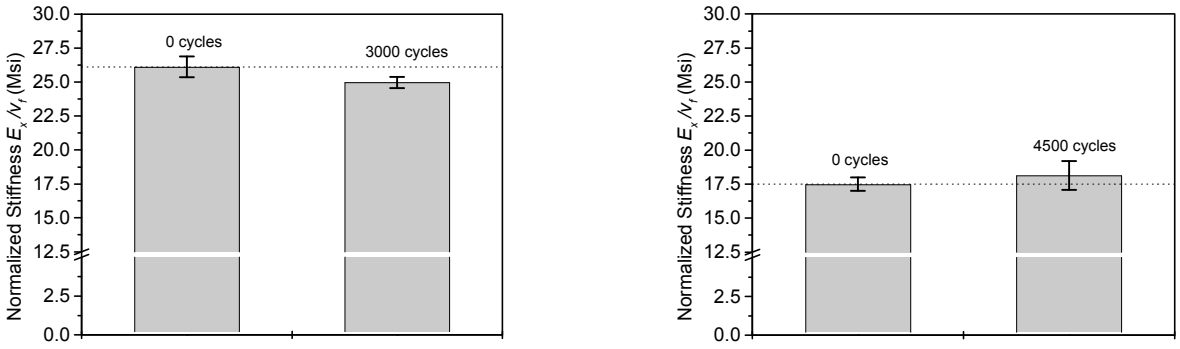

(a) 0.005 in. layer thickness (b) 0.001 in. layer thickness

Figure 3.13. Effect of layer thickness on normalized laminate stiffness in P75/ERL1962.Q2.*.G specimens.

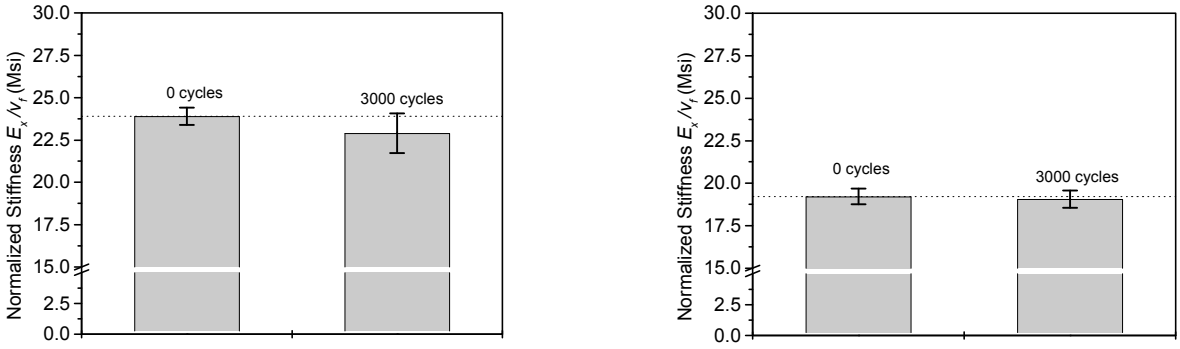

(a) 0.005 in. layer thickness (b) 0.002 in. layer thickness

Figure 3.14. Effect of layer thickness on normalized laminate stiffness in P75/RS3.Q2.*.G specimens.

3.3 EFFECT OF FIBER TYPE

Two different comparisons are made in this investigation regarding fiber type. The first comparison looks at the effect of fiber precursor. In this comparison results from two composites, one with a PAN-based fiber and one with a pitch-based fiber, are studied. All other properties of the two fibers are similar. The second comparison considers three different pitch-based fibers, the fibers varying in stiffness and thermal expansion coefficients. For all the comparisons in this section, fiber type is the only variable. All other material and loading parameters, namely, matrix type, lamination sequence, layer thickness, and thermal cycling temperature range, are nominally the same.

3.3.1 Effect of Fiber Precursor PAN-Based versus Pitch-Based Fibers

The present investigation includes two material series that are intended to yield information regarding the effect of fiber precursor. The T50/ERL1962 and P55/ERL1962 cross-ply and quasi-isotropic (Q1) specimens have fibers that are very similar in stiffness and CTE, but are derived from two entirely different materials. The T50 fiber is a synthetic polyacrylonitrile (PAN-based) fiber. The P55 fiber is an organic pitch-based fiber. The nominal properties for the two fibers are summarized in Table 3.3.

Table 3.3 Axial Direction Fiber Properties for PAN-Based and Pitch-Based Fibers[†]

Fiber	Stiffness (Msi)	Strength (Ksi)	CTE (με/°F)
T50 (PAN)[52]	55	375	-0.50
P55 (pitch)[53]	55	275	-0.70

[†] Fiber data from Amoco Performance Products, Inc. vendor product information bulletin.

The specimens containing the PAN-based and pitch-based fibers were cycled between –250°F and +250°F for 3500 cycles. The next section examines the accumulation of microcracks as the number of thermal cycles increases.

3.3.1.1 Microcrack Density

Nondimensional lineal microcrack densities are first presented for the cross-ply specimens, noted by */ERL1962.X.5.G. Data for both T50 and P55 fiber types and for both the o90 layer and for the c90 layer are summarized in Figure 3.15 (a) and (b). It can be said for both materials that, in general, microcracking occurs more rapidly in the early stages of thermal cycling with what appears to be an asymptotic approach to some value that depends on the fiber type in the specimen. Microcrack densities are noticeably higher in the specimens containing the P55 fiber. It appears that a delayed onset of microcracking is present in specimens containing the T50 fibers. For both specimen types, it appears that microcrack density does not reach saturation in 3500 cycles. Comparing the microcracking data using the log scale in Figure 3.15 (b), the microcracking rates appear to be slightly higher in the T50 specimens in both layers, with a greater delay in the onset of microcracking predicted in the T50 specimens as well. These results indicate that the T50 specimens may in fact reach microcrack densities equal to the P55 specimens after additional thermal cycling.

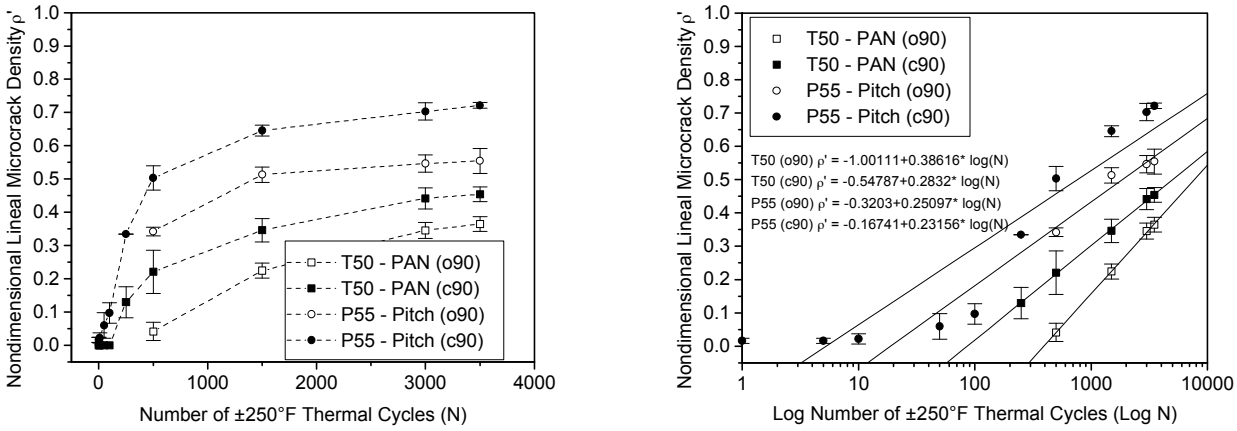

(a) (b)

Figure 3.15. Effect of fiber precursor on microcrack density in T50 and P55/ERL1962.X.5.G specimens.

Below are the dimensional microcrack densities in tabular form for the specimens with T50 and P55 fibers in cross-ply configuration.

Table 3.4 Dimensional Microcrack Densities (in cracks/in.)
for T50 and P55/ERL1962.X.5.G Specimens

	Layer	0	1	5	10	50	100	250	500	1500	3000	3500
T50	o90								8	43	66	69
Fiber									+4	+4	+4	+5
									-6	-4	-4	-3
Specimen	c90	0	0	0	0	0	0	12	21	33	42	43
Series		+0	+0	+0	+0	+0	+0	+5	+7	+3	+3	+2
J		-0	-0	-0	-0	-0	-0	-4	-5	-4	-4	-2

	Layer	0	1	5	10	50	100	250	500	1500	2500	3000	3500
P55	o90								63†	95	99‡	102	103†
Fiber									+2	+4	+0	+5	+5
									-2	-5	-0	-5	-5
Specimen	c90	0†	2†	2†	2†	6†	9†	31†	47†	60	66‡	65	67†
Series		+0	+1	+1	+1	+3	+2	+0	+2	+2	+0	+3	+1
O		-0	-1	-1	-1	-3	-2	-0	-2	-2	-0	-2	-1

† Specimens O-3 and O-4 only; ‡ Specimen O-2 only.

The photographs in Figure 3.16 illustrate the edge view of the T50 and P55/ERL1962.X.5.G specimens after 3500 cycles between -250°F and +250°F. There is little detectable difference in the manner in which each of these specimens microcrack. X-ray photographs of T50 and P55 cross-ply specimens are shown in Figure 3.17. Again, there is little detectable difference in the manner in which these specimens microcrack. It is noted that the cracks appear to propagate throughout the width of both specimens.

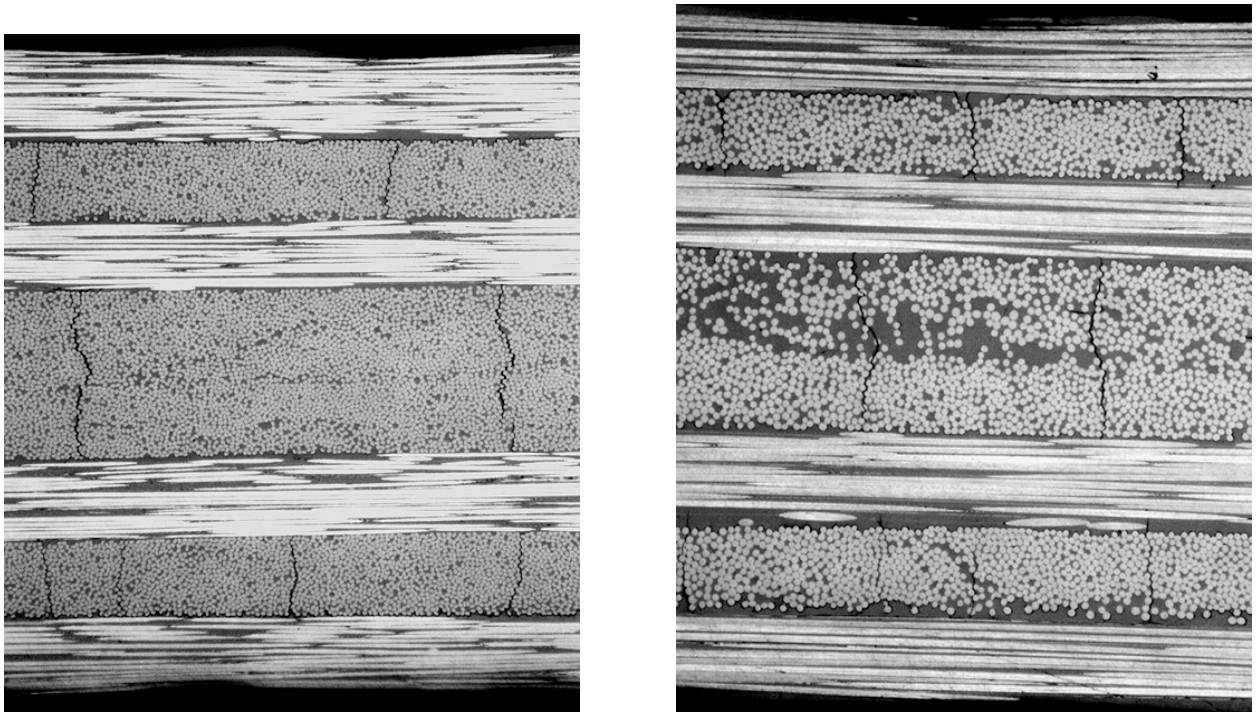

(a) J-2 (T50) 3500 ±250°F cycles (100X) (b) O-4 (P55) 3500 ±250°F cycles (100X)

Figure 3.16. Edge-view photographs of T50 and P55/ERL1962.X.5.G specimens containing microcracks.

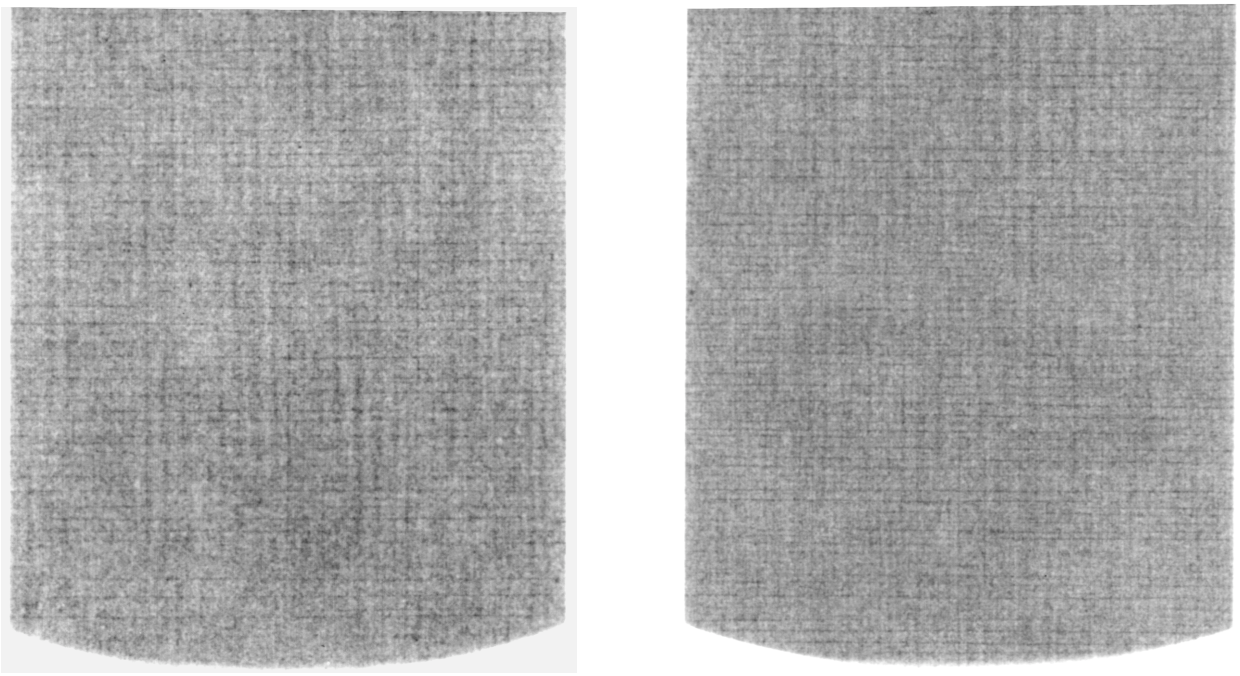

(a) J-2 (T50) 3500 ±250°F cycles (b) O-2 (P55) 3500 ±250°F cycles

Figure 3.17. X-ray photographs of T50 and P55/ERL1962.X.5.G specimens containing microcracks.

The only significant geometric difference in the two specimens is due to the fiber geometry of the PAN-based versus the pitch-based fibers. The T50 PAN-based fiber is typically kidney shaped in cross-section and smaller in diameter compared to the P55 pitch fiber, which is typically circular or oval in cross-section. In addition, the PAN-based fiber tends to have a rough surface compared to the smooth surface of the pitch-based fibers. These characteristics are better illustrated in the high magnification edge-view photographs in Figure 3.18 that show a 90° layer in both specimens.

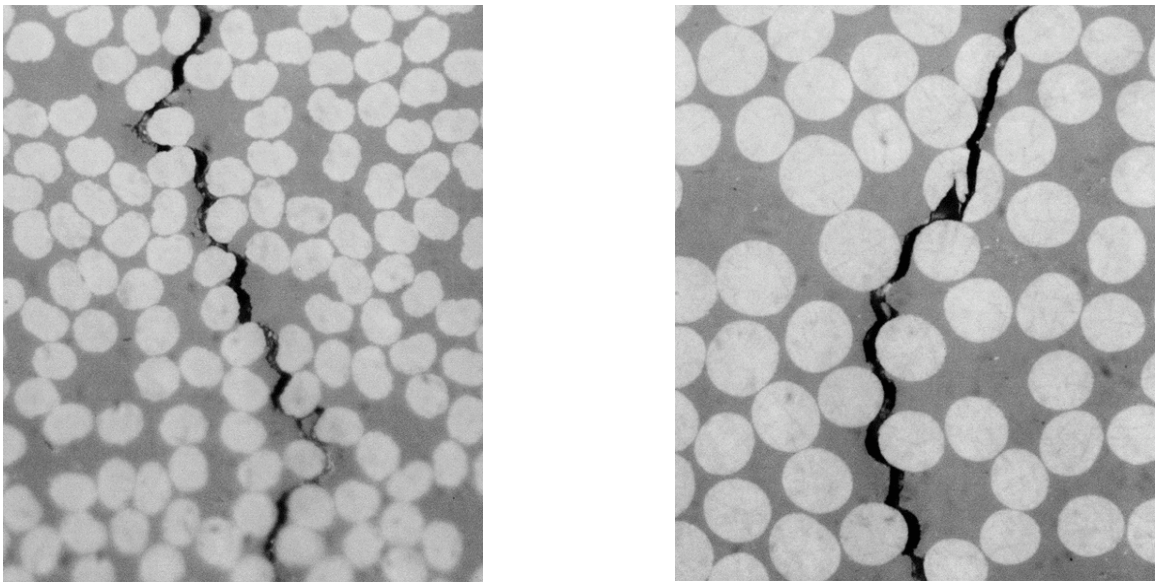

(a) J-2 (T50) 3500 ±250°F cycles (1000X) (b) O-4 (P55) 3500 ±250°F cycles (1000X)

Figure 3.18. Edge-view photographs at high magnification of 90° layer in T50 and P55/ERL1962.X.5.G specimens containing microcracks.

The smaller fiber diameter in the T50 PAN-based fibers may explain the lower microcrack densities compared to the pitch-based fibers. According to reference [54], thermally-induced hoop stresses at the fiber/matrix interface increase as fiber diameter increases. This would imply that for the same thermal loading, the larger diameter fibers would have a greater tendency to initiate a crack at this location. It is also true that the P55 fiber is reported to have a more negative axial CTE (see Table 3.3) than the T50 fiber. Due to the larger mismatch in CTE between the P55 fiber and the surrounding matrix, this would also tend to result in higher thermal stresses in the P55-based specimens compared to the T50-based specimens. In fact, the sensitivity analysis that is presented later in Chapter 4 that examines the effect of various material parameters on microcracking behavior indicates that, in fact, the more negative CTE of the P55 fiber would result in slightly higher microcrack densities at a given cycle count compared to the T50 fiber.

Microcrack density results are presented in Figure 3.19 for specimens including the same T50 and P55 fibers, but in the quasi-isotropic lamination sequence, denoted by T50 and P55/ERL1962.Q1.5.G. The same general trends are seen for the quasi-isotropic specimens that were seen for the cross-ply specimens, namely, the specimens containing P55 pitch-based fibers have higher microcrack densities than those with the T50 PAN-based fibers. The microcracking rates for the T50-based and P55-based composites are similar for each of the three layer types

containing cracks. The delayed onset of microcracking is again more prevalent in the T50-based composites. In the +45° layer, the microcracking rate for the T50 specimens is seen to be slightly lower that that of the P55 specimens. The opposite is true in the 90° and –45° layers. Note also that the scatter in the microcrack densities for these quasi-isotropic specimens is larger than that seen previously for the cross-ply specimens.

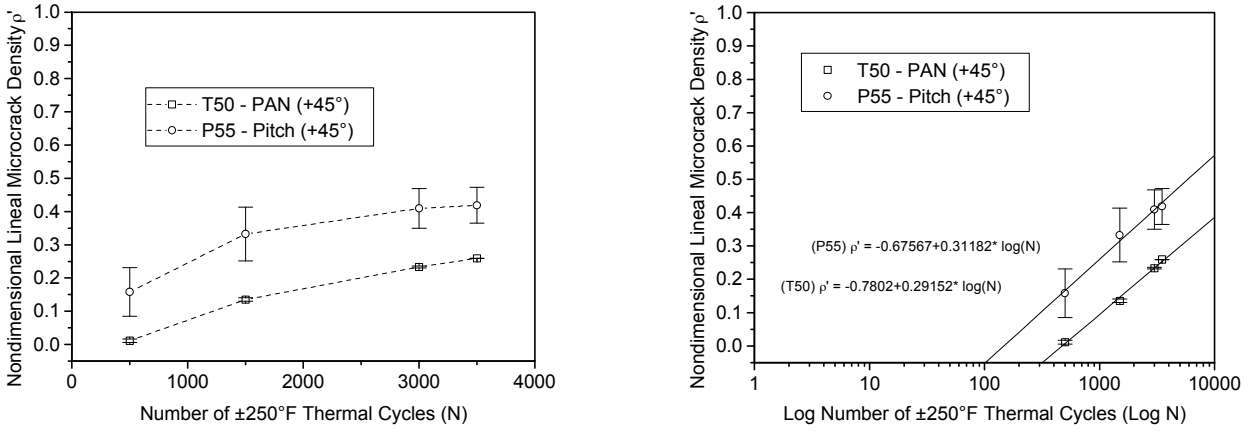

(a) +45° layer

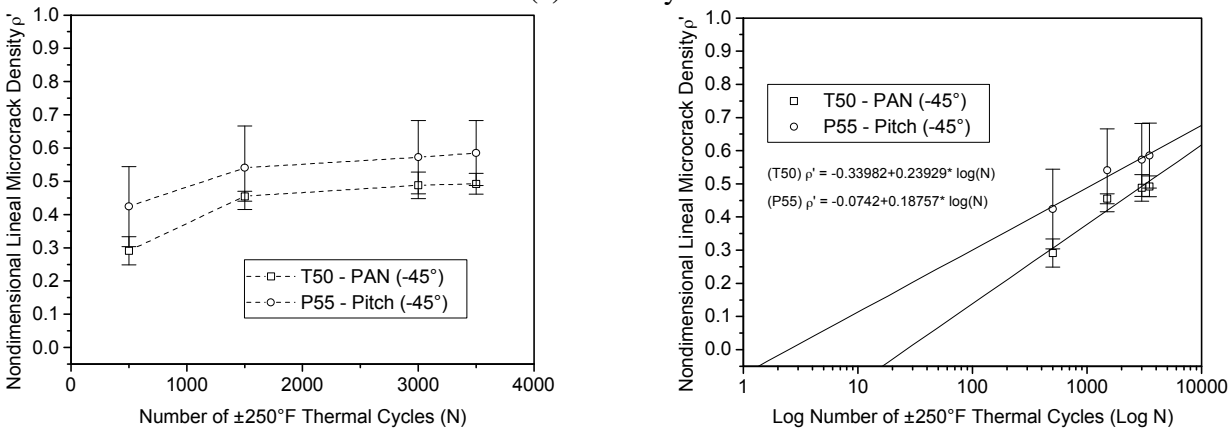

(b) –45° layer

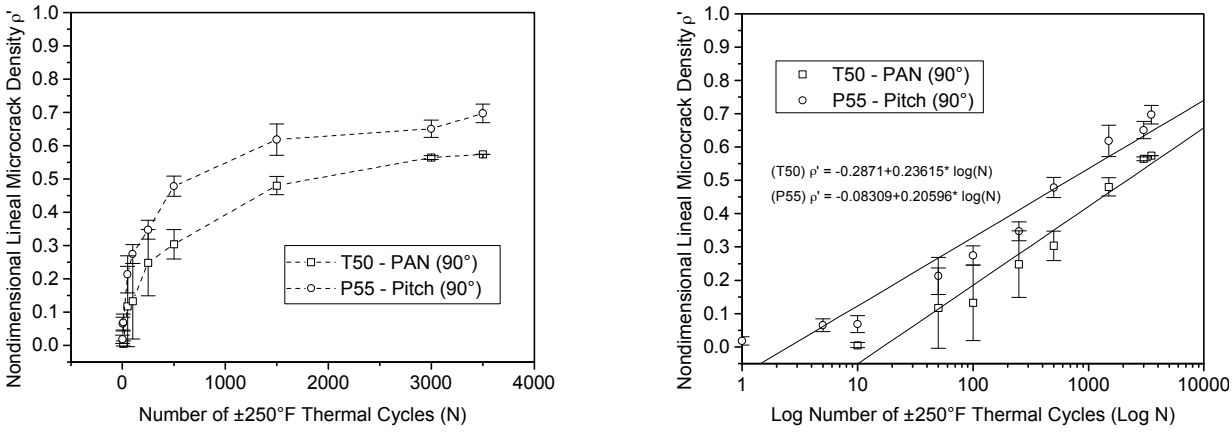

(c) 90° layer

Figure 3.19. Effect of fiber precursor on microcrack density in T50 and P55/ERL1962.Q1.5.G specimens.

The dimensional microcrack densities for the T50 and P55/ERL1962.Q1.5.G specimens are shown in Table 3.5.

Table 3.5 Dimensional Microcrack Densities (in cracks/in.)
for T50 and P55/ERL1962.Q1.5.G Specimens

	Layer	0	1	5	10	50	100	250	500	1500	3000	3500
T50 Fiber	45								2 +1 -1	18 +1 -1	31 +0 -0	35 +0 -0
	-45								39 +4 -4	61 +1 -1	65 +3 -3	66 +3 -3
Specimen Series K*	90	0 +0 -0	0 +0 -0	0 +0 -0	1 +1 -1	11 +8 -8	13 +8 -8	24 +7 -7	29 +3 -3	46 +2 -2	54 +0 -0	54 +0 -0

* Specimens K-3 and K-4 only

	Layer	0	1	5	10	50	100	250	500	1500	3000	3500
P55 Fiber	45								21 +11 -6	43 +10 -11	54 +5 -9	55 +4 -8
	-45								55 +14 -17	71 +11 -19	75 +9 -17	76 +8 -15
Specimen Series P	90	0 +0 -0	2 +1 -1	6 +2 -1	6 +3 -1	20 +5 -5	25 +3 -2	32 +2 -2	44 +3 -3	57 +3 -5	60 +2 -3	64 +3 -3

The photographs in Figure 3.20 illustrate typical microcracks in T50 and P55/ERL1962.Q1.5.G specimens cycled 3500 times between -250°F and +250°F. The near-45° direction with which some of the microcracks propagate through the thickness of the layers implies the presence of through-the-thickness shear stresses in the quasi-isotropic specimens that were not present in the cross-ply specimens seen previously in Figure 3.16.

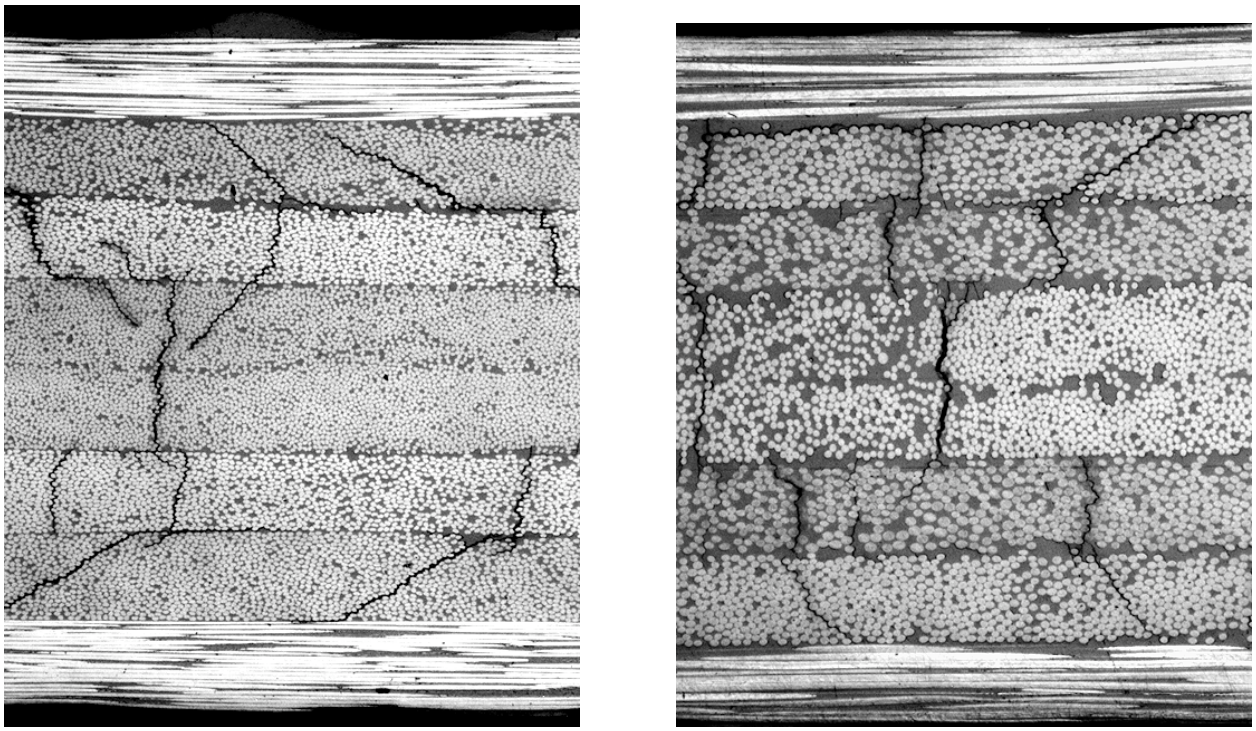

(a) K-3 (T50) 3500 ±250°F cycles (100X) (b) P-3 (P55) 3500 ±250°F cycles (100X)

Figure 3.20. Edge-view photographs of T50 and P55/ERL1962.Q1.5.G specimens containing microcracks.

X-ray photographs of T50 and P55/ERL1962.Q1.5.G specimens are shown in Figure 3.21. The +45° and –45° layers in these specimens are all single thickness layers, making cracks difficult to detect. Note the uniformity of cracking throughout the width of both specimens. The dark spot in the lower right corner of Figure 3.21(b) is a surface blemish that attracted additional dye penetrant.

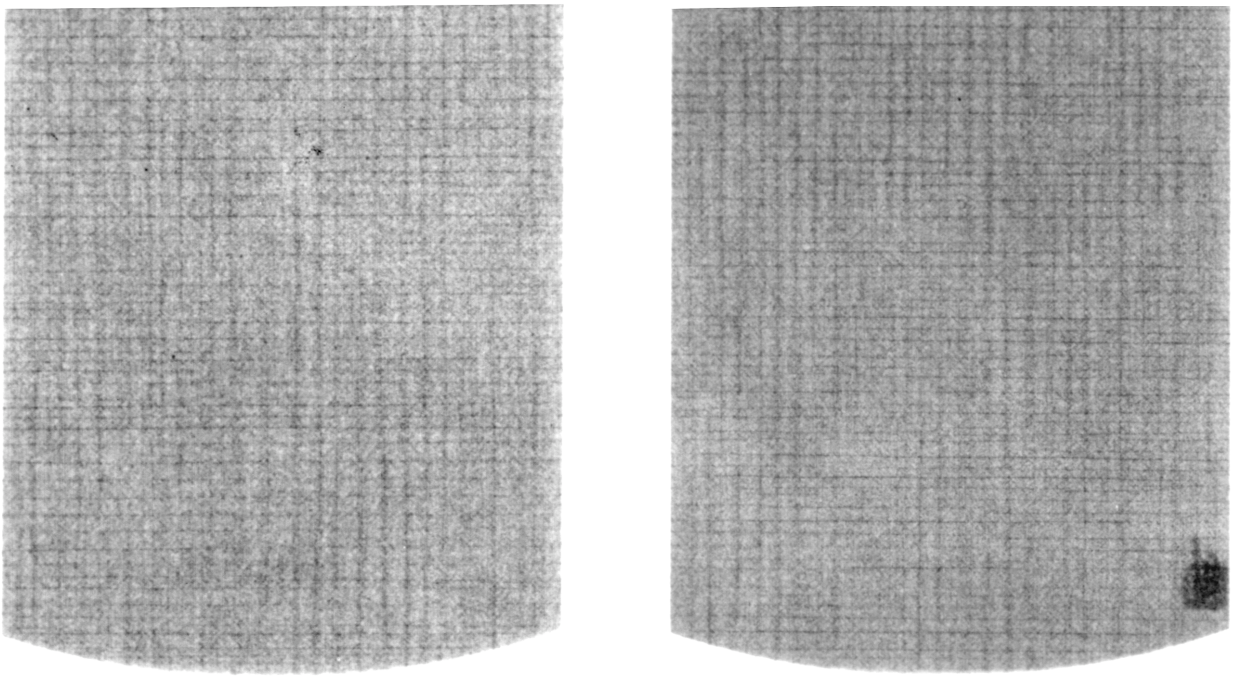

(a) K-3 (T50) 3500 ±250°F cycles (b) P-1 (P55) 3500 ±250°F cycles

Figure 3.21. X-ray photographs of T50 and P55/ERL1962.Q1.5.G specimens containing microcracks.

3.3.1.2 Thermal Expansion Behavior

Average room temperature CTE data are presented for the T50 and P55/ERL1962 specimens cycled 0 and 3500 times between -250°F and +250°F. The set of graphs seen in Figure 3.22 contains data for the cross-ply configuration (X), and the set of graphs in Figure 3.23 contains data for the quasi-isotropic configuration (Q1).

It is seen in both figures that the uncycled room temperature CTE is less positive for the specimens with the T50 fibers compared to that of the specimens with P55 fibers. All other material properties being the same in the two fibers, the more negative CTE of the P55 fiber would normally make the laminate CTE for the P55 specimens less positive. However, all other material properties for the two materials are *not* the same and, in fact, the laminate CTE of the T50 specimens *should* be less positive based on calculated lamina properties in Appendix F for both materials. The change in CTE from 0 cycles to 3500 cycles, i.e., Δ, is greater in the specimens with P55 fibers for both the cross-ply and quasi-isotropic lamination sequence. This correlates well with the microcrack densities reported earlier. Namely, the higher the microcrack

density, the greater the change in CTE. From a dimensional stability viewpoint, the T50 PAN-based fiber performs better than the P55 pitch-based fiber in regards to thermal expansion.

(a) T50 PAN-based fiber (b) P55 pitch-based fiber

Figure 3.22. Effect of fiber precursor on room temperature CTE in T50 and P55/ERL1962.X.5.G specimens.

(a) T50 PAN-based fiber (b) P55 pitch-based fiber

Figure 3.23. Effect of fiber precursor on room temperature CTE in T50 and P55/ERL1962.Q1.5.G specimens.

3.3.1.3 Laminate Stiffness

The laminate stiffnesses, normalized by fiber volume fraction, for the T50 and P55/ERL1962 cross-ply and quasi-isotropic specimens before and after thermal cycling are shown in Figure 3.24. For the most part the average uncycled stiffness falls within one standard deviation of the average post-cycled stiffness. The one exception is the T50 quasi-isotropic composites. However, because the uncycled stiffness for this series is based on only one specimen, no conclusion is appropriate from this observed behavior.

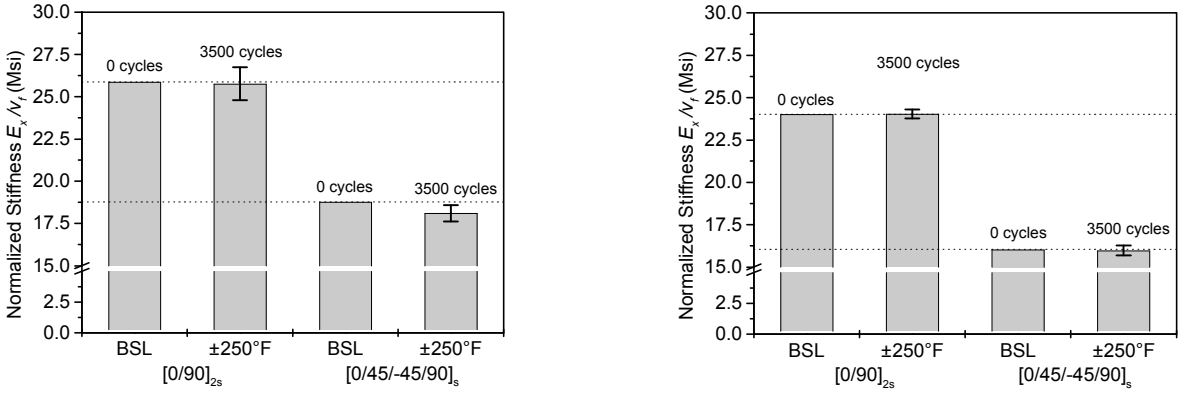

(a) T50 PAN-based fiber (b) P55 pitch-based fiber

Figure 3.24. Effect of fiber precursor on normalized laminate stiffness in T50 and P55/ERL1962.X.5.G and T50 and P55/ERL1962.Q1.5.G specimens.

3.3.2 Effect of Fiber Modulus and Fiber CTE in Pitch-Based Fibers

The effect of PAN-based versus pitch-based fibers on the thermal cycling behavior has been reviewed. This section will now address the effect of three different fibers, all of which are pitch-based. The fibers considered are the P55, P75, and P120 fibers with the nominal properties listed in Table 3.6.

Table 3.6 Axial Direction Fiber Properties for Pitch-Based Fibers†

Fiber	Stiffness (Msi)	Strength (Ksi)	CTE (με/°F)
P55 (Pitch)	55	275	-0.70
P75 (Pitch)	75	300	-0.75
P120 (Pitch)	122	325	-0.80

† Fiber data from Amoco Performance Products, Inc. vendor product information bulletin.

Two lamination sequences are again considered. The cross-ply configuration, $[0/90]_{2s}$, and the quasi-isotropic configuration $[0/+45/-45/90]_s$. All specimens contain the ERL1962 matrix and have a nominal layer thickness of 0.005 in. These specimens have all been cycled 3500 times between –250°F and +250°F. Microcrack densities as a function of thermal cycles are reported first.

3.3.2.1 Microcrack Density

Nondimensional lineal microcrack densities are shown in Figure 3.25 for the cross-ply lamination sequence as a function of the number of thermal cycles. The o90 layer results are

shown in part (a) and the c90 layer results in part (b). It is seen in Figure 3.25(a) that the microcrack density in the o90 layer of the specimens containing the P55 fibers is somewhat lower throughout cycling than either of the specimens containing the P75 or the P120 fibers. A characteristic that is evident from the left-hand graph in Figure 3.25(b) is that the initial rate of cracking in the c90 layer appears to be related to the modulus of the fiber. A higher fiber modulus results in a higher initial microcracking rate and hence higher initial microcrack densities. This trend was also observed by Knouff et al. [5] for up to 500 cycles for the same fibers in the ERL1939-3 blended epoxy-cyanate resin system. From Table 3.6 it is seen that the nominal axial CTE of the higher modulus fibers is more negative than that of the lower modulus fibers. This could account for the initially higher cracking rate due to the higher initial thermal stresses. As the number of cycles increases beyond 500, this trend reverses itself as indicated by the microcracking rates in the right-hand graph in Figure 3.25(b) which are higher for the lower modulus fibers. Recall that the logarithmic microcracking rates are biased towards the high-cycle behavior. After 3000 cycles are complete, the microcrack density in the c90 layer appears to be roughly equal for all three fiber types.

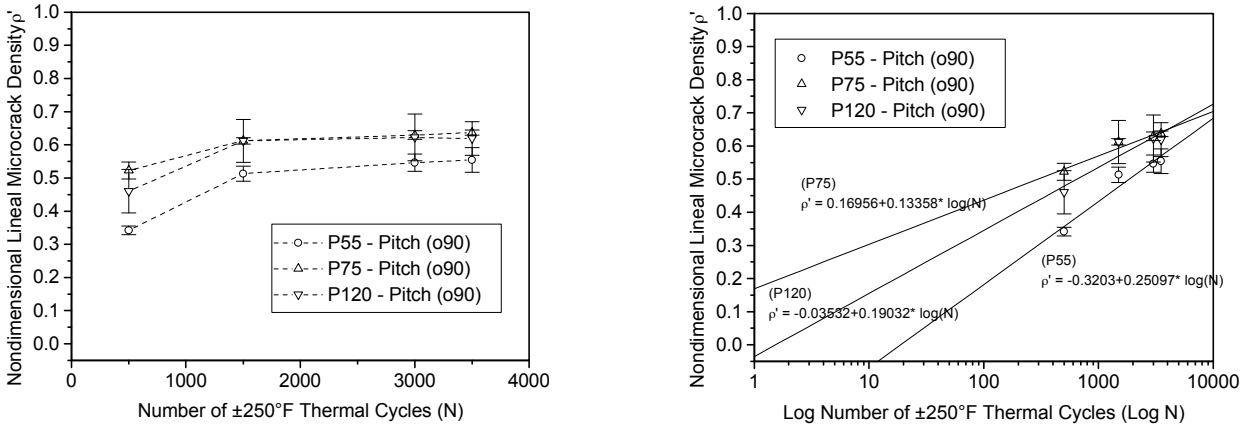

(a) o90 layer

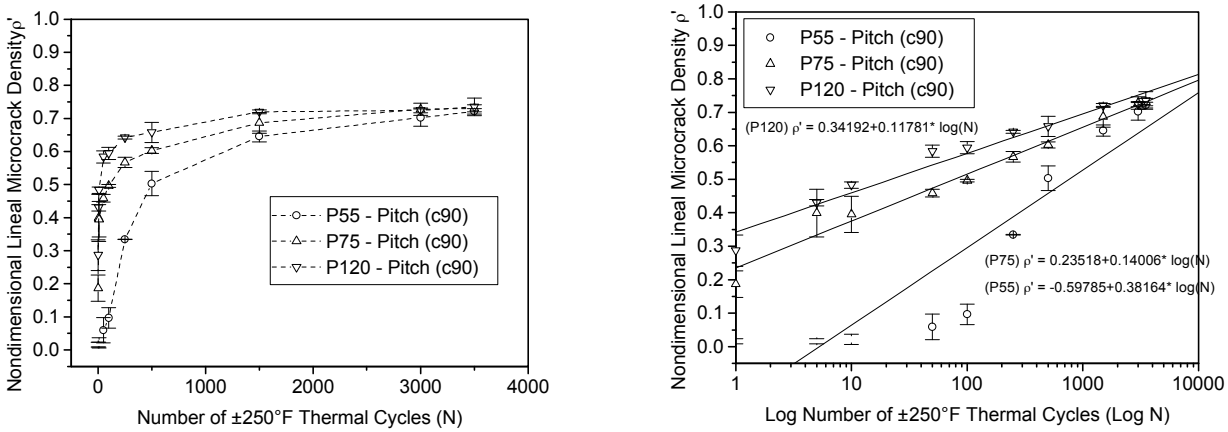

(b) c90 layer

Figure 3.25. Effect of fiber type on microcrack density in P55, P75, and P120/ERL1962.X.5.G specimens.

Dimensional microcrack densities are shown in Table 3.7 for the P55, P75, and P120/ERL1962.X.5.G specimens.

Table 3.7 Dimensional Microcrack Densities (in cracks/in.)
for P55, P75, and P120/ERL1962.X.5.G Specimens

	Layer	0	1	5	10	50	100	250	500	1500	2500	3000	3500
P55	o90								63†	95	99‡	102	103†
Fiber									+2	+4	+0	+5	+5
									-2	-5	-0	-5	-5
Specimen	c90	0†	2†	2†	2†	6†	9†	31†	47†	60	66‡	65	67†
Series		+0	+1	+1	+1	+3	+2	+0	+2	+2	+0	+3	+1
O		-0	-1	-1	-1	-3	-2	-0	-2	-2	-0	-2	-1

† Specimens O-3 and O-4 only; ‡ Specimen O-2 only

	Layer	0	1	5	10	50	100	250	500	1500	3000	3500
P75	o90								84	98	101	102
Fiber									+2	+2	+3	+2
									-3	-2	-2	-2
Specimen	c90	0	15	32	32	37	40	45	48	55	58	58
Series		+0	+2	+5	+3	+1	+0	+2	+1	+3	+0	+1
H		-0	-4	-7	-6	-2	-1	-2	-1	-2	-0	-1

	Layer	0	1	5	10	50	100	250	500	1500	2000	3000	3500
P120	o90								82	115†	107‡	114	114
Fiber									+14	+8	+0	+13	+9
									-9	-8	-0	-7	-6
Specimen	c90	0†	27†	41†	46†	55†	56†	61†	54	68†	67‡	69	70
Series		+0	+3	+1	+1	+1	+1	+1	+11	+1	+0	+2	+1
Q		-0	-3	-1	-1	-1	-1	-1	-17	-1	-0	-1	-3

† Specimens Q-1 and Q-2 only; ‡ Specimen Q-3 only

Photographs of edge views of the cross-ply specimens are shown in Figure 3.26. Each of these photographs was taken of the specimens after 3500 thermal cycles were complete. Note the variation in thickness of the specimens, indicating the need for the nondimensional crack density for this comparison. The actual thickness of these specimens can be seen in Table 2.7.

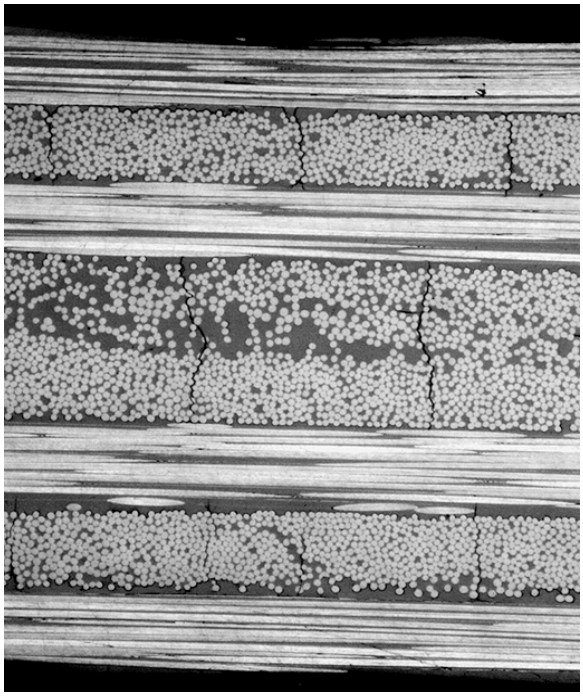

(a) O-4 (P55) 3500 ±250°F cycles (100X)

(b) H-2 (P75) 3500 ±250°F cycles (100X)

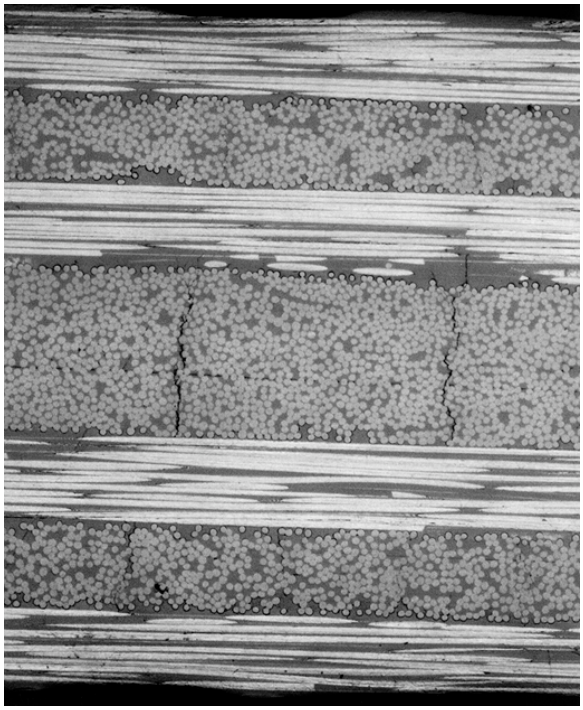

(c) Q-2 (P120) 3500 ±250°F cycles (100X)

Figure 3.26. Edge-view photographs of P55, P75, and P120/ERL1962.X.5.G specimens containing microcracks.

Nondimensional lineal microcrack densities for the P55, P75, and P120 quasi-isotropic specimens are shown in Figure 3.27. Observations can be made about these quasi-isotropic specimens similar to those made previously for the cross-ply specimens. In general, the initial cracking behavior in the specimens seems to be affected by the fiber type, with a higher fiber modulus resulting in a higher microcracking rate. After 3000 cycles or so, all the specimens have roughly the same microcrack density, regardless of fiber type. This is true for all three layer orientations in the quasi-isotropic configuration.

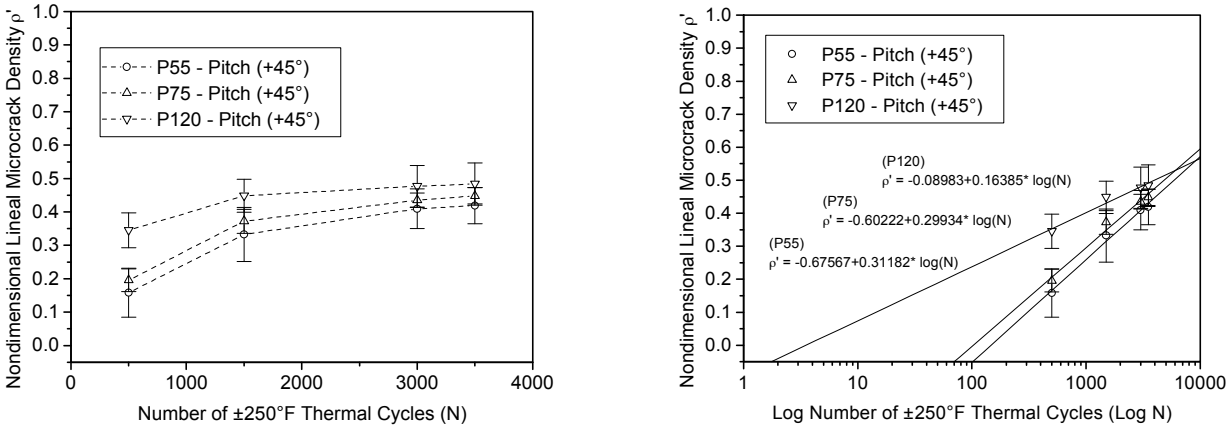

(a) +45° layer

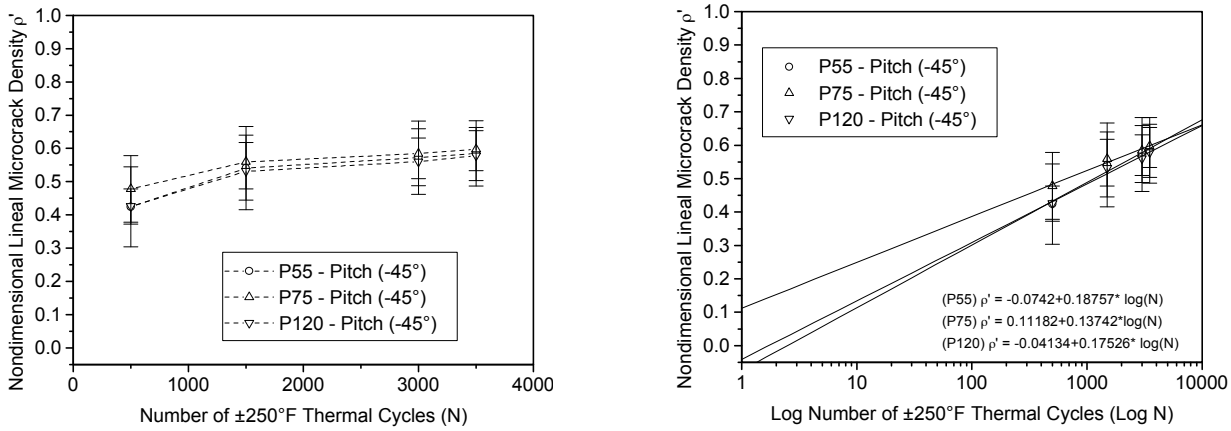

(b) –45° layer

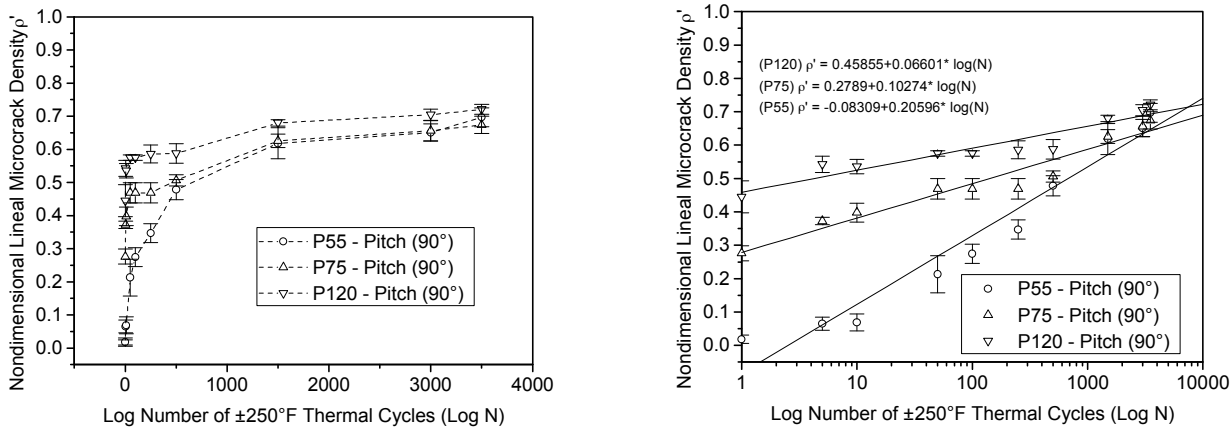

(c) 90° layer

Figure 3.27. Effect of fiber type on microcrack density in P55, P75, and P120/ERL1962.Q1.5.G specimens.

Dimensional microcrack densities are shown in Table 3.8 for the P55, P75, and P120/ERL1962.Q1.5.G specimens.

Table 3.8 Dimensional Microcrack Densities (in cracks/in.)
for P55, P75, and P120/ERL1962.Q1.5.G Specimens

	Layer	0	1	5	10	50	100	250	500	1500	3000	3500
P55 Fiber	45								21 +11 -6	43 +10 -11	54 +5 -9	55 +4 -8
	-45								55 +14 -17	71 +11 -19	75 +9 -17	76 +8 -15
Specimen Series P	90	0 +0 -0	2 +1 -1	6 +2 -1	6 +3 -1	20 +5 -5	25 +3 -2	32 +2 -2	44 +3 -3	57 +3 -5	60 +2 -3	64 +3 -3

	Layer	0	1	5	10	50	100	250	500	1500	3000	3500
P75 Fiber	45								22 +2 -4	42 +4 -3	49 +3 -3	51 +3 -3
	-45								54 +8 -13	63 +7 -11	66 +6 -10	67 +5 -9
Specimen Series I	90	1 +1 -0	22 +2 -1	30 +1 -1	32 +2 -3	37 +3 -1	37 +3 -1	37 +3 -1	40 +1 -2	50 +2 -1	52 +3 -3	54 +2 -3

	Layer	0	1	5	10	50	100	250	500	1500	3000	3500
P120 Fiber	45								45 +5 -8	58 +7 -4	62 +8 -6	63 +9 -5
	-45								55 +7 -6	69 +12 -8	73 +10 -6	75 +10 -7
Specimen Series R	90	0 +0 -0	41 +4 -4	50 +2 -1	49 +2 -1	53 +1 -1	53 +1 -1	54 +3 -2	54 +2 -4	63 +1 -0	65 +1 -1	66 +1 -1

Edge-view photographs of representative quasi-isotropic specimens containing each of the three fiber types are included in Figure 3.28. All photographs were taken after these specimens had been cycled 3500 times between –250°F and +250°F.

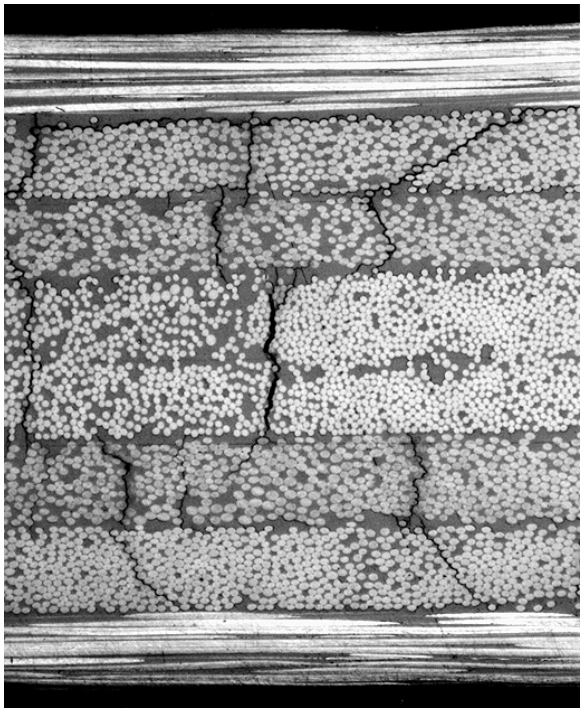

(a) P-3 (P55) 3500 ±250°F cycles (100X)

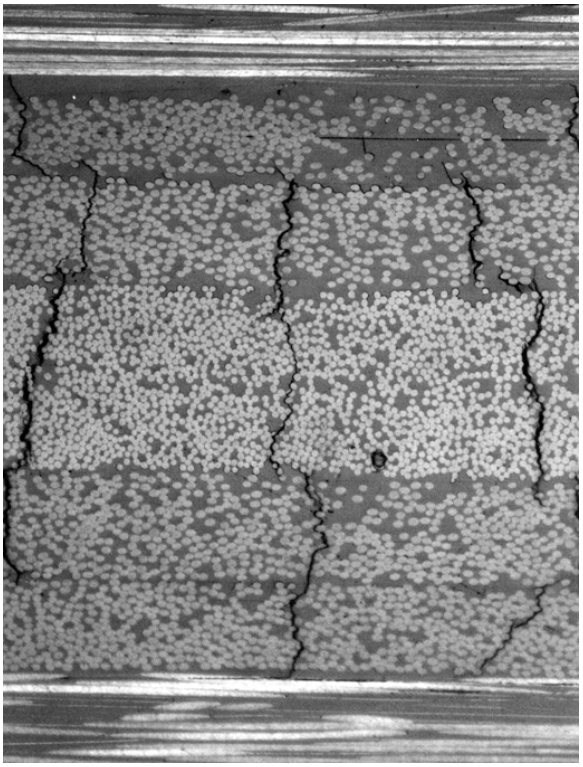

(b) I-3 (P75) 3500 ±250°F cycles (100X)

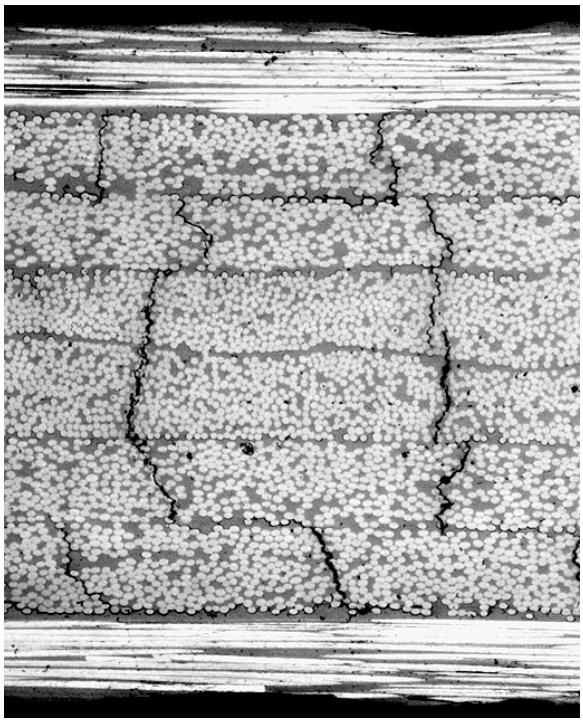

(c) R-1 (P120) 3500 ±250°F cycles (100X)

Figure 3.28. Edge-view photographs of P55, P75, and P120/ERL1962.Q1.5.G specimens containing microcracks.

3.3.2.2 Thermal Expansion Behavior

Room temperature laminate CTE data for the P55, P75, and P120/ERL1962 specimens are presented in Figure 3.29 and Figure 3.30 for the cross-ply and quasi-isotropic lamination sequences, respectively. Note that the uncycled CTE for the three material types varies according to fiber type. The more negative the CTE of the fiber (see Table 3.6), the more negative the laminate CTE. This trend holds for both cross-ply and quasi-isotropic lamination sequences. It is also true that the change in laminate CTE from the uncycled to the cycled condition, i.e., Δ, varies according to fiber type. One might expect that based on the comparable microcrack densities at 3500 cycles for all three materials, each of the specimens would experience similar changes in CTE. Instead, it is observed that laminate CTE is least affected in specimens with higher modulus fibers. This trend was also observed by Knouff et al. [5] for the ERL1939-3 blended epoxy-cyanate resin system. This would tend to make the higher modulus fibers a better choice from a dimensional stability consideration. On the other hand, the greater negative value of the laminate CTE for these high modulus specimens might make them a poor choice.

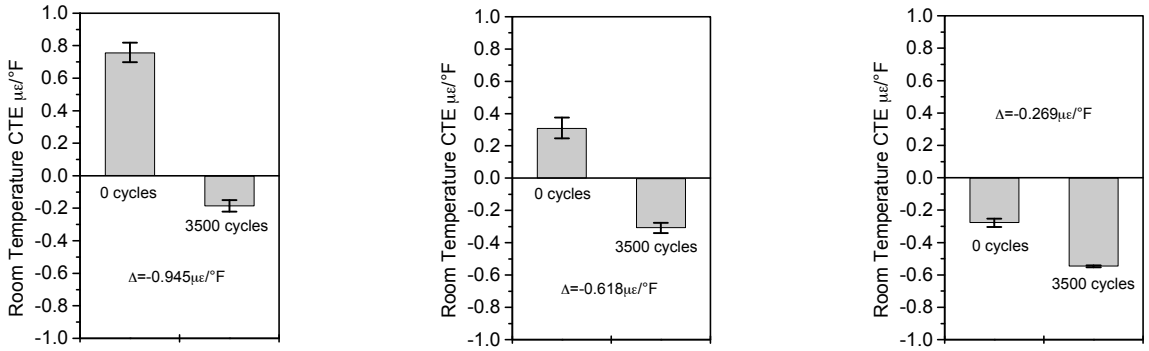

(a) P55 fiber (b) P75 fiber (c) P120 fiber

Figure 3.29. Effect of fiber type on room temperature CTE in P55, P75, and P120/ERL1962.X.5.G specimens.

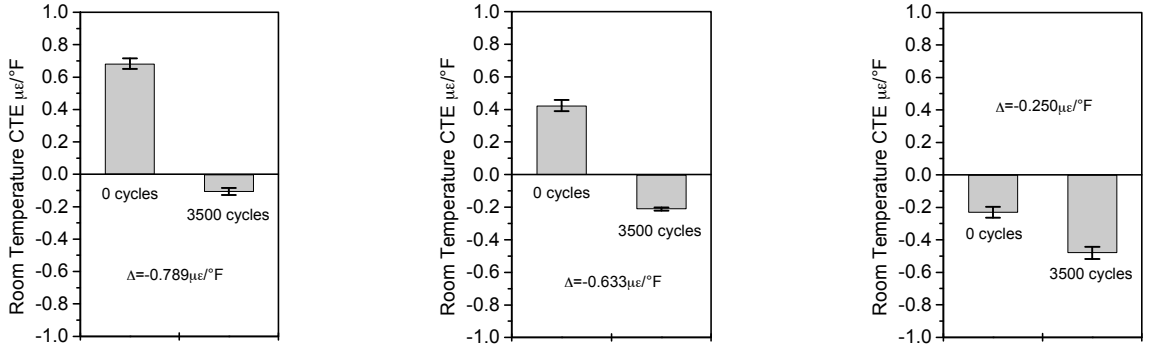

(a) P55 fiber (b) P75 fiber (c) P120 fiber

Figure 3.30. Effect of fiber type on room temperature CTE in P55, P75, and P120/ERL1962.Q1.5.G specimens.

3.3.2.3 Laminate Stiffness

Laminate stiffnesses, normalized by fiber volume fraction, for the P55, P75, and P120/ERL1962 pitch-based fiber composites are presented in Figure 3.31. The cross-ply and quasi-isotropic uncycled and post-cycled laminate stiffness are presented in Figure 3.31(a) for the P55 fiber specimens, Figure 3.31(b) for the P75 fiber specimens, and Figure 3.31(c) for the P120 fiber specimens. In almost all cases, the uncycled stiffness falls within one standard deviation of the average post-cycled stiffness. The laminate stiffness is essentially unaffected by microcracking.

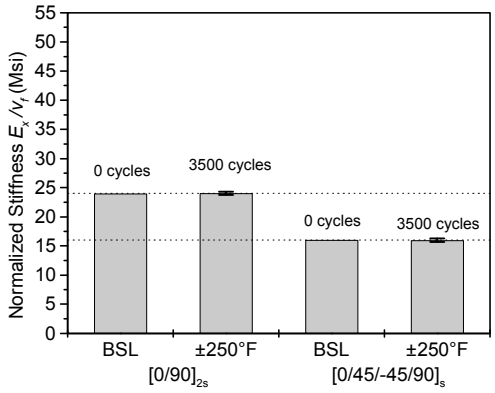

(a) P55 pitch-based fiber

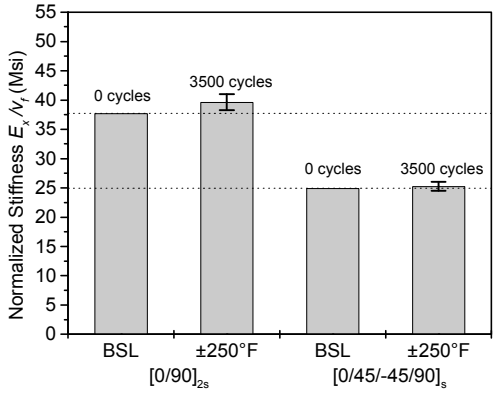

(b) P75 pitch-based fiber

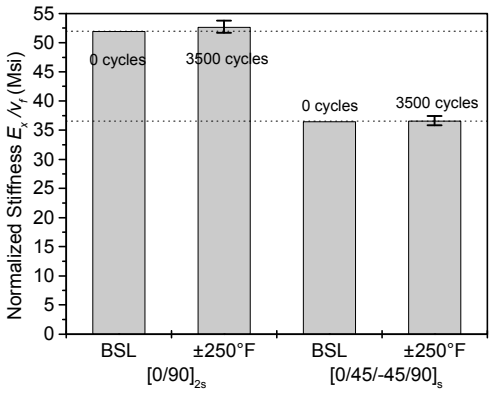

(c) P120 pitch-based fiber

Figure 3.31. Effect of fiber type on normalized laminate stiffness in P55, P75, and P120/ERL1962.X.5.G and P55, P75, and P120/ERL1962.Q1.5.G specimens.

3.4 EFFECT OF MATRIX TYPE

The effect of matrix type will be studied by comparing results from materials with three different resin systems. The resin systems include Fiberite's 934 epoxy, Amoco's ERL1962 toughened epoxy, and YLA's RS-3 cyanate ester. The nominal neat resin properties for these three materials are listed in Table 3.9.

Table 3.9 Room Temperature Neat Resin Properties†

Resin	Tensile Strength (Ksi)	CTE (με/°F)	T_g (°F)	Density (lb/in^3)
Fiberite 934	4.0	28	381	0.047
Amoco ERL1962	*	24	320	0.046
YLA RS-3	12.0	31.5	490	0.043

† Resin data from vendor product information bulletins.
* Data were unavailable.

Microcracking, laminate CTE, and laminate stiffness results are presented in the following sections for quasi-isotropic Q2 specimens, i.e., $[0/+45/90/-45]_s$, containing P75 pitch-based fibers with each of the three matrix materials. The layer thickness is nominally 0.005 in. for all of these specimens. Each of the materials is subjected to cycling temperatures ranging from −250°F to +250°F for up to 3000 cycles. The designation for these materials is P75/*.Q2.5.G.

3.4.1 Microcrack Density

Nondimensional microcrack densities are presented in Figure 3.32 for the P75/934, P75/ERL1962, and P75/RS3 quasi-isotropic specimens. Comparing the three layer orientations in Figure 3.32(a), (b), and (c), the 934 specimens typically have the highest microcrack densities, with the RS3 specimens having the lowest microcrack densities. It is noted that both the 934 and ERL1962 specimens have a significant microcrack density after one cycle. Data for the RS3 specimens after one cycle were not recorded, but as seen in the right-hand graphs for all three layers, cracking in the RS3 specimens is not expected to occur until after 10 thermal cycles.

It is also noted that although the RS3 specimens have lower microcrack densities for up to 3000 thermal cycles, the microcracks in these specimens appear to accumulate more rapidly in the late stages of cycling compared to the other two specimen types. Specifically, referring to Figure 3.32 (c) for the −45° layer, the microcrack density in the RS3 specimens is projected to exceed that in the 934 and ERL1962 specimens prior to completion of 10,000 thermal cycles. This projection is, however, based on limited data and must be cautiously applied to design considerations.

In summary, from a microcracking viewpoint, the performance of the RS3 resin system exceeds that of the 934 and ERL1962 resin systems for up to 3000 cycles. The performance of the RS3 resin system beyond 3000 thermal cycles is unclear.

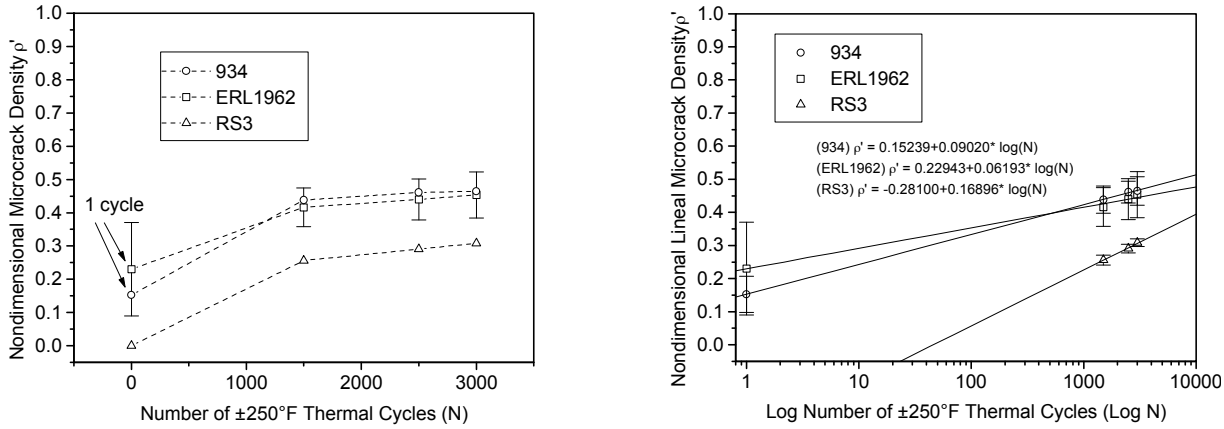

(a) +45° layer

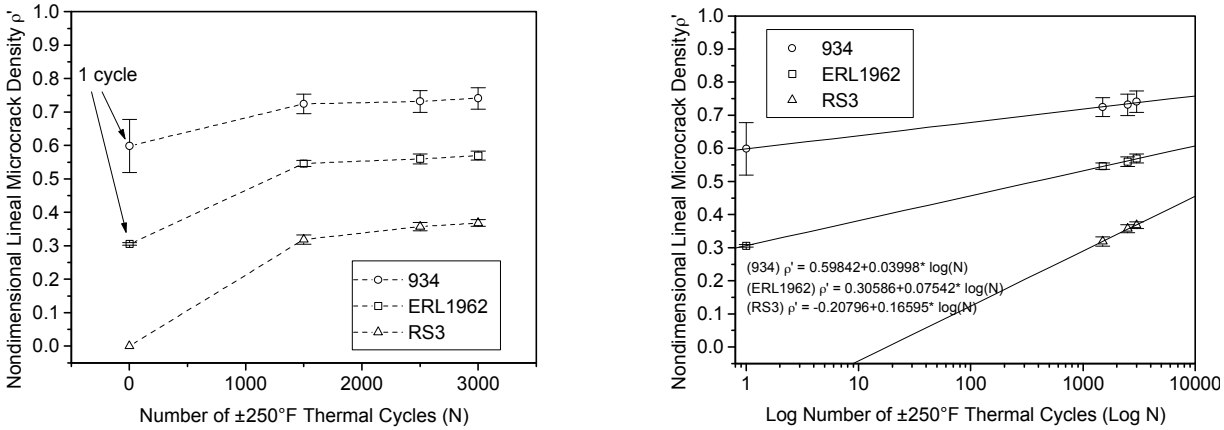

(b) 90° layer

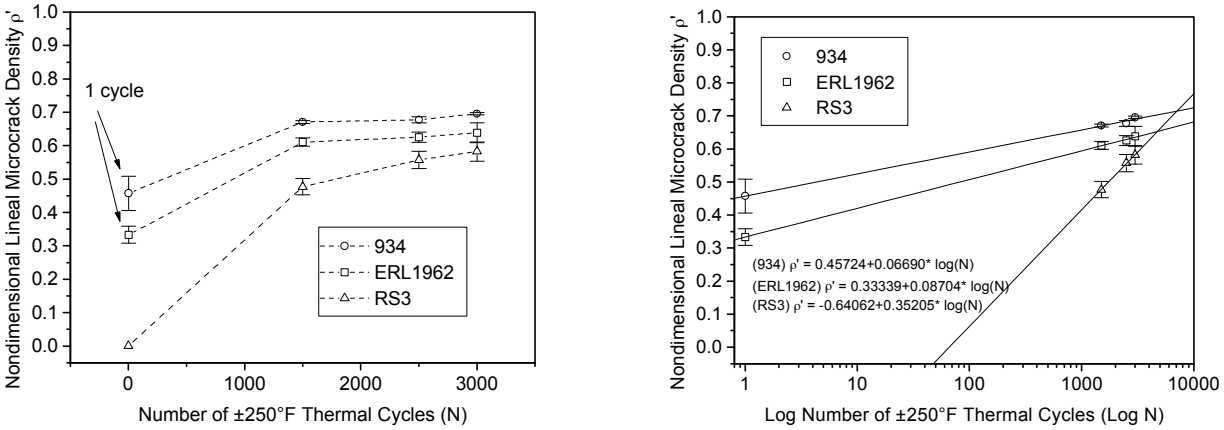

(c) –45° layer

Figure 3.32. Effect of matrix type on microcrack density in P75/*.Q2.5.G specimens.

Dimensional microcrack densities as a function of the number of thermal cycles are shown in Table 3.10 for the P75/*.Q2.5.G specimens. It should be noted that the 934 specimens have dimensional microcrack densities very similar to the ERL1962 specimens, which at first glance indicates similar performance for the two resin systems. The 934 specimens, however, are significantly thicker than either the ERL1962 or the RS3 specimens. This translates into higher nondimensional microcrack densities for the 934 specimens.

Table 3.10 Dimensional Microcrack Densities (in cracks/in.) for P75/*.Q2.5.G Specimens

Specimen Series P734Q	Layer	1	1500	2500	3000
934 Resin	45	19 +8 -6	55 +4 -5	58 +3 -4	59 +5 -5
	90	107 +11 -15	130 +5 -4	131 +6 -4	133 +6 -3
	-45	29 +3 -4	42 +0 -0	43 +1 -1	44 +0 -0

Specimen Series 6762	Layer	1	1500	2500	3000
ERL1962 Resin	45	35 +21 -22	63 +9 -10	66 +10 -9	69 +12 -11
	90	65 +1 -1	117 +2 -2	119 +2 -1	122 +3 -2
	-45	25 +3 -2	46 +1 -1	47 +0 -1	48 +2 -1

Specimen Series 75RS3	Layer	0	1500	2500	3000
RS3 Resin	45	0 +0 -0	37 +2 -1	42 +2 -2	45 +1 -2
	90	0 +0 -0	66 +3 -2	74 +3 -2	76 +2 -2
	-45	0 +0 -0	35 +1 -2	41 +2 -2	42 +2 -2

Edge-view photographs of representative specimens are shown in Figure 3.33. A specimen containing the 934 resin system is shown in (a), the ERL1962 resin system in (b), and the RS3 resin system in (c). In all cases, photographs were taken after 3000 thermal cycles between –250°F and +250°F. The microcracking appears to be relatively similar for all three specimens. The characteristic near-45° crack propagation that was observed previously for the quasi-isotropic Q1 lamination sequence is also present for the Q2 lamination sequence shown here.

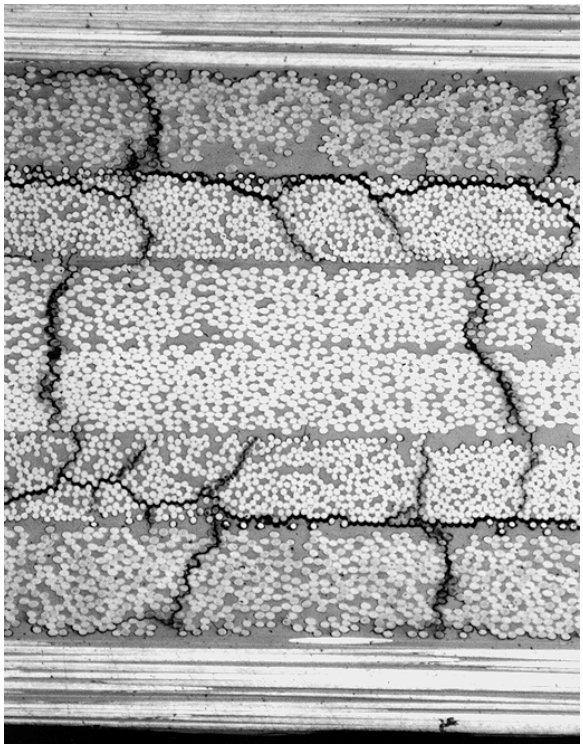

(a) P734Q-2 (934)
3000 ±250°F cycles (100X)

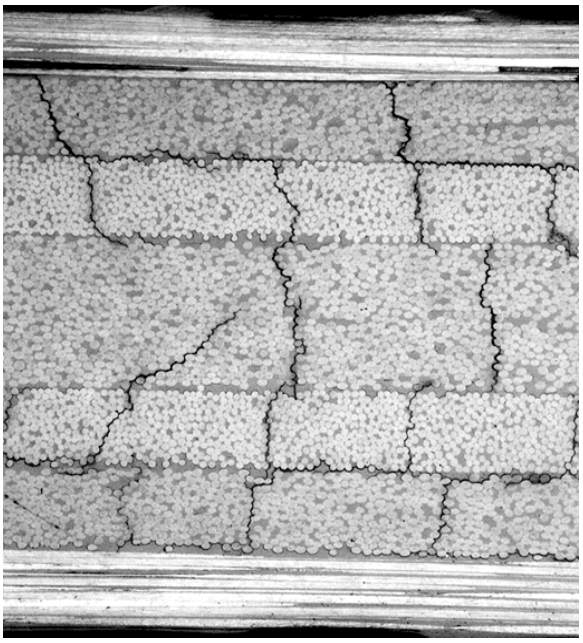

(b) 6762-3 (ERL1962)
3000 ±250°F cycles (100X)

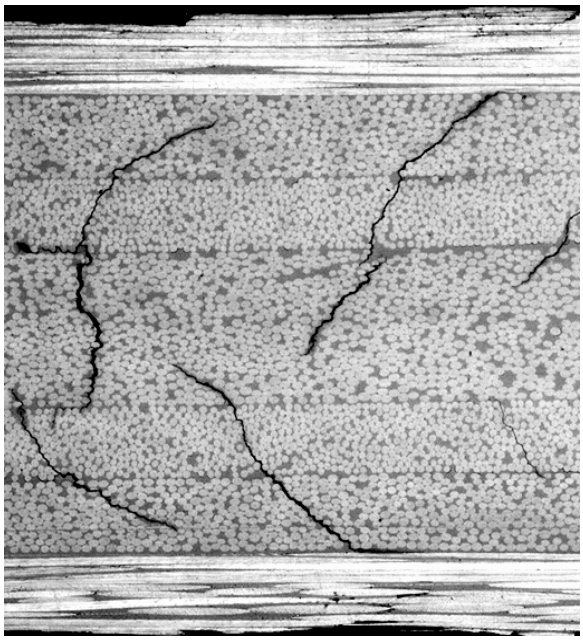

(c) 75RS3-2 (RS3) 3000 ±250°F cycles (100X)

Figure 3.33. Edge-view photographs of P75/*.Q2.5.G specimens containing microcracks.

3.4.2 Laminate Thermal Expansion Behavior

Room temperature CTE's for the P75/934, P75/ERL1962, and P75/RS3 quasi-isotropic specimens are shown in Figure 3.34 for the uncycled and post-cycled condition. The uncycled values for the three materials are comparable, particularly when considering the standard deviations. Comparing the change in CTE from the uncycled to the post-cycled condition, the RS3 material exhibits the most stable response of the three materials. This is not surprising, considering the significantly lower microcrack densities in the RS3 specimens compared to the ERL1962 and 934 specimens at 3000 thermal cycles. It is surprising, however, that the 934 specimens exhibit only a slightly greater change in CTE compared to the RS3 specimens, despite the fact that the 934 specimens showed the highest microcrack densities.

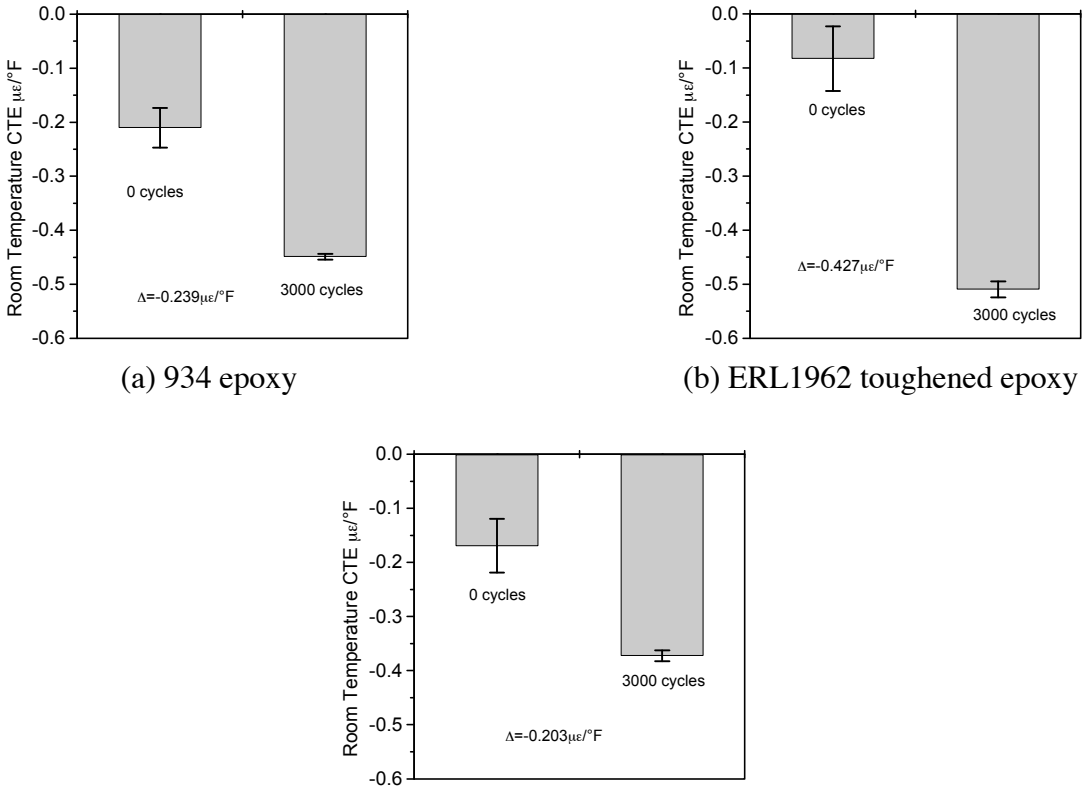

(a) 934 epoxy

(b) ERL1962 toughened epoxy

(c) RS3 toughened polycyanate

Figure 3.34. Effect of matrix type on room temperature CTE in P75/*.Q2.5.G specimens.

3.4.3 Laminate Stiffness

The laminate stiffnesses, normalized by fiber volume fraction, for the P75/934, P75/ERL1962, and P75/RS3 quasi-isotropic specimens are shown in Figure 3.35. There is no consistent trend observed in the uncycled and post-cycled stiffness results for the three resin systems. Average stiffness is observed to increase in the 934 specimens, decrease in the ERL1962 specimens, and decrease slightly in the RS3 specimens. Unlike previous stiffness results, the average baseline stiffnesses for the specimens do not always fall within one standard deviation from the mean post-cycled stiffness.

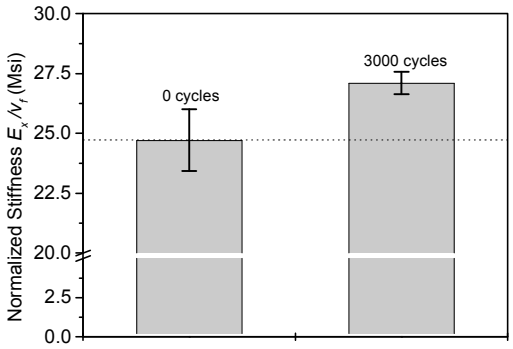

(a) 934 epoxy

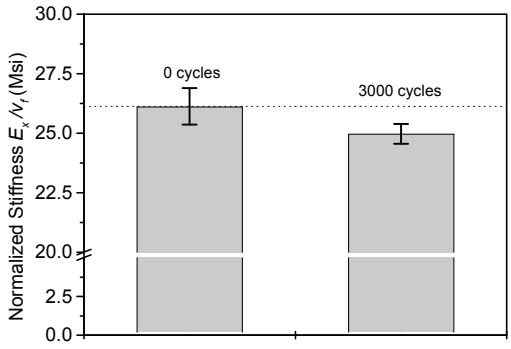

(b) ERL1962 toughened epoxy

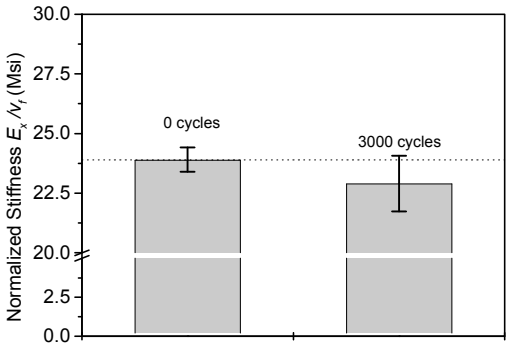

(c) RS3 toughened polycyanate

Figure 3.35. Effect of matrix type on normalized laminate stiffness in P75/*.Q2.5.G specimens.

3.4.4 Glass Transition Temperature

This section addresses the glass transition temperature, T_g, of the three matrix materials before and after thermal cycling. All of the materials considered here have experienced 3000 thermal cycles ranging from –250°F to 250°F. The T_g of the materials before and after thermal cycling are summarized in Table 3.11. No significant change has occurred in the T_g of the three resin systems as a result of the thermal history experienced by the specimens.

Table 3.11 Glass Transition Temperatures for the 934, ERL1962, and RS3 Resin Systems Before and After Thermal Cycling

		Measured T_g	
Resin	Mfg. Quoted T_g (°F)	0 cycles (BSL) (°F)	3000 cycles (°F)
934	381	412	403
ERL1962	320	313	318
RS3	490	542	544

3.5 EFFECT OF THERMAL CYCLING TEMPERATURE RANGE

Results are presented in this section demonstrating the effect of thermal cycling temperature range on the response of various material systems. As seen in the test matrix (see Table 2.4), there are three different material/specimen configurations in this investigation which look at the effect of three different thermal cycling ranges, ±250°F(G), ±150°F(L), and ±50°F(C). The three material/specimen configurations all have the quasi-isotropic Q2, i.e., $[0/+45/90/-45]_s$, lamination sequence. The first configuration is a P75/ERL1962 material with a 0.005 in. nominal layer thickness. The other two configurations are both P75/RS3 materials, one with a 0.005 in. nominal layer thickness and one with a 0.002 in. nominal layer thickness. The designations for these specimens are P75/ERL1962.Q2.5.*, P75/RS3.Q2.5.*, and P75/RS3.Q2.2.*, respectively.

One of the goals of this comparison is to determine if there is a stress ratio effect for thermal cycling analogous to the stress ratio effect in mechanical fatigue loading. By thermally cycling specimens in less extreme temperature ranges, can the ultimate level of damage in the specimen be reduced? And if so, is there a threshold temperature range such that if specimens are cycled below this range, damage can be prevented completely? These issues will be addressed in the following sections.

3.5.1 Microcrack Density

This section illustrates the effect of thermal cycling temperature range on microcrack density as a function of the number of thermal cycles. It is hoped that insight will be gained into the issue of microcrack density saturation, or characteristic damage state, which assumes that every material/specimen configuration has a characteristic state [15] at which no further microcracking will occur with continued loading. If, in fact, this characteristic damage state does exist for a material, then it is presumable that regardless of thermal cycling temperature range,

every specimen will eventually reach the same microcrack density. To reach this saturation microcrack density, larger numbers of thermal cycles at the lower thermal ranges may be required.

Nondimensional lineal microcrack densities as a function of the number of thermal cycles for the P75/ERL1962.Q2.5.* specimens are shown in Figure 3.36. Significantly different behavior is seen for the three thermal cycling temperature ranges. As might be expected, for equal numbers of thermal cycles, the ±250°F temperature range results in the highest microcrack densities for all layer orientations, whereas the ±50°F temperature range results in the lowest densities. Also of interest is the delayed onset of microcracking that varies with thermal cycling temperature range. Again as might be expected, the specimens cycled in the ±50°F range have the largest delayed onset of microcracking, whereas the specimens cycled in the ±250°F range have no delayed onset, microcracking significantly after one thermal cycle.

The microcracking rate information from the right-hand graphs is somewhat conflicting. For instance, in Figure 3.36 (a) for the +45° layer, the rates seem to vary randomly from one cycling range to the next. The data for the specimens cycled between ±150°F tend to indicate that those specimens will never reach microcrack densities equal to those specimens cycled between ±250°F, whereas the data for the specimens cycled between ±50°F indicate the opposite. Similar conflicts occur in the 90° layer in figure (b). The most consistent results are seen in figure (c) for the –45° layer orientation, where it appears as though all specimens, regardless of thermal cycling range, will have equal microcrack densities after a large number of thermal cycles, i.e., the three lines seem to converge to a point.

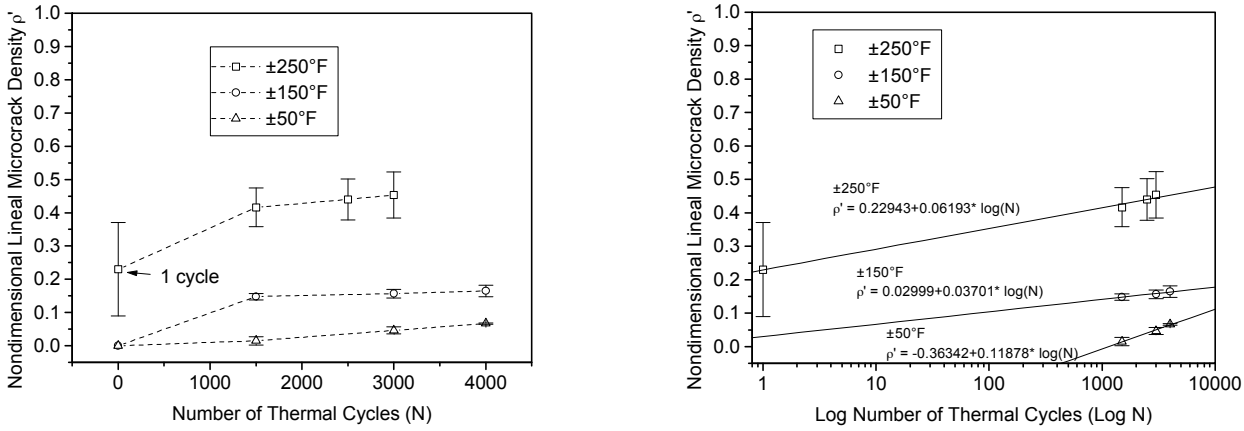

(a) +45° layer

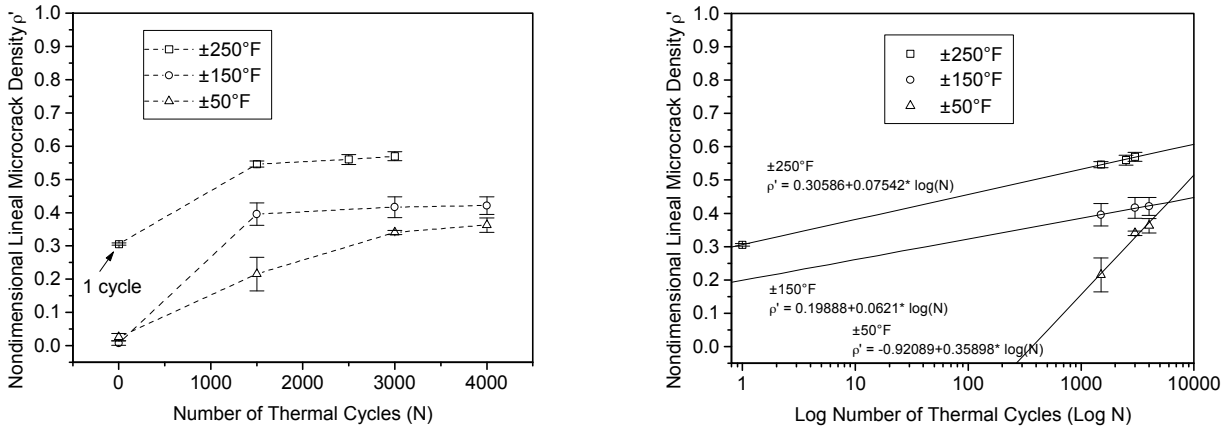

(b) 90° layer

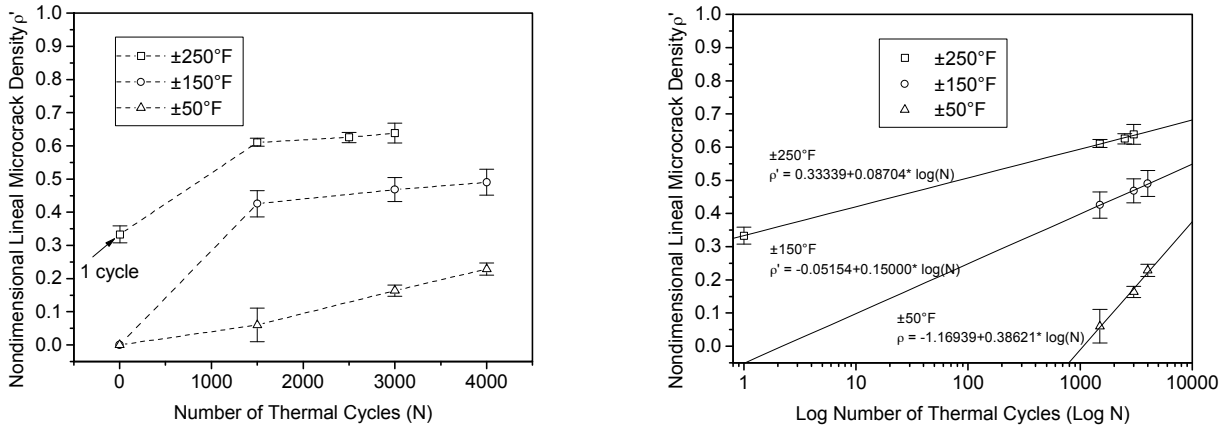

(c) –45° layer

Figure 3.36. Effect of thermal cycling temperature range on microcrack density in P75/ERL1962.Q2.5.* specimens.

Dimensional microcrack densities are shown in Table 3.12 for P75/ERL1962.Q2.5.* specimens.

Table 3.12 Dimensional Microcrack Densities (in cracks/in.) for P75/ERL1962.Q2.5.* Specimens

	Layer	1	1500	2500	3000
±250°F Thermal Cycling Range	45	35 +21 -22	63 +9 -10	66 +10 -9	69 +12 -11
	90	65 +1 -1	117 +2 -2	119 +2 -1	122 +3 -2
	-45	25 +3 -2	46 +1 -1	47 +0 -1	48 +2 -1

	Layer	0	1500	3000	4000
±150°F Thermal Cycling Range	45	0 +0 -0	23 +3 -3	25 +2 -3	26 +3 -4
	90	2 +2 -2	87 +2 -3	92 +2 -2	93 +1 -1
	-45	0 +0 -0	33 +3 -2	37 +3 -2	38 +3 -2

	Layer	0	1500	3000	4000
±50 Thermal Cycling Range	45	0 +0 -0	2 +2 -2	7 +1 -2	9 +0 -0
	90	5 +2 -2	43 +7 -12	68 +1 -1	73 +4 -5
	-45	0 +0 -0	4 +4 -3	12 +1 -1	16 +1 -1

Edge-view photographs of P75/ERL1962.Q2.5.* specimens containing microcracks are shown in Figure 3.37. Thermal cycling range has little or no effect on the manner in which microcracking occurs in these specimens.

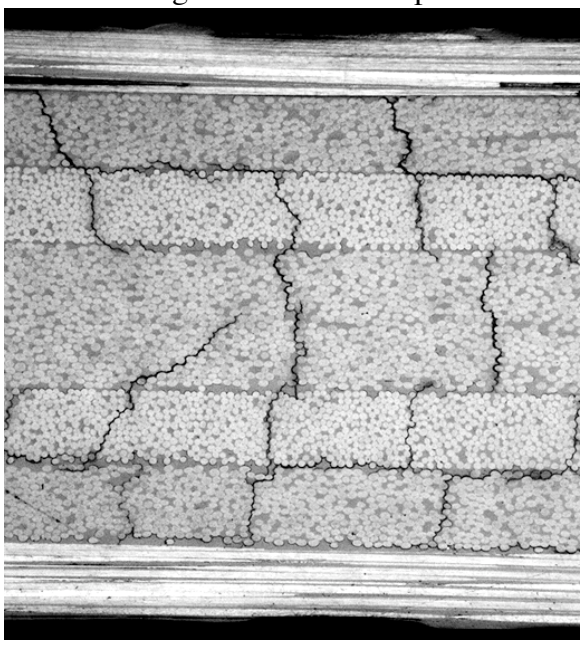

(a) 6762-3 3000 ±250°F cycles (100X)

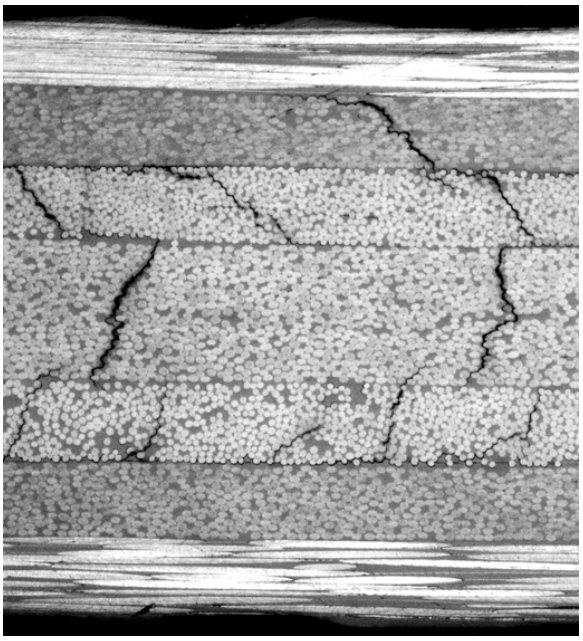

(b) 6762-2 4000 ±150°F cycles (100X)

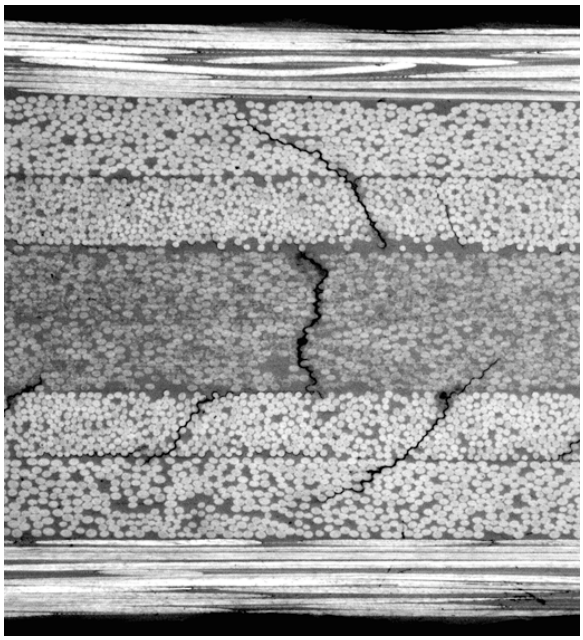

(c) 6762-8 4000 ±50°F cycles (100X)

Figure 3.37. Edge-view photographs of P75/ERL1962.Q2.5.* specimens containing microcracks.

X-ray photographs of the P75/ERL1962.Q2.5.* specimens subjected to the extreme temperature ranges, i.e., ±250°F(G) and ±50°F(L), are shown in Figure 3.38. The cracks in the double-thickness –45° layer located at the midplane of the specimen show up most clearly due to the higher concentration of dye penetrant in these cracks with larger crack opening displacements. The important thing to note is that regardless of thermal cycling temperature range, the microcracks appear to traverse the entire width of the specimen.

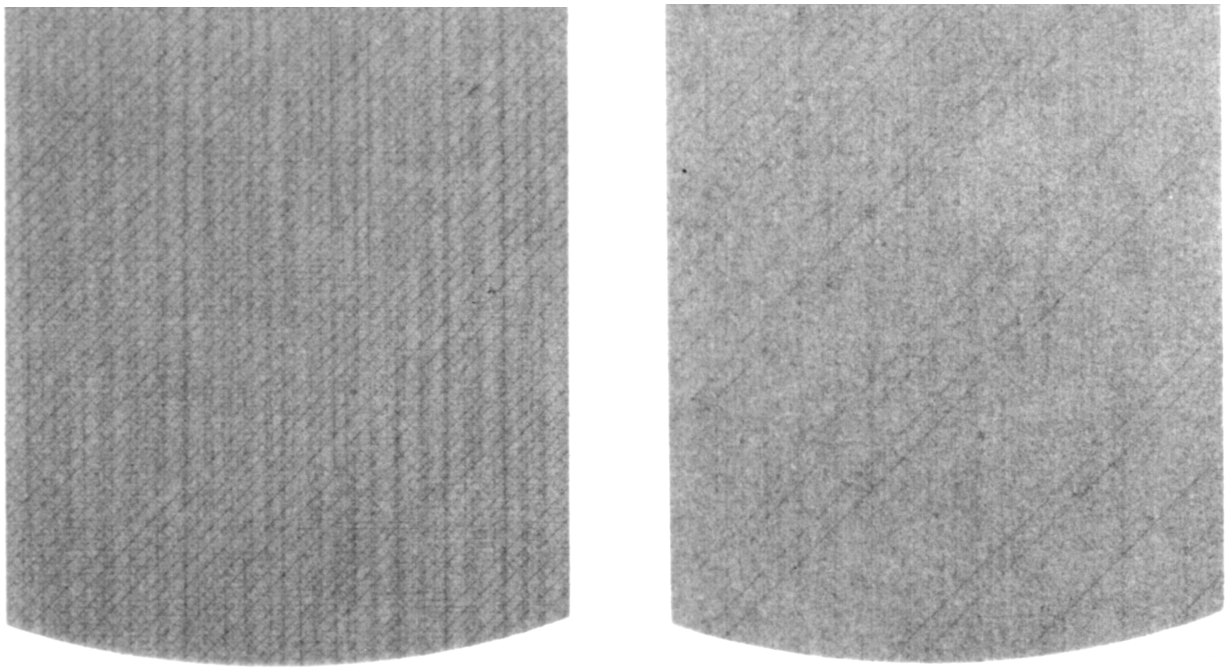

(a) 6762-1 (±250°F) (b) 6762-7 (±50°F)

Figure 3.38. X-ray photographs of P75/ERL1962.Q2.5.G and C specimens containing microcracks.

It is noted here that the microcrack densities for the P75/RS3.Q2.5.* series specimens cycled between ±150°F and ±50°F were negligible for the number of cycles completed in this study. Only tabulated dimensional values for the ±250°F temperature range of this series are reported here and are summarized in Table 3.13.

Table 3.13 Dimensional Microcrack Densities (in cracks/in.) for P75/RS3.Q2.5.G Specimens

	Layer	0	1500	2500	3000
±250°F Thermal Cycling Range	45	0 +0 -0	37 +2 -1	42 +2 -2	45 +1 -2
	90	0 +0 -0	66 +3 -2	74 +3 -2	76 +2 -2
	-45	0 +0 -0	35 +1 -2	41 +2 -2	42 +2 -2

Nondimensional lineal microcrack densities are shown in Figure 3.39 for the P75/RS3.Q2.2.* specimens. Observations can be made about these specimens similar to those made previously for the P75/ERL1962.Q2.5.* specimens. It should be noted, however, that microcrack densities in the +45° and –45° layer of the P75/RS3.Q2.2.* specimens cycled at ±50°F were negligible and have not been included in the figures.

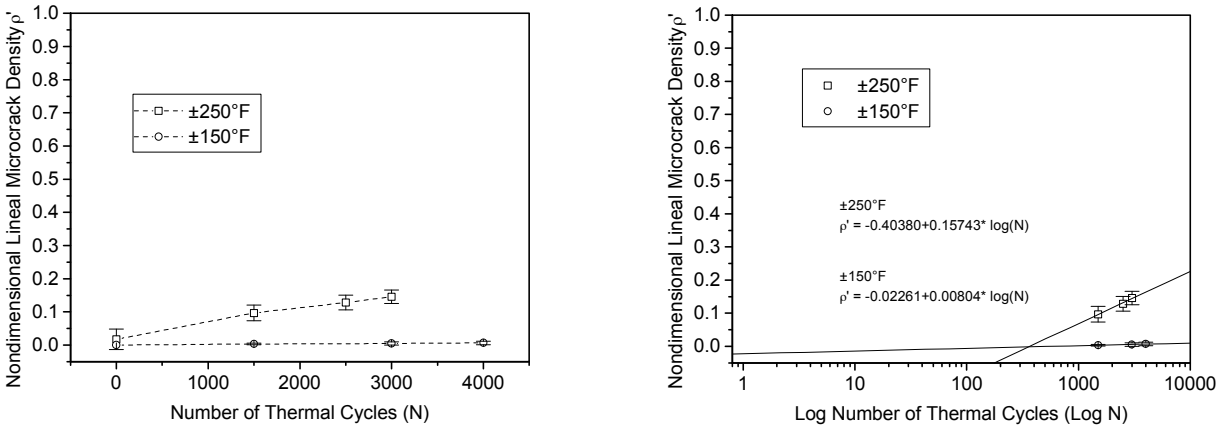

(a) +45° layer

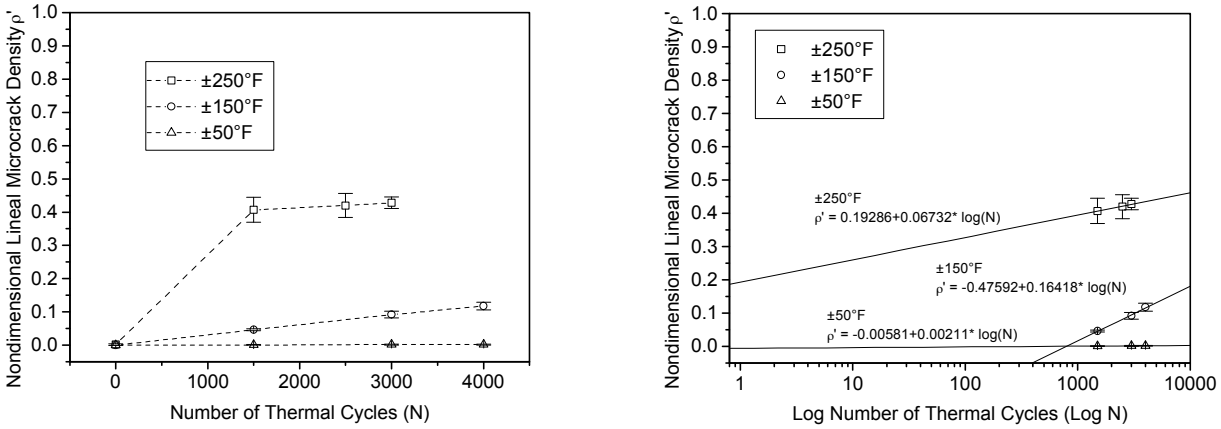

(b) 90° layer

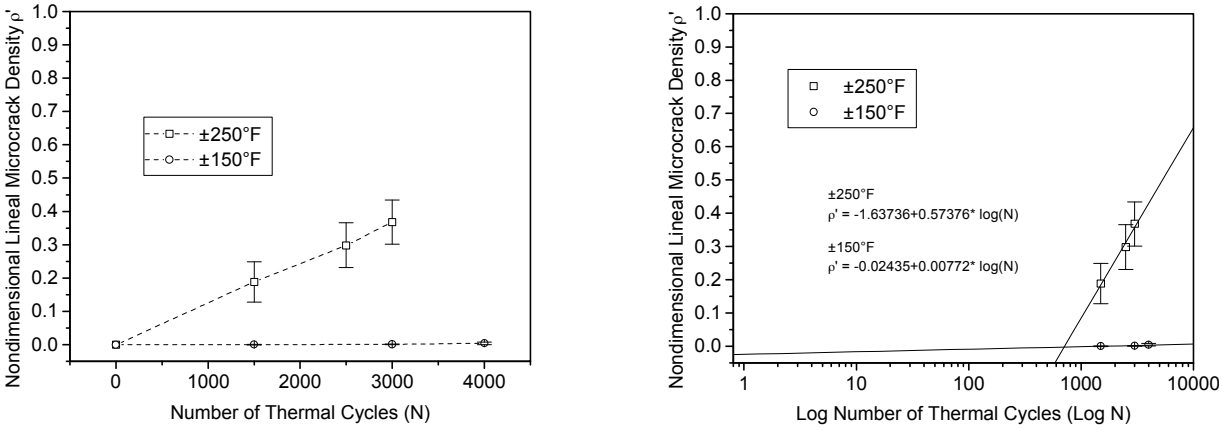

(c) –45° layer

Figure 3.39. Effect of thermal cycling temperature range on microcrack density in P75/RS3.Q2.2.* specimens.

Dimensional microcrack densities for the P75/RS3.Q2.2.* specimens are shown below in Table 3.14.

Table 3.14 Dimensional Microcrack Densities (in cracks/in.) for P75/RS3.Q2.2.* Specimens

	Layer	0	1500	2500	3000
±250°F Thermal Cycling Range	45	5 +11 -5	29 +6 -8	38 +7 -6	44 +6 -6
	90	1 +1 -1	172 +14 -17	178 +16 -14	181 +8 -5
	-45	0 +0 -0	28 +9 -8	45 +10 -9	55 +11 -7

	Layer	0	1500	3000	4000
±150 Thermal Cycling Range	45	0 +0 -0	1 +1 -1	2 +2 -2	2 +1 -2
	90	0 +0 -0	20 +1 -2	39 +4 -4	50 +4 -6
	-45	0 +0 -0	0 +0 -0	0 +0 -0	1 +0 -1

	Layer	0	1500	3000	4000
±50 Thermal Cycling Range	45	0 +0 -0	0 +0 -0	0 +0 -0	0 +0 -0
	90	0 +0 -0	0 +1 -0	1 +1 -1	1 +1 -1
	-45	0 +0 -0	0 +0 -0	0 +0 -0	0 +0 -0

Edge-view photographs of the P75/RS3.Q2.2.* configuration specimens containing microcracks are shown in Figure 3.40. Differences in the number of microcracks depending on thermal cycling temperature range can clearly be seen.

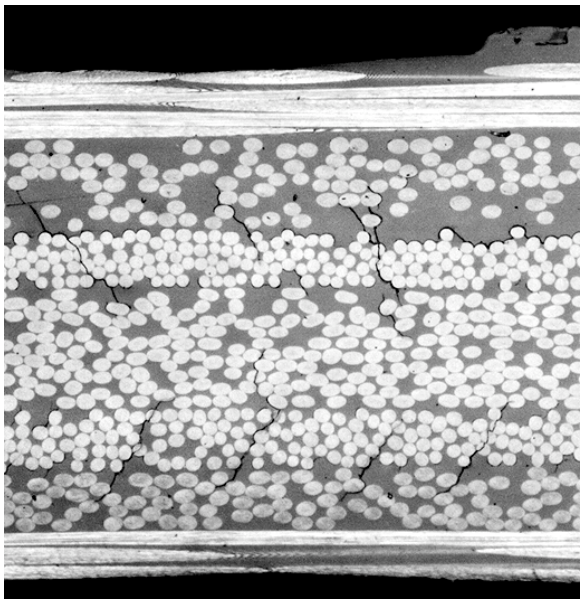

(a) 275RS3-2 3000 ±250°F cycles (200X)

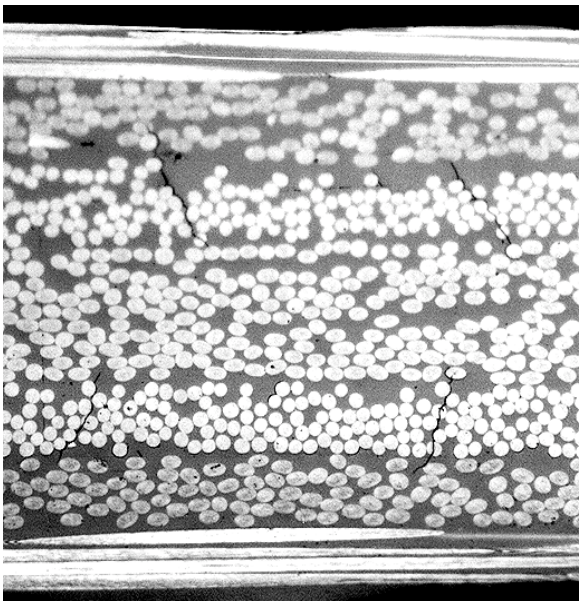

(b) 275RS3-4 4000 ±150°F cycles (200X)

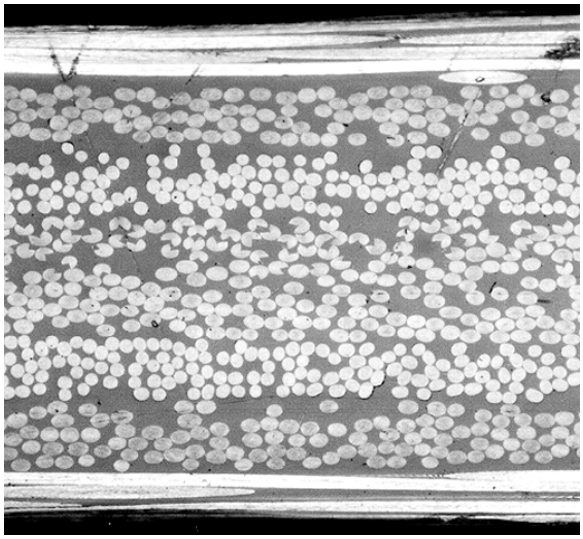

(c) 275RS3-8 4000 ±50°F cycles (200X)

Figure 3.40. Edge-view photographs of P75/RS3.Q2.2.* specimens containing microcracks.

An X-ray photograph of specimen 275RS3-1 cycled 3000 times at the ±250°F temperature range was shown previously in Figure 3.7. Microcracks were difficult to detect in the X-ray for

this specimen cycled at the ±250°F temperature range. X-rays were also taken of series 275RS3 specimens cycled at the ±150°F and ±50°F temperature ranges. The X-rays for these specimens appeared identical to that of the 275RS3-1 specimen and have not been included for this reason.

Since the thermal stresses induced on the specimens increase with decreasing temperature, it is expected that the ±250°F temperature range induces the highest level of damage in specimens in the form of microcracks. The data presented in this section has shown this point to be true for the materials in this study. Based on the number of thermal cycles completed in this study, it is still uncertain if there exists a stress ratio effect analogous to that in mechanical fatigue loading. In other words, if a material is cycled to less extreme temperatures, i.e., ±50°F compared to ±250°F, will the material ever develop a microcrack density equal to that in the specimen cycled at the more extreme temperature range? And if so, is there a threshold temperature range such that the material will never microcrack? Based on the empirical microcracking rates presented in this section, it would appear that some of the materials, i.e., P75/ERL1962.Q2.5.*, cycled at the less extreme temperature ranges may indeed reach microcrack densities equaling those in the materials cycled at the more extreme temperature ranges. It is also true, however, that for other materials, i.e., the P75/RS3.Q2.5.* series, that negligible microcracking has occurred for the less extreme temperature ranges for the 4000 cycles completed. This, in fact, implies the existence of a threshold temperature range for these P75/RS3 specimens. The next section will address changes in laminate CTE for these same material series, and to see if, in fact, there is no change in CTE for the specimens that did not develop microcracks. Predictive models will also be examined in the following chapter to address this issue more fully.

3.5.2 Thermal Expansion Behavior

This section examines the effect of thermal cycling temperature range on room temperature CTE of the three material/specimen configurations. In general, the ±250°F temperature range induced the highest microcrack densities in all specimens, and therefore is expected to influence the thermal expansion behavior more significantly than the ±150°F and ±50°F temperature ranges.

Room temperature CTE's for the P75/ERL1962.Q2.5.* specimens are shown in Figure 3.41 for the three temperature ranges, as well as the uncycled (BSL) condition. As expected, the greatest change in thermal expansion behavior from uncycled to cycled condition occurs in the specimens subjected to the ±250°F temperature range. The specimens subjected to the ±150°F

temperature range see a moderate change in thermal expansion behavior, while the specimens subjected to the ±50°F temperature range experience very little change.

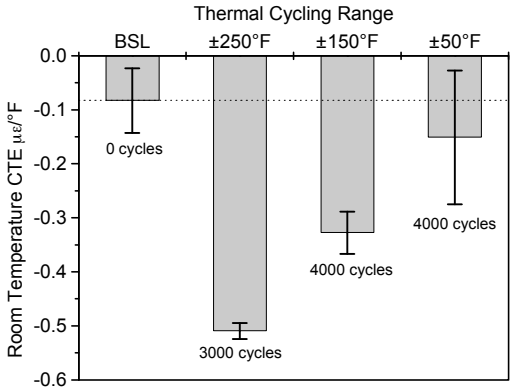

Figure 3.41. Effect of thermal cycling temperature range on room temperature CTE in P75/ERL1962.Q2.5.* specimens.

Microcrack densities for the P75/RS3.Q2.5.* configuration were previously shown to be negligible for specimens exposed to the ±150°F and ±50°F temperature ranges. As seen in Figure 3.42, the average room temperature CTE's for the specimens cycled in the ±50°F temperature range very closely matches that of the uncycled specimens, implying very little damage in these specimens. Similarly, there is very little change in the CTE of the specimens cycled in the ±150°F temperature range. The CTE of the specimens cycled in the ±250°F temperature range shows significant change resulting from the presence of microcracks. These results are in agreement with the previous microcrack density results. These data provide further support of a threshold temperature range for this material, below which, damage due to thermal cycling is avoided.

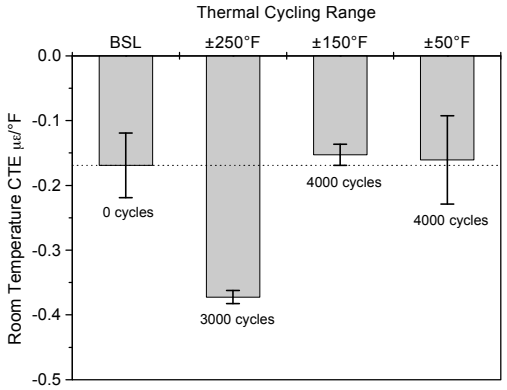

Figure 3.42. Effect of thermal cycling temperature range on room temperature CTE in P75/RS3.Q2.5.* specimens.

Room temperature CTE's for the P75/RS3.Q2.2.* configuration specimens are shown in Figure 3.43. Some change in the behavior of the specimens cycled between ±150°F and ±50°F is detectable. It is unexpected that, compared to the uncycled specimens, the average behavior of the specimens cycled between ±50°F appears different than the average behavior of the specimens cycled between ±150°F, although only slightly so. Considering the standard deviation in the data, there seems to be little difference in these two temperature ranges. The specimens cycled between ±250°F show significant change in the CTE, which correlates well with the high microcrack densities recorded in these specimens.

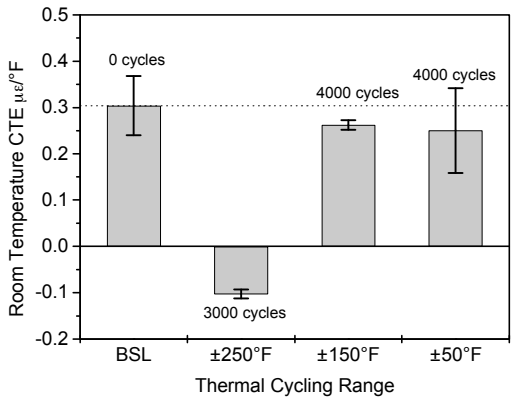

Figure 3.43. Effect of thermal cycling temperature range on room temperature CTE in P75/RS3.Q2.2.* specimens.

3.5.3 Laminate Stiffness

Normalized laminate stiffness results are presented in this section for these three material/specimen series. Past experimental results for tensile testing [15] indicate that specimen stiffness should decrease as the number of microcracks in the specimen increases. It is therefore logical to assume that as the number of microcracks increases due to thermal cycling, the stiffness of the specimen should decrease. It is also logical to assume that since the more severe thermal cycling temperature range, i.e., ±250°F compared to ±50°F, results in higher numbers of microcracks in the specimens, the specimen stiffness should decrease more as the severity of the thermal cycling range increases. As shown in Figure 3.44, this is not seen to always be the case. Only the P75/ERL1962.Q2.5.* series appears to show this type of trend, and with only one exception, the average uncycled stiffness for these specimens falls within one standard deviation of the average post-cycled stiffness. Taking into consideration the scatter in the uncycled specimens as well, there appears to be little statistical difference in the stiffness for any of the

specimens, regardless of temperature range imposed on the specimens. This holds true for the remaining two material/specimen series as well. This is largely due to the fact that the laminate stiffness, even in the quasi-isotropic specimens, is dominated by the fiber direction stiffness (see Appendix E) which is affected very little by the presence of microcracks.

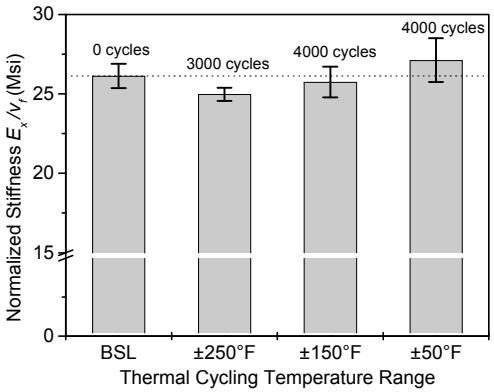

(a) P75/ERL1962.Q2.5.*

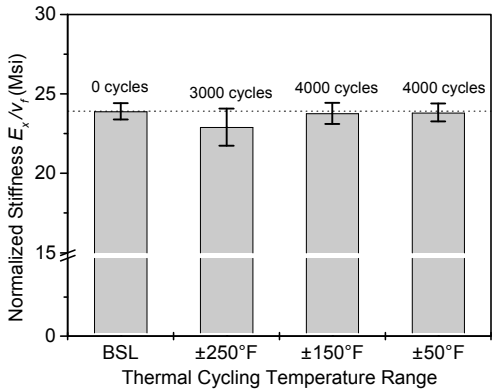

(b) P75/RS3.Q2.5.*

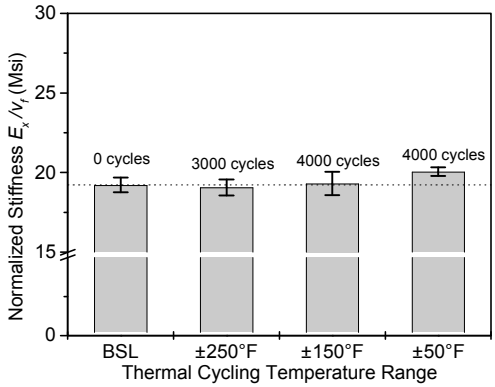

(c) P75/RS3.Q2.2.*

Figure 3.44. Effect of thermal cycling temperature range on normalized laminate stiffness in P75/ERL1962.Q2.5.*, P75/RS3.Q2.5.*, and P75/RS3.Q2.2.* specimens.

3.5.4 Glass Transition Temperature

Glass transition temperature was measured for each of the materials undergoing thermal cycling at the three different temperature ranges. The results are summarized in Table 3.15. Little change in T_g is observed for any of the materials, regardless of thermal cycling temperature range.

Table 3.15 Glass Transition Temperatures for the ERL1962 and RS3 Resin Systems Before and After Thermal Cycling

			Measured T_g			
Resin	Material Series	Mfg. Quoted T_g (°F)	Uncycled (°F)	±250°F (°F)	±150°F (°F)	±50°F (°F)
ERL1962	6762	320	313	318	318	320
RS3	75RS3	490	542	544	544	545

3.6 SUMMARY

This concludes the details of experimental results for this investigation. A significant amount of new and interesting information has been presented. The influence of fiber type, matrix type, layer thickness, and thermal cycling temperature range have all been studied in some detail. A concise summary of the major conclusions from this chapter are presented later in Chapter 5 along with the additional findings yet to be presented in Chapter 4. As alluded to previously, the experimental results from this chapter will be used together with existing analyses to further study thermally-induced microcracking and its effect on laminate CTE and laminate stiffness. These analytical predictions are presented next in Chapter 4.

4. ANALYTICAL PREDICTIONS

This chapter contains a summary of the analytical formulation developed in references [2, 3, 4] and comparisons of predictions based on that formulation to current experimental results. A somewhat detailed review of the formulation is presented, followed by a study to determine the sensitivity of the model to various material parameters. The chapter concludes with analytical predictions of microcrack density and laminate CTE for specimens in the present investigation. Limited laminate stiffness predictions are also presented.

4.1 SHEAR LAG MODEL FORMULATION

Much of the past analytical work in the area of microcrack prediction has focused on the shear lag phenomenon to model the state of stress in a laminate containing microcracks. As mentioned in Chapter 1, this is a phenomenon that was first introduced in the context of fiber breakage in unidirectional composite laminates. This same idea has been applied to the transverse matrix cracking phenomenon by many researchers, whereby the normal tensile stress in the cracking ply is transmitted to adjoining layers through a shear stress transfer. In a series of investigations [2, 3, 4], the shear lag stress formulation and energy principles are used to predict how the microcracking will occur in the laminate due to thermal loading, as well as mechanical loading. In the work by McManus et al. [2], the analysis is presented for cross-ply laminates only, but considers monotonic thermal loading as well as thermal cyclic loading. Park [3] extends that work to consider thermal loading in quasi-isotropic laminates. The work by Maddocks and McManus [4] then considers more general thermomechanical loading in a variety of laminates.

The basic shear lag formulation and energy-based cracking criterion used in references [2, 3, 4] were developed by Laws and Dvorak [18] for cross-ply laminates subjected to mechanical loading. The original formulation [18] included residual thermal stresses to account for cooling from processing temperature to operating temperature, but does not consider thermal loading as the primary loading parameter. In the analysis the cross-ply laminate is represented by a one-dimensional shear lag model, as illustrated in Figure 4.1. Microcracks are assumed to propagate through the entire width of the laminate, i.e., the y direction. Also, the displacement in the x direction in each of the layers is assumed to be uniform in the thickness direction, i.e., the z direction. In the vicinity of the crack, the normal stress (σ_x) in the cracking layer is transferred to the adjacent layers by way of shear stresses that develop in a negligibly thin layer with effective shear stiffness, K. The shear lag principle dictates that these shear stresses are directly proportional to the relative displacement between the cracked and adjacent uncracked layers.

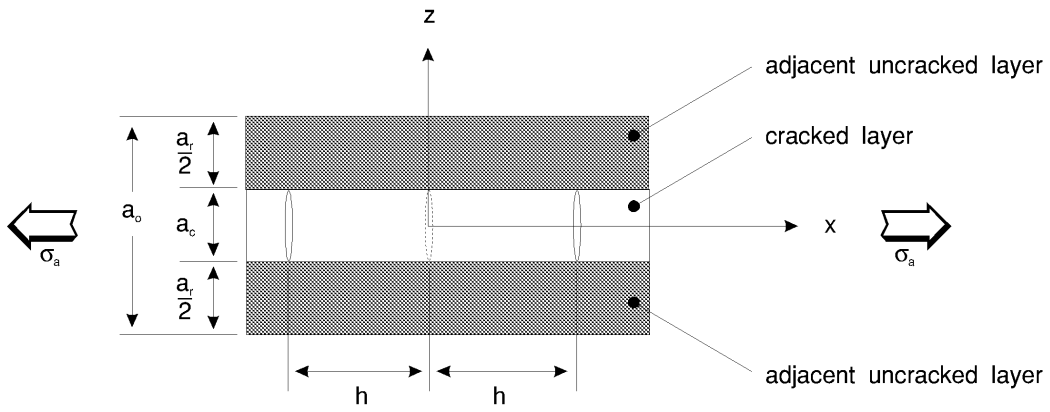

Figure 4.1. One-dimensional shear lag model geometry.

A single second-order differential equation representing equilibrium in the x direction is formed using strain-displacement and constitutive relations for the cracked and uncracked layers. This equilibrium equation is written as

$$\frac{d^2\sigma_c}{dx^2} - \frac{4\xi^2}{a_c^2}\sigma_c = -\lambda\,, \tag{4.1}$$

where σ_c is the stress in the cracked layer and ξ and λ are defined as

$$\xi = \sqrt{\frac{Ka_c\left(a_rE_r + a_cE_c\right)}{2a_rE_rE_c}} \tag{4.2}$$

$$\lambda = \frac{2K\left(a_rE_r + a_cE_c\right)\sigma_a}{a_ra_cE_rE_o} - \frac{2K}{a_c}\left(\alpha_c - \alpha_r\right)\Delta T\,. \tag{4.3}$$

The variable ξ is known as the shear lag parameter, a dimensionless quantity which includes both material properties and geometric parameters. In general, the value of the shear lag parameter is chosen by matching analytical predictions to experimental data. The shear lag parameter is the same as that used by Laws and Dvorak [18], while λ is a thermomechanical loading parameter introduced for convenience by Park [3]. In Equation 4.2 E_r is the stiffness of the layers adjacent to the cracking layer and E_c is the stiffness of the cracking layer. In Equation 4.3 σ_a is the applied mechanical stress, E_o is the stiffness of the uncracked laminate, α_c is the CTE of the cracking layer, α_r is the CTE of the layers adjacent to the cracking layer, and ΔT is the change in temperature calculated as the operating temperature minus the stress-free temperature. The homogeneous solution to the governing differential equation includes hyperbolic sine and cosine terms. The particular solution is a constant. Solving the equation results in stress and

displacement forms for the cracked and uncracked layers. These solutions can be seen in reference [4].

The above formulation assumes that two cracks initially exist, one at $x=-h$ and one at $x=h$, as seen in Figure 4.1. To address the issue of new crack formation, references [2, 3, 4] use the same approach used by Laws and Dvorak [18]. Namely, a new crack will form between the two existing cracks when the strain energy released by forming the new crack (ΔG) exceeds the critical value required to form two new crack surfaces, i.e., the critical strain energy release rate (G_{IC}). The critical strain energy release rate is generally thought to be a material property, while the strain energy release rate is calculated for a given volume of material using the Griffith energy balance written as

$$\Delta G = \frac{\Delta W - \Delta U}{a_c}, \tag{4.4}$$

where ΔW and ΔU are the changes in work and internal energy in the volume, respectively, between the states before and after the new crack forms. The details of the work and internal energy terms are detailed in reference [4]. For a strictly thermal application, the work term does not exist.

The remaining issue is to determine the location between the two existing cracks where the new crack will form. Laws and Dvorak [18] deal with this issue using three probability functions. The first assumes that the new crack will form exactly halfway between the two existing cracks. The second assumes that the new crack will form randomly between the two existing cracks. The third assumes that the location of the new crack is related to the stress in the cracking ply. References [2, 3, 4] use the first of these whereby an explicit solution to the problem is obtained. It should be noted that Laws and Dvorak [18] show best correlation with experimental data by using the third probability function.

Using the stress and displacement relations derived by solving the second order differential equation, Equation 4.1, the work and internal energy terms are combined to obtain the expression for ΔG. In its most general thermomechanical form, the strain energy release rate due to the formation of a new crack located halfway between two existing cracks is given by

$$\Delta G = \frac{a_c E_c}{2\xi a_o a_r E_r E_o}\left[a_o \sigma_a - a_r E_r (\alpha_c - \alpha_r)\Delta T\right]^2 \left[2\tanh\left(\frac{\xi h}{a_c}\right) - \tanh\left(\frac{2\xi h}{a_c}\right)\right]. \tag{4.5}$$

By setting ΔG equal to G_{IC}, one can solve for the temperature or mechanical stress at which the material will form a new crack between two existing cracks.

To account for cyclic loading, References [2, 3, 4] use the same form for the strain energy release rate, but modify the critical strain energy release rate to be a function of the number of cycles. The cyclic loading results that References [2, 3] present include only thermal cycling, but mechanical cycling could be analyzed as well.

To obtain an expression for critical strain energy release rate as a function of the number of cycles, an expression is derived for the stress required to form the first crack. This is done by setting the crack spacing h in Equation 4.5 to infinity, along with setting ΔG equal to G_{IC}. This expression reduces to

$$G_{Ic} = \frac{a_c a_o E_o}{2\xi a_r E_r E_c} \sigma_{fc}^2, \tag{4.6}$$

where σ_{fc} is the stress required to form the first crack. McManus et al. [2] argue that by knowing the failure stress as a function of the number of loading cycles N, be they mechanical or thermal loading cycles, a ratio can be formed whereby the critical strain energy release rate as a function of the number of loading cycles can be determined by the ratio

$$G_{Ic}(N) = G_{Ic}(0)\left[\sigma_{fc}(N)/\sigma_{fc}(0)\right]^2, \tag{4.7}$$

where the (0) notation indicates the uncycled condition. The key to this ratio is that the critical strain energy release rate is proportional to the square of the failure stress. It is presumed in this derivation that the stress required to form a new crack at a given number of cycles is better known than the critical strain energy release rate. In fact, failure stress values as a function of number of cycles are also very limited and McManus et al. [2] must make extrapolations from limited mechanical fatigue data. Assuming that these data are available, it is then a fairly simple task to calculate the crack spacing as a function of static or cyclic, mechanical or thermal, loading. It should be noted that the cyclic loading predictions assume constant stress ratio loading, i.e., repeated cycles to the same load or temperature.

Knowing the crack spacing, h, McManus et al. [2] follow the derivation of Laws and Dvorak for reduced laminate stiffness. This reduced stiffness is summarized as

$$E_o^c = E_o\left(1 + \frac{\rho a_c^2 E_c}{2\xi a_r E_r}\tanh\frac{2\xi}{\rho a_c}\right)^{-1}, \tag{4.8}$$

where ρ is referred to as the microcrack density, simply calculated as the inverse of the crack spacing. E_o and E_o^c are the uncracked and cracked stiffness of the laminate, respectively.

McManus et al. [2] argue that the reduction in stiffness of the cracked laminate, E_o^c, is due to the reduction in the cracking layer stiffness, E_c. They define a knockdown factor, κ, as

$$E_c^c = \kappa E_c, \tag{4.9}$$

where E_c^c is the reduced stiffness, or cracked stiffness, of the cracking layer. Using Equation 4.9 with a rule-of-mixtures for the laminate, another expression for the cracked laminate stiffness is derived, namely,

$$E_o^c = \frac{E_r a_r + \kappa E_c a_c}{a_o}. \tag{4.10}$$

Combining Equations 4.8 and 4.10 results in the following expression for the knockdown factor

$$\kappa = \frac{E_r a_r \left(1 - \frac{\rho a_c}{2\xi} \tanh \frac{2\xi}{\rho a_c}\right)}{E_r a_r + E_c a_c \frac{\rho a_c}{2\xi} \tanh \frac{2\xi}{\rho a_c}}. \tag{4.11}$$

McManus et al. [2] use this knockdown factor together with classical laminated plate theory to predict the effect of microcracking on the laminate stiffness and thermal expansion behavior due to monotonic or cyclic loading. This knockdown factor is used to reduce the transverse lamina stiffness on an individual basis according to the microcrack density for the given layer. This knockdown factor, although derived from a one-dimensional model, is also used in conjunction with classical laminated plate theory to modify the inplane shear stiffness and Poisson's ratio of the lamina in the same manner as the transverse stiffness. This is more of a physical assessment of what should occur in the laminate as opposed to a rigorous analytical solution.

4.2 SENSITIVITY ANALYSIS

A computer program, Crackomatic II, was developed by the authors of references [2, 3, 4] based on the shear lag formulation described in the previous section. The present section examines the sensitivity of this program to the various material parameters required to execute the program. For an analysis of thermal cyclic loading, the computer program requires the following:

1) Lamina material properties E_1, E_2, ν_{12}, G_{12}, α_1, α_2
2) Laminate stacking sequence and layer thicknesses
3) Fatigue toughness as a function of the number of thermal cycles, i.e., G_{IC} versus N
4) Shear lag factor, ξ
5) Laminate stress-free temperature

6) ΔT of the thermal cycles (assumes repeated cycles to the same temperature).

For the thermal cycling analysis, temperature-dependent material properties are not included as an option.

The baseline values chosen for each of the material properties in this sensitivity study do not represent properties for a specific material, but instead represent a typical combination of properties taken from the database of materials studied in this investigation. These baseline values are specified as

$$\begin{array}{lll} E_1 = 35.0\,Msi & \alpha_1 = -0.5x10^{-6}/°F & \\ E_2 = 1.0\,Msi & \alpha_2 = 20.0x10^{-6}/°F & t = 0.005\,in. \\ G_{12} = 0.7\,Msi & G_{IC}(0) = 0.571\,in\cdot lb/in^2 & \Delta T = -600°F \\ \nu_{12} = 0.3 & \xi = 0.65 & \end{array} , \qquad (4.12)$$

where the inplane lamina properties, E_1, E_2, G_{12}, ν_{12}, α_1, and α_2 are the longitudinal extensional modulus, transverse extensional modulus, shear modulus, Poisson's ratio, longitudinal coefficient of thermal expansion, and transverse coefficient of thermal expansion, respectively. The values for both $G_{IC}(0)$ and ξ are representative of values published previously by McManus et al. [2]. The layer thickness is represented by t. A ΔT of –600°F is assumed based on a laminate stress-free temperature of 350°F and a minimum cycling temperature of –250°F.

To determine the sensitivity of the model to various material properties, each of the above properties, with the exception of t and ΔT, is varied separately from –25% to +25% of their baseline values, while keeping all other material parameters constant. Note that for this analysis, a positive percentage increase in α_1 implies a more negative value. Microcrack densities are calculated using Crackomatic II and plotted as a function of the number of thermal cycles and as a function of the single material parameter being varied. An important factor to be considered is how G_{IC} varies as a function of the number of cycles, i.e., $G_{IC}(N)$. McManus et al. [2] dealt with this issue by adopting the empirical results of Petipas et al. [41], whereby the transverse failure stress decreases logarithmically as a function of cycling. McManus et al. [2] then relate transverse failure stress to critical strain energy release rate to derive an expression for $G_{IC}(N)$. The details of this derivation follow.

The experiments of Petipas et al. [41] yielded the following empirical equations for transverse failure strength as a function of cycling:

$$\sigma_{2u}(N) = \sigma_{2u}(0)\left[1.0 - 0.0322\log_{10} N\right] \qquad (4.13)$$

and

$$\sigma_{2u}(N) = \sigma_{2u}(0)\left[1.0 - 0.0336\log_{10} N\right] \tag{4.14}$$

for two different composite material systems. In these relations, σ_2 is the transverse failure strength of the lamina, and N represents the number of mechanical cycles. The first material system consisted of a Toray T400 fiber in an Elf Aquitane 202S matrix. The second material system consisted of a Toray T300 fiber in a Ciba Geigy 914 CTS resin system.

Following Equation 4.7, McManus et al. [2] adopted the latter expression for the T300 system and used the expression

$$\frac{G_{\mathrm{IC}}(N)}{G_{\mathrm{IC}}(0)} = \left[\frac{\sigma_{2u}(N)}{\sigma_{2u}(0)}\right]^2, \tag{4.15}$$

for critical strain energy release rate as a function of transverse failure stress to derive an expression for critical strain enery release rate as a function of the number of cycles. The resulting expression for critical strain energy release rate was given by

$$G_{\mathrm{IC}}(N) = G_{\mathrm{IC}}(0)\left[1.0 - 0.0336\right]^{2\log_{10} N}, \tag{4.16}$$

although there appears to be an error in the derivation. According to the results of Petipas et al. [41], the expression should be

$$G_{\mathrm{IC}}(N) = G_{\mathrm{IC}}(0)\left[1.0 - 0.0336\log_{10} N\right]^2. \tag{4.17}$$

The value of G_{IC} as a function of the number of cycles depends on which expression is used. Using the baseline value of $G_{IC}(0)$ shown in Equation 4.12, tabulated values are shown in Table 4.1 for the original equation by McManus et al. [2], the corrected version, and an arbitrary reduction in $G_{IC}(0)$ of 10 percent per decade. For the purpose of the sensitivity study, it was decided not to use either of the logarithmic expressions for $G_{IC}(N)$. Instead, the arbitrary reduction of 10% per cycle decade was chosen. This results in a greater reduction in $G_{IC}(N)$ than that proposed by McManus et al. [2], as seen in Table 4.1.

Table 4.1 Critical Strain Energy Release Rate as a Function of the Number of Thermal Cycles

Number of Cycles	McManus et al.[2] $G_{IC}(N) = G_{IC}(0)\left[1.0 - 0.0336\right]^{2\log_{10} N}$	McManus et al.[2] (corrected) $G_{IC}(N) = G_{IC}(0)\left[1.0 - 0.0336\log_{10} N\right]^{2}$	10% reduction per decade
0	0.571	0.571	0.571
1	0.571	0.571	0.571
10	0.533	0.533	0.514
100	0.498	0.497	0.457
1000	0.465	0.462	0.400
10,000	0.434	0.428	0.343
100,000	0.406	0.395	0.289

Microcrack density results are shown in Figure 4.2 and Figure 4.3 for each of the eight material parameters being studied. In all cases, the laminate considered has eight total layers, each 0.005 in. in thickness, and arranged in a $[0/+45/90/-45]_s$ lamination sequence. The results shown are for microcracks in the 90° layers only. Each of the individual contour plots represent the effect of varying a single material parameter on the microcrack density. In the extreme cases, nearly horizontal contours would indicate virtually no dependence of microcracking on the material property being varied, and dependence only on the number of thermal cycles. Nearly vertical contours, on the other hand, would indicate a strong dependence of microcracking on the material property being varied, and no dependence on the number of thermal cycles.

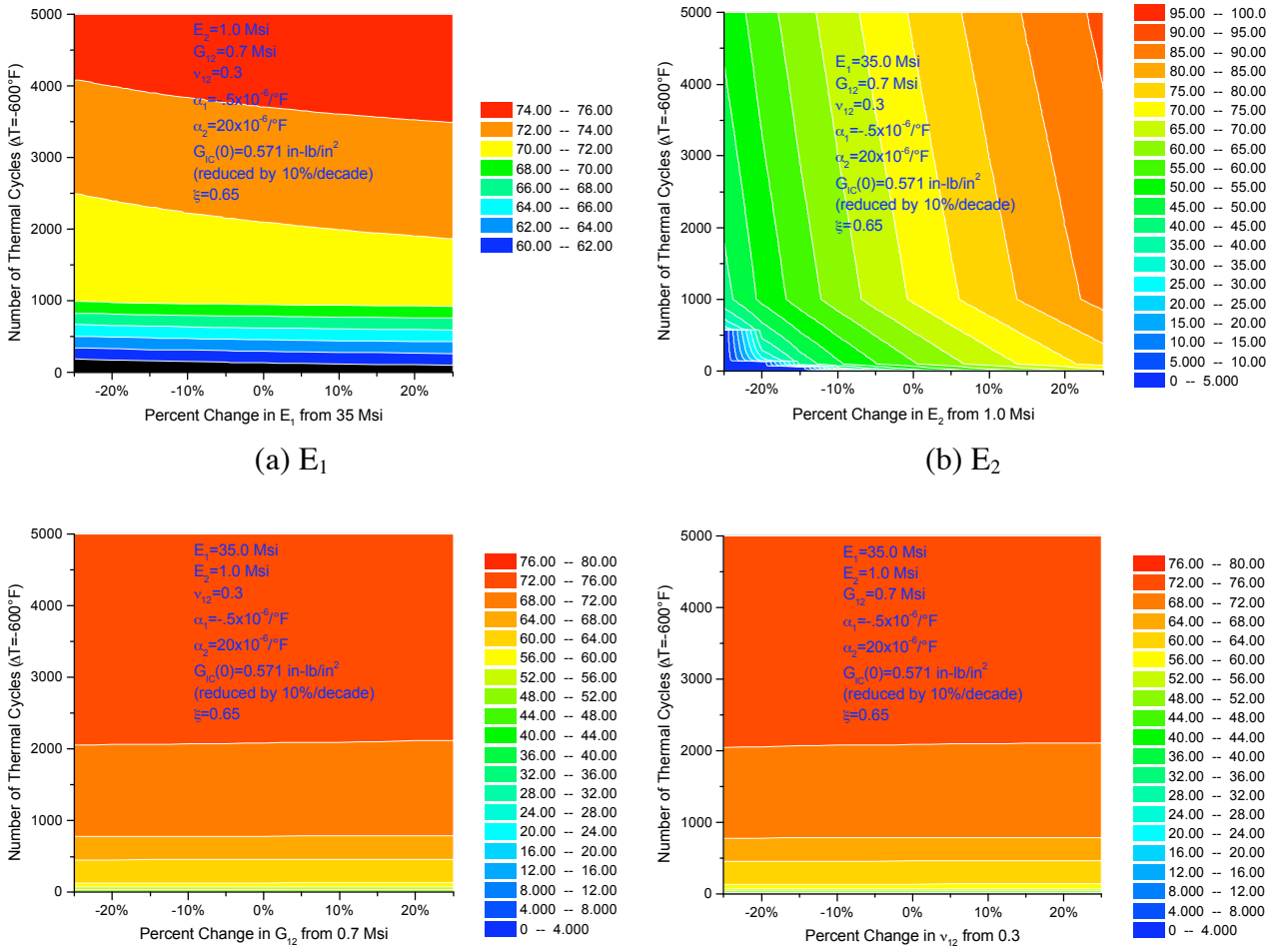

Figure 4.2. Effect of various material parameters on microcrack density predictions from Crackomatic II. ([0/+45/90/–45]$_s$ 0.005 in. ply thickness)

The results shown in Figure 4.2 indicate that a variation in E_1 has only a small effect on microcrack density, a variation in E_2 has a significant effect, and variations in both G_{12} and ν_{12} have a negligible effect. Similarly, from Figure 4.3, a variation in α_1 is seen to have only a small effect on microcrack density, variations in both α_2 and $G_{IC}(0)$ are seen to have significant effect on microcrack density, and finally, a variation in ξ is seen to have an effect on microcrack density.

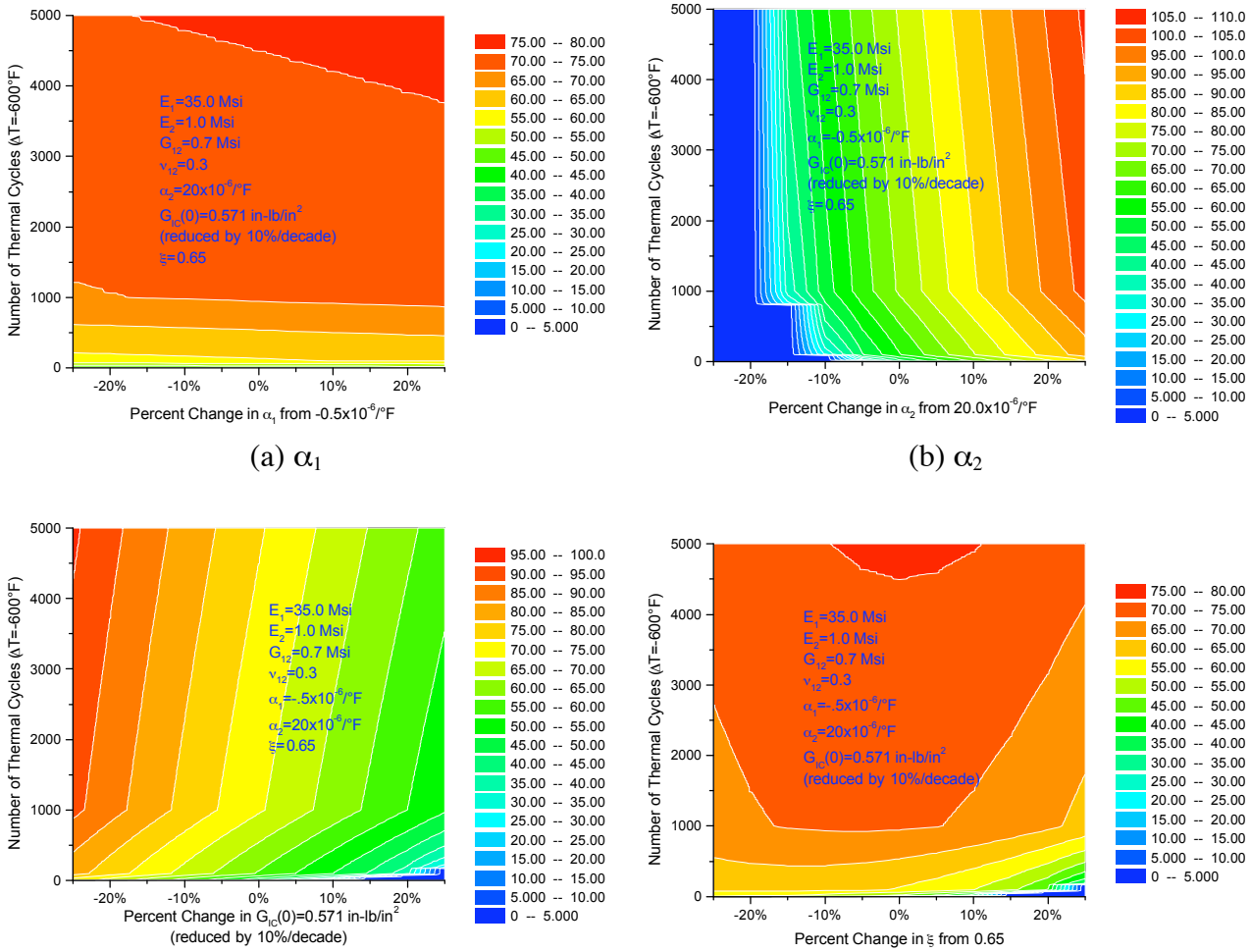

(a) α_1 (b) α_2

(c) $G_{IC}(0)$ (d) ξ

Figure 4.3. Effect of various material parameters on microcrack density predictions from Crackomatic II. ($[0/+45/90/-45]_s$ 0.005 in. ply thickness)

In summary, for a fixed reduction in $G_{IC}(0)$ of 10 percent per decade of cycles, six of the eight material parameters have varying effects, ranging from slight to significant, on microcrack density according to the Crackomatic II model developed by the authors in References [2, 3, 4]. The three parameters E_2, α_2, and $G_{IC}(0)$ have, by far, the most significant effect. The values for E_2 and α_2 are readily measurable. There are problems, however, associated with the transverse tensile test to measure E_2. Specifically, there is often significant scatter in the data from a transverse tensile test. Nonetheless, E_2 is a readily measurable parameter. The other three parameters having a slight effect on microcrack density are E_1, α_1, and ξ. Again, E_1 and α_1 are readily measurable parameters. That leaves $G_{IC}(0)$ and ξ as being the difficult-to-determine parameters governing the prediction of microcrack density as a function of the number of thermal cycles. That, of course, in addition to the manner in which $G_{IC}(0)$ varies as a function of the

number of cycles, i.e., $G_{IC}(N)$. As will be seen later, the expression for $G_{IC}(N)$ will be separated into the baseline parameter, $G_{IC}(0)$, and a rate parameter, μ, to more accurately model experimental behavior. It is proposed, therefore, that some of the database of experimental results be used to empirically determine the values for $G_{IC}(0)$, μ, and ξ. Many of the figures that follow will include variations in these three parameters showing their effects. The remaining experimental results will be compared with predictions based on the empirically determined values of $G_{IC}(0)$, μ, and ξ.

4.3 ANALYTICAL PREDICTIONS VERSUS EXPERIMENTAL RESULTS

This section contains the Crackomatic predictions for each of the material systems included in this investigation. The shear lag parameter, ξ, and the critical strain energy release rate as a function of the number of thermal cycles, $G_{IC}(N)$, are adjusted such that the nondimensional lineal microcrack densities predicted by Crackomatic match those measured experimentally. In the case of the T50/ERL1962, P55/ERL1962, P75/ERL1962, and P120/ERL1962 materials, microcrack densities from the cross-ply specimens are used to adjust ξ and $G_{IC}(N)$. This information is then used to predict the microcrack densities in the corresponding quasi-isotropic specimens of the same material. Additionally, after the values for the parameters ξ and $G_{IC}(N)$ are established, the experimentally measured laminate stiffness, E_x, and CTE, α_x, are compared to those predicted by Crackomatic. It should be noted that empirically determining the most appropriate values for the microcracking parameters ξ and $G_{IC}(N)$ is a lengthy process. The results presented in the following sections are a small percentage of the total number of analyses performed for these materials in the course of this study.

4.3.1 T50/ERL1962 Material System

Microcrack Density

The following is a summary of the Crackomatic analyses performed on the T50/ERL1962.X.5.G specimens. The room temperature lamina properties for these specimens are summarized in Table 4.2. These lamina properties, and the properties for all other material systems, have been derived using unidirectional material data and the analysis presented in Appendix F. It should be noted that every specimen series has a unique set of material properties as a result of variation in fiber volume fraction. This is explained in detail in Appendix F. Briefly, a range of lamina properties is calculated in Appendix F based on the average unidirectional properties plus and minus one standard deviation. This range of values was modified to account

for variations in fiber volume fraction in each of the specimen series. The final set of lamina properties presented here was chosen out of the range of properties that resulted in the best agreement between measured and predicted laminate CTE in the uncycled condition.

Table 4.2 Room Temperature Lamina Properties for T50/ERL1962.X.5.G Specimens

E_1 (Msi)	E_2 (Msi)	G_{12} (Msi)	ν_{12}	α_1 (με/°F)	α_2 (με/°F)
31.5	1.11	.631	.270	-.357	16.2

Before using the experimentally measured microcrack densities to adjust their values, the parameters ξ and $G_{IC}(N)$ presented by McManus et al. [2] for the identical material are considered. The expression for $G_{IC}(N)$ was given by Equation 4.17 as

$$G_{IC}(N) = G_{IC}(0)\left[1.0 - 0.0336\log_{10} N\right]^2. \qquad \text{(4.17, rewritten)}$$

Note that this is the corrected version compared to that presented in the original paper by McManus et al. [2] They use a value of 0.90 for ξ and a value of 0.754 in-lb/in^2 for $G_{IC}(0)$ for the T50/ERL1962 material system. The predicted results from Crackomatic based on these values for ξ and $G_{IC}(N)$ and the lamina properties in Table 4.2 are shown in Figure 4.4 along with the experimentally measured microcrack densities, indicated in the figure by Exp., to 3500 cycles. Note there are two layers of interest for this specimen. The single 90° layer near the surface of the specimen, referred to as the outer 90° layer, or o90, and the double thickness layer at the midplane of the specimen, referred to as the center 90° layer, or c90.

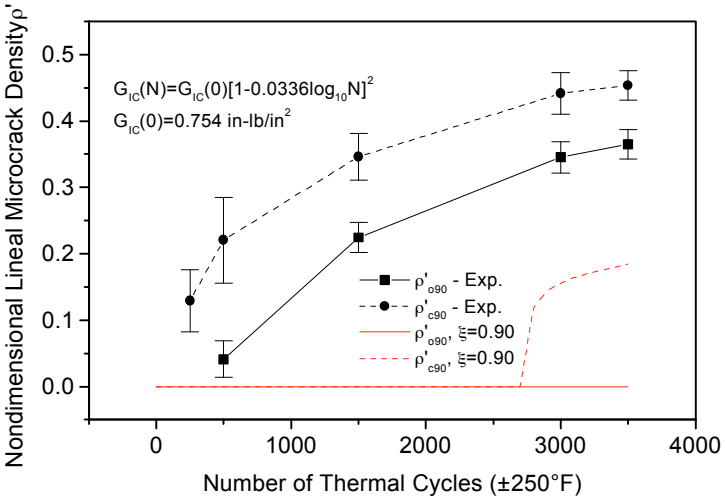

Figure 4.4. Measured and predicted microcrack density in T50/ERL1962.X.5.G specimens using parameters from literature.

Note that for these values of $G_{IC}(N)$ and ξ, no cracking is predicted in the o90 layer to 3500 cycles. Cracking is not predicted to occur until after 2500 cycles in the double-thickness c90 layer. These predictions do not agree well with experimentally observed behavior. The parameters ξ and $G_{IC}(N)$ will now be adjusted in an effort to improve the agreement.

The influence of the shear lag factor is first studied. Using the same value for $G_{IC}(0)$ and the corrected logarithmic expression proposed by McManus et al. [2] results in the behavior shown in Figure 4.5 for the shear lag parameter ranging from 0.10 to 0.50. The original choice of 0.90 is also included for comparison. An important observation from Figure 4.5 is that the shear lag factor tends to control the ratio of microcrack densities in the two different layers, i.e., the c90 and o90 layers. Note that at high cycle numbers, a higher value of ξ, i.e., ξ=0.50, results in a significantly higher ratio of predicted microcrack densities in the c90 layer compared to the o90 layer. As the value of ξ is reduced, this ratio decreases. It is also noted that the shear lag factor can control the onset of microcracking, as seen for the ξ=0.50 and ξ=0.90 cases. Comparing the c90 to o90 microcrack density ratio for the various values of ξ, a value between 0.20 and 0.30 appears to most closely match the experimental data, particularly at 3500 cycles.

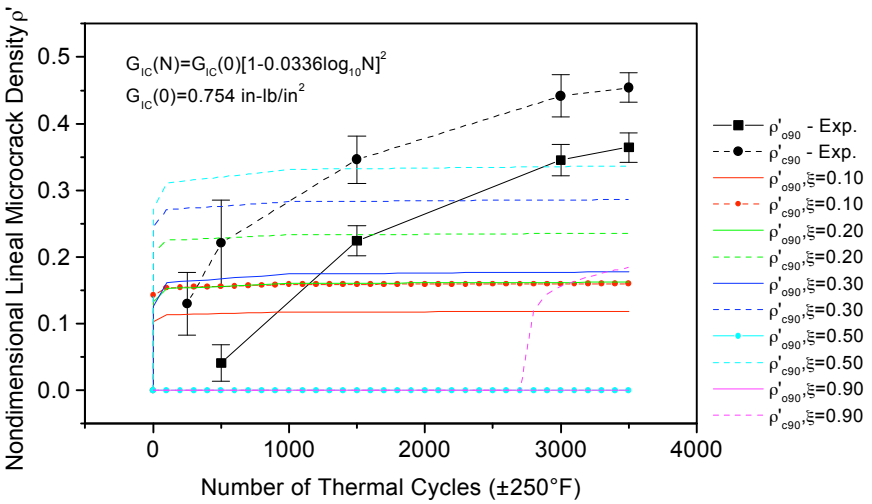

Figure 4.5. Effect of shear lag factor on predicted microcrack density in T50/ERL1962.X.5.G specimens.

The effect of $G_{IC}(N)$ on the microcracking behavior is now considered by holding ξ constant and varying $G_{IC}(N)$. A value of ξ=0.25 is chosen for this analysis. The corrected expression of McManus et al. [2] for $G_{IC}(N)$ shown in Equation 4.17 can be represented by

$$G_{IC}(N) = G_{IC}(0)\left[1 - \mu \log_{10} N\right]^2 . \qquad (4.18)$$

In order to maintain the character of this expression, there are two parameters which can be modified: $G_{IC}(0)$ and μ. The effect of $G_{IC}(0)$ will first be considered, followed by considering the effect of μ. The first term in square brackets in Equation 4.18 must remain unity in order to retain the character of the derivation by McManus et al. [2] So that the $G_{IC}(N)$ expression is well behaved for up to 10^5 cycles, an upper limit of 0.20 is placed on μ. For this upper limit of μ, reductions in $G_{IC}(N)$ will continue to occur for up to 10^5 cycles. Above 10^5 cycles, the value of $G_{IC}(N)$ will begin to increase, a contradiction to physical behavior. This upper limit is somewhat of an arbitrary restriction, but it is thought that reductions in $G_{IC}(N)$ should continue for at least 10^5 cycles. The following expression for $G_{IC}(N)$ is therefore considered first:

$$G_{IC}(N) = G_{IC}(0)\left[1 - 0.20\log_{10} N\right]^2. \tag{4.19}$$

The value for $G_{IC}(0)$ was allowed to vary from 0.5 to 2.0 in-lb/in^2. The results for this analysis are shown in Figure 4.6. As expected, the lower the initial critical strain energy release rate, the higher the predicted microcrack density. For the material considered, a value of 2.0 matches very closely the experimental values at the high cycle count. Note that the choice of parameters resulting in the best agreement is indicated by the '«' in the legend to the right of the figure. This indication is included in figures to follow as well.

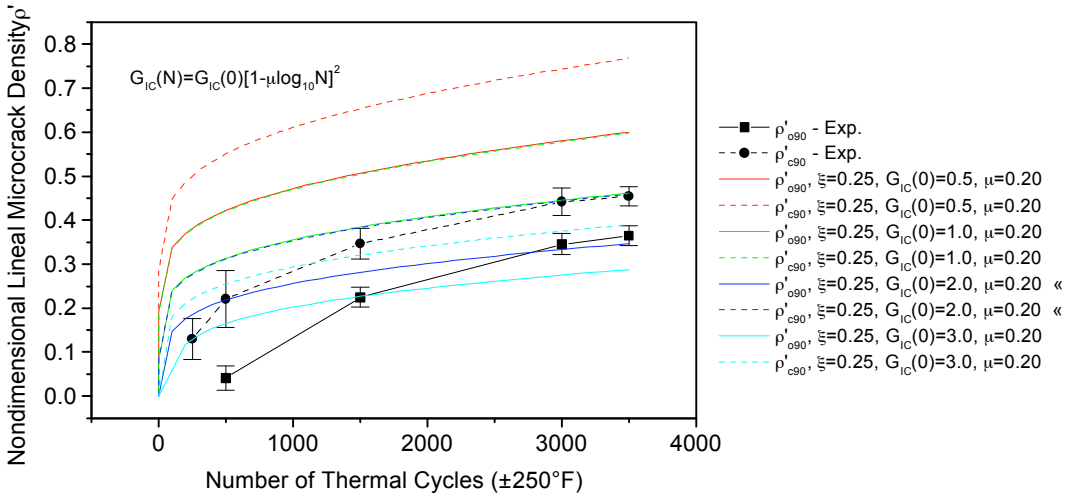

Figure 4.6. Effect of $G_{IC}(0)$ on predicted microcrack density in T50/ERL1962.X.5.G specimens.

In Figure 4.7, the value for $G_{IC}(0)$ is held constant at 2.0 in-lb/in^2 and the value for μ is allowed to vary from 0.05 to 0.20. From the figure, it appears that the higher values of μ result in additional microcracking at high cycle numbers that is not present for the lower values of μ. The initial cracking rates do not seem to be significantly affected by the value of μ, with the exception

that delayed onset of microcracking is observed in some cases. A value of μ=0.20 appears to most closely match the behavior of the T50/ERL1962.X.5.G specimens. The predictions based on the microcracking parameters presented by McManus et al. [2] are included for completeness.

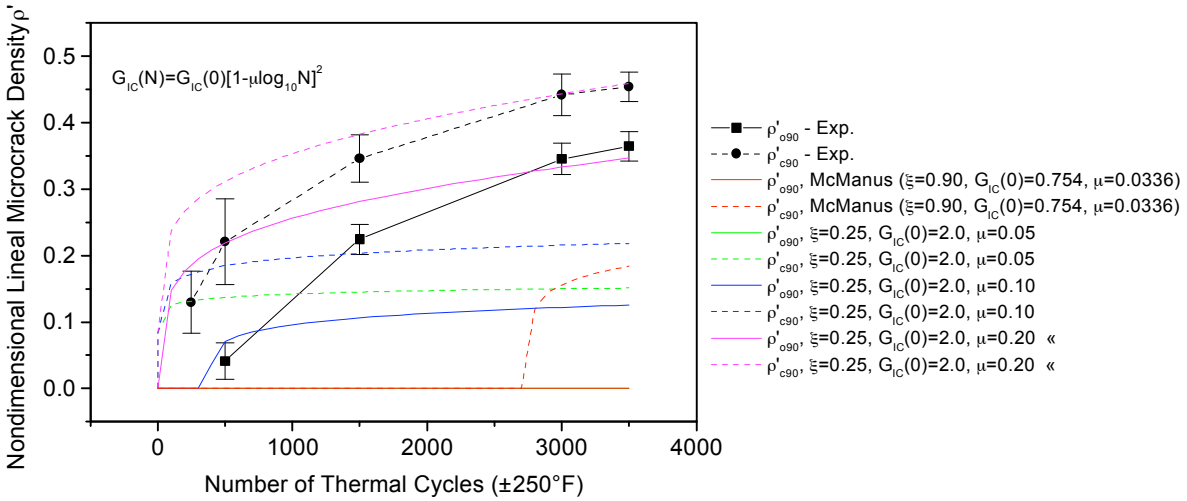

Figure 4.7. Effect of μ on predicted microcrack density in T50/ERL1962.X.5.G specimens.

In summary, the three microcracking parameters (ξ, $G_{IC}(0)$, and μ) can be adjusted to reasonably match observed experimental behavior in the T50/ERL1962 cross-ply specimens. These three parameters are dependent upon one another, although each of them has a distinguishing characteristic. The shear lag parameter, ξ, tends to control the ratio of the microcrack densities in the layers of the specimen. The initial critical strain energy release rate, $G_{IC}(0)$, tends to control the maximum microcrack density for a given material. Finally, the rate parameter, μ, tends to control the rate at which microcrack density increases in the material. These three parameters will now be used to correlate measured and predicted microcrack densities in the quasi-isotropic specimens for the T50/ERL1962 material, and for the other materials in this investigation.

The room temperature lamina properties for the T50/ERL1962.Q1.5.G specimens are shown in Table 4.3. Using the three values of the microcracking parameters from the previous analysis for the cross-ply specimen, i.e., ξ=0.25, $G_{IC}(0)$=2.0 in-lb/in^2, and μ=0.20, the Crackomatic predictions for the same T50/ERL1962 material in the Q1 quasi-isotropic specimens are shown in Figure 4.8. Recall there are three layer orientations (+45°, –45°, and 90°) in these specimens for which crack densities are recorded. Note that the microcrack density predictions for the +45° and –45° layers coincide with one another. This will be seen to be the case for all single thickness layers in the quasi-isotropic configurations, i.e., the +45° and –45° layers in the

Q1 configuration and the +45° and 90° layers in the Q2 configuration, despite the experimentally measured densities which are usually significantly different from one another. It is interesting to note, however, that the predicted values for the +45° and –45° layers very closely predict the average measured microcrack densities in these two layers. The predictions for the 90° layer are low compared to the measured values, but are within reason. Overall, the microcrack density predictions agree reasonably well with the measured values. The predictions using the parameter values presented by McManus et al. [2] are also included in the figure. No microcracking is predicted in the +45° and –45° layers using their parameters and the predictions for the 90° layer are quite low.

Table 4.3 Room Temperature Lamina Properties for T50/ERL1962.Q1.5.G Specimens

E_1 (Msi)	E_2 (Msi)	G_{12} (Msi)	ν_{12}	α_1 (με/°F)	α_2 (με/°F)
31.3	1.15	.633	.280	-.344	16.3

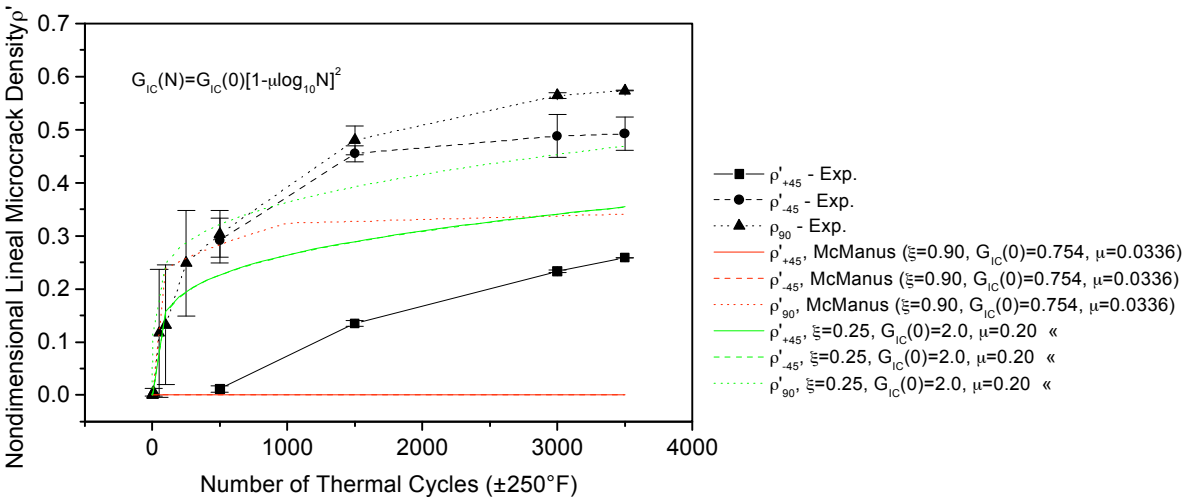

Figure 4.8. Measured and predicted microcrack density in T50/ERL1962.Q1.5.G specimens.

Before moving on to the next material system, the predictions for laminate CTE and laminate stiffness will now be considered for both the cross-ply and quasi-isotropic T50/ERL1962 specimens. Again, the same values for the three microcracking parameters, i.e., ξ=0.25, $G_{IC}(0)$=2.0 in-lb/in^2, and μ=0.20, are used for these predictions. The predictions based on the parameter values presented by McManus et al. [2], i.e., ξ=0.90, $G_{IC}(0)$=0.754, and μ=0.0336, are included as well for comparison.

Laminate CTE

The measured room temperature laminate CTE as a function of the number of thermal cycles for the T50/ERL1962 specimens is presented in Figure 4.9, along with the predictions from Crackomatic. The predictions match the trend correctly, namely, the laminate CTE tends to become more negative with cycling. However, using the parameter values derived in the previous section, the analysis overpredicts the change in CTE by almost double the actual change. One could argue that the overprediction is a result of matching microcrack densities that are artificially high. If, in fact, the microcrack densities used to adjust the three microcracking parameters were, on average, lower, then the predicted laminate CTE would more closely match the experimental values. Again one could argue that the experimentally measured microcrack densities, recorded from specimen edge views, are not representative of the microcrack densities in the interior of the specimen. This has long been an issue associated with this type of experimental characterization, and a number of investigators have attempted to deal with this problem [3, 55]. The X-ray photography performed on the specimens in this investigation was performed to address this very issue. This is certainly an area for debate, however, work done in this investigation leads to the conclusion that the microcrack densities recorded from specimen edge views are representative of values in the interior of the specimen. For this reason, it can be stated that the Crackomatic analysis overpredicts the change in CTE of the T50/ERL1962 specimens. The predictions based on the values presented by McManus et al. [2] are equally inaccurate. Not surprisingly, their values significantly underpredict the change in CTE as a result of the microcrack densities being significantly underpredicted.

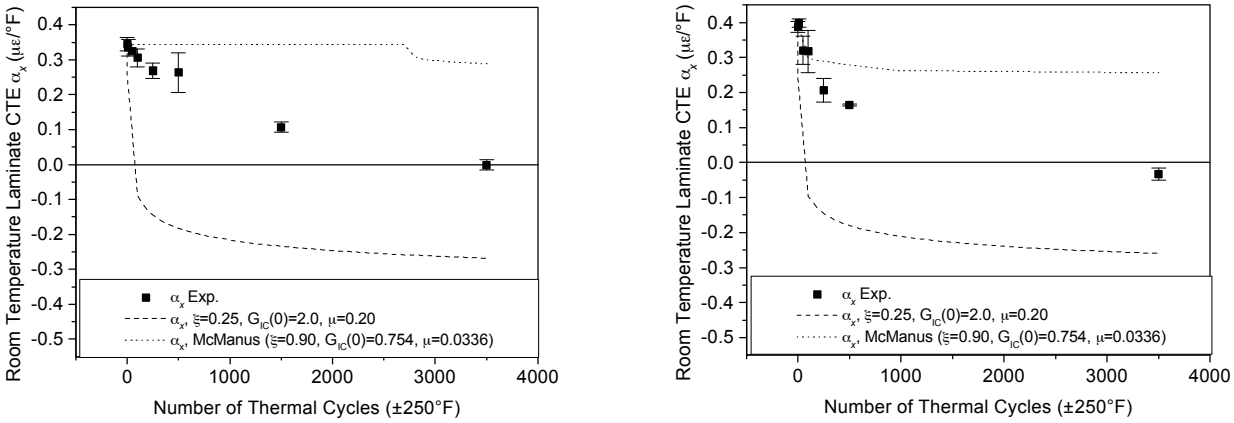

(a) T50/ERL1962.X.5.G (b) T50/ERL1962.Q1.5.G

Figure 4.9. Measured and predicted room temperature CTE for T50/ERL1962.X.5.G and T50/ERL1962.Q1.5.G specimens.

Laminate Stiffness

The uncycled and post-cycled laminate stiffnesses for the T50/ERL1962 specimens are presented in Figure 4.10, along with the Crackomatic stiffness predictions using the current microcracking parameters and the ones presented by McManus et al. [2], as a function of the number of thermal cycles. The analysis predicts a slight overall decrease in laminate stiffness as the number of cycles increases. Based on previous investigations considering the effect of microcrack density on stiffness [15], this trend is expected. As shown previously in Chapter 3, the average uncycled stiffness typically falls within one standard deviation of the average post-cycled stiffness, making it impossible to draw conclusions regarding experimental changes in stiffness. The scatter in the post-cycled measured stiffnesses in Figure 4.10 exceeds the predicted change in stiffness for the cross-ply specimens and very nearly does the same for the quasi-isotropic specimens. Note that the predicted uncycled stiffnesses do not match the measured values. This is a result of the derived lamina properties not accurately representing *both* the measured laminate CTE and measured laminate stiffness. Because of the difficulty in accurately measuring laminate stiffness experimentally, it was decided that uncycled laminate CTE was the more important of the two properties to match correctly. Based on these considerations, the Crackomatic prediction using the microcracking parameters derived in this section is therefore assumed to be only a reasonable representation of the change in stiffness in these specimens. Due to the lack of significant changes in experimentally measured laminate stiffness for the remainder of the specimens in this investigation, additional laminate stiffness results are not presented.

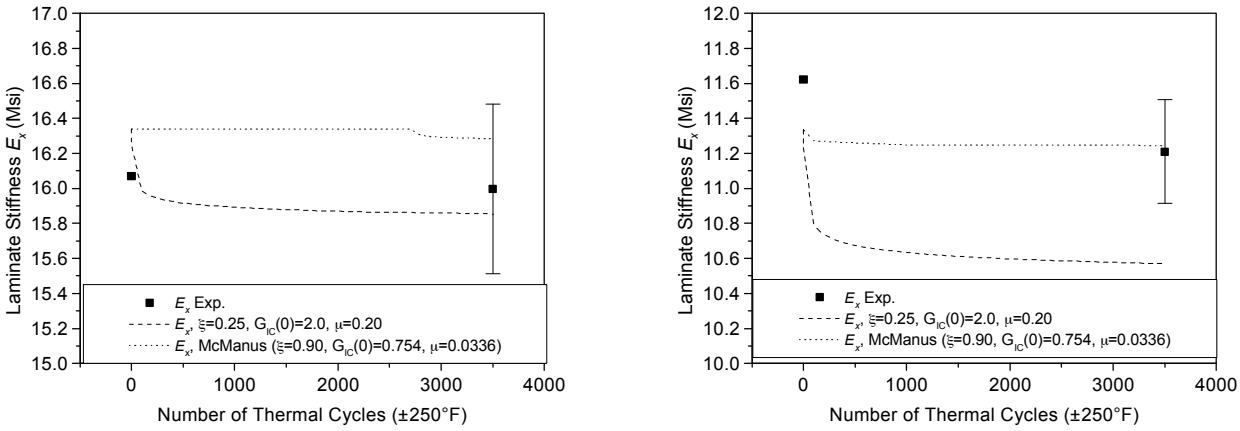

(a) T50/ERL1962.X.5.G (b) T50/ERL1962.Q1.5.G

Figure 4.10. Measured and predicted laminate stiffness for T50/ERL1962.X.5.G and T50/ERL1962.Q1.5.G specimens.

The remainder of this chapter includes comparisons of measured values and analytical predictions of microcrack density and laminate CTE for the other materials included in this investigation. For the microcrack density predictions, the original parameter values of McManus et al. [2] are shown along with one or more of the final parameter values derived in the present investigation. The final parameter values for each material were determined in the same manner they were determined for the T50/ERL1962.X.5.G specimens in Section 4.3.1...educated trial and error. Recall, the final parameter values are indicated in the figure legends by '«'.

.

4.3.2 P55/ERL1962 Material System

Microcrack Density

The room temperature lamina properties for the P55/ERL1962.X.5.G specimens are shown in Table 4.4. The measured and predicted microcrack densities as a function of the number of thermal cycles are shown in Figure 4.11. The predictions based on the original microcracking parameters presented by McManus et al. [2] for this material are shown along with the prediction using the parameters derived in the last section for the T50/ERL1962 specimens, i.e., ξ=0.25, $G_{IC}(0)$=2.0 in-lb/in^2, and μ=0.20. The parameter values presented by McManus et al. [2] predict saturation too early for this material and underpredict the microcrack densities at high cycle numbers. The best correlation with measured microcrack densities for this P55/ERL1962 material was found using ξ=0.25, $G_{IC}(0)$=0.75 in-lb/in^2, and μ=0.20. Note that better agreement is seen for these P55/ERL1962 specimens than for the T50/ERL1962 specimens. In fact, better agreement between measured and predicted microcrack densities is observed for all of the pitch-based fibers in the ERL1962 matrix. These composites tend to crack rapidly in the early stages of cycling and the analysis predicts this trend well.

Table 4.4 Room Temperature Lamina Properties for P55/ERL1962.X.5.G Specimens

E_1 (Msi)	E_2 (Msi)	G_{12} (Msi)	ν_{12}	α_1 ($\mu\varepsilon$/°F)	α_2 ($\mu\varepsilon$/°F)
24.5	1.23	.700	.368	-.367	17.4

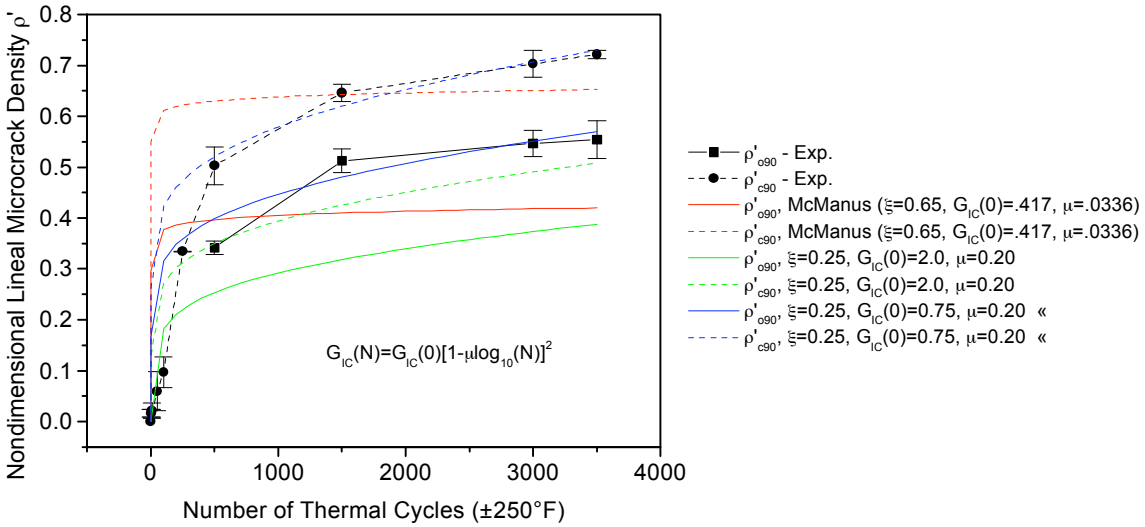

Figure 4.11. Measured and predicted microcrack density in P55/ERL1962.X.5.G specimens.

The microcracking parameters derived using the cross-ply P55/ERL1962 specimens are now used to predict the behavior in the quasi-isotropic specimens. The room temperature lamina properties for these specimens, i.e., P55/ERL1962.Q1.5.G, are shown in Table 4.5. The measured and predicted microcrack densities for the quasi-isotropic specimens are shown in Figure 4.12. Very good agreement is seen for the 90° layer and good agreement, on average, for the +45° and –45° layers using the microcracking parameters from the P55/ERL1962.X.5.G specimens. Note also that the predictions based on the original parameters presented by McManus et al. [2] are also shown in Figure 4.12. The predictions based on their parameters show better correlation for these quasi-isotropic specimens compared to the cross-ply specimens shown previously. However, microcrack saturation is still predicted to occur too early using their parameter values.

Table 4.5 Room Temperature Lamina Properties for P55/ERL1962.Q1.5.G Specimens

E_1 (Msi)	E_2 (Msi)	G_{12} (Msi)	ν_{12}	α_1 (με/°F)	α_2 (με/°F)
24.6	1.17	.700	.361	-.369	16.9

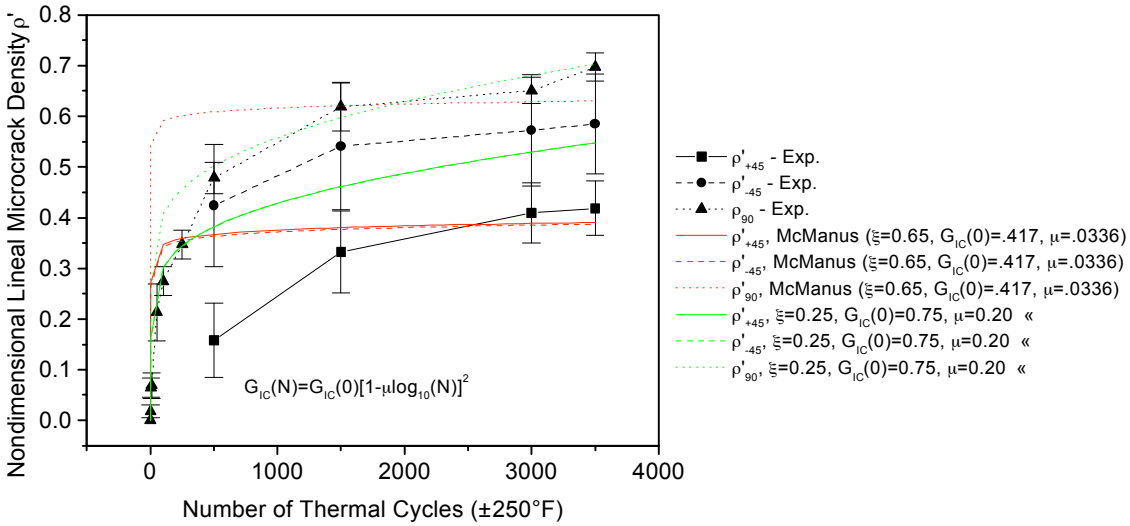

Figure 4.12. Measured and predicted microcrack density in P55/ERL1962.Q1.5.G specimens.

Laminate CTE

The measured and predicted room temperature laminate CTE's are shown in Figure 4.13 for the cross-ply and quasi-isotropic P55/ERL1962 specimens. As noted previously for the T50/ERL1962 specimens, the Crackomatic analysis tends to overpredict the change in laminate CTE, although predictions for this material system appear to be in better agreement with measured values.

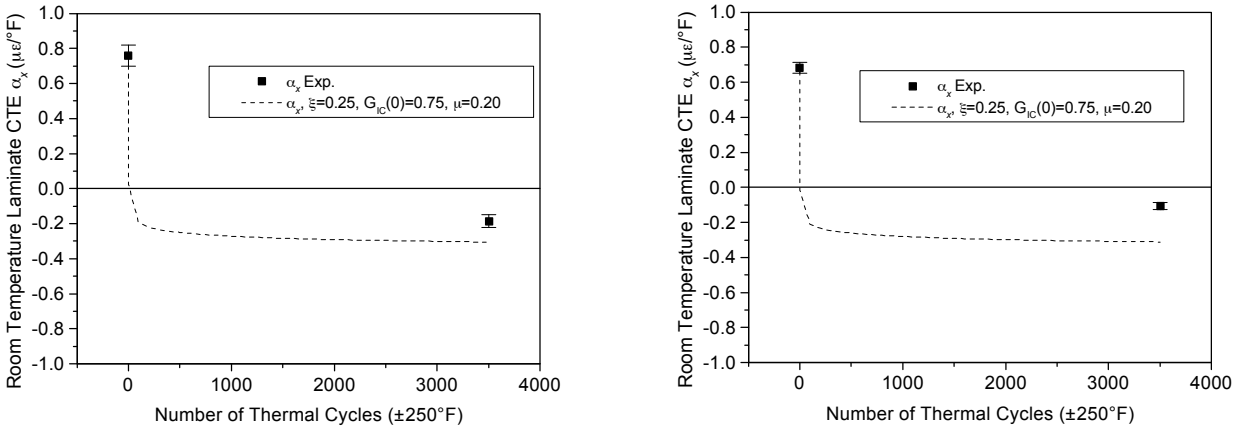

(a) P55/ERL1962.X.5.G (b) P55/ERL1962.Q1.5.G

Figure 4.13. Measured and predicted laminate CTE for P55/ERL1962.X.5.G and P55/ERL1962.Q1.5.G specimens.

4.3.3 P75/ERL1962 Material System

Measured and predicted results are presented in this section for several specimen configurations, all of which are P75/ERL1962 materials. The results include a combination of lamination sequence effects, temperature range effects, and layer thickness effects.

Microcrack Density

The room temperature lamina properties for the P75/ERL1962.X.5.G specimens are shown in Table 4.6. The measured and predicted microcrack densities as a function of the number of thermal cycles are shown in Figure 4.14. The predictions using the parameters presented by McManus et al. [2] are shown together with three sets of parameters covering a variety of the microcracking parameters. The best agreement is obtained by using values of ξ=0.20, $G_{IC}(0)$=0.25 in-lb/in^2, and μ=0.15. Note that the predictions based on the parameters of McManus et al. [2] tend to underpredict the microcrack density at any given cycle count. Note also the larger ratio of microcrack density in the c90 layer compared to the o90 layer. This is a direct result of the ξ=0.65 parameter used by McManus et al. [2], a value too high for this material.

Table 4.6 Room Temperature Lamina Properties for P75/ERL1962.X.5.G Specimens

E_1 (Msi)	E_2 (Msi)	G_{12} (Msi)	ν_{12}	α_1 (με/°F)	α_2 (με/°F)
32.2	.889	.700	.298	-.463	22.0

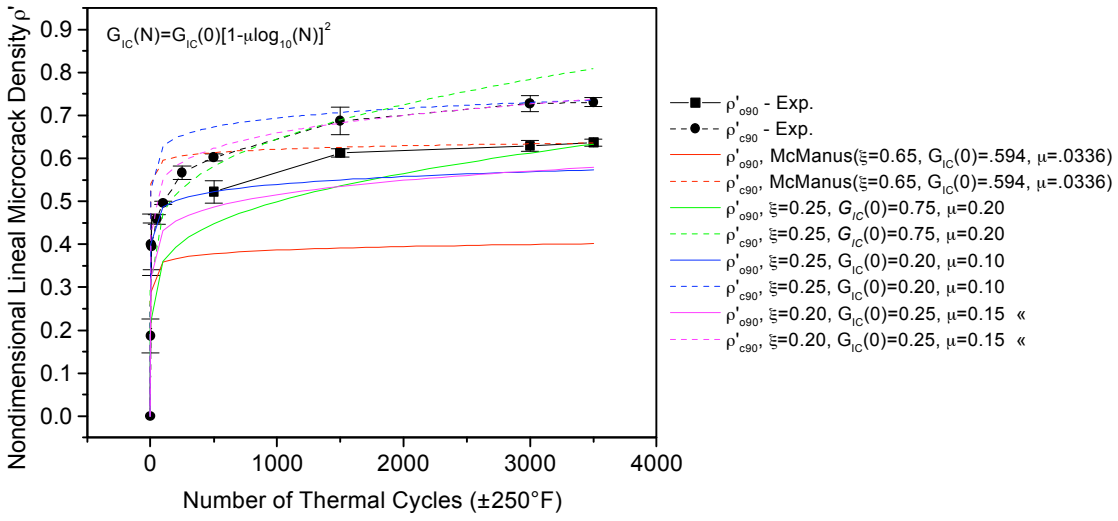

Figure 4.14. Measured and predicted microcrack density in P75/ERL1962.X.5.G specimens.

The room temperature lamina properties for the P75/ERL1962.Q1.5.G specimens are shown in Table 4.7. Using the microcracking parameters from the cross-ply P75/ERL1962 specimens, i.e., ξ=0.20, $G_{IC}(0)$=0.25 in-lb/in^2, and μ=0.15, results in the predictions shown in Figure 4.15. The agreement between measured and predicted values is good, although for this choice of microcracking parameters, the predictions are slightly high. Note that the predictions based on the parameter values presented by McManus et al. [2] are very good for the 90° layer at high cycle counts and slightly low for the +45° and –45° layers. The rate parameter, μ, presented by McManus et al. [2] is somewhat low, as evidenced by the premature saturation prediction.

Table 4.7 Room Temperature Lamina Properties for P75/ERL1962.Q1.5.G Specimens

E_1 (Msi)	E_2 (Msi)	G_{12} (Msi)	ν_{12}	α_1 (με/°F)	α_2 (με/°F)
32.0	.889	.700	.299	-.459	22.1

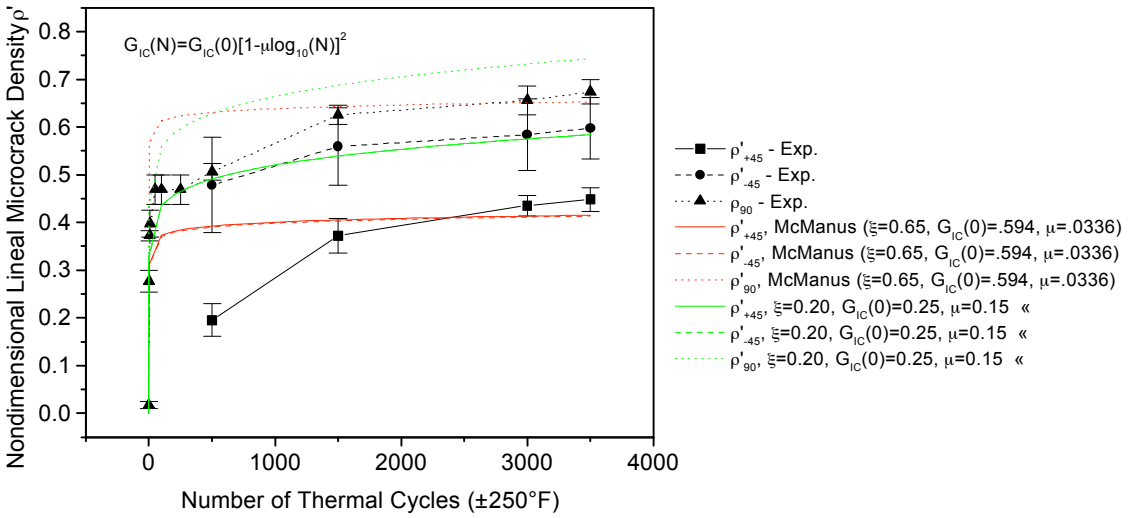

Figure 4.15. Measured and predicted microcrack density in P75/ERL1962.Q1.5.G specimens.

Results are now presented for the P75/ERL1962.Q2.5.* specimens. These specimens undergo cycling at three different temperature ranges: G, L, and C. The same P75/ERL1962 material has just been analyzed, but in the Q1 lamination sequence. The values from this previous analysis for the P75/ERL1962.Q1.5.G specimens, i.e., ξ=0.20, $G_{IC}(0)$=0.25, and μ=0.15, are therefore used as initial values for these Q2 quasi-isotropic specimens. The lamina material properties derived for the P75/ERL1962.Q2.5.* specimens are summarized in Table 4.8. Note the higher value for E_1 of 42.4 Msi, roughly 30 percent higher than for the previous P75/ERL1962 materials. This results from the significantly higher fiber volume fraction in the P75/ERL1962.Q2.5.* specimens, as shown in Appendix F.

Table 4.8 Room Temperature Lamina Properties for P75/ERL1962.Q2.5.* Specimens

E_1 (Msi)	E_2 (Msi)	G_{12} (Msi)	ν_{12}	α_1 (με/°F)	α_2 (με/°F)
42.4	1.00	.700	.294	-.593	16.8

Thermal Cycling Range G (±250°F). The measured and predicted microcrack densities are shown in Figure 4.16 for the P75/ERL1962.Q2.5.G specimens. Note that the analysis tends to underpredict the measured microcrack density using the previously derived set of parameters, i.e., ξ=0.20, $G_{IC}(0)$=0.25, and μ=0.15. Decreasing the value of $G_{IC}(0)$ to 0.18 in-lb/in^2 results in much better agreement, particularly in the central –45° layer. This does not imply that the change in lamination sequence from Q1 to Q2 results in a lower value for $G_{IC}(0)$. The change in $G_{IC}(0)$ most likely results from the variation in lamina properties as previously noted. Note also that the Crackomatic code predicts virtually identical microcrack densities for the single thickness +45° and 90° layers of this Q2 quasi-isotropic configuration. This is analogous to the earlier predictions for the Q1 quasi-isotropic configuration in which the single thickness +45° and –45° layers were predicted to have identical microcrack densities. As was seen previously, the prediction here for the two single-thickness layers is roughly equivalent to the average values observed experimentally. Note that the predictions based on the microcracking parameter values presented by McManus et al. [2] are also shown in the figure. In general, those values are considerably low, particularly for the +45° and 90° layers for which microcracking is not predicted to occur prior to 3500 cycles.

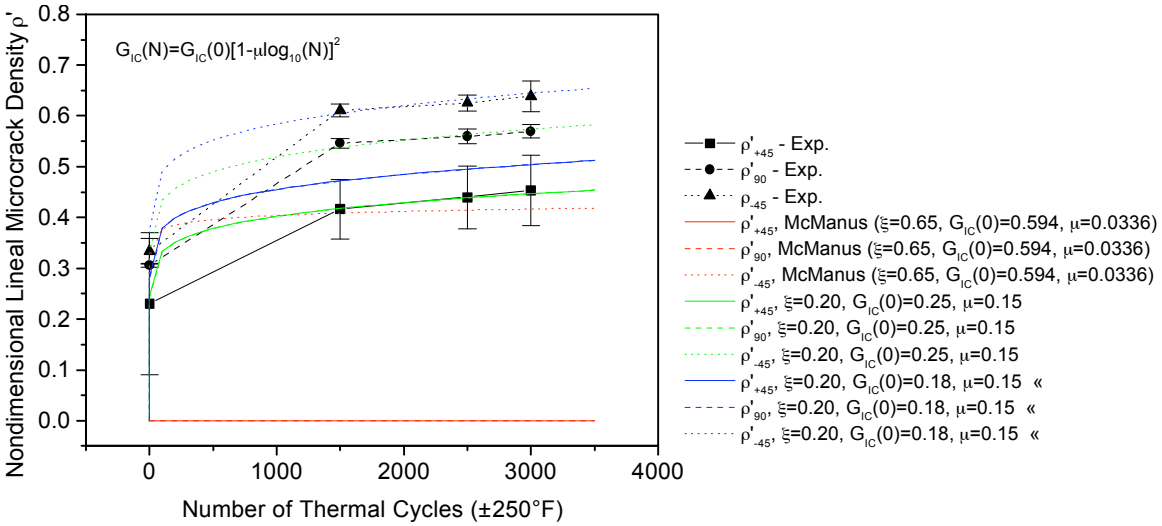

Figure 4.16. Measured and predicted microcrack density in P75/ERL1962.Q2.5.G specimens.

Thermal Cycling Range L (±150°F). The microcracking parameters derived for the temperature range G, i.e., ξ=0.20, $G_{IC}(0)$=0.18, and μ=0.15, are now used to predict the microcrack density in the specimens cycled at temperature range L. As seen in Figure 4.17, the predictions for these parameters exceed the measured microcrack densities. It is likely that $G_{IC}(N)$ is affected differently by thermal cycling at different temperature ranges. If this is indeed the case, the rate parameter, μ, should be affected but the baseline value, $G_{IC}(0)$, should remain the same. By reducing the rate parameter from 0.15 to 0.10, the predictions do, in fact, more closely match the experimentally measured values, particularly at high cycle numbers, and are shown in Figure 4.17. The trends observed here in the predictions based on the parameter values presented by McManus et al. [2] are similar to those seen previously for the G temperature range.

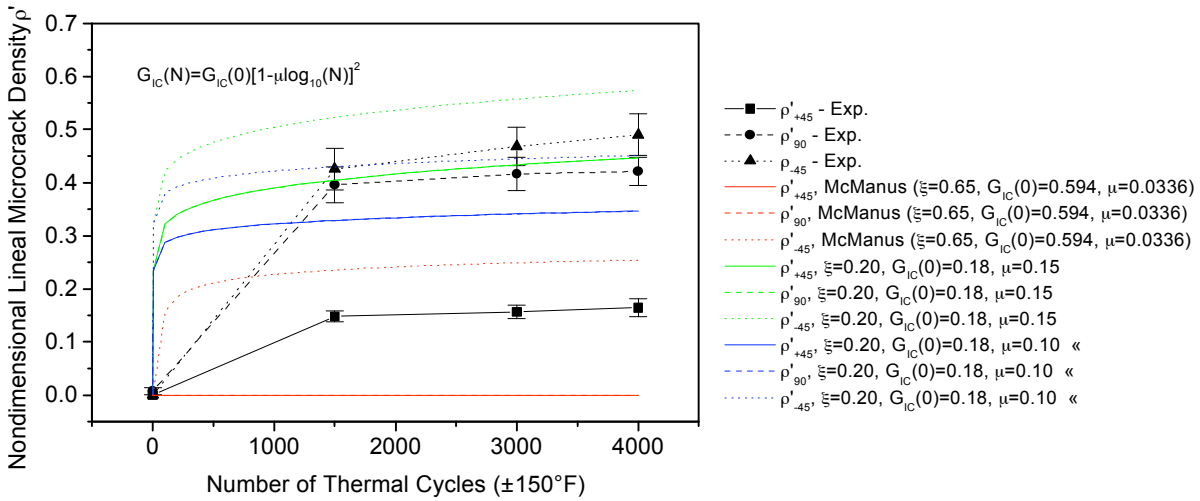

Figure 4.17. Measured and predicted microcrack density in P75/ERL1962.Q2.5.L specimens.

Thermal Cycling Range C (±50°F). Similar reductions in the microcracking rate parameter, μ, are shown in Figure 4.18 for the C temperature range. Again, reducing the rate parameter to 0.05 improves the agreement between prediction and measured microcrack density. The predictions, however, indicate much higher initial microcrack accumulation than that measured experimentally. It is noted for this temperature range that, unlike results for the previous two temperature ranges, the measured microcrack density in the double-thickness –45° layer is less than that in the single thickness 90° layer. From the results presented previously in Figure 3.36, the microcrack density in the –45° layer is predicted to eventually exceed that in the 90° layer due to the slightly higher empirical microcracking rate of 0.38621 in the –45° layer compared to

0.35898 in the 90° layer. This is a trend the analysis could not predict. Note that the predictions based on the parameter values presented by McManus et al. [2] indicate no microcracking in any of the layers prior to 4000 cycles.

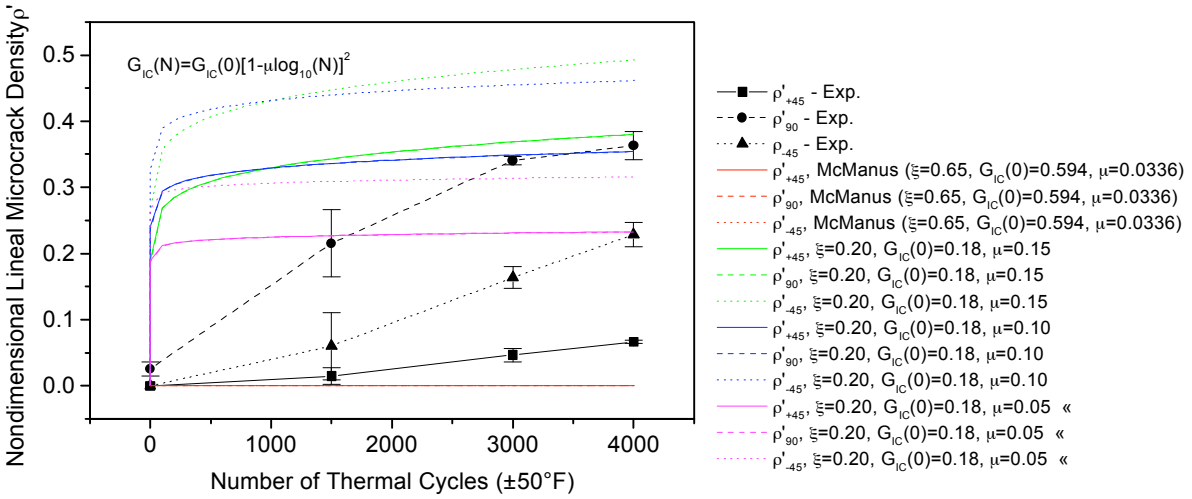

Figure 4.18. Measured and predicted microcrack density in P75/ERL1962.Q2.5.C specimens.

Results are now presented for the P75/ERL1962.X.1.G and P75/ERL1962.Q2.1.G specimens. Recall these specimens have a 0.001 in. nominal layer thickness compared to the 0.005 in. nominal layer thickness in specimens presented to this point. In addition, recall that it was impossible to experimentally record microcrack densities in all but the c90 layers of the thin-layer cross-ply specimens. The lack of experimental microcrack densities prevents a thorough trial and error procedure of establishing the three microcracking parameters. Nonetheless, an attempt has been made and the results are presented here.

The room temperature lamina properties for the P75/ERL1962.X.1.G specimens are shown in Table 4.9. The initial values of the microcracking parameters are chosen to be the same as those previously derived for the P75/ERL1962.X.5.G material, i.e., ξ=0.20, $G_{IC}(0)$=0.25 in-lb/in^2, and μ=0.15. As shown in Figure 4.19, poor correlation is observed between measured and predicted values for this set of parameters. Also included in the figure are the measured and predicted results for the c90 layer of the P75/ERL1962.X.5.G specimens from Figure 4.14. These results have been included to show that, although for this set of parameters the correlation for the 0.001 in. specimens is poor, the analysis *does* predict the correct trend due to the change in layer thickness. Namely, the thinner layers result in a lower nondimensional microcrack density. To improve correlation for the thin-layer specimens, the parameters were adjusted

accordingly. The results of the various iterations are shown in the figure. It was necessary to increase the value of ξ and $G_{IC}(0)$ to obtain reasonable agreement with measured behavior, in particular the characteristic delay in the onset of microcracking. Not having measured values for the o90 layer does not allow for a check of the ratio between microcrack densities in the two layers, as was done previously when establishing a value for ξ. As will be shown later for the P75/RS3 material system, however, a value of ξ=0.65 is reasonable.

Table 4.9 Room Temperature Lamina Properties for P75/ERL1962.X.1.G Specimens

E_1 (Msi)	E_2 (Msi)	G_{12} (Msi)	ν_{12}	α_1 (με/°F)	α_2 (με/°F)
36.2	.940	.700	.299	-.520	19.9

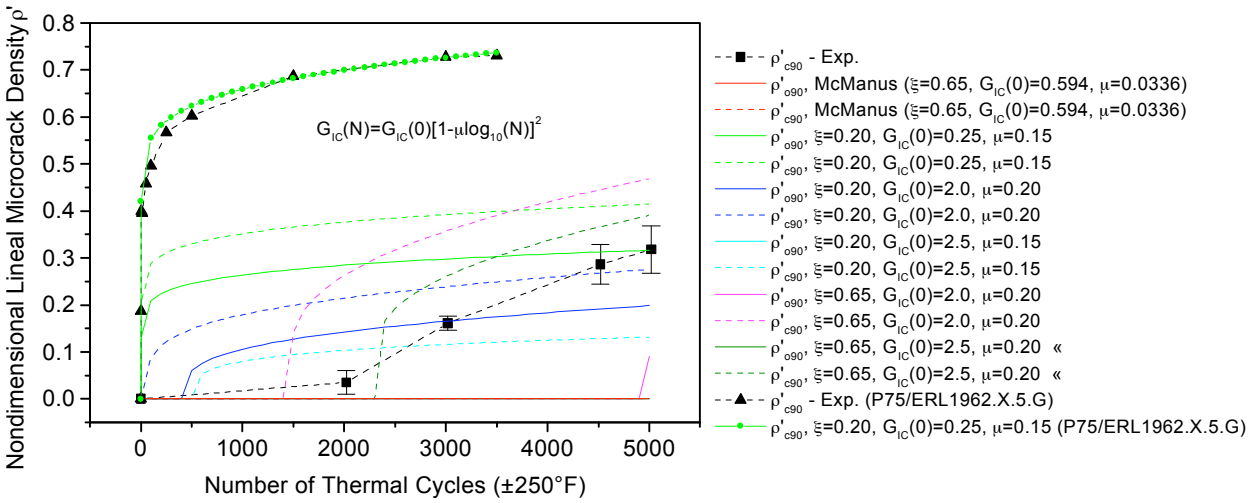

Figure 4.19. Measured and predicted microcrack density in P75/ERL1962.X.1.G specimens.

By adjusting the microcracking parameters accordingly, the characteristic delayed onset of microcracking and the eventual microcracking rate can be reasonably well predicted in the c90 layer. It is also noted that for the final prediction in Figure 4.19, i.e., ξ=0.65, $G_{IC}(0)$=2.5 in-lb/in^2, and μ=0.20, microcracking in the o90 layer is predicted not to occur for up to 5000 cycles. This is contrary to observed behavior. Although microcrack densities could not be experimentally recorded for the o90 layer, microcracks were observed in these layers prior to 5000 cycles. Note also that the predictions based on the parameter values presented by McManus et al. [2] indicate no microcracking in either layer prior to 5000 cycles.

The microcracking parameters derived for the P75/ERL1962.X.1.G specimens are now applied to the P75/ERL1962.Q2.1.G specimens. Recall that microcrack densities were not recorded experimentally for any of these specimens. The room temperature lamina properties for

these quasi-isotropic specimens are shown in Table 4.9 and the predicted microcrack densities in Figure 4.20. Note that microcracking is predicted in only the double-thickness –45° layer. The predictions based on the parameter values presented by McManus et al. [2] again indicate no microcracking in any of the layers prior to 5000 cycles.

Table 4.10 Room Temperature Lamina Properties for P75/ERL1962.Q2.1.G Specimens

E_1 (Msi)	E_2 (Msi)	G_{12} (Msi)	ν_{12}	α_1 (με/°F)	α_2 (με/°F)
37.6	.958	.700	.299	-.537	19.2

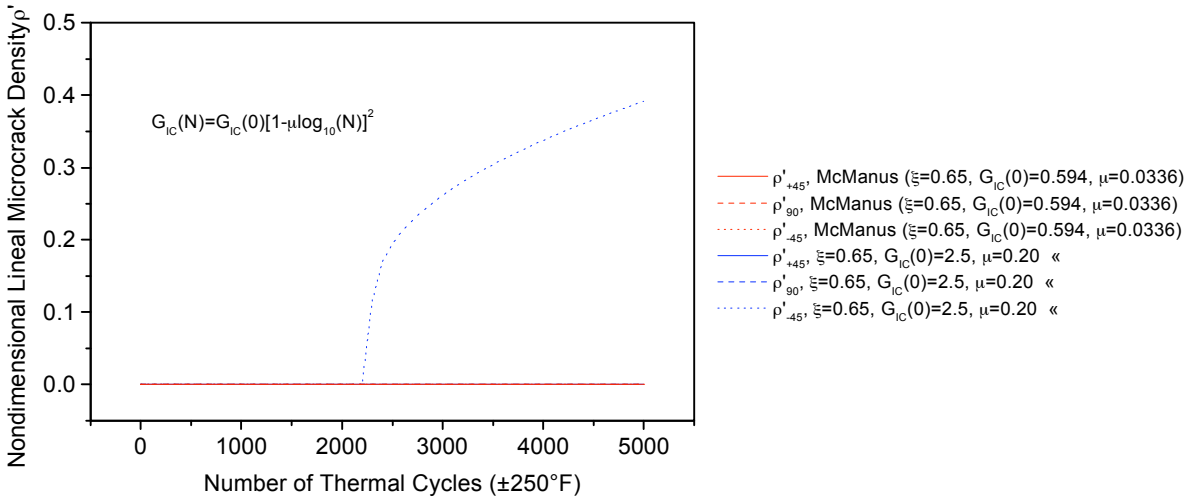

Figure 4.20. Predicted microcrack density for P75/ERL1962.Q2.1.G.specimens.

Laminate CTE

Room temperature laminate CTE as a function of the number of thermal cycles are presented in Figure 4.21 for all of the P75/ERL1962 materials considered in this section. In general, good agreement is observed between measured and predicted values. Note that measured values are only presented for the uncycled and post-cycled condition. Based on the observed buildup of microcracks in all of the specimens, the manner in which the predicted CTE changes appears reasonable. In all cases, the analysis overpredicts the change in CTE. From a dimensional stability viewpoint, this is slightly conservative.

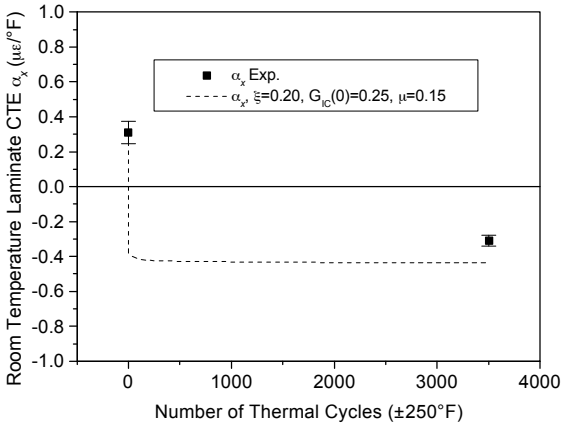

(a) P75/ERL1962.X.5.G

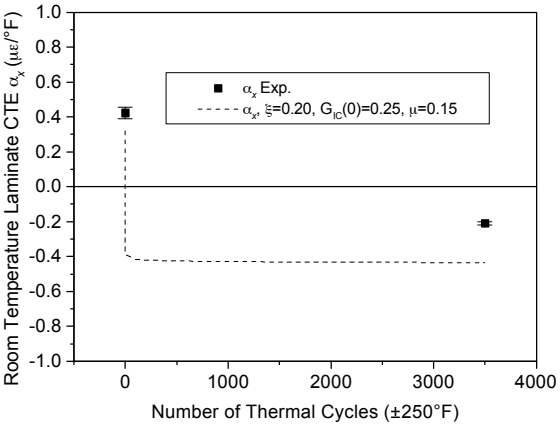

(b) P75/ERL1962.Q1.5.G

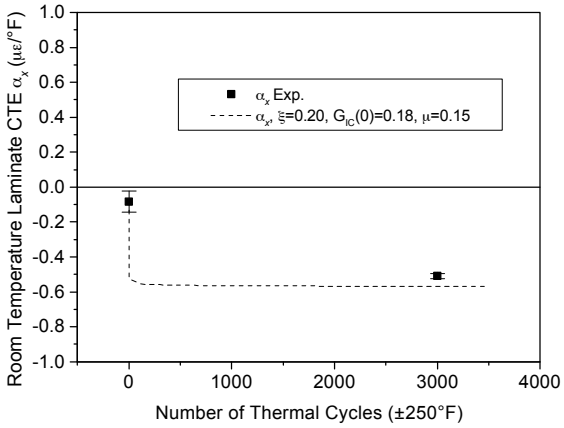

(c) P75/ERL1962.Q2.5.G

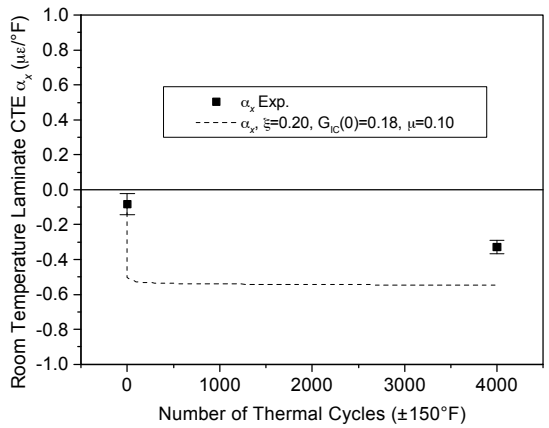

(d) P75/ERL1962.Q2.5.L

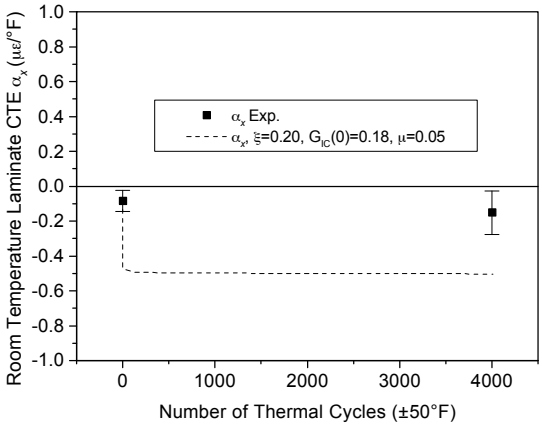

(e) P75/ERL1962.Q2.5.C

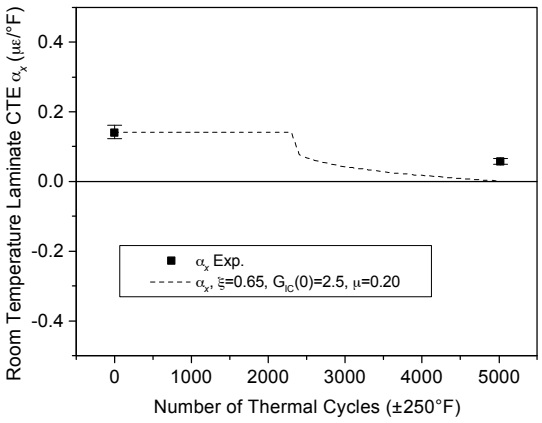

(f) P75/ERL1962.X.1.G

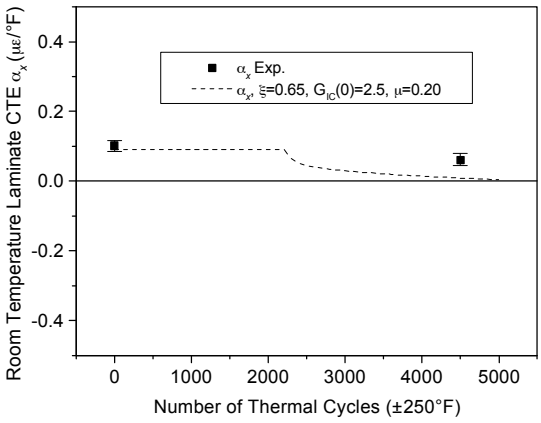

(g) P75/ERL1962.Q2.1.G

Figure 4.21. Measured and predicted room temperature laminate CTE in P75/ERL1962 specimens.

4.3.4 P120/ERL1962 Material System

Microcrack Density

The room temperature lamina properties for the P120/ERL1962.X.5.G specimens are shown in Table 4.11. The measured and predicted microcrack densities are shown in Figure 4.22. The prediction using the microcracking parameters presented by McManus et al. [2] are shown along with a prediction using their $G_{IC}(0)$ and μ but a modified ξ which is more representative of values derived in this section. In order to obtain good agreement between measured and predicted values, the microcracking parameters were modified to ξ=0.25, $G_{IC}(0)$=0.09 in-lb/in^2, and μ=0.10.

Table 4.11 Room Temperature Lamina Properties for P120/ERL1962.X.5.G Specimens

E_1 (Msi)	E_2 (Msi)	G_{12} (Msi)	ν_{12}	α_1 (με/°F)	α_2 (με/°F)
57.6	.880	.700	.308	-.673	15.6

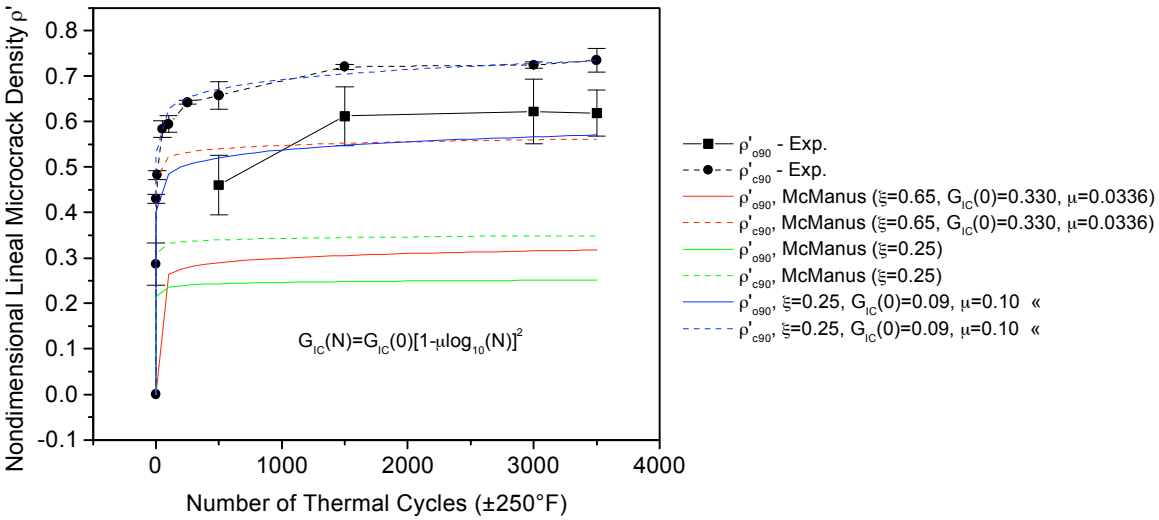

Figure 4.22. Measured and predicted microcrack density in P120/ERL1962.X.5.G specimens.

Predicted microcrack densities for the P120/ERL1962.Q1.5.G specimens are calculated using the same microcracking parameters from the cross-ply specimens, i.e., ξ=0.25, $G_{IC}(0)$=0.09 in-lb/in^2, and μ=0.10, and the room temperature lamina properties in Table 4.12. The measured and predicted values are shown in Figure 4.23. Good agreement between measured and predicted values is seen in the 90° layer. The predictions for the +45° and –45° layers are somewhat high, but still good.

Table 4.12 Room Temperature Lamina Properties for P120/ERL1962.Q1.5.G Specimens

E_1 (Msi)	E_2 (Msi)	G_{12} (Msi)	ν_{12}	α_1 (με/°F)	α_2 (με/°F)
55.3	.865	.700	.308	-.663	16.1

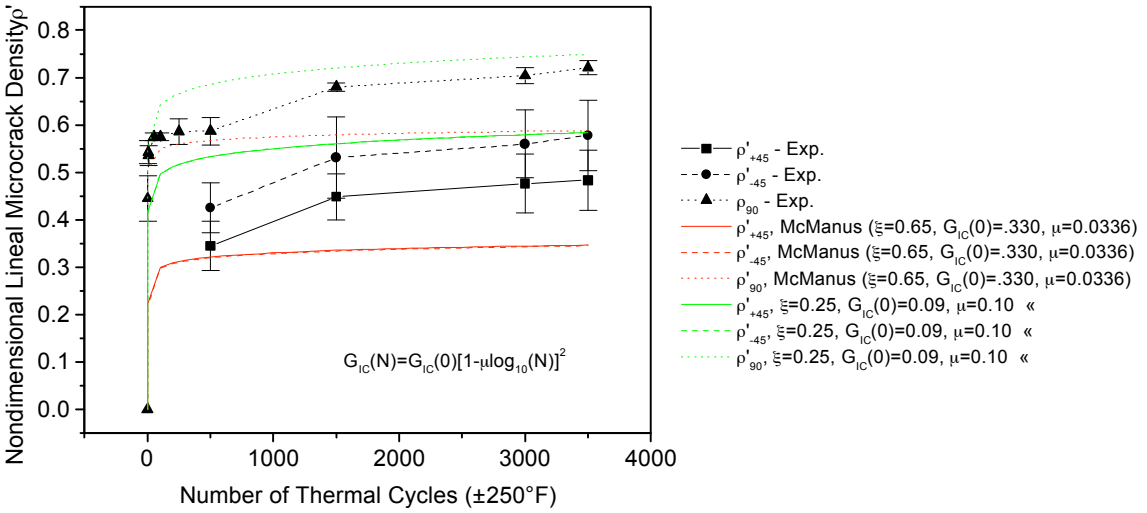

Figure 4.23. Measured and predicted microcrack density in P120/ERL1962.Q1.5.G specimens.

Laminate CTE

The measured and predicted room temperature laminate CTE's are shown in Figure 4.24 for the P120/ERL1962.*.5.G specimens. Note that the prediction for the uncycled CTE deviates slightly from the measured value due to the slight error in the derived lamina material properties. Taking this into consideration, the predicted change in CTE closely matches that measured experimentally.

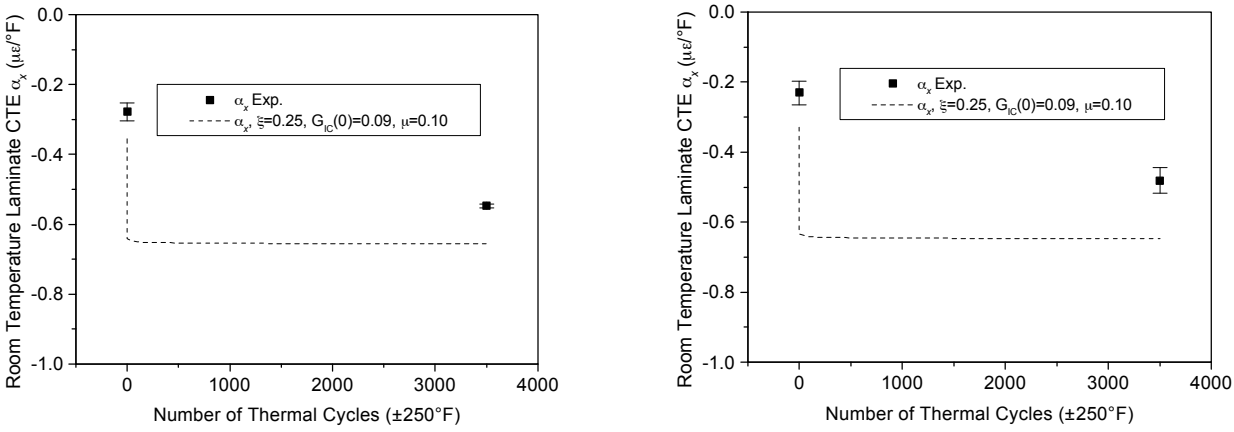

(a) P120/ERL1962.X.5.G (b) P120/ERL1962.Q1.5.G

Figure 4.24. Measured and predicted room temperature laminate CTE in P120/ERL1962.X.5.G and P120/ERL1962.Q1.5.G.specimens.

4.3.5 P75/RS3 Material System

This section contains comparisons of measured and predicted results for the P75/RS3.Q2.5.* and P75/RS3.Q2.2.* specimens. These specimens undergo cycling at three different temperature ranges: G, L, and C.

Microcrack Density

The room temperature lamina properties for the P75/RS3.Q2.5.* specimens are shown in Table 4.13.

Table 4.13 Room Temperature Lamina Properties for P75/RS3.Q2.5.* Specimens

E_1 (Msi)	E_2 (Msi)	G_{12} (Msi)	ν_{12}	α_1 (με/°F)	α_2 (με/°F)
41.7	.958	.700	.275	-.651	16.0

Thermal Cycling Range G (±250°F). As a first attempt, the microcracking parameters used for the P75/ERL1962.X.5.G and P75/ERL1962.Q1.5.G specimens in Section 4.3.3, i.e., ξ=0.20, $G_{IC}(0)$=0.25, and μ=0.15, were applied to the P75/RS3 specimens and the predictions are shown in Figure 4.25. These predictions approach a saturation value too quickly, indicating a need to increase μ. In order to obtain good agreement between measured and predicted values, all three parameters were modified, with the final result also shown in Figure 4.25. Note that the combined effect of increasing the shear lag parameter to 0.60 and increasing the baseline $G_{IC}(0)$ to 1.7 in-lb/in^2 predicts a delay in the onset of microcracking in the single-thickness +45° and 90° layers.

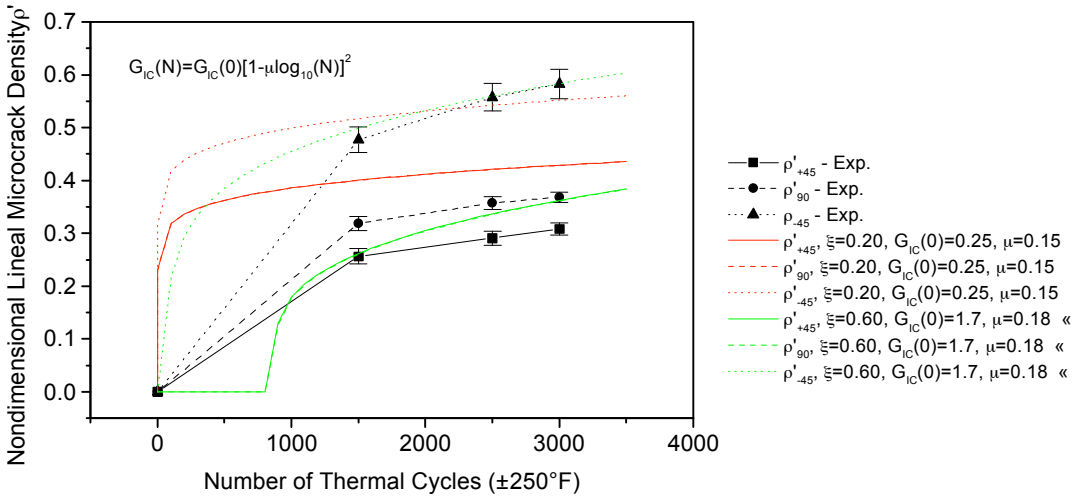

Figure 4.25. Measured and predicted microcrack density in P75/RS3.Q2.5.G specimens.

Thermal Cycling Range L (±150°F) and C (±50°F). Investigating the L temperature range using the values for the three parameters from the G temperature range, i.e., ξ=0.60, $G_{IC}(0)$=1.7, and μ=0.18, predicts significant cracking in all three layers, as indicated in Figure 4.26. However, very little microcracking is observed experimentally. By reducing the value of the rate parameter, μ, to 0.10, no microcracking is predicted. Similar results are observed for the specimens cycled at the C temperature range.

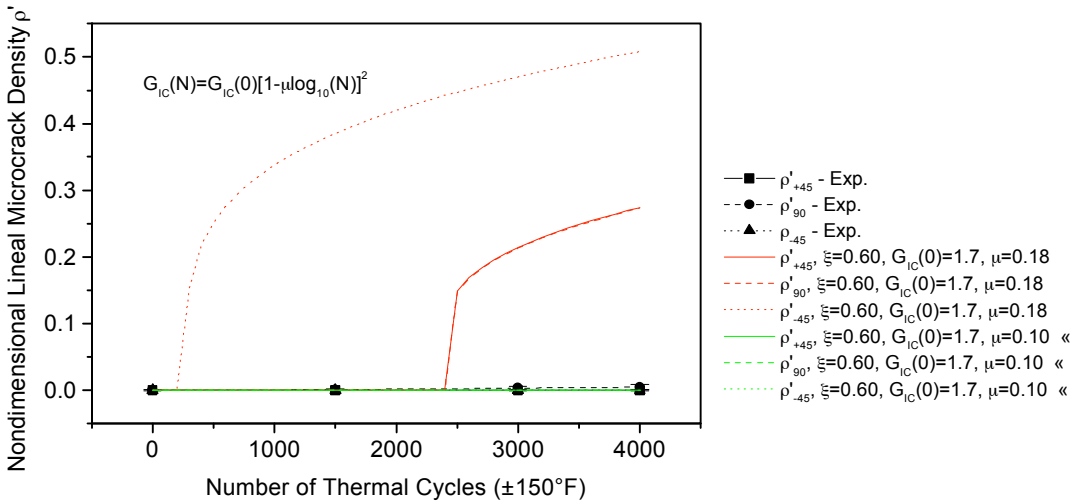

Figure 4.26. Measured and predicted microcrack density in P75/RS3.Q2.5.L specimens.

Measured and predicted results for the P75/RS3.Q2.2.* specimens are now presented. These specimens also underwent cycling at three different temperature ranges: G, L, and C, but have a nominal layer thickness of 0.002 in. rather than 0.005 in., as was the case for the specimens just discussed. The room temperature lamina properties for these specimens are shown in Table 4.14.

Table 4.14 Room Temperature Lamina Properties for P75/RS3.Q2.2.* Specimens

E_1 (Msi)	E_2 (Msi)	G_{12} (Msi)	ν_{12}	α_1 (με/°F)	α_2 (με/°F)
29.6	.854	.700	.347	-.509	21.2

Thermal Cycling Range G (±250°F). Using the same three microcracking parameters derived for the P75/RS3.Q2.5.G specimens, i.e., ξ=0.60, $G_{IC}(0)$=1.7, and μ=0.18, the predictions for the P75/RS3.Q2.2.G specimens were calculated. These predictions are shown in Figure 4.27,

along with the experimentally measured values. Interestingly, the predictions for the single thickness +45° and 90° layers closely match the average of the measured values, particularly at the high cycle numbers, whereas the prediction for the double thickness –45° layer does not agree well with measured values. This is due to the slow increase in microcrack density for this thin-layer specimen. As noted previously, the Crackomatic predictions agree well with specimens cracking rapidly in the early stages of cycling, but tend to deviate considerably from experimentally measured behavior in specimens with slow initial cracking rates.

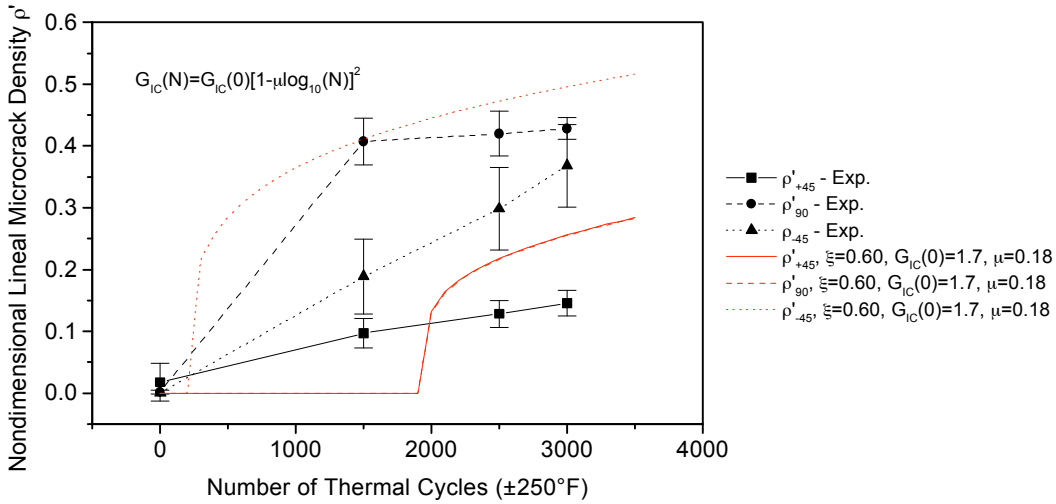

Figure 4.27. Measured and predicted microcrack density in P75/RS3.Q2.2.G specimens.

Thermal Cycling Range L (±150°F). As seen previously, the microcracking rate parameter, μ, must be reduced relative to the value used for the specimens cycled at the G temperature range in order to improve the agreement between measured and predicted values for the P75/RS3.Q2.5.L specimens. The effect of reducing μ is seen in Figure 4.28. It is unclear just how much μ needs to be reduced because the analysis predicts that the double-thickness –45° layer is the only layer with a non-zero microcrack density after 4000 cycles are completed. Experimental measurements are contrary to this and instead indicate that only the 90° layer has cracks. Considering the values presented, ξ=0.60, $G_{IC}(0)$=1.7, and μ=0.12 are considered to be the best choice.

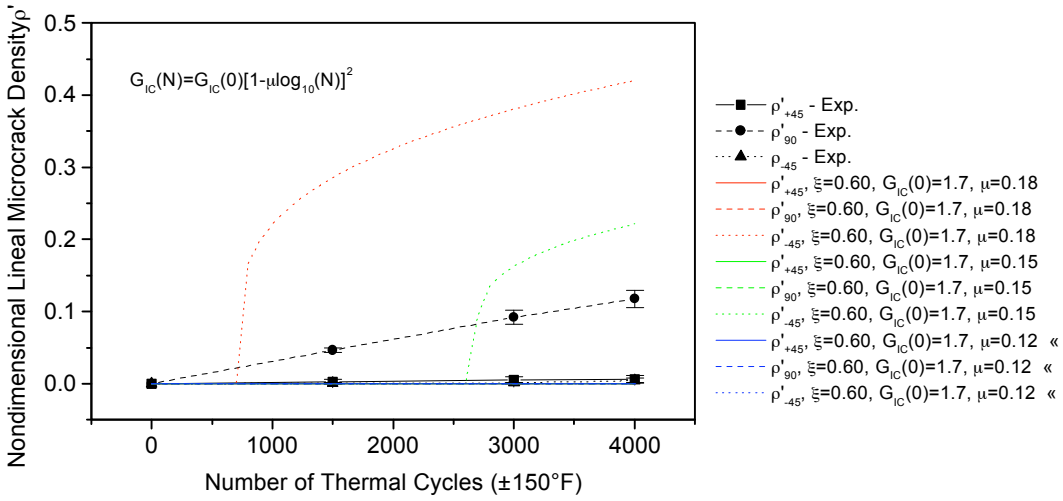

Figure 4.28. Measured and predicted microcrack density in P75/RS3.Q2.2.L specimens.

Thermal Cycling Range C (±50°F). The measured microcrack densities in the P75/RS3.Q2.2.C specimens were negligible and therefore results for these specimens have not been included.

Laminate CTE

Measured and predicted room temperature laminate CTE's for the P75/RS3 specimens are shown in Figure 4.29. The predictions are reasonable compared to the uncycled and post-cycled measured values.

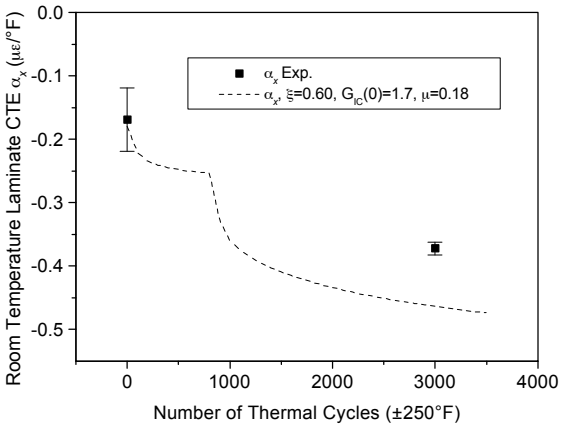

(a) P75/RS3.Q2.5.G

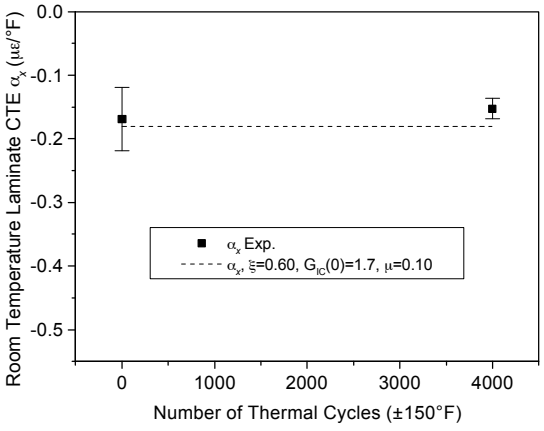

(b) P75/RS3.Q2.5.L

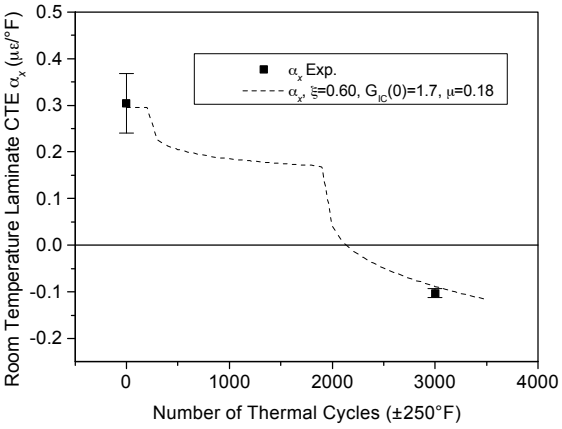

(c) P75/RS3.Q2.2.G

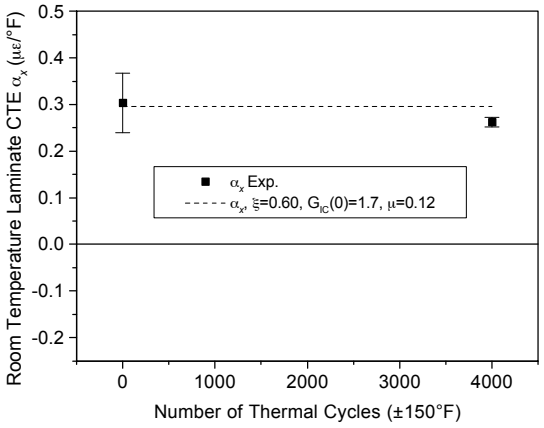

(d) P75/RS3.Q2.2.L

Figure 4.29. Measured and predicted room temperature CTE's for P75/RS3 specimens.

4.3.6 P75/934 Material System

Microcrack Density

Measured and predicted results for the P75/934.Q2.5.G specimens are presented in this section. The room temperature lamina properties for these specimens are shown in Table 4.15.

Table 4.15 Room Temperature Lamina Properties for P75/934.Q2.5.G Specimens

E_1 (Msi)	E_2 (Msi)	G_{12} (Msi)	ν_{12}	α_1 (με/°F)	α_2 (με/°F)
40.5	.869	.700	.300	-.609	21.5

Predictions using the microcracking parameters presented by McManus et al. [2] are shown together with the parameters from the P75/ERL1962.Q1.5.G from Section 4.3.3. The $G_{IC}(0)$ value was reduced to 0.18 in-lb/in^2 to improve agreement between measured and predicted values. Coincidentally, this is the same set of parameters derived for the P75/ERL1962.Q2.5.G specimens.

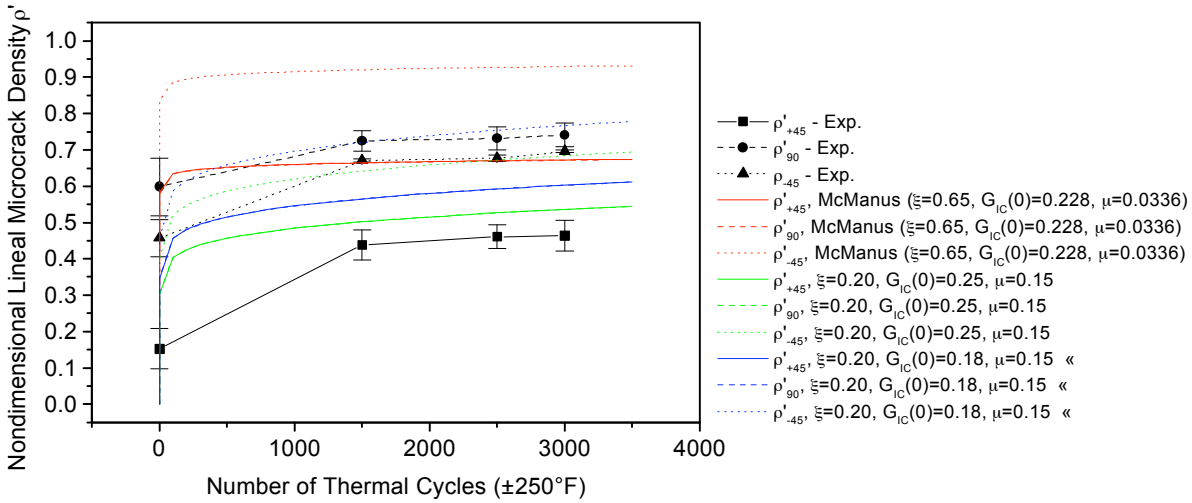

Figure 4.30. Measured and predicted microcrack density in P75/934.Q2.5.G specimens.

Laminate CTE

The measured and predicted room temperature laminate CTE is presented in Figure 4.31 for the P75/934.Q2.5.G specimens. The change in CTE is significantly overpredicted by the analysis, especially when considering that the uncycled values are different. The predicted CTE is, however, in line with expectations based on microcrack densities. Recall from Chapter 3 (see Section 3.4.2) that the measured change in CTE for the P75/934 specimens contradicted the high microcrack densities in those same specimens. It is not surprising, therefore, that the CTE predictions here, being based on parameters adjusted to fit the experimentally measured microcrack densities, substantially overpredict the change in CTE for these specimens.

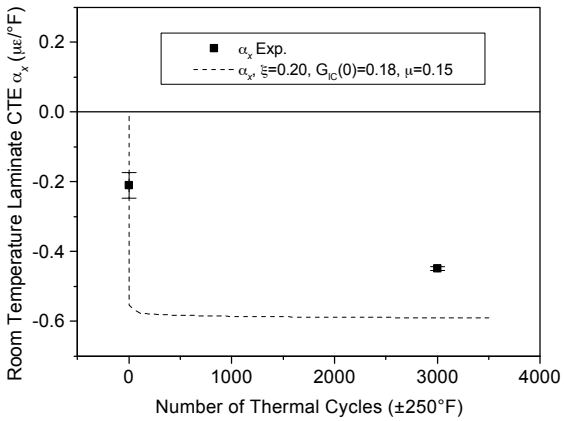

Figure 4.31. Measured and predicted room temperature laminate CTE's for P75/934.Q2.5.G specimens.

4.4 SUMMARY OF CRACKOMATIC PARAMETERS

A summary of the derived microcracking parameters is included in Table 4.16 for all of the materials considered in this investigation. The definition of $G_{IC}(N)$ is shown again for convenience to be

$$G_{IC}(N) = G_{IC}(0)\left[1 - \mu \log_{10} N\right]^2 . \qquad \text{(4.18, rewritten)}$$

From the analyses presented in this chapter, the shear lag parameter, ξ, has been observed to control the interaction of microcrack formation in the multiple cracking layers in the specimen. As stated earlier, a higher value for ξ results in higher ratios of microcrack density in one cracking layer of the specimen compared to another. In the case of the cross-ply specimens, it was the ratio of microcrack density in the c90 layer to the o90 layer. The shear lag factor can also control the onset of cracking in a particular material. Generally, the higher values for ξ result in a delay in the onset of microcracking. This is particularly important for the thinner specimens that were tested in this investigation that demonstrate significant delays in the microcrack initiation.

The combination of the uncycled critical strain energy release rate, $G_{IC}(0)$, and the rate parameter, μ, are seen to affect the microcrack saturation values experienced after large numbers of thermal cycles. The baseline value, $G_{IC}(0)$, also has an effect on the onset of microcracking, particularly when combined with the effect of ξ. The rate parameter is particularly important to the thermal cycling temperature range effects. Based on the measured microcrack data available for comparison, it is apparent that $G_{IC}(N)$ is predicted to be a function of the thermal cycling temperature range imposed on the material.

Table 4.16 Summary of Crackomatic Parameters

Material Designation	Series	ξ	$G_{IC}(0)$	μ
T50/ERL1962.X.5.G	J	0.25	2.0	0.20
T50/ERL1962.Q1.5.G	K	0.25	2.0	0.20
P55/ERL1962.X.5.G	O	0.25	0.75	0.20
P55/ERL1962.Q1.5.G	P	0.25	0.75	0.20
P75/ERL1962.X.5.G	H	0.20	0.25	0.15
P75/ERL1962.Q1.5.G	I	0.20	0.25	0.15
P75/ERL1962.Q2.5.G	6762	0.20	0.18	0.15
P75/ERL1962.Q2.5.L	6762	0.20	0.18	0.10
P75/ERL1962.Q2.5.C	6762	0.20	0.18	0.05
P75/ERL1962.X.1.G	UT8X	0.65	2.5	0.20
P75/ERL1962.Q2.1.G	UTQ	0.65	2.5	0.20
P120/ERL1962.X.5.G	Q	0.25	0.09	0.10
P120/ERL1962.Q1.5.G	R	0.25	0.09	0.10
P75/RS3.Q2.5.G	75RS3	0.60	1.7	0.18
P75/RS3.Q2.5.L	75RS3	0.60	1.7	0.10
P75/RS3.Q2.2.G	275RS3	0.60	1.7	0.18
P75/934.Q2.5.G	P734Q	0.20	0.18	0.15

Note that, in general, the value of the shear lag parameters in Table 4.16 are significantly lower than those previously proposed by McManus et al. [2] The $G_{IC}(0)$ parameters have not been derived from mechanical strength data as done previously, but were instead adjusted to fit experimental data. For comparison, the $G_{IC}(0)$ values calculated by McManus et al. [2] using Equation 4.15 are presented in Table 4.17 along with the current values empirically derived in this study. The strength data used by McManus et al. [2] to calculate $G_{IC}(0)$ are listed in the table as well.

Table 4.17 Comparison of $G_{IC}(0)$ Values from Previous and Current Analyses

	Avg±S.D.	$G_{IC}(0)$ (in-lb/in^2)	
Material	Strength (Ksi)	McManus et al.[2]	Current
T50/ERL1962	4.36±.858	.754±.029	2.00
P55/ERL1962	3.25±.347	.417±.005	0.75
P75/ERL1962	3.88±.527	.594±.011	0.25
P120/ERL1962	2.89±.014	.330±.000	0.09
P75/RS3	4.16±.494	.687±.010	1.70
P75/934	2.55±.273	.228±.003	0.18

The $G_{IC}(0)$ values from Table 4.17 are presented in Figure 4.32 as a function of transverse tensile strength. Note that although the $G_{IC}(0)$ values presented by McManus et al. [2] result in microcrack density predictions that do not agree well with experimentally measured values, the general trend as a function of transverse tensile strength is correct.

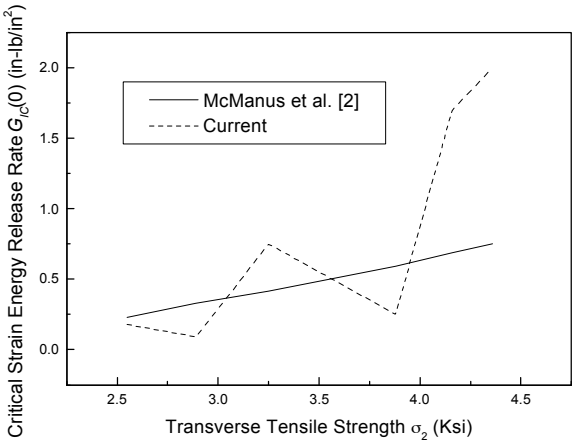

Figure 4.32. Previous [2] and Current $G_{IC}(0)$ values as a function of transverse tensile strength.

The results presented in this chapter help to show the strengths and weaknesses in the Crackomatic analysis developed in references [2, 3, 4]. Overall, the analysis shows reasonable correlation with experimental data, provided the correct microcracking parameters (ξ, $G_{IC}(0)$, and μ) are known for the material. The method of calculating the various microcracking parameters is necessarily empirical in nature, although a range of appropriate values has been established in this

chapter. The following chapter will summarize all of the important conclusions made in this investigation, including various analytical findings presented here.

5. CONCLUSIONS AND RECOMMENDATIONS

This chapter contains summaries and conclusions from the experimental and analytical results obtained in this investigation. The summaries and conclusions are arranged by the material or geometric parameter of interest and are listed in bulleted form for convenience. A separate section is included that summarizes key findings specific to the analysis. Also included is a section examining the implications of these conclusions as they apply to similar graphite-epoxy and graphite-polycyanate material systems. The chapter concludes with a list of recommendations for further study in this research area.

5.1 LAYER THICKNESS

The following conclusions regarding layer thickness are based on results from the ±250°F thermal cycling temperature range. These trends apply to both cross-ply and quasi-isotropic specimens.

• Layer thickness has a significant effect on the onset of microcracking and the microcrack density at a given number of cycles. Relatively thick-layer specimens, i.e., 0.005 in. layer thickness, tend to crack rapidly in the first 500 cycles and reach an asymptotic microcrack density by several thousand cycles. Thin-layer specimens, i.e., 0.002 in. layer thickness or less, tend to have a delayed onset of microcracking and do not reach asymptotic microcrack densities prior to several thousand cycles.

• After thousands of thermal cycles, dimensional microcrack densities in thin-layer specimens typically exceed those in their thick-layer counterpart specimens. For some of the specimens in this investigation, the microcrack densities in thin-layer specimens (0.001 in.) have exceeded those in thick-layer specimens (0.005 in.) by a factor of 2.4.

• Despite the higher dimensional microcrack densities in thin-layer specimens, the laminate CTE is affected little compared to that of the thick-layer specimens. From the viewpoint of dimensional stability, this motivates the introduction of a nondimensional microcrack density as a better measure of composite ‘damage’.

• Change in laminate stiffness as a result of thermally-induced microcracking is unaffected by layer thickness.

5.2 FIBER TYPE

The following conclusions regarding fiber type are based on results from the ±250°F thermal cycling temperature range. These trends apply to both cross-ply and quasi-isotropic specimens.

5.2.1 PAN-based versus Pitch-based Fibers

• For specimens differing only in fiber type, microcrack densities in all T50 PAN-based fiber specimens are lower than those in P55 pitch-based fiber specimens for up to 3500 thermal cycles. It is not known whether this trend will continue to a higher number of thermal cycles. Analysis indicates that this trend may in fact be a result of the slightly more negative axial CTE of the pitch-based fiber compared to the PAN-based fiber. The smaller fiber diameter of the PAN-based fibers is another possible explanation.

• T50 PAN-based fiber specimens exhibit smaller changes in CTE compared to the P55 pitch-based fiber specimens with similar modulus. The PAN-based fiber appears to exhibit better dimensional stability.

• Change in laminate stiffness as a result of thermally-induced microcracking is unaffected by the presence of PAN-based versus pitch-based fibers.

5.2.2 Fiber Modulus/Fiber CTE

• Initial microcracking rates are observed to be higher in specimens with higher modulus (more negative CTE) fibers. These same specimens with higher modulus fibers tend to approach an asymptotic saturation density more rapidly when compared to specimens with lower modulus (less negative CTE) fibers. After several thousand thermal cycles, microcrack densities are virtually identical, regardless of fiber modulus and CTE.

• Change in laminate CTE as a result of thermal cycling is observed to be greatest in specimens with lower modulus (less negative CTE) fibers. The specimens with high modulus (more negative CTE) fibers are therefore considered to be more dimensionally stable. It should, however, be noted that the overall laminate CTE of these specimens is significantly more negative than that of the specimens with lower modulus (less negative CTE) fibers.

• The effect of fiber stiffness and fiber CTE has no effect on the change in laminate stiffness as a result of thermal cycling.

5.3 MATRIX TYPE

The following conclusions regarding matrix type, i.e., epoxy, toughened epoxy, and cyanate ester, are based on results from the ±250°F thermal cycling temperature range.

• Data for up to 3000 thermal cycles shows that the cyanate ester develops the least number of microcracks due to thermal cycling and the epoxy develops the most. Extrapolations to higher numbers of thermal cycles indicates that the margin of difference may, in fact, diminish with additional thermal cycling.

•Matrix type affects the cycle count at which the onset of microcracking occurs. The RS3 cyanate ester resin tends to have the greatest delay in the onset of microcracking of the three resin systems considered.

• Specimens containing the RS3 cyanate ester resin system exhibit the least change in CTE of the three resin systems considered. The change in CTE is, however, only slightly less than that shown by specimens containing the 934 epoxy system. Surprisingly, the change in CTE of specimens containing the ERL1962 toughened epoxy exhibit changes in CTE almost twice that of the other two materials, despite the lower microcrack densities compared to specimens containing the 934 epoxy system.

• The glass transition temperature of the three resin systems considered is unaffected by the thermal cycling.

5.4 THERMAL CYCLING TEMPERATURE RANGE

• For up to 3000 thermal cycles, thermal cycling temperature range does affect the onset and development of microcracks in the specimens in this investigation. Extrapolations to higher cycle numbers indicate that for specimens containing the ERL1962 toughened epoxy, microcrack saturation may occur such that regardless of temperature range, all specimens will eventually have the same number of microcracks after a sufficiently large number of thermal cycles.

• For the P75/RS3 specimens, there does appear to exist a threshold cycling temperature such that if the specimens are never exposed to more severe temperature extremes, microcracking is not expected to occur. For the specimens with 0.005 in. nominal layer thickness, this threshold temperature range is observed to be ±150°F. For the specimens with 0.002 in. nominal layer thickness, this threshold temperature range is observed to be ±50°F. This conclusion is based on both microcracking and CTE data for up to 4000 thermal cycles.

• The change in laminate stiffness does not appear to be dependent on thermal cycling temperature range.

• The glass transition temperature of the materials considered is unaffected by the thermal cycling temperature range.

5.5 COMPARISONS BETWEEN ANALYSIS AND EXPERIMENT

The following general comments and conclusions can be made about the Crackomatic analysis.

• The analysis is a simplified one-dimensional analysis using a shear lag stress formulation and an energy-based cracking criterion.

• The analysis requires either $G_{IC}(N)$ or transverse failure strength as a function of the number of cycles in order to predict microcrack accumulation.

• The analysis is sensitive to variations in E_2, α_2, $G_{IC}(N)$, and ξ.

• The analysis is somewhat sensitive to variations in E_1 and α_1.

• The analysis is insensitive to variations in G_{12} and ν_{12}.

• In general, the analysis overpredicts the change in laminate CTE as a result of microcracking.

• The analysis predicts reasonably well the change in laminate stiffness as a result of microcracking.

• Microcrack predictions have been shown to match measured microcrack densities for a variety of materials and laminates by adjusting three microcracking parameters: ξ, $G_{IC}(0)$, and μ. For the materials in this investigation, the values for ξ ranged from 0.10 to 0.25 with some exceptions for the RS3 material system which required values of 0.60. It is also true that decreases in layer thickness required a higher value of the ξ. Values for $G_{IC}(0)$ ranged from 0.18 to 2.0 in-lb/in2. Values for μ ranged from 0.05 to 0.20.

• Some degree of success was observed in predicting results in quasi-isotropic laminates based on microcracking parameters derived for cross-ply laminates of the same material.

• The effect of thermal cycling temperature range was modeled by adjusting μ. It is proposed that $G_{IC}(N)$ is indeed affected differently by the different thermal cycling temperature ranges.

The following items are considered as specific strengths and weaknesses of the model.

Strengths:

• From the viewpoint of dimensional stability, the analysis tends to be slightly conservative in its predictions of the change in laminate CTE.

• The analysis predicts qualitatively the layer thickness effects.

Weaknesses:

• The material data required to predict microcrack accumulation is not readily available for the materials of interest.

• All thermal cycling temperature range effects are not well predicted by the analysis.

5.6 IMPLICATIONS TO OTHER MATERIAL SYSTEMS AND DESIGNS

The conclusions stated above are based on specific graphite-epoxy and graphite-polycyanate materials. There are, however, general findings that can be applied to other materials and also offer guidance for design. Unlike mechanically-induced microcracking, which is governed primarily by the stiffness of the individual layers of the composite, and hence the stiffness of the fibers, thermally-induced microcracking is governed by stiffness of the fibers as well as the thermal expansion of the fibers and matrix. As the composite accumulates more and more microcracks as a result of thermal cycling, the fibers continue to dominate the overall behavior of the composite. The stiffness of the composite is virtually unaffected by microcracking, and the CTE tends to become more negative, reflecting increasing control by the fibers. A contradiction to this statement occurs for the thin-layer composites which are virtually unaffected by microcracking.

For design purposes, the combination of thin layers with high modulus fibers is desirable, if a negative CTE can be tolerated. Using the cyanate ester resin system is even better. On the other hand, if a change in CTE can be tolerated, thicker layer materials with very high modulus fibers will microcrack rapidly with cycling and then saturate, resulting in little additional change in CTE. Having the change in CTE occur quickly but then stabilize may be an advantage. If moderate modulus fibers are required, saturation will occur in the thicker layer materials, but will do so more slowly.

5.7 RECOMMENDATIONS FOR FUTURE WORK

The following recommendations are based on results from the current study and some questions that still remain after its completion.

• To aid in the calculation of logarithmic microcracking rates, in future experimental efforts, it would be worthwhile to record experimental microcrack densities at decade intervals.

• Additional thermal cycling of specimens to evaluate even longer-term behavior would be valuable. This is particularly important for specimens containing the cyanate ester resin systems that appear to exhibit threshold cycling temperature ranges, and the thin-layer specimens that develop microcracks in latter stages of thermal cycling.

• An experimental determination of critical strain energy release rates as a function of the number of thermal cycles for representative materials would be valuable. This would aid the analytical predictions presented in Chapter 4.

REFERENCES

1. Bowles, D. E., “The Effects of Microcracking on the Thermal Expansion of Graphite-Epoxy Composites,” Presented at the Third Annual Technical Review of Large Space Systems Technology - 1981, NASA Langley Research Center, Hampton, VA, November 16-19, 1981, pp. 67-79.

2. McManus, H. L., Bowles, D. E., and Tompkins, S. S., "Prediction of Thermal Cycling Induced Matrix Cracking," Proceedings of the 8th Technical Conference on Composite Materials, American Society for Composites, Cleveland, OH, October 19-21, 1993, pp. 1120-1129.

3. Park, C. H. S., "Analysis of Thermally Induced Damage in Composite Space Structures," TELAC Report 94-2, Technology Laboratory for Advanced Composites, Department of Aeronautics and Astronautics, Massachusetts Institute of Technology, Cambridge, MA, January, 1994.

4. Maddocks, J. R. and McManus, H. L., “Prediction of Microcracking in Composite Laminates Under Thermomechanical Loading,” Presented at the Tenth International Conference on Composite Materials (ICCM-10), Whistler, British Columbia, Canada, August 1995, vol. 1, pp. 415-422.

5. Knouff, B., Tompkins, S. S., and Jayaraman, N., “The Effect of Graphite Fiber Properties on Microcracking Due to Thermal Cycling of Epoxy-Cyanate Matrix Laminates,” ASTM STP 1230, R. H. Martin, Ed., Presented at the ASTM 5th Symposium on Composite Materials: Fatigue and Fracture, May 4-6, 1993, Atlanta, GA, pp. 268-282.

6. Sykes, G. F., Funk, J. G., and Slemp, W. S., “Assessment of Space Environment Induced Microdamage in Toughened Composite Materials,” Presented at the 18th International SAMPE Technical Conference, Society for the Advancement of Materials and Process Engineering, Seattle, WA, October 7-9, 1986, pp. 520-534.

7. Rawal, S. P., Misra, M. S., and Wendt, R. G., “Composite Materials for Space Applications,” NASA CR 187472, August 1990.

8. Adams, D. S., Bowles, D. E., and Herakovich, C. T., “Thermally Induced Transverse Cracking in Graphite-Epoxy Cross-Ply Laminates,” Journal of Reinforced Plastics and Composites, vol. 5, July 1986, pp. 152-169.

9. Tompkins, S. S., Shen, J. Y., and Lavoie, A. J., “Thermal Cycling of Thin and Thick Ply Composites,” Engineering, Construction, and Operations in SPACE IV, Proceedings of Space ‘94, Aerospace Division/ASCE, Feb. 26-March 3, 1994, Albuquerque, NM, pp. 326-335.

10. Knouff, B., Tompkins, S. S., and Jayaraman, N., “The Effect of Microcracking Due to Thermal Cycling on the Coefficient of Thermal Expansion of Graphite Fiber Reinforced Epoxy-Cyanate Matrix Laminates,” Advanced Materials: Expanding the Horizons, Proceedings of the 25th International SAMPE Technical Conference, Oct. 26-28, 1993, Philadelphia, PA, pp. 610-621.

11. Bowles, D. E. and Shen, J. , “Thermal Cycling Effects on the Dimensional Stability of P75 and P75-T300(Fabric) Hybrid Graphite/Epoxy Laminates,” Proceedings of the 33rd International SAMPE Symposium, March 7-10, 1988, pp. 1659-1671.

12. Highsmith, A. L. and Reifsnider, K. L., "Stiffness-Reduction Mechanisms in Composite Laminates," Damage in Composite Materials, ASTM STP 775, K. L. Reifsnider, Ed., American Society for Testing and Materials, 1982, pp. 103-117.

13. Garrett, K. W. and Bailey, J. E., "Multiple Transverse Fracture in 90° Cross-Ply Laminates of a Glass Fibre-Reinforced Polyester," Journal of Materials Science, vol. 12, 1977, pp. 157-168.

14. Hedgepeth, J. M., NASA TN D-882, Langley Research Center, 1961.

15. Highsmith, A. L. and Reifsnider, K. L., "Stiffness-Reduction Mechanisms in Composite Laminates," Damage in Composite Materials, ASTM STP 775, K. L. Reifsnider, Ed., American Society for Testing and Materials, 1982, pp. 103-117.

16. Reifsnider, K. L., "Some Fundamental Aspects of the Fatigue and Fracture Response of Composite Materials," Proceedings of the 14th Annual Meeting of the Society for Engineering Science, Bethlehem, PA, 1977, pp. 373-383.

17. Flaggs, D. L., and Kural, M. H., "Experimental Determination of the In-Situ Transverse Lamina Strength in Graphite/Epoxy Laminates," Journal of Composite Materials, vol. 16, March 1982, pp. 103-116.

18. Laws, N. and Dvorak, G. J., "Progressive Transverse Cracking in Composite Laminates," Journal of Composite Materials, vol. 22, October, 1988, pp. 900-916.

19. Flaggs, D. L., "Prediction of Tensile Matrix Failure in Composite Laminates," Journal of Composite Materials, vol. 19, January, 1985, pp. 29-50.

20. Lim, S. G. and Hong, C. S., "Prediction of Transverse Cracking and Stiffness Reduction in Cross-Ply Laminated Composites," Journal of Composite Materials, vol. 23, July, 1989, pp. 695-713.

21. Fukunaga, H., Chou, T. W., Peters, P. W. M., and Schulte, K., "Probabilistic Failure Strength Analyses of Graphite/Epoxy Cross-Ply Laminates," Journal of Composite Materials, vol. 18, no. 4, 1984, pp. 339-356.

22. Lee, J. -W. and Daniel, I. M., "Progressive Transverse Cracking of Crossply Composite Laminates," Journal of Composite Materials, vol. 24, November, 1990, pp. 1225-1243.

23. Tsai, C. -L., Daniel, I. M., and Lee, J. -W., "Progressive Matrix Cracking of Crossply Composite Laminates Under Biaxial Loading," ASME AMD, vol. 111, Presented in Dallas, TX, Nov. 25-30, 1990, pp. 9-18.

24. Thomas, D. J. and Wetherhold, R. C., "Progressive Matrix Cracking in Off-Axis Plies of a General Symmetric Laminate," Proceedings of the 34th Annual Structures, Structural Dynamics, and Materials Conference, La Jolla, CA, April 19-22, 1993, pp. 1613-1623.

25. Nairn, J. A., "The Strain Energy Release Rate of Composite Microcracking: A Variational Approach," Journal of Composite Materials, vol. 23, Nov., 1989, pp. 1106-1129.

26. Hashin, Z., "Analysis of cracked laminates: A variational approach," Mechanics of Materials, vol. 4, 1985, pp. 121-136.

27. Varna, J. and Berglund, L. A., "A Model for Prediction of the Transverse Cracking Strain in Cross-Ply Composites," Journal of Reinforced Plastics and Composites, vol. 11, July, 1992, pp. 708-728.

28. Sriram, P. and Armanios, E. A., "A Shear Deformation Model for Transverse Cracking in Composite Laminates," International Journal of Damage Mechanics, vol. 2, January, 1993, pp. 73-91.

29. Nuismer, R. J. and Tan, S. C., "Constitutive Relations of a Cracked Composite Lamina," Journal of Composite Materials, vol. 22, 1988, pp. 115-122.

30. Tan, S. C. and Nuismer, R. J., "A Theory for Progressive Matrix Cracking in Composite Laminates," Journal of Composite Materials, vol. 23, October, 1989, pp. 1029-1047.

31. Allen, D. H. and Lee, J-. W., "Matrix Cracking in Laminated Composites Under Monotonic and Cyclic Loadings," ASME AMD, vol. 111, American Society of Mechanical Engineers, Dallas, TX, Nov. 25-30, 1990, pp. 65-75.

32. Hashin, Z., "Failure Criteria for Unidirectional Fiber Composites," Journal of Applied Mechanics, vol. 47, June 1980, pp. 329-334.

33. Aveston, J. and Kelly, A., "Theory of Multiple Fracture of Fibrous Composites," Journal of Materials Science, vol. 8, 1973, p. 352.

34. Parvizi, A., Garrett, K. W., and Bailey, J. E., "Constrained Cracking in Glass Fibre-Reinforced Epoxy Cross-Ply Laminates," Journal of Materials Science, vol. 13, 1978, pp. 195-201.

35. Burr, S. T. and Sikarskie, D. L., "Damage Characterization of Woven Composites Under Static Tensile Loading," Proceedings of the 1995 SEM Spring Conference on Experimental Mechanics and Exhibit, Grand Rapids, MI, June 12-14, 1995, pp. 837-846.

36. Chang, F-K. and Lessard, L. B., "Damage Tolerance of Laminated Composites Containing an Open Hole and Subjected to Compressive Loadings: Part I-Analysis," Journal of Composite Materials, vol. 25, Jan. 1991, pp. 2-43.

37. Bader, M. G., Bailey, J. E., Curtis, P. T., and Parvizi, A., Proceedings of the 3rd International Conference on Mechanical Behavior of Materials, vol. 3, 1979, p. 227.

38. Parvizi, A. and Bailey, J. E., Journal of Material Science, vol. 13, 1978, p. 2131.

39. Bailey, J. E. and Parvizi, A., Journal of Material Science, vol. 16, 1981, p. 649.

40. Wang, A. S. D., "Fracture Mechanics of Sublaminate Cracks in Composite Materials," Composites Technology Review, vol. 6, 1984, p. 45.

41. Petitpas, E., Renault, M., and Valentin, D., "Fatigue Behavior of Cross-Ply CFRP Laminates Made of T300 or T400 Fibres," International Journal of Fatigue, vol. 12, no. 4, 1990, pp. 245-251.

42. Talreja, R., "Transverse Cracking and Stiffness Reduction in Composite Laminates," Journal of Composite Materials, vol. 19, July, 1985, pp. 355-375.

43. Kistner, M. D., Whitney, J. M., and Browning, C. E., "First Ply Failure of Graphite/Epoxy Laminates," Recent Advances in Composites in the U.S. and Japan, ASTM STP 864, J.R. Vinson and M. Taya, Eds., American Society for Testing and Materials, 1985, pp. 44-61.

44. Talreja, R., "Stiffness Properties of Composite Laminates with Matrix Cracking and Interior Delamination," Engineering Fracture Mechanics, vol. 25, nos. 5/6, 1986, pp. 751-762.

45. Talreja, R., Yalvac, S., Yats, L. D., and Wetters, D. G., "Transverse Cracking and Stiffness Reduction in Cross Ply Laminates of Different Matrix Toughness," Journal of Composite Materials, vol. 26, no. 11, 1992, pp. 1644-1663.

46. Chumbley, L., "Easy Rider," Aerospace Composites & Materials, The Shephard Press Ltd., Buckinghamshire, England, vol. 3, no. 6, Nov-Dec. 1991, pp. 19-20.

47. Tompkins, S. S., Bowles, D. E., Slemp, W. S., and Teichman, L. A., "Response of Composite Materials to the Space Station Orbit Environment," AIAA SDM Issues of the International Space Station Conference, April 21-22, 1988, Williamsburg, VA, pp. 108-116.

48. M.W. Hyer, Stress Analysis of Fiber Reinforced Composite Materials, WCB/McGraw-Hill, New York, 1998, ISBN 0-07-016700-1, pp. 9-14.

49. Michno, M. J. , Jr., “High Modulus Composite Properties,” AIAA Space Systems Technology Conference, AIAA-1187, San Diego, CA, June 9-12, 1986, pp. 126-131.

50. Short, J. S., Hyer, M. W., Post, D., Bowles, D. E., and Tompkins, S. S., “Development of a Priest Interferometer for Measurement of the Thermal Expansion of Graphite-Epoxy in the Temperature Range 116-366K,” Report VPI-E-82-18, Virginia Polytechnic Institute and State University, Blacksburg, VA, September, 1982.

51. Tompkins, S. S., Bowles, D. E., and Kennedy, W. R., “A Laser Interferometer Dilatometer for Thermal Expansion Measurements of Composites,” Proceedings of the V International Congress on Experimental Mechanics, Society for Experimental Stress Analysis, Montreal, Canada, June 10-15, 1984, pp. 367-376.

52. NASA Langley Research Center Precision Segmented Reflector Program.

53. Thornel Technical Information Sheet, September, 1986.

54. Hyer, M. W., “A Brief Review of Residual Thermal Stresses: Micromechanics to Structural Mechanics,” Workshop on ‘Modeling the Development of Residual Stresses During Thermoset Composite Curing’, University of Illinois, Champaign-Urbana, IL, September 15-16, 1995.

55. Coats, T.W., "Experimental Verification of a Progressive Damage Model for Composite Laminates Based on Continuum Damage Mechanics," NASA CR 195020, December, 1994.

APPENDIX A - THERMAL CYCLING SOAK TIME CALCULATION

This appendix contains calculations based on the lumped capacitance heat transfer method. The purpose of this calculation is to determine the minimum time required for the thickest of the specimens included in this investigation to reach a uniform temperature throughout its volume after changing the air temperature surrounding the specimen. The worst case temperature gradient experienced by any of the specimens in this investigation is the thermal cycling profile with extremes of –250°F and +250°F. Because the thermal stresses typically increase with decreasing temperature, there is the most concern with the time required for the specimen to stabilize at the minimum temperature, i.e., –250°F. For this analysis, it is assumed that the specimen is initially at +250°F throughout, after which the surrounding air temperature is lowered to –250°F. The time it takes for the specimen to reach –250°F throughout will be calculated.

It should be noted that this is, in fact, a worst case scenario that does not accurately portray the experimental procedure. In reality it takes time for the air surrounding the specimen to cool from +250°F to –250°F as well. As the air is cooling to –250°F, the specimen begins to cool. To be conservative, the time that is calculated from the above worst-case scenario will be used in the experiments as a soak time to be applied *after* the thermocouples attached to the surface of the specimen indicate –250°F. In doing so, this 'soak' time should be more than enough time for the specimen to reach uniform temperature throughout.

The lumped capacitance method assumes infinite thermal conductivity such that the specimen is assumed to have a constant through-the-thickness temperature at any given instant [A1]. The validity of this assumption is tested using the Biot number. For a Biot number much less than 1.0, the assumption of infinite conductivity is assumed to be valid. The equation for the lumped capacitance method which gives specimen temperature, T, as a function of time, t, is given by

$$\frac{T - T_\infty}{T_i - T_\infty} = \exp\left[-\left(\frac{hA_s}{\rho Vc}\right)t\right], \tag{A.1}$$

where

T_i = initial temperature of specimen

T_∞ = air temperature

h = convection coefficient of air

A_s = surface area of specimen

ρ = density of specimen

V = volume of specimen

c = specific heat of specimen.

The equation for the Biot number is given by

$$B_i = \frac{hV}{kA_s}, \tag{A.2}$$

where k = thermal conductivity of specimen.

The following values were assumed for the problem parameters:

T_i = +250°F
T_∞ = -250°F
h = 0.88060 – 17.612 Btu/h·ft^2·°F
(free convection vs. forced convection) [A2]
A_s = 4.1667 $x10^{-2}$ ft^2
ρ = 95.155 lbm/ft^3
V = 6.9444 $x10^{-5}$ ft^3
c = 0.22333 Btu/lbm·°F [A3]
k = 0.50270 Btu/h·ft·°F [A3].

The value for the convection coefficient of air depends on the flow of air in proximity to the specimen. Values for free convection, in which there is no air movement, and forced convection are shown. It is assumed that the actual experimental conditions result in a convection coefficient somewhere closer to the forced convection value.

Using the above listed values, a Biot number range of 0.003-0.058 is calculated. It is therefore assumed that the lumped capacitance method is suitable to this calculation and, based on Equation A.1, the specimen temperature as a function of time is illustrated in Figure A.1. A convection coefficient of h=0.88060 Btu/h·ft^2·°F for free convection results in a time of approximately 600 seconds for the specimen to reach the air temperature of -250°F. The forced convection of h=17.612 Btu/h·ft^2·°F results in a time of approximately 60 seconds. Because the experimental conditions are somewhere between the two extremes for convection, and thought to be closer to the forced convection, a conservative value of 300 seconds, or 5 minutes, was chosen. Again this soak time is added to the time it takes for the thermocouples at the surface of the specimen to reach –250°F. Because the ±250°F temperature cycle is the worst case of all the

thermal cycling ranges in this investigation, a soak time of 300 seconds was used for all thermal cycling temperature ranges, and applied to both the heating and cooling times.

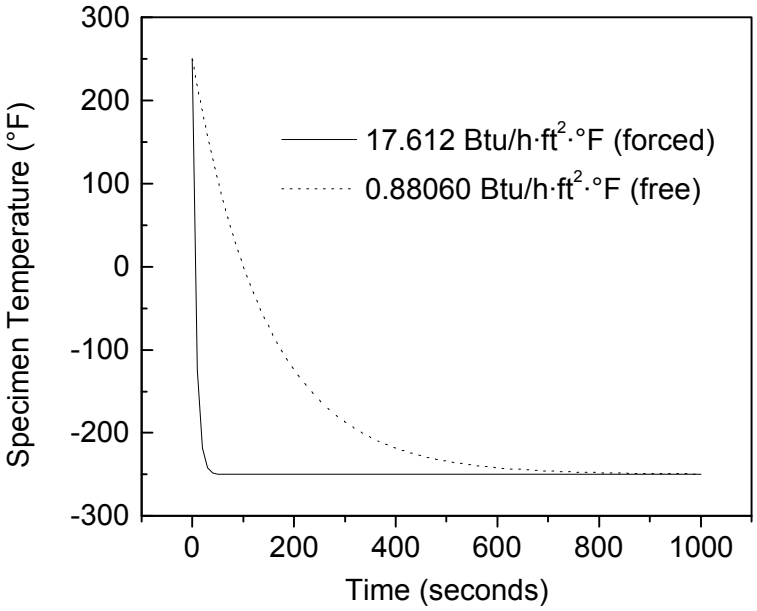

Figure A.1. Specimen temperature as a function of time for free and forced convection.

REFERENCES

A1. Incropera, F. P. and DeWitt, D. P., Fundamentals of Heat and Mass Transfer, 2nd. Ed., John Wiley & Sons, New York, NY, 1985, pp. 174-181.

A2. Incropera, F. P. and DeWitt, D. P., Fundamentals of Heat and Mass Transfer, 2nd. Ed., John Wiley & Sons, New York, NY, 1985, (Table 1.1) p. 8.

A3. Incropera, F. P. and DeWitt, D. P., Fundamentals of Heat and Mass Transfer, 2nd. Ed., John Wiley & Sons, New York, NY, 1985, (Table A.2) p. 759.

APPENDIX B - EXTENSOMETER CALIBRATION

This appendix contains experimental tensile stiffness results from testing an aluminum and a composite calibration specimen. The purpose of these measurements is to determine the accuracy and repeatability of the extensometer that is used to measure the tensile stiffness of each of the specimens in this test program. Measurements Group, Inc. CEA-06-250UW-350 strain gages with a 0.3 in. gage length are used as the standard against which the extensometer measurements are compared.

Since only a single extensometer is used, two tests are needed to obtain front and back stiffness using the extensometer. As seen in the table, Aluminum/1 and Aluminum/2 correspond to the first and second aluminum specimen tests, with the extensometer attached to side A and B of the specimen, respectively. Note that the specimen remained gripped in the load frame between these two tests, and the second test occurred within minutes of the first. The same is true for the composite specimen 6762-14. The Aluminum/3 and Aluminum/4 and the 6762-14/3 and 6762-14/4 represent a second set of tests done after the specimen was removed and regripped in the load frame. This second set of tests was done to determine repeatability of the stiffness measurements. All stiffness values shown below are calculated from a linear least squares regression fit to the stress-strain data using a strain range of 0.10% to the maximum strain in the test, usually 0.25%-0.30%. Unless otherwise noted, the same method is used for all stiffness results derived in this investigation.

From Table B.1 it can be seen that the largest discrepancy between the extensometer and strain gage derived stiffness is 3.20% and occurred for the aluminum specimen. In the case of the composite specimen, the largest discrepancy is 2.32%. These are good correlations. Realistically, however, the specimen stiffness is obtained by averaging front and back stiffnesses. These average measurements are compared in Table B.2.

Table B.1 Experimental Tensile Stiffness Measurements
for Extensometer Calibration Specimens

Specimen / Test Number Specimen Side	Strain Gage Measured Stiffness (Msi)	Extensometer Measured Stiffness (Msi)	% Error Strain Gage vs. Extensometer
Aluminum / 1 side A	10.252	10.247	0.05
side B	10.436	N/A	N/A
Aluminum / 2 side A	10.372	N/A	N/A
side B	10.405	10.280	1.20
Aluminum / 3 side A	10.288	10.265	0.22
side B	10.599	N/A	N/A
Aluminum / 4 side A	10.292	N/A	N/A
side B	10.473	10.138	3.20
6762-14 / 1 side A	14.360	14.693	2.32
side B	13.493	N/A	N/A
6762-14 / 2 side A	14.331	N/A	N/A
side B	13.495	13.194	2.23
6762-14 / 3 side A	14.426	14.356	0.49
side B	13.527	N/A	N/A
6762-14 / 4 side A	14.323	N/A	N/A
side B	13.524	13.400	0.92

The front and back stiffness measurements from the strain gages and the extensometer were averaged and are summarized in Table B.2. It is seen that by averaging the front and back stiffness measurements from the extensometer, the extensometer results more closely match those of the strain gage. The largest discrepancy for the aluminum specimen is 2.32% compared to the earlier maximum discrepancy of 3.20%. For the composite specimen, the largest discrepancy is now 0.33% compared to the earlier discrepancy of 2.32%.

Table B.2 Comparisons of Average Tensile Stiffness Calculated by Strain Gage vs. Extensometer

Specimen / Test Number	Average Stiffness (Msi) Strain Gage	Average Stiffness (Msi) Extensometer	% Error Strain Gage vs. Extensometer
Aluminum / 1	10.344	10.264*	0.78
Aluminum / 2	10.389	10.264*	1.20
Aluminum / 3	10.444	10.202*	2.32
Aluminum / 4	10.383	10.202*	1.74
6762-14 / 1	13.927	13.944*	0.12
6762-14 / 2	13.913	13.944*	0.22
6762-14 / 3	13.842	13.878*	0.26
6762-14 / 4	13.924	13.878*	0.33

* Two tests are required to determine average stiffness using the single extensometer. Therefore, the average stiffness calculated from these two tests are used for both tests.

The repeatability characteristics of the strain gage and extensometer are shown in Table B.3 and were calculated based on the average front and back stiffness measurements in Table B.2. The values represent the percentage difference in average stiffness between tests #1 and #3 and tests #2 and #4, respectively. It is noted that for the extensometer measurements only one value is shown because two tests are required to obtain average stiffness using the extensometer. It is seen that the repeatability of the stiffness measured with the extensometer is, in fact, better in some cases than the stiffness measured with the strain gage. This is the true for both the aluminum specimen and the composite specimen.

Table B.3 Repeatability Characteristics of Average Tensile Stiffness Measurements

Specimen	Strain Gage	Extensometer
Aluminum	0.97%, 0.06%	0.60%
6762-14	0.61%, 0.08%	0.47%

Based on the results presented above, it was concluded that the extensometer is capable of providing accurate and repeatable measurements of specimen tensile stiffness. For convenience, the extensometer was therefore used to measure tensile laminate stiffness for all of the specimens in this test program.

APPENDIX C - EXPERIMENTALLY MEASURED MICROCRACK DENSITIES

This appendix contains experimentally measured dimensional microcrack densities, in microcracks per inch, for each of the individual specimens in the test program as a function of the number of thermal cycles. This information can be considered raw data. The specimen number and layer type are indicated in the first two columns, respectively. The number of thermal cycles is shown in the first row at the top of each table. The material series name and specimen designation are indicated with each table. The specimen designation is summarized in a 4-term naming scheme separated by periods, i.e., I.II.III.IV. The 'I' represents the fiber and matrix combination, 'II' represents the laminate stacking sequence (X–$[0/90]_{2s}$, Q1–$[0/+45/–45/90]_{s}$, Q2–$[0/+45/90/–45]_{s}$), 'III' represents the nominal thickness of a single layer within the laminate (in mils), and 'IV' represents the thermal cycling range for the specimen (G – ±250°F, L – ±150°F, C – ±50°F).

Series J – T50/ERL1962.X.5.G

		Number of Thermal Cycles										
Specimen	Layer	0	1	5	10	50	100	250	500	1500	3000	3500
J-2	o90								12	43	66	68
	c90	0	0	0	0	0	0	8	16	29	39	41
J-3	o90								10	47	70	74
	c90	0	0	0	0	0	0	12	19	34	43	43
J-4	o90								2	38	61	66
	c90	0	0	0	0	0	0	17	28	36	45	46

Series O – P55/ERL1962.X.5.G

		Number of Thermal Cycles											
Specimen	Layer	0	1	5	10	50	100	250	500	1500	2500	3000	3500
O-2	o90									96	99	102	
	c90									62	66	69	
O-3	o90								65	99		106	108
	c90	0	2	2	3	8	11	31	49	60		64	66
O-4	o90								62	91		97	98
	c90	0	1	1	1	3	7	31	44	59		64	68

Series H – P75/ERL1962.X.5.G

		Number of Thermal Cycles										
Specimen	Layer	0	1	5	10	50	100	250	500	1500	3000	3500
H-2	o90								84	100	103	104
	c90	0	17	37	35	38	40	47	49	58	59	59
H-3	o90								81	98	100	102
	c90	0	17	34	34	37	40	46	48	53	58	59
H-4	o90								86	96	99	100
	c90	0	11	25	26	35	39	43	47	54	58	58

Series Q – P120/ERL1962.X.5.G

		Number of Thermal Cycles											
Specimen	Layer	0	1	5	10	50	100	250	500	1500	2000	3000	3500
Q-1	o90								96	107		108	110
	c90	0	24	40	45	54	55	61	64	69		68	71
Q-2	o90								78	124		126	123
	c90	0	30	41	46	56	57	60	60	67		69	67
Q-3	o90								73		107	107	108
	c90								37		67	71	71

Series UT8X – P75/ERL1962.X.1.G

		Number of Thermal Cycles							
Specimen	Layer	1	1500	2022	2500	3000	3020	4520	5020
UT8X-2	c90			21			68	125	140
UT8X-4	c90	0	48		80	92			
UT8X-5	c90			7			60	102	112

Series K – T50/ERL1962.Q1.5.G

		Number of Thermal Cycles										
Specimen	Layer	0	1	5	10	50	100	250	500	1500	3000	3500
K-3	45								2	18	31	35
	-45								43	62	69	69
	90	0	0	0	1	19	20	30	32	47	54	54
K-4	45								1	19	31	35
	-45								35	60	62	64
	90	0	0	0	0	3	5	17	26	44	54	55

Series P – P55/ERL1962.Q1.5.G

		Number of Thermal Cycles										
Specimen	Layer	0	1	5	10	50	100	250	500	1500	3000	3500
P-1	45								15	32	44	46
	-45								38	52	58	61
	90	0	1	8	9	25	28	30	41	52	57	62
P-2	45								32	53	58	59
	-45								70	82	83	83
	90	0	1	5	5	15	25	34	47	60	62	67
P-3	45								15	45	58	59
	-45								58	79	84	85
	90	0	3	5	5	19	23		44	60	61	64

Series I – P75/ERL1962.Q1.5.G

		Number of Thermal Cycles										
Specimen	Layer	0	1	5	10	50	100	250	500	1500	3000	3500
I-1	45								24	41	47	48
	-45								41	52	56	59
	90	2	21	29	29	36	36	36	39	49	49	51
I-2	45								24	46	52	53
	-45								62	70	72	72
	90	1	24	29	32	40	40	40	41	49	53	54
I-3	45								18	39	49	51
	-45								59	67	70	72
	90	1	21	31	34	36	36	36	42	52	55	56

Series R – P120/ERL1962.Q1.5.G

		Number of Thermal Cycles										
Specimen	Layer	0	1	5	10	50	100	250	500	1500	3000	3500
R-1	45								37	65	71	72
	-45								62	81	83	86
	90	0	45	52	51	52	52	52	51	63	66	67
R-3	45								50	54	56	59
	-45								55	66	69	72
	90	0	37	49	49	53	53	53	56	62	64	66
R-4	45								49	56	60	59
	-45								50	61	67	69
	90	0	41	49	48	54	54	57	56	63	65	67

Series 6762 – P75/ERL1962.Q2.5.G

		Number of Thermal Cycles			
Specimen	Layer	1	1500	2500	3000
6762-1	45	13	53	57	58
	90	65	115	119	119
	-45	24	46	48	50
6762-3	45	56	72	77	80
	90	65	119	121	125
	-45	24	45	47	47
6762-5	45	36	64	66	68
	90	66	117	118	121
	-45	28	47	48	48

Series 6762 – P75/ERL1962.Q2.5.L

		Number of Thermal Cycles			
Specimen	Layer	0	1500	3000	4000
6762-2	45	0	20	21	22
	90	0	90	94	94
	-45	0	32	36	37
6762-4	45	0	26	26	26
	90	2	85	90	93
	-45	0	31	35	37
6762-6	45	0	24	27	29
	90	3	88	92	93
	-45	0	36	39	42

Series 6762 – P75/ERL1962.Q2.5.C

		Number of Thermal Cycles			
Specimen	Layer	0	1500	3000	4000
6762-7	45	0	1	5	9
	90	7	32	67	73
	-45	0	1	10	15
6762-8	45	0	2	7	10
	90	3	47	68	68
	-45	0	3	13	17
6762-9	45	0	4	8	9
	90	6	51	70	77
	-45	0	8	12	17

Series 75RS3 – P75/RS3.Q2.5.G

		Number of Thermal Cycles			
Specimen	Layer	0	1500	2500	3000
75RS3-1	45	0	36	42	46
	90	0	65	72	74
	-45	0	33	39	41
75RS3-2	45	0	40	44	46
	90	0	69	76	78
	-45	0	36	41	42
75RS3-3	45	0	36	41	43
	90	0	64	73	75
	-45	0	36	43	45

Series 75RS3 – P75/RS3.Q2.5.L

		Number of Thermal Cycles			
Specimen	Layer	0	1500	3000	4000
75RS3-4	45	0	0	0	0
	90	0	1	1	2
	-45	0	0	0	0
75RS3-5	45	0	0	0	0
	90	0	0	1	1
	-45	0	0	0	0
75RS3-6	45	0	0	0	0
	90	0	0	1	1
	-45	0	0	0	0

Series 75RS3 – P75/RS3.Q2.5.C

		Number of Thermal Cycles			
Specimen	Layer	0	1500	3000	4000
75RS3-7	45	0	0	0	0
	90	0	0	0	0
	-45	0	0	0	0
75RS3-8	45	0	0	0	0
	90	0	0	0	0
	-45	0	0	0	0
75RS3-9	45	2	2	2	2
	90	0	0	0	0
	-45	0	0	0	0

Series 75R-A – P75/RS3.Q2.5.G

		Number of Thermal Cycles								
Specimen	Layer	0	500	1000	1500	2000	2500	3000	3500	4000
75R-A-41	45			4		28			41	44
	90			54		83			87	88
	-45			23		27			31	33
75R-A-43	45		0		20			31	34	
	90		9		51			72	75	
	-45		9		24			35	39	
75R-A-44	45	0			42		43	45		
	90	0			67		69	70		
	-45	0			41		43	46		

Series 75R-A – P75/RS3.Q2.5.L

		Number of Thermal Cycles			
Specimen	Layer	0	1500	3000	4000
75R-A-36	45	0	0	0	0
	90	0	1	2	2
	-45	0	0	0	0
75R-A-37	45	0	0	0	0
	90	0	3	3	4
	-45	0	0	0	0
75R-A-45	45	0	1	1	1
	90	0	4	7	9
	-45	0	0	0	0

Series 75R-A – P75/RS3.Q2.5.C

		Number of Thermal Cycles			
Specimen	Layer	0	1500	3000	4000
75R-A-38	45	0	0	0	0
	90	0	0	0	0
	-45	0	0	0	0
75R-A-39	45	0	0	0	0
	90	0	0	0	0
	-45	0	0	0	0
75R-A-46	45	0	0	0	0
	90	0	0	0	0
	-45	0	0	0	0

Series P734Q – P75/934.Q2.5.G

		Number of Thermal Cycles			
Specimen	Layer	1	1500	2500	3000
P734Q-2	45	18	50	54	54
	90	92	126	127	129
	-45	32	43	43	44
P734Q-3	45	13	57	59	59
	90	111	129	129	130
	-45	25	43	44	44
P734Q-4	45	27	60	62	64
	90	118	134	137	138
	-45	30	42	42	44

Series 275RS3 – P75/RS3.Q2.2.G

		Number of Thermal Cycles			
Specimen	Layer	0	1500	2500	3000
275RS3-1	45	0	31	38	43
	90	0	187	193	189
	-45	0	38	55	66
275RS3-2	45	0	21	32	38
	90	0	175	176	178
	-45	0	20	36	48
275RS3-3	45	16	35	45	50
	90	2	156	164	177
	-45	0	27	43	51

Series 275RS3 – P75/RS3.Q2.2.L

		Number of Thermal Cycles			
Specimen	Layer	0	1500	3000	4000
275RS3-4	45	0	2	3	3
	90	0	21	39	52
	-45	0	0	0	1
275RS3-5	45	0	1	2	3
	90	0	21	35	45
	-45	0	0	0	1
275RS3-6	45	0	0	0	0
	90	0	18	43	54
	-45	0	0	0	0

Series 275RS3 – P75/RS3.Q2.2.C

		Number of Thermal Cycles			
Specimen	Layer	0	1500	3000	4000
275RS3-7	45	0	0	0	0
	90	0	0	0	0
	-45	0	0	0	0
275RS3-8	45	0	0	0	0
	90	0	1	2	2
	-45	0	0	0	0
275RS3-9	45	0	0	0	0
	90	0	0	1	1
	-45	0	0	0	0

APPENDIX D - LAMINATE THERMAL EXPANSION DATA

This appendix contains laminate thermal strain data and laminate coefficients of thermal expansion for the materials included in this investigation. The data are presented in figures as continuous functions of temperature based on polynomial regressions to discrete thermal strain data. Also included in the figures are the goodness of fit parameters for the polynomial regressions: the correlation coefficient (R), the square of the correlation (R^2), and the standard deviation of the fit (SD). A value of R=1 implies a perfect fit with no residual error. In some cases the thermal strain behavior is seen to be a cubic function of temperature, while being a quadratic function in other cases. This reflects the best fit to the actual data. In some cases, the choice of curve fit order is modified to reflect the predominant behavior of the other specimens for a given series. However, there are isolated cases where varying fit orders occur within the same series.

During thermal expansion testing each of the specimens are heated from room temperature (75°F) to the maximum temperature, i.e., +250°F, +150°F, or +50°F, and then cooled to the minimum temperature, i.e., -250°F, -150°F, or -50°F, and finally reheated to room temperature. The thermal strain relation for each individual specimen is obtained by fitting a polynomial curve to data from the cooling portion of this cycle only, i.e., from the maximum temperature to the minimum temperature. This thermal strain response for each specimen is shown in a separate figure in this appendix along with the defining equation for the polynomial. The individual strain relations are then shifted vertically such that a value of zero strain is obtained at a reference temperature of 77°F (25°C). These shifted strain relations are shown plotted together in a separate graph included with the graphs for the individual specimens.

The thermal strain response for each specimen is included at 0 cycles (uncycled) and at the maximum cycle count for that specimen. The shifted thermal strain relations for each specimen are used to form an average thermal strain response for the given series at the given number of thermal cycles. The average thermal strain response at 0 cycles and at the maximum cycle count are shown together for the given specimen series, along with the equation for the average thermal strain response, indicated by ε. The average CTE as a function of temperature is obtained by differentiating the average thermal strain response with respect to temperature over the given temperature range. The equation for CTE is shown alongside the curve, in units of microstrain per degree Fahrenheit, as a function of temperature in degrees Fahrenheit.

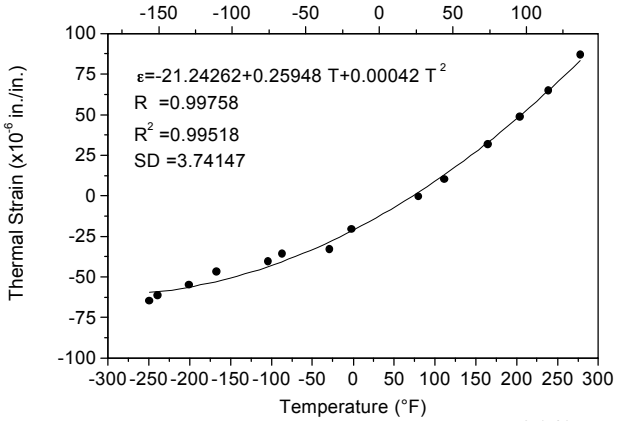

(a) J-2 - 0 cycles

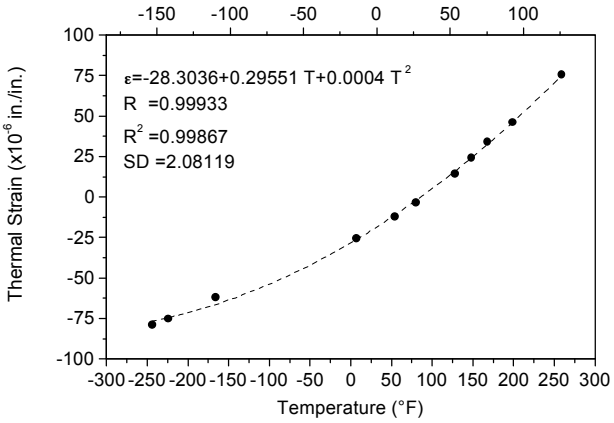

(b) J-3 - 0 cycles

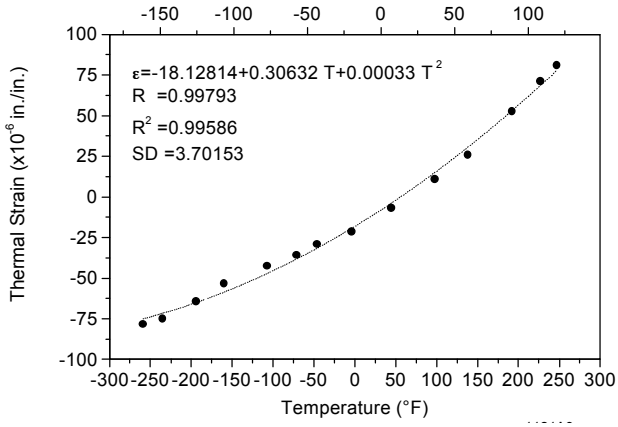

(c) J-4 - 0 cycles

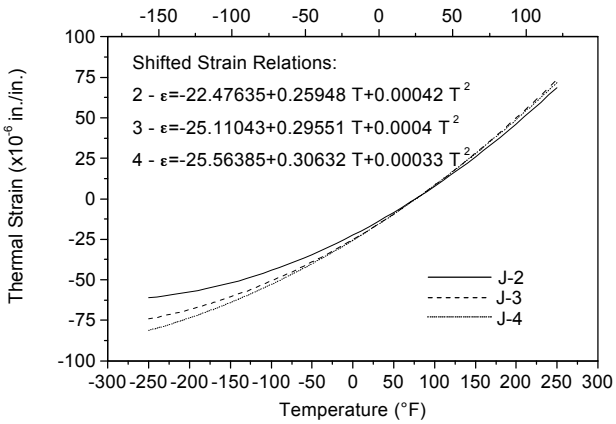

(d) Shifted strain data for J-2, 3, and 4

Figure D.1. Thermal strain data for specimens J-2, 3, and 4 at 0 cycles.

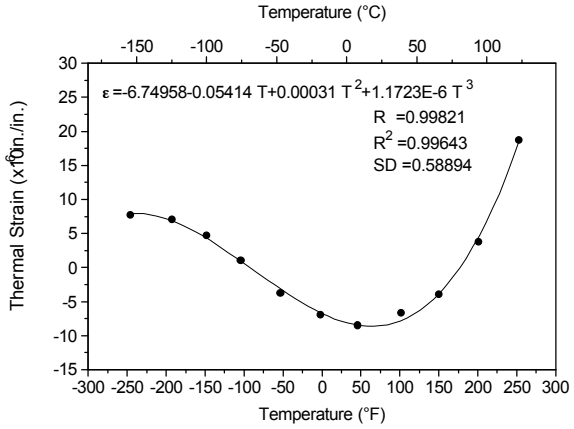

(a) J-2 - 3500 cycles

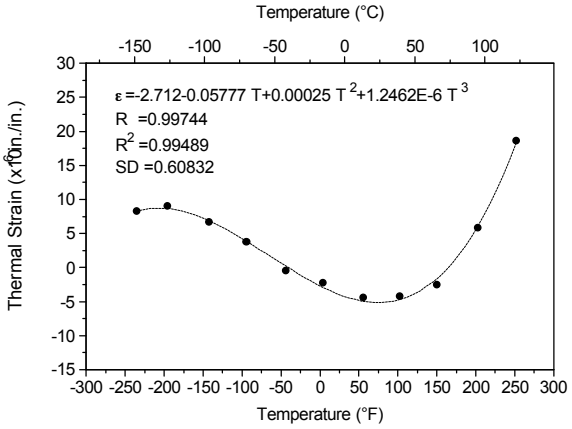

(b) J-3 - 3500 cycles

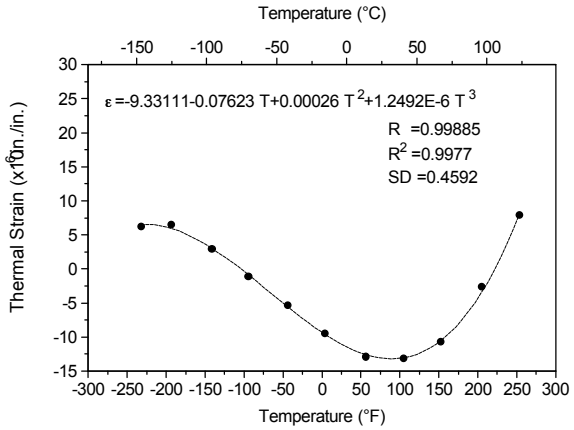

(c) J-4 - 3500 cycles

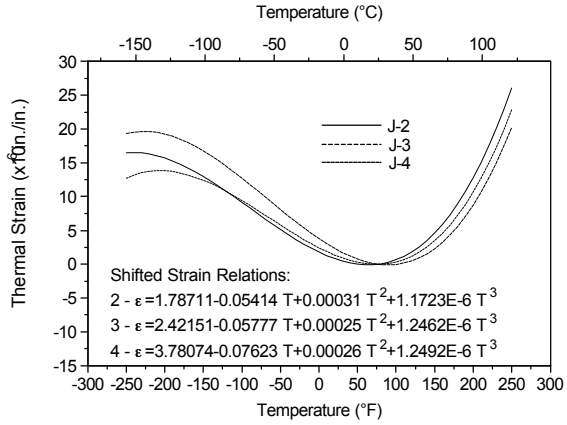

(d) Shifted strain data for J-2, 3, and 4

Figure D.2. Thermal strain data for specimens J-2, 3, and 4 at 3500 cycles.

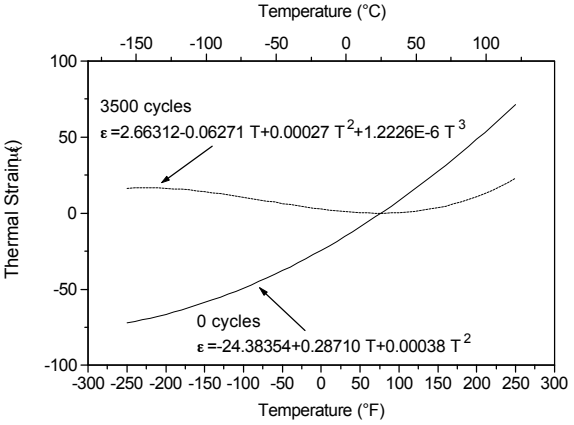

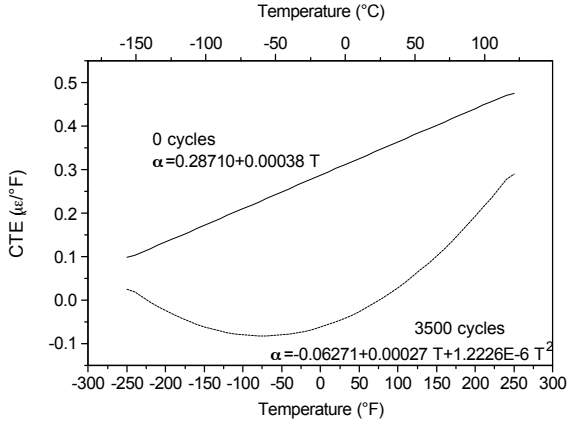

Figure D.3. Average thermal expansion data for specimen series J - T50/ERL1962.X.5.G - T50/ERL1962, $[0/90/0/90]_S$, 5 mil, ±250°F

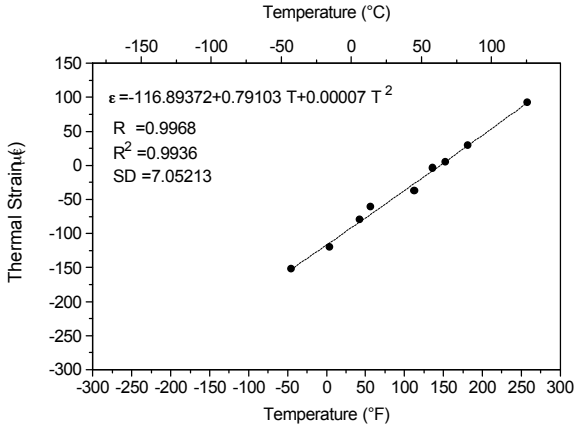

(a) O-2 - no data available

(b) O-3 - 0 cycles

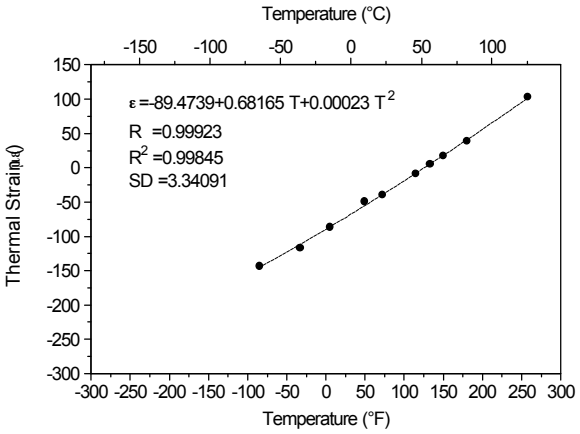

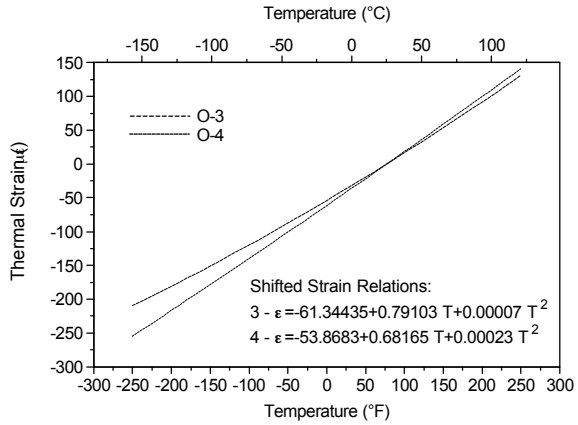

(c) O-4 - 0 cycles

(d) Shifted strain data for O-3 and 4

Figure D.4. Thermal strain data for specimens O-3 and 4 at 0 cycles.

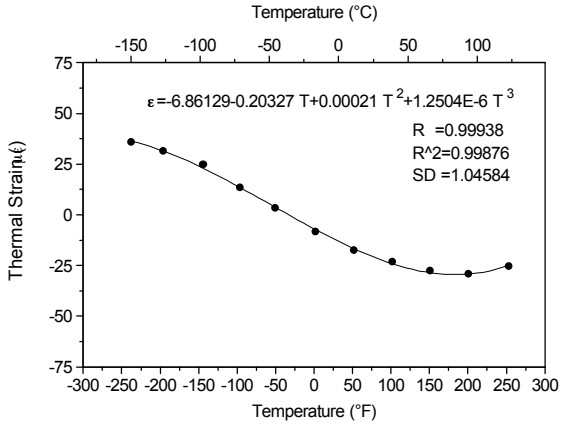

(a) O-2 - 3000 cycles

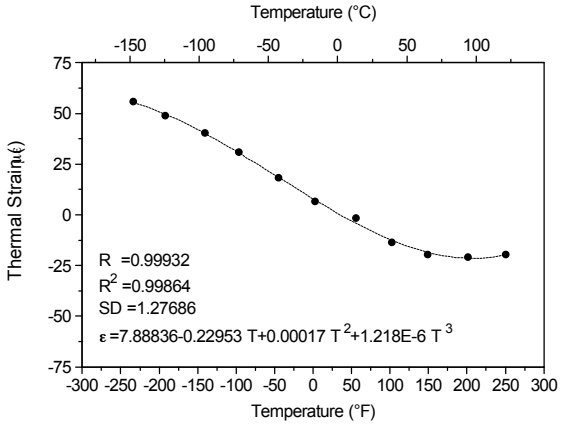

(b) O-3 - 3500 cycles

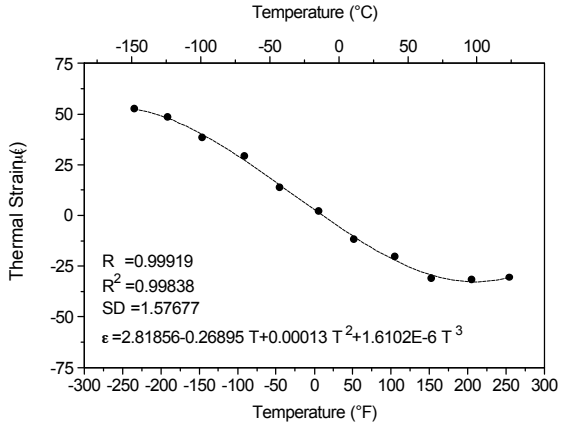

(c) O-4 - 3500 cycles

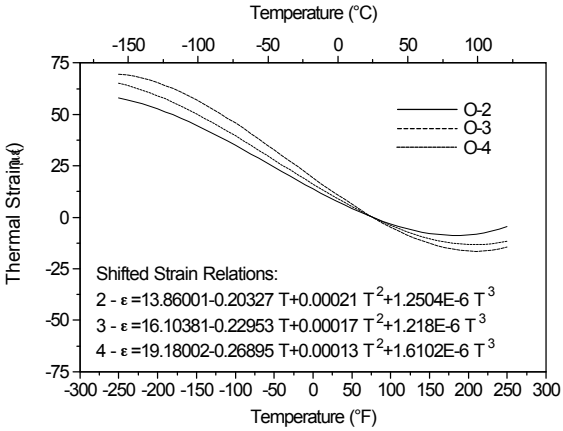

(d) Shifted strain data for O-2, 3, and 4

Figure D. 5. Thermal strain data for specimens O-2, 3, and 4 at 3500(3000 for O-2) cycles.

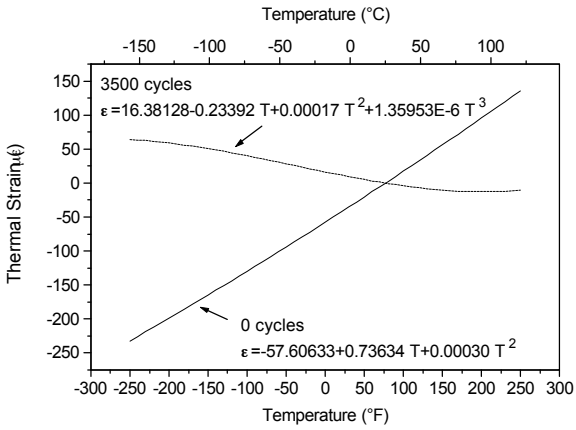

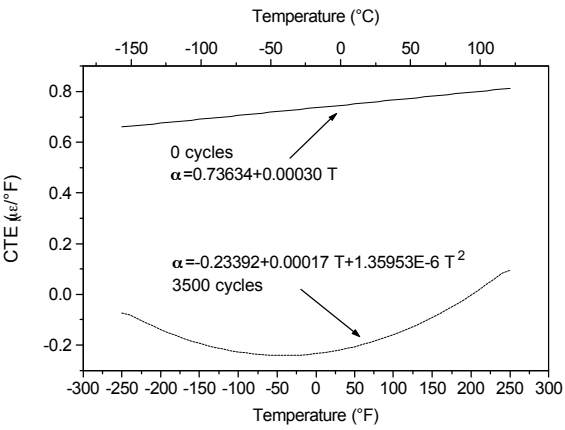

Figure D.6. Average thermal expansion data for specimen series O - P55/ERL1962.X.5.G - P55/ERL1962, $[0/90/0/90]_S$, 5 mil, ±250°F

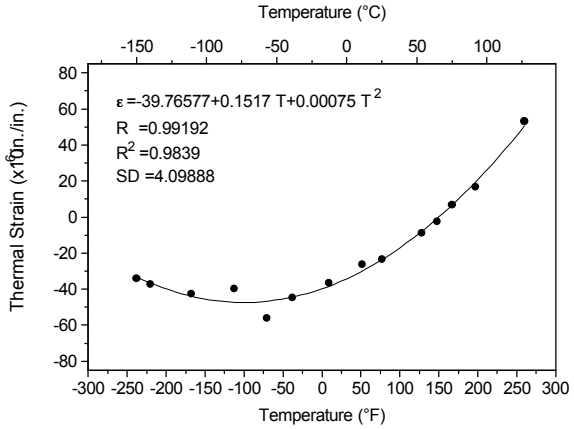

(a) H-2 - 0 cycles

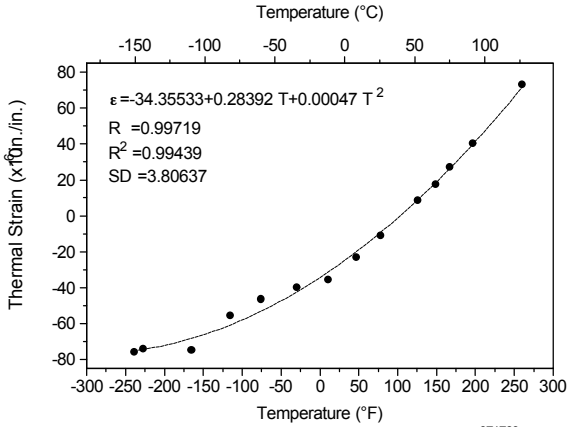

(b) H-4 - 0 cycles

No 0 cycle data available for H-3

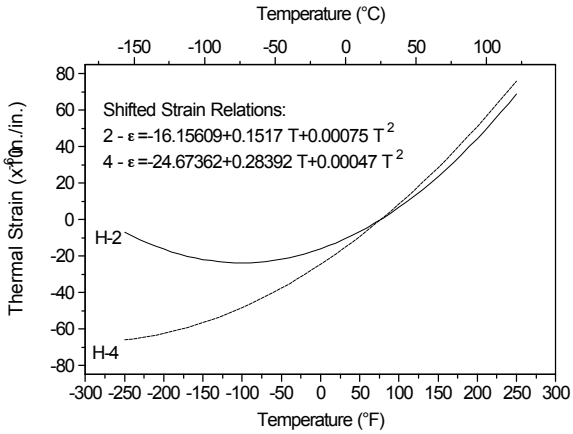

(c) Shifted strain data for H-2 and H-4

Figure D.7. Thermal strain data for specimens H-2 and H-4 at 0 cycles.

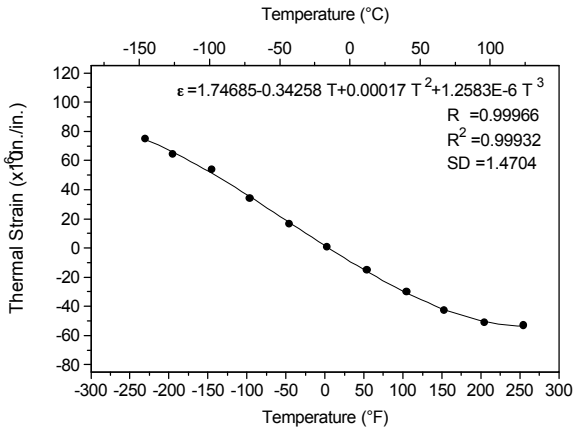

(a) H-2 - 3500 cycles

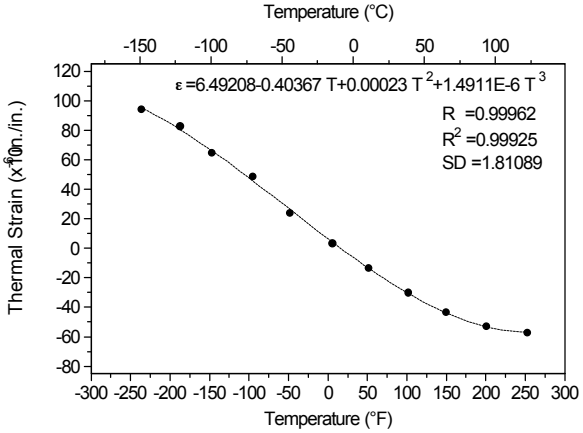

(b) H-3 - 3500 cycles

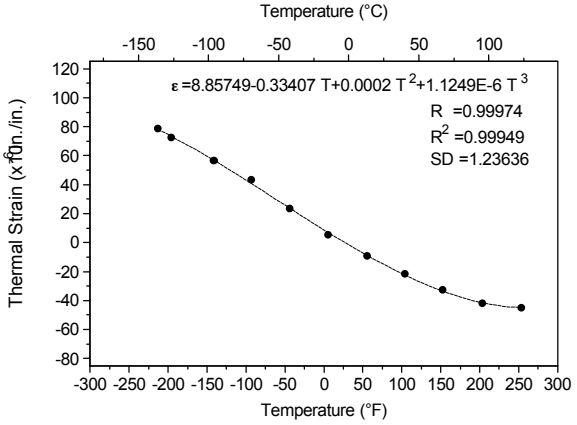

(c) H-4 - 3500 cycles

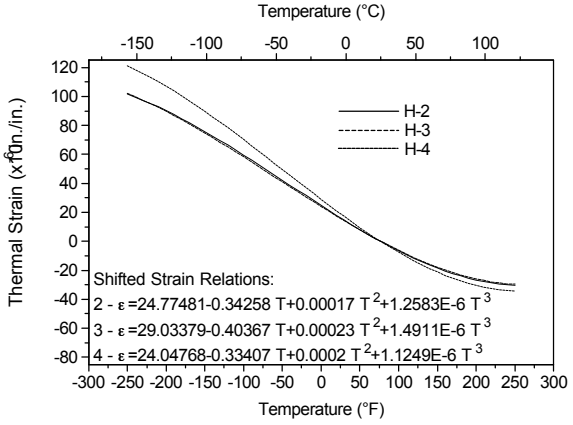

(d) Shifted strain data for H-2, 3, 4

Figure D.8. Thermal strain data for specimens H-2, 3, 4 at 3500 cycles.

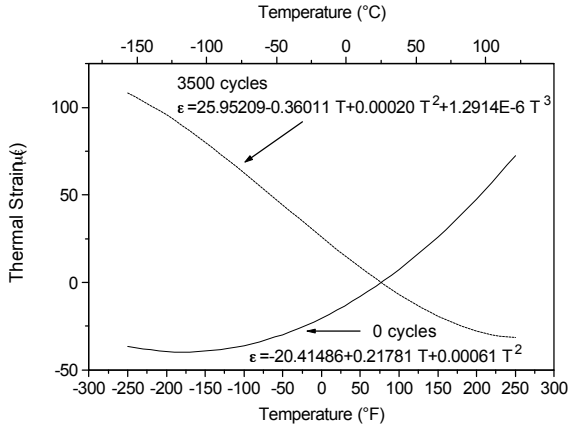

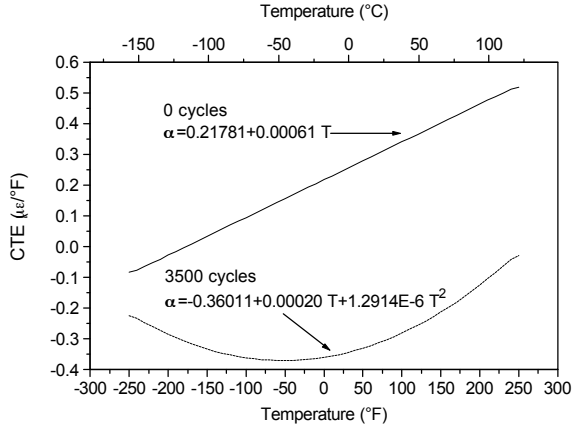

Figure D.9. Average thermal expansion data for specimen series H - P75/ERL1962.X.5.G - P75/ERL1962, $[0/90/0/90]_S$, 5 mil, ±250°F

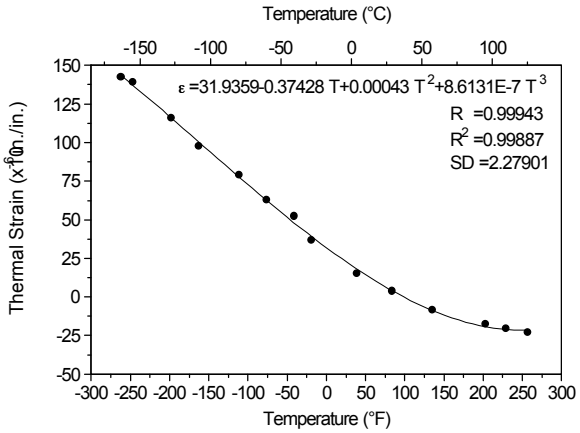

(a) Q-1 - 0 cycles

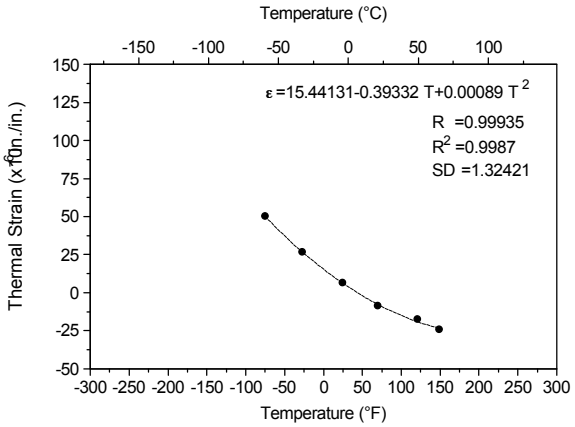

(b) Q-3 - 0 cycles

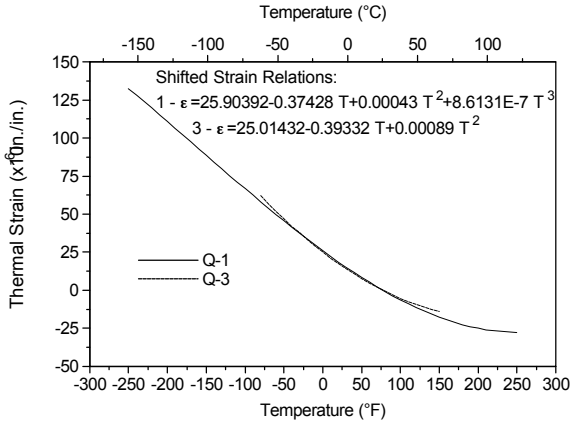

(d) Shifted strain data for Q-1 and 3

Figure D.10. Thermal strain data for specimens Q-1 and 3 at 0 cycles.

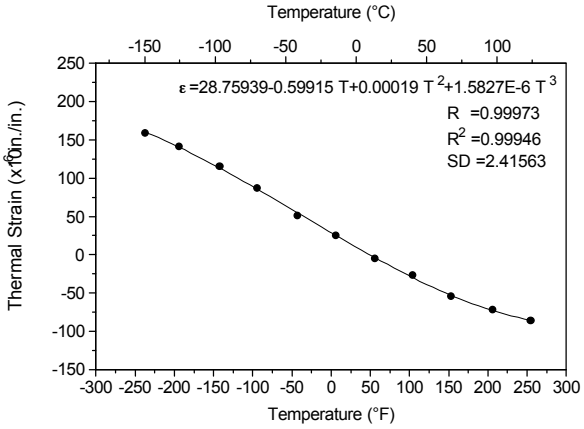

(a) Q-1 - 3500 cycles

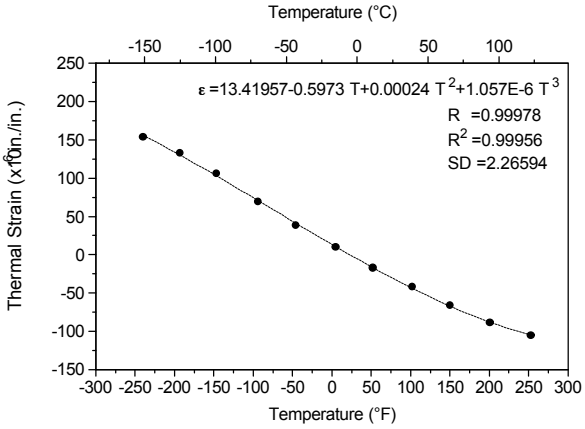

(b) Q-2 - 3500 cycles

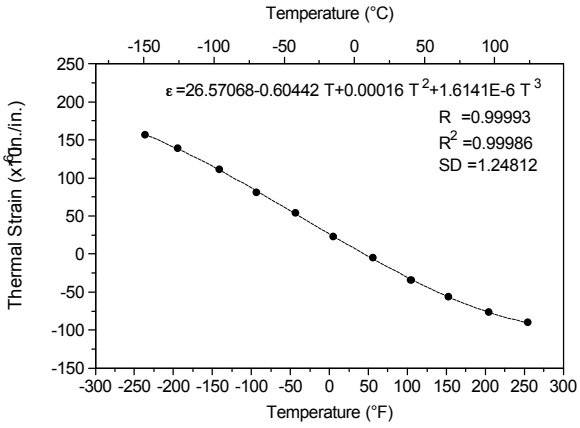

(c) Q-3 - 3500 cycles

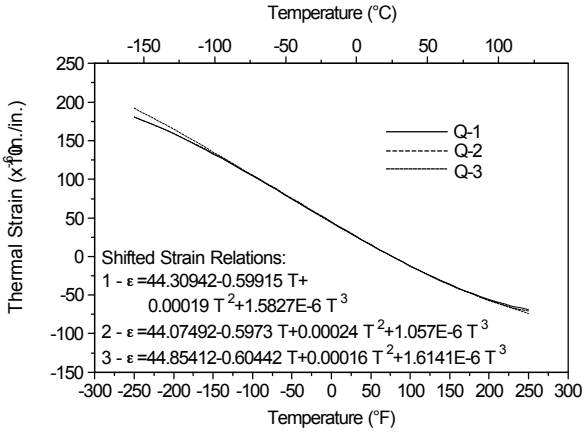

(d) Shifted strain data for Q-1, 2, and 3

Figure D.11. Thermal strain data for specimens Q-1, 2, and 3 at 3500 cycles.

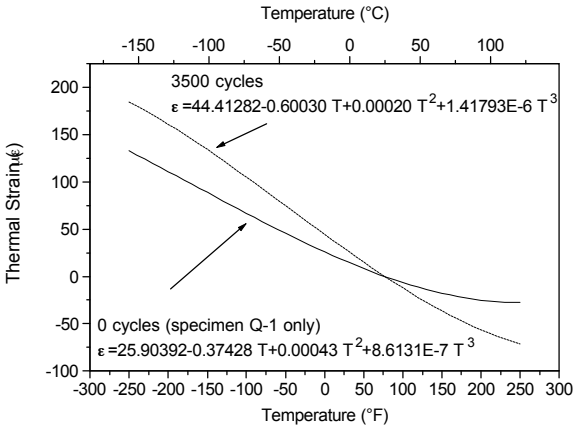

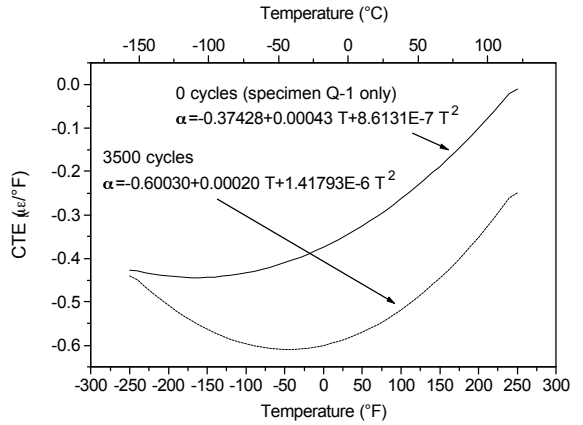

Figure D.12. Average thermal expansion data for specimen series Q - P120/ERL1962.X.5.G - P120/ERL1962, $[0/90/0/90]_S$, 5 mil, ±250°F

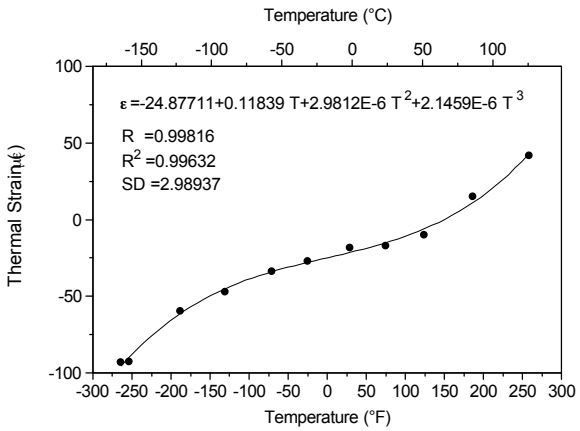

(a) UT8X-2 - 0 cycles

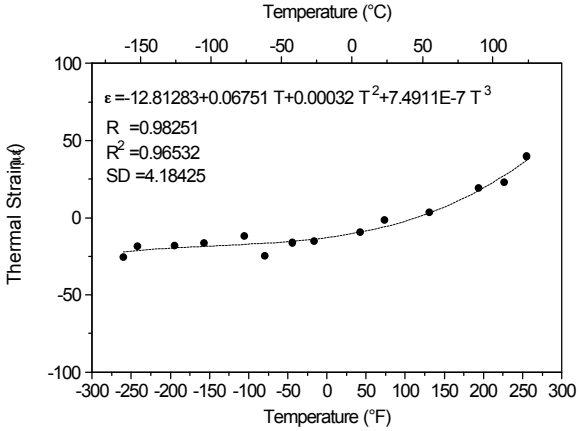

(b) UT8X-4 - 0 cycles

no 0 cycle data for UT8X-5

(c)

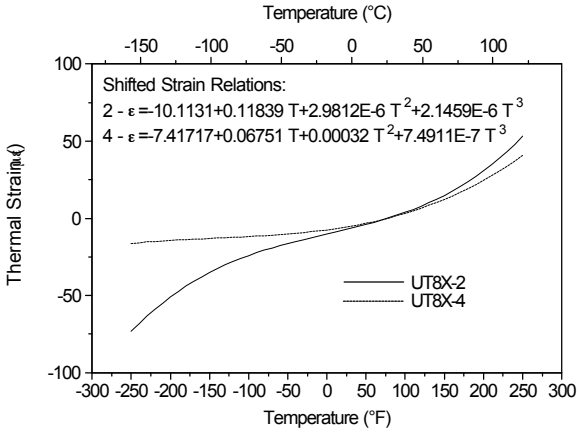

(d) Shifted strain data for UT8X-2 and 4

Figure D.13. Thermal strain data for specimens UT8X-2 and 4 at 0 cycles.

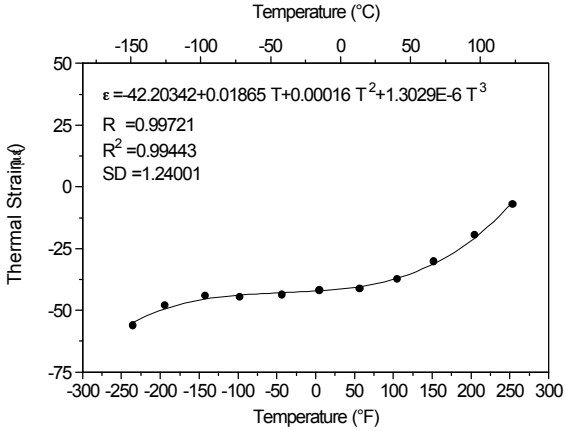

(a) UT8X-2 - 5020 cycles

no data for UT8X-4 at 5020 cycles

(b)

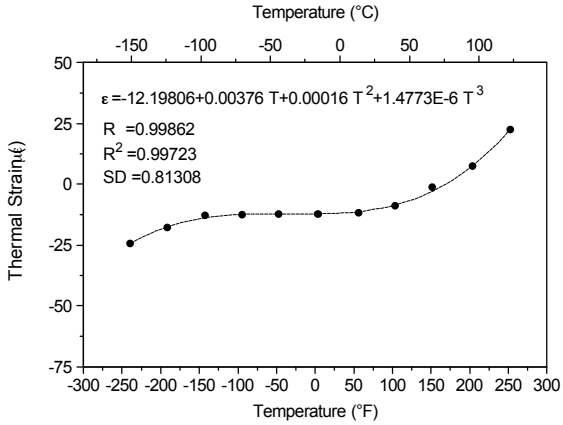

(c) UT8X-5 - 5020 cycles

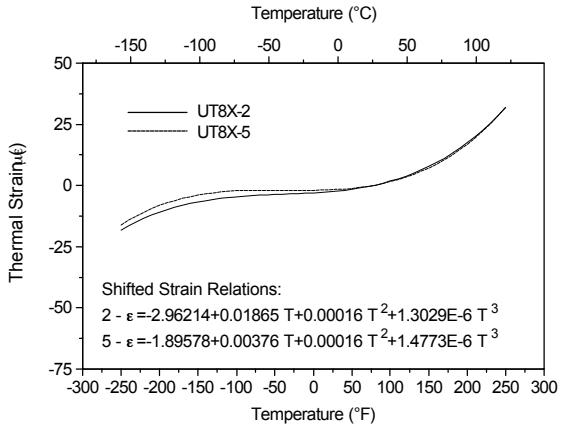

(d) Shifted strain data for UT8X-2 and 5

Figure D.14. Thermal strain data for specimens UT8X-2 and 5 at 5020 cycles.

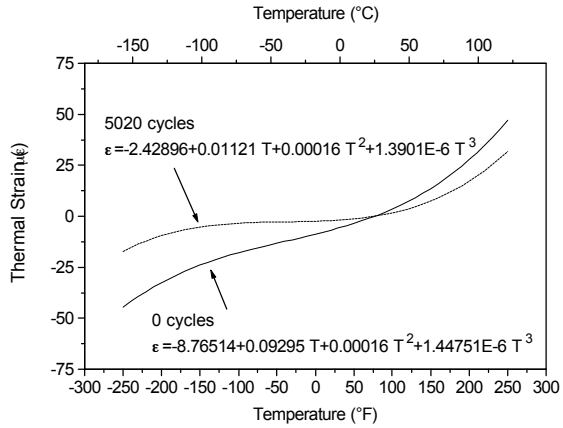

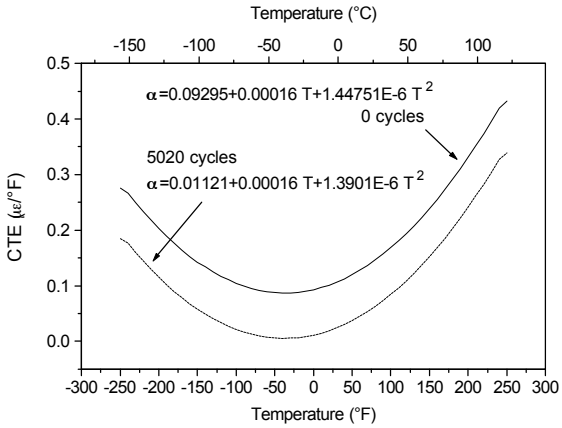

Figure D.15. Average thermal expansion data for specimen series UT8X - P75/ERL1962.X.1.G - P75/ERL1962, $[0/90/0/90]_S$, 1 mil, ±250°F

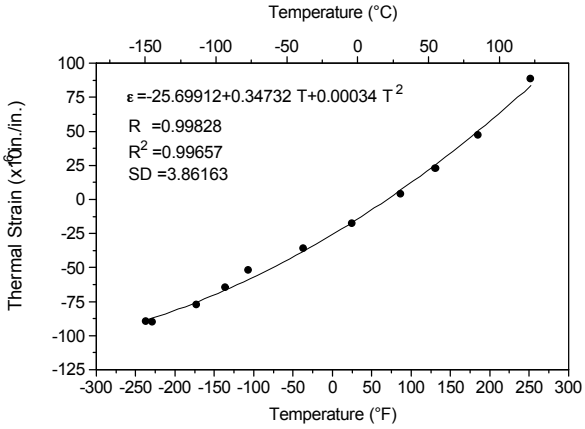

(a) K-3 - 0 cycles

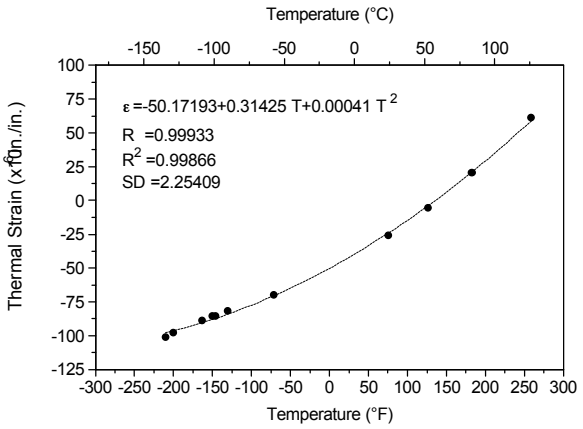

(b) K-4 - 0 cycles

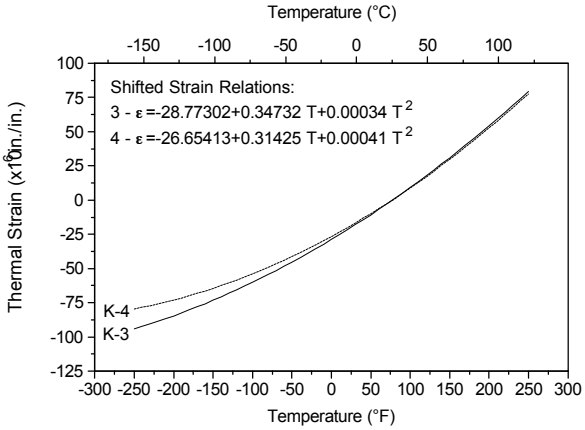

(c) Shifted strain data for K-3 and 4

Figure D.16. Thermal strain data for specimens K-3 and 4 at 0 cycles.

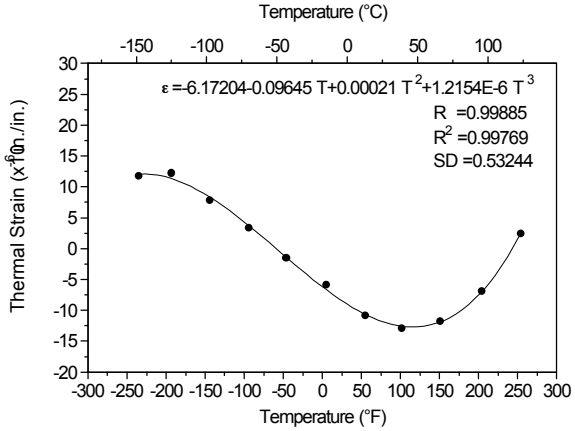

(a) K-3 - 3500 cycles

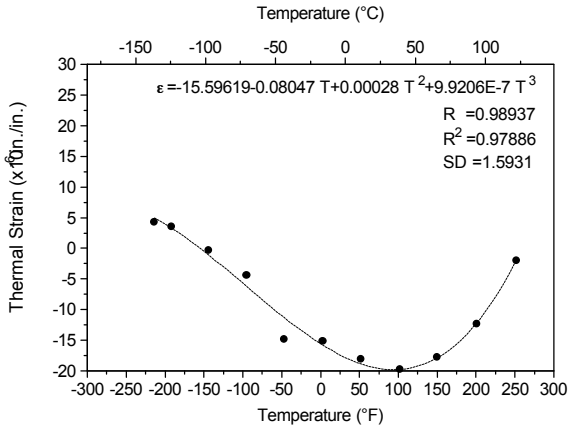

(b) K-4 - 3500 cycles

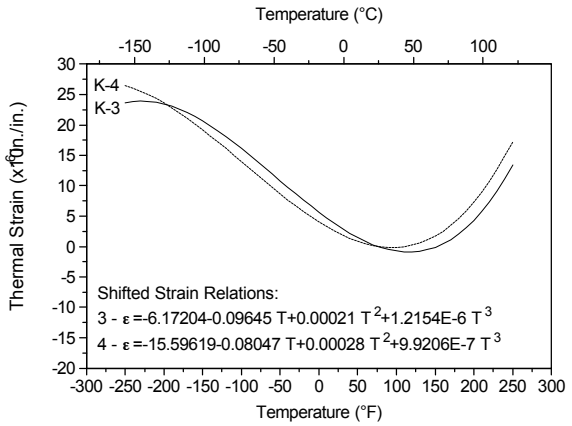

(c) Shifted strain data for K-3, and 4

Figure D.17. Thermal strain data for specimens K-3 and 4 at 3500 cycles.

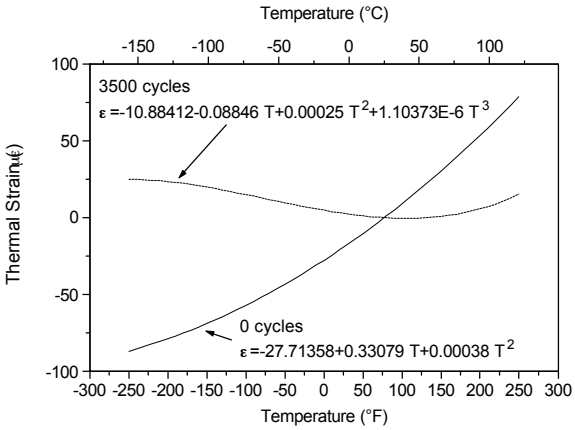

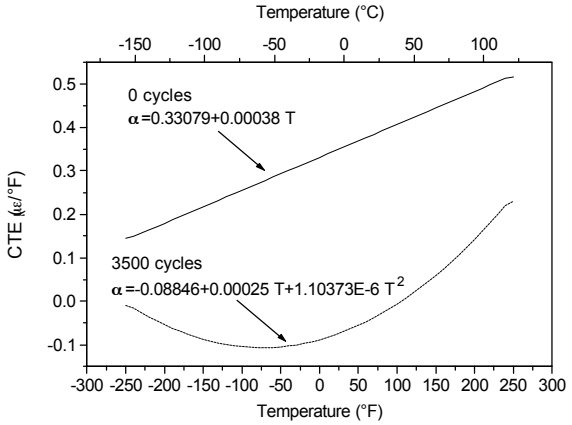

Figure D.18. Average thermal expansion data for specimen series K - T50/ERL1962.Q1.5.G - T50/ERL1962, $[0/+45/-45/90]_S$, 5 mil, ±250°F

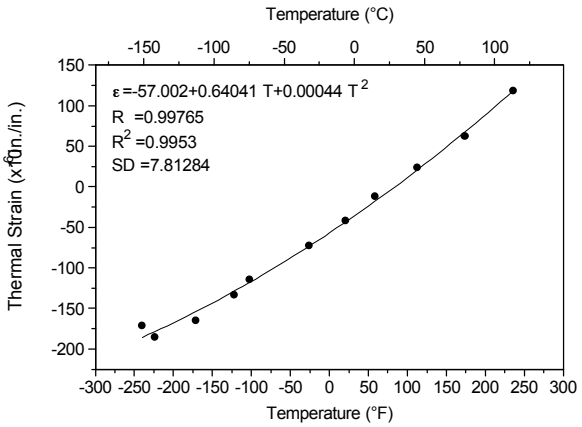

(a) P-1 - 0 cycles

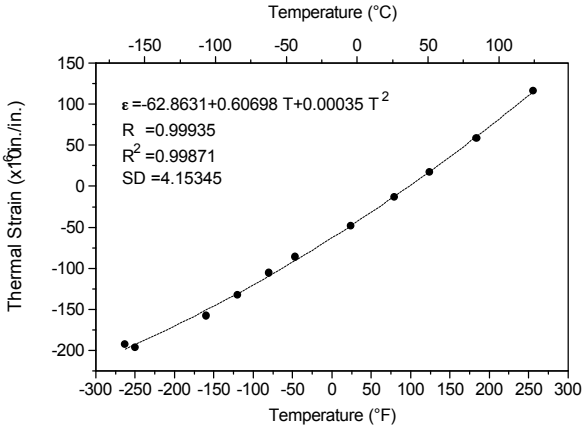

(b) P-2 - 0 cycles

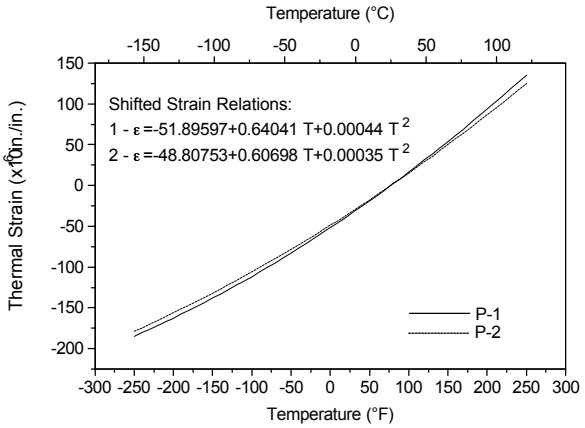

(d) Shifted strain data for P-1 and 2

Figure D.19. Thermal strain data for specimens P-1 and 2 at 0 cycles.

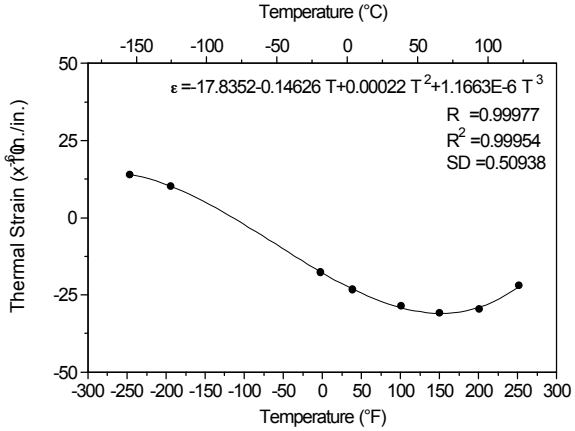

(a) P-1 - 3500 cycles

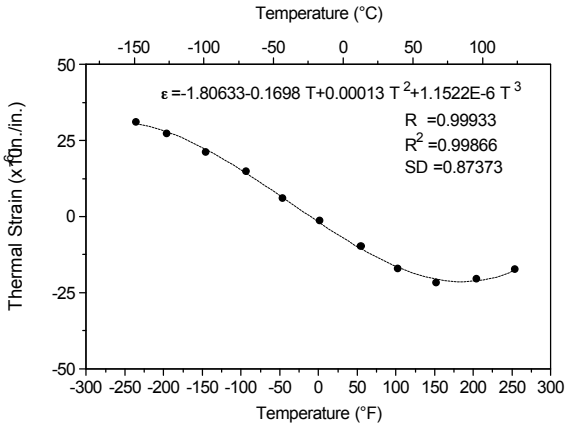

(b) P-2 - 3500 cycles

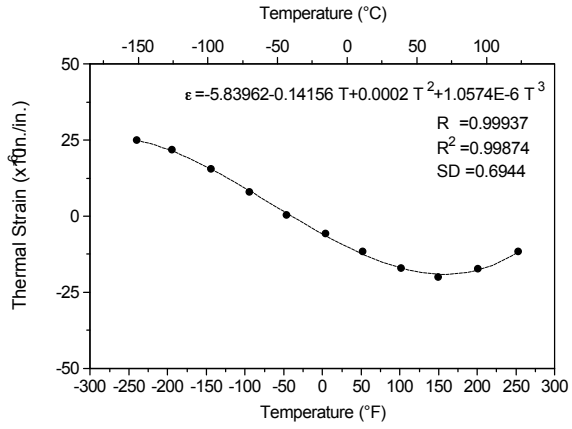

(c) P-3 - 3500 cycles

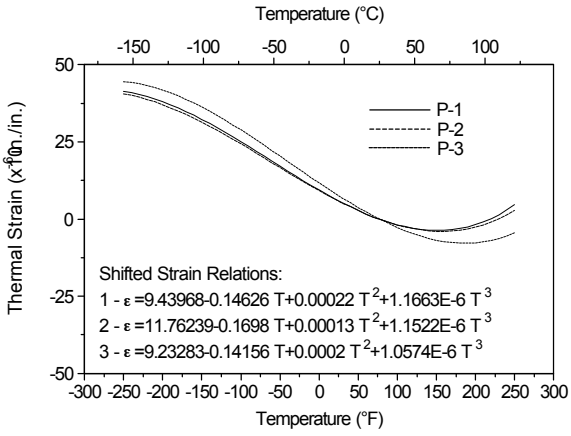

(d) Shifted strain data for P-1, 2, and 3

Figure D.20. Thermal strain data for specimens P-1, 2, and 3 at 3500 cycles.

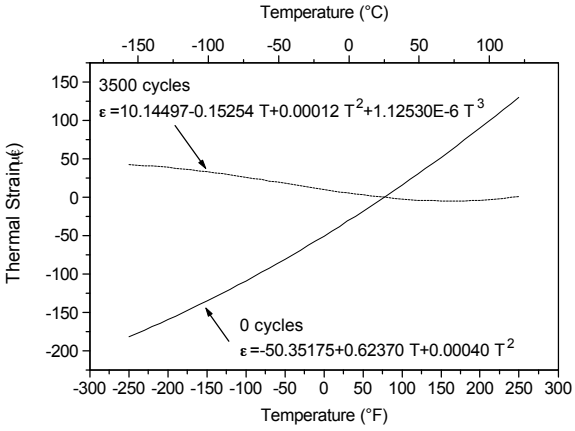

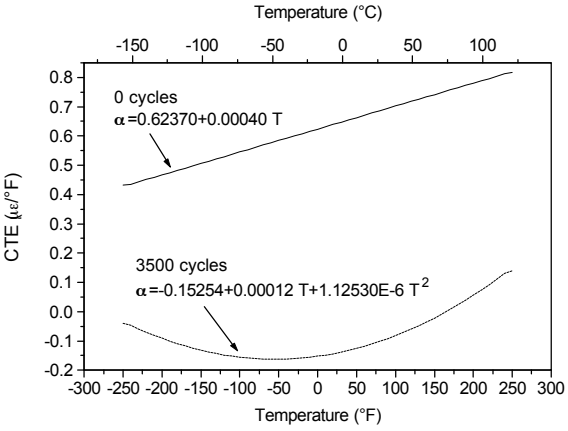

Figure D.21. Average thermal expansion data for specimen series P - P55/ERL1962.Q1.5.G - P55/ERL1962, $[0/+45/-45/90]_S$, 5 mil, ±250°F.

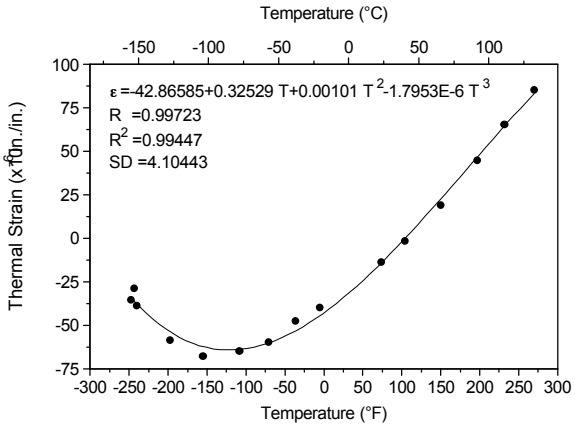

(a) I-1 - 0 cycles

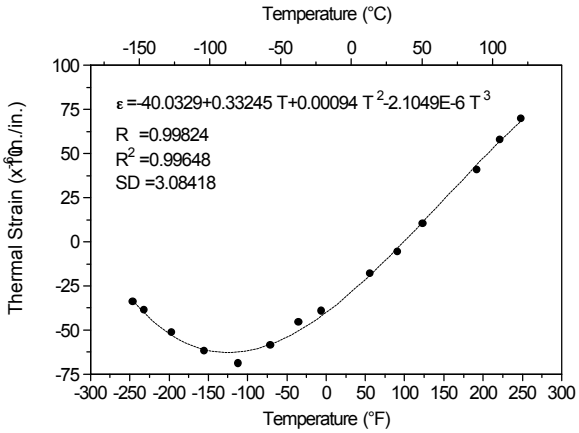

(b) I-2 - 0 cycles

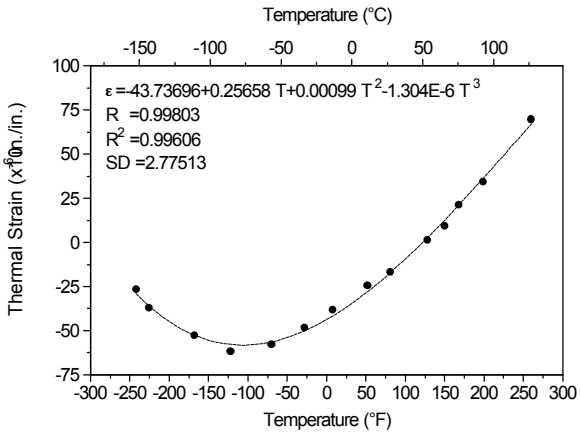

(c) I-3 - 0 cycles

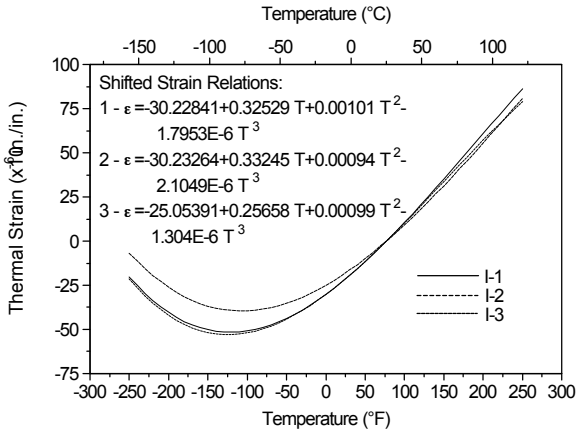

(d) Shifted strain data for I-1,2,3

Figure D.22. Thermal strain data for specimens I-1, 2, 3 at 0 cycles.

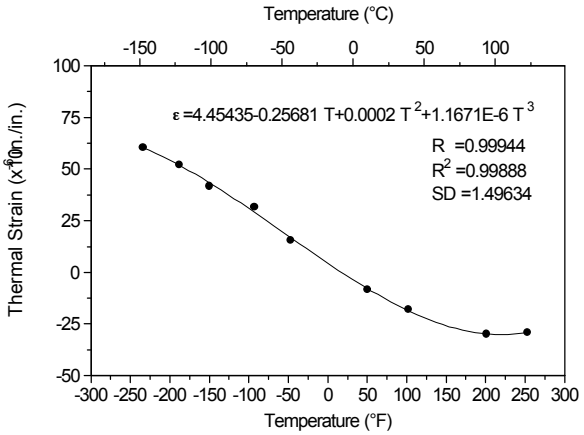

(a) I-1 - 3500 cycles

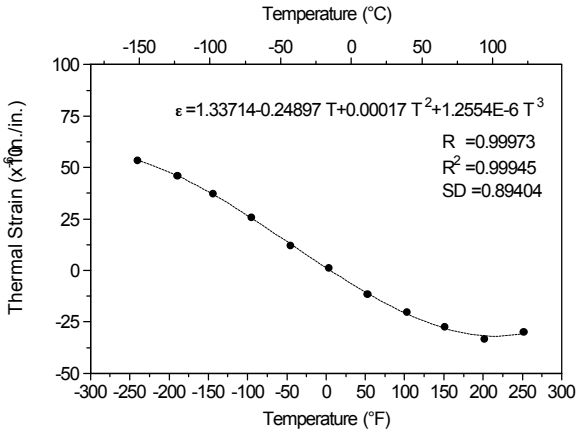

(b) I-2 - 3500 cycles

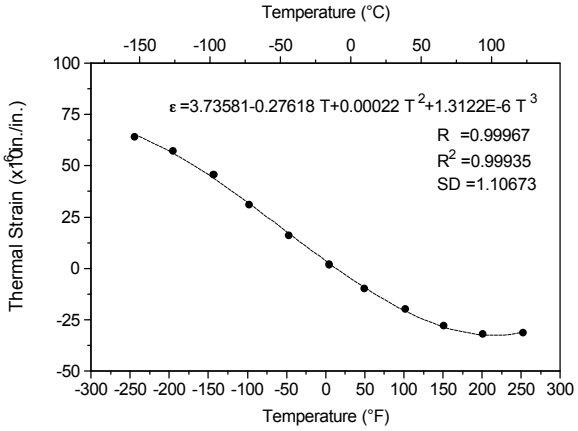

(c) I-3 - 3500 cycles

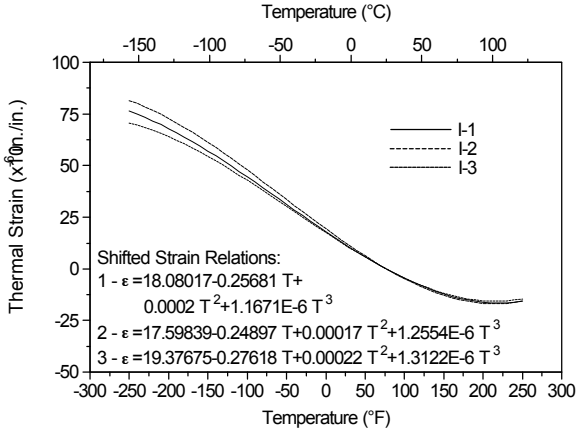

(d) Shifted strain data for I-1, 2, and 3

Figure D.23. Thermal strain data for specimens I-1, 2, 3 at 3500 cycles.

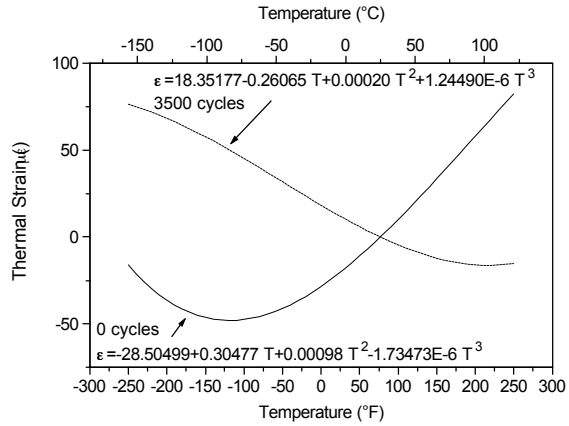

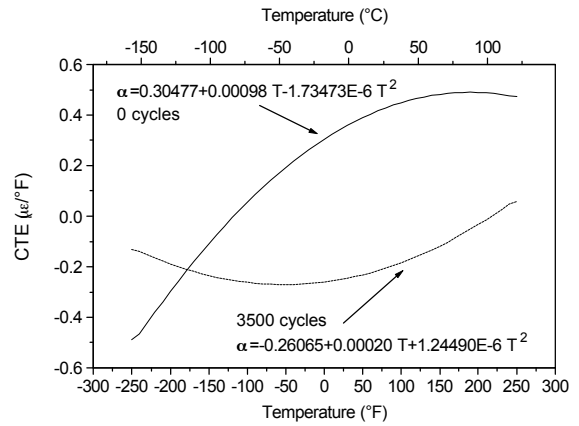

Figure D.24. Average thermal expansion data for specimen series I - P75/ERL1962.Q1.5.G - P75/ERL1962, $[0/+45/-45/90]_S$, 5 mil, ±250°F.

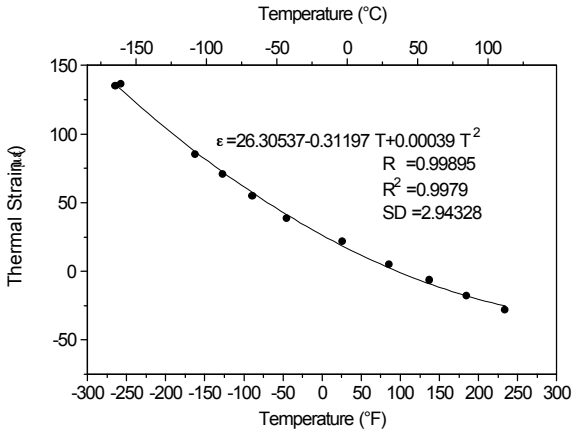

(a) R-1 - 0 cycles

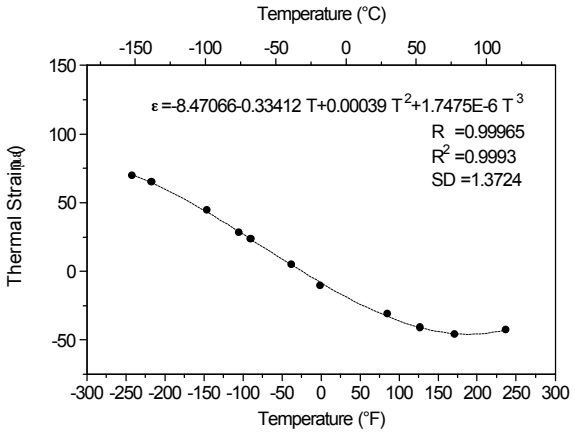

(b) R-3 - 0 cycles

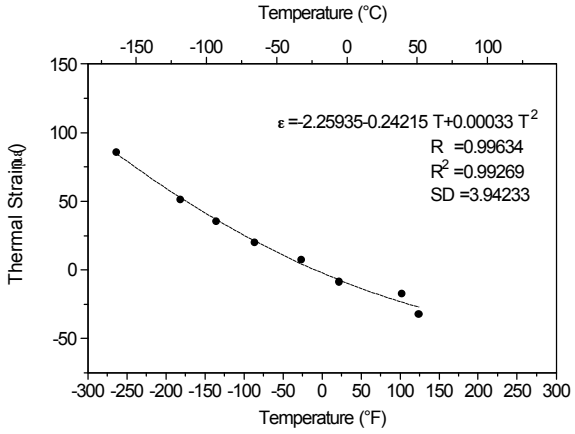

(c) R-4 - 0 cycles

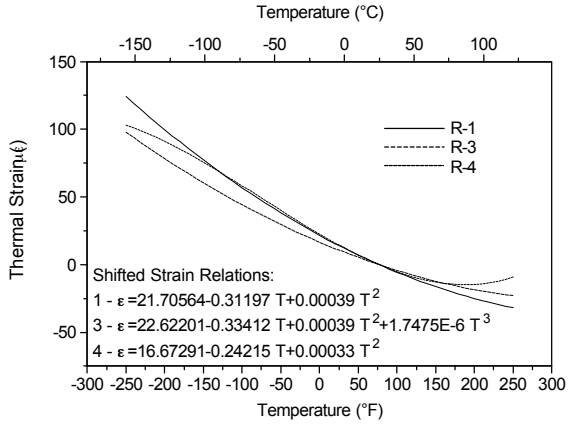

(d) Shifted strain data for R-1, 3, and 4

Figure D.25. Thermal strain data for specimens R-1, 3, and 4 at 0 cycles.

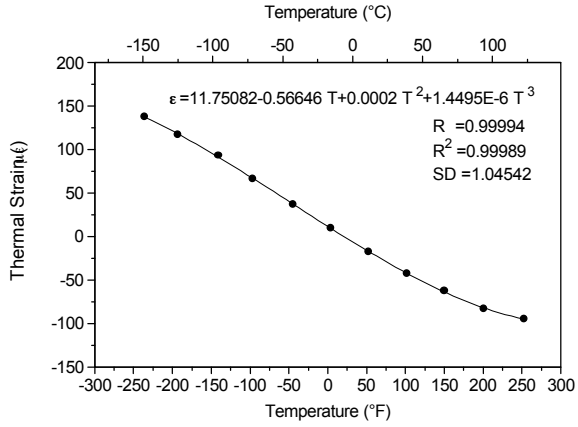

(a) R-1 - 3500 cycles

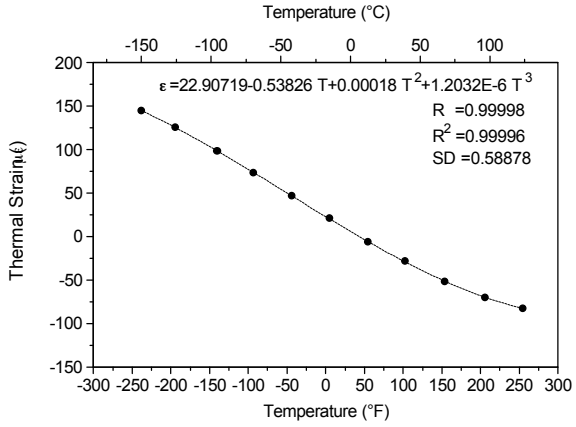

(b) R-3 - 3500 cycles

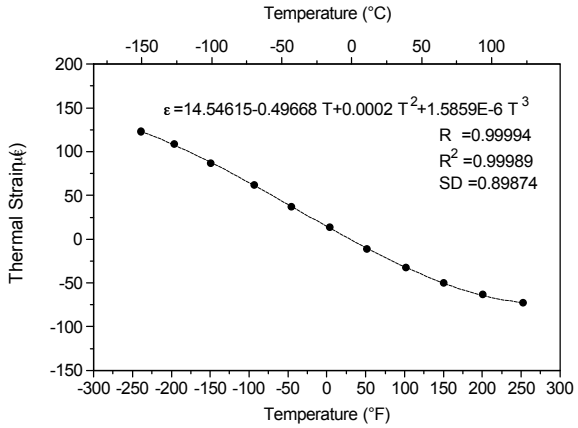

(c) R-4 - 3500 cycles

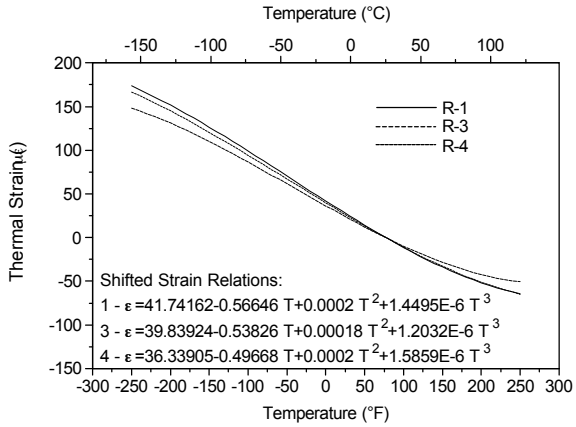

(d) Shifted strain data for R-1, 3, and 4

Figure D.26. Thermal strain data for specimens R-1, 3, and 4 at 3500 cycles.

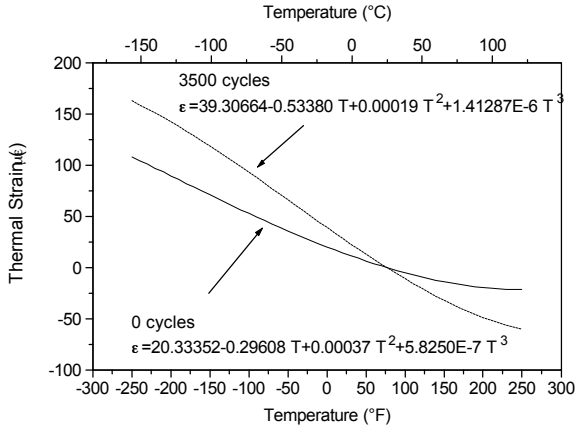

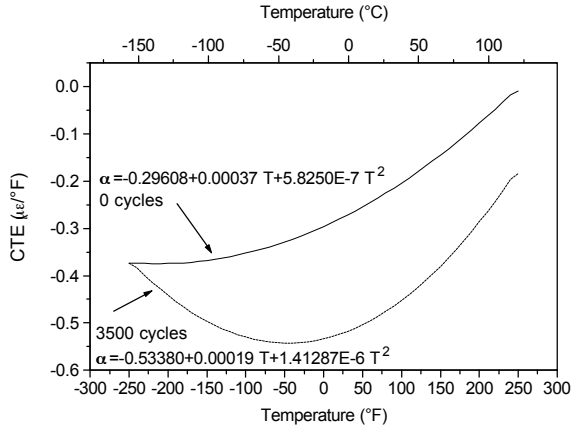

Figure D.27. Average thermal expansion data for specimen series R - P120/ERL1962.Q1.5.G - P120/ERL1962, $[0/+45/-45/90]_S$, 5 mil, ±250°F.

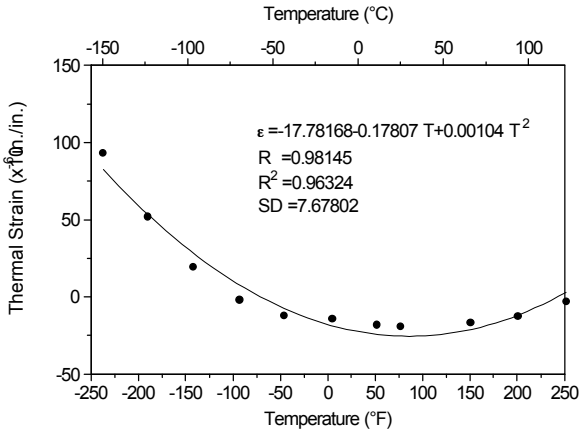

(a) 6762-1 - 0 cycles

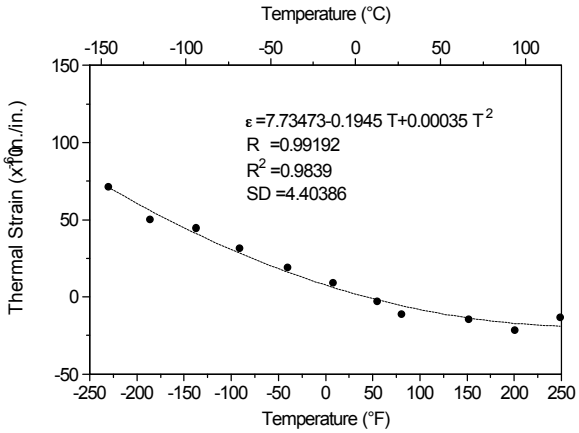

(b) 6762-3 - 0 cycles

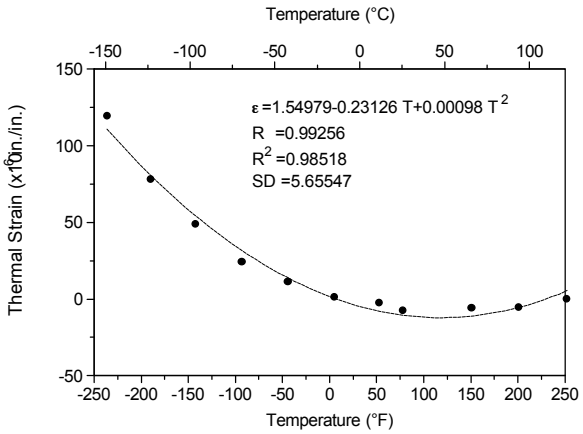

(c) 6762-5 - 0 cycles

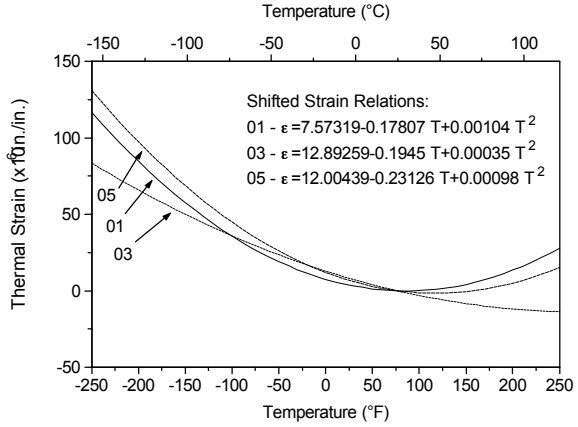

(d) Shifted strain data for 6762-1, 3, 5

Figure D.28. Thermal strain data for specimens 6762-1, 3, and 5 at 0 cycles.

It is noted that for the L (±150°F) and C (±50°F) thermal cycling temperature ranges for specimen series 6762, zero cycle data were not recorded, but instead were assumed to be characterized by the zero cycle data for the G (±250°F) thermal cycling range shown in Figure D.28. Therefore, data from the G thermal cycling range specimens are included with results for the L and C temperature ranges as a reference. This same philosophy is used for specimen series 75RS3, 75R-A, and 275RS3 that will be seen later in this appendix.

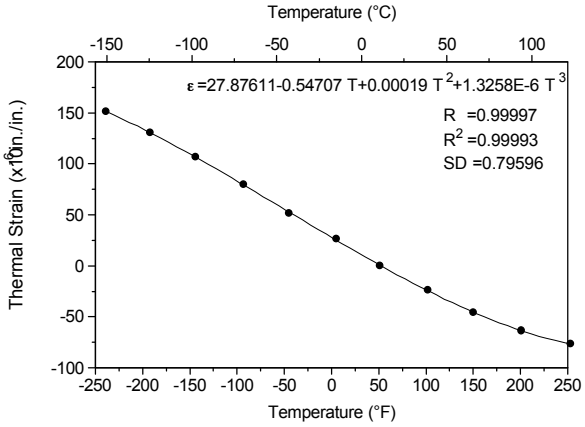

(a) 6762-1 - 3000 cycles

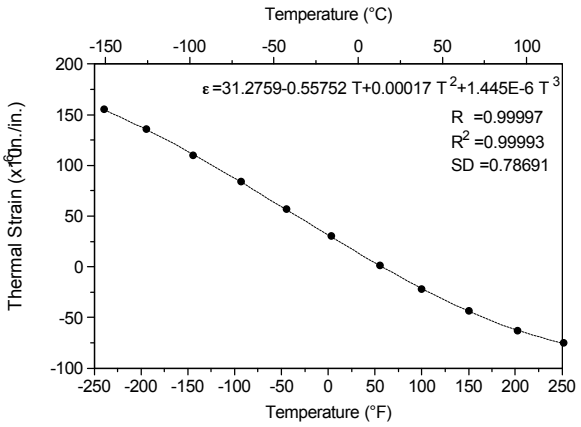

(b) 6762-3 - 3000 cycles

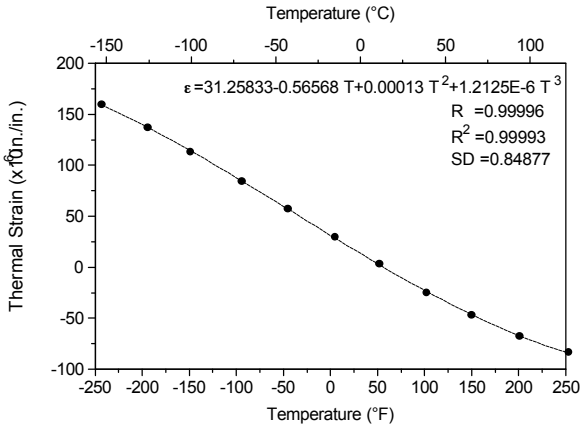

(c) 6762-5 - 3000 cycles

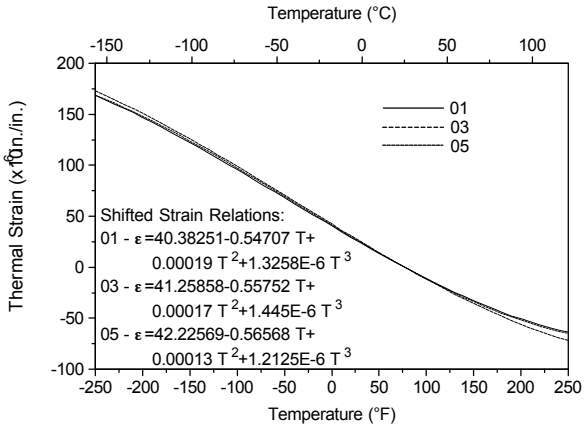

(d) Shifted strain data for 6762-1, 3, 5

Figure D.29. Thermal strain data for specimens 6762-1, 3, and 5 at 3000 cycles.

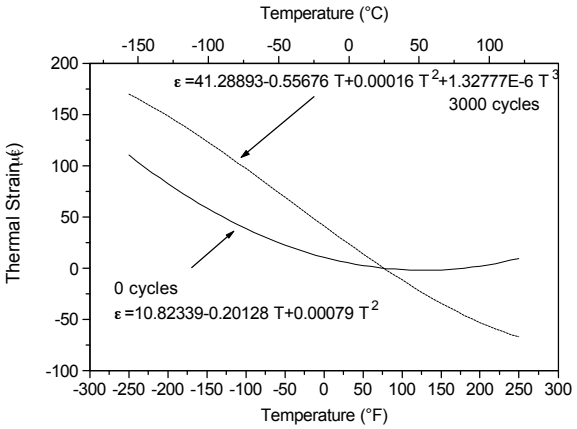

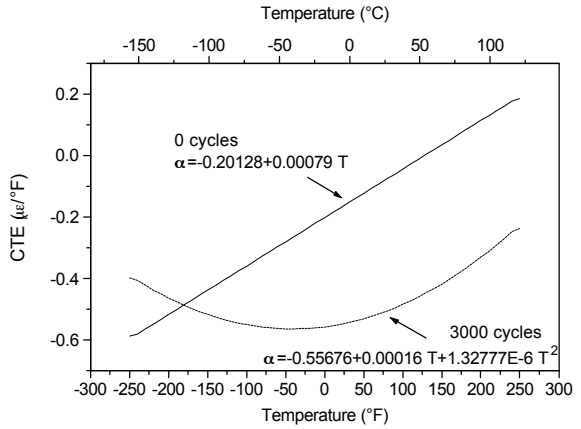

Figure D.30. Average thermal expansion data for specimen series 6762 - P75/ERL1962.Q2.5.G - P75/ERL1962, $[0/+45/90/-45]_S$, 5 mil, ±250°F.

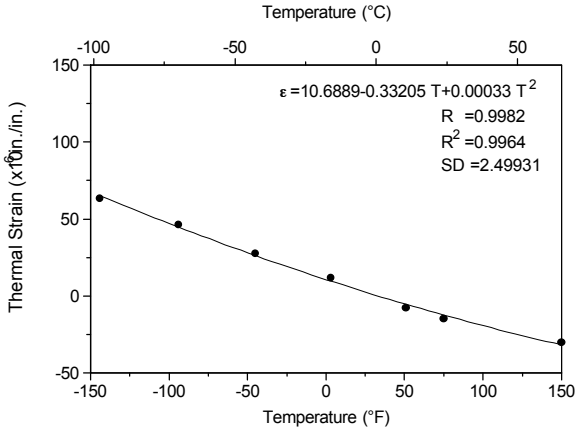

(a) 6762-02 - 4000 cycles

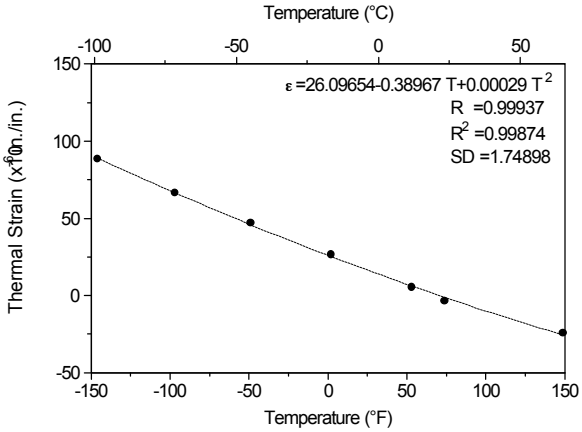

(b) 6762-04 - 4000 cycles

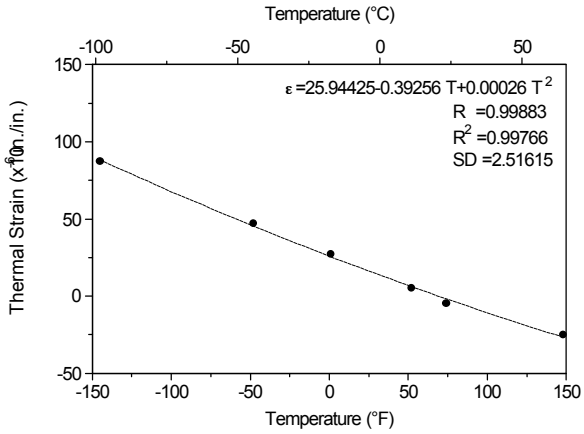

(c) 6762-06 - 4000 cycles

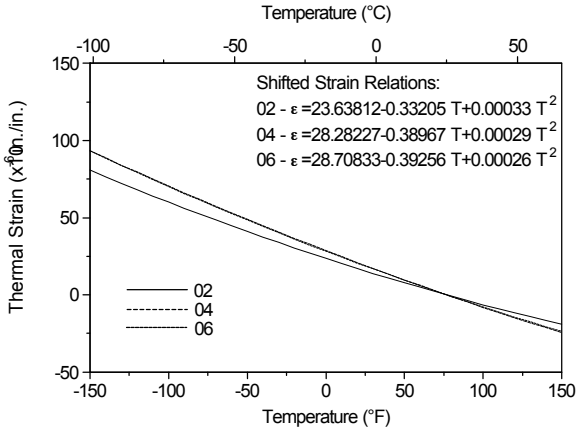

(d) Shifted strain data for 6762-02, 04, 06

Figure D.31. Thermal strain data for specimens 6762-02, 04, and 06 at 4000 cycles.

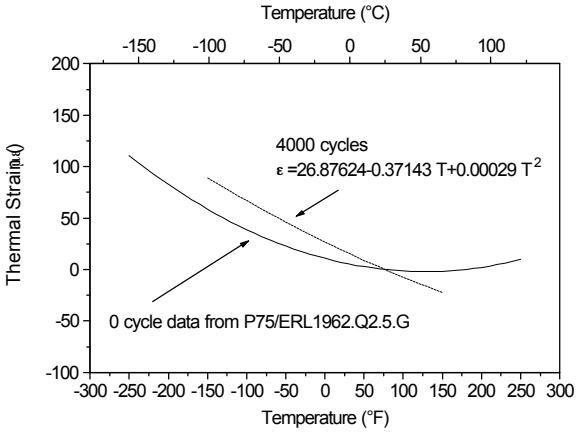

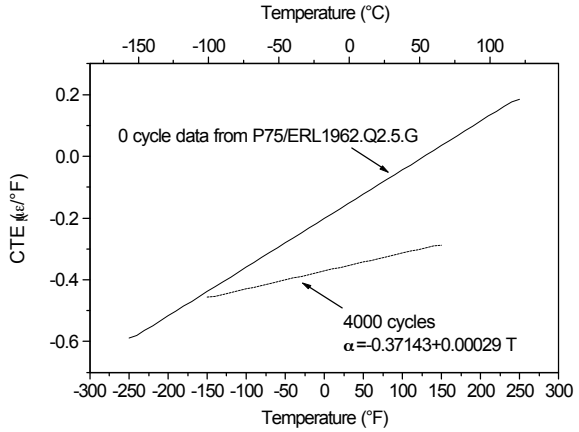

Figure D.32. Average thermal expansion data for specimen series 6762 - P75/ERL1962.Q2.5.L - P75/ERL1962, $[0/+45/90/-45]_S$, 5 mil, ±150°F.

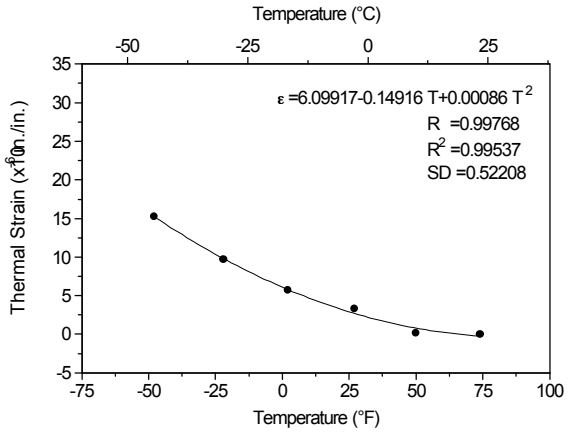

(a) 6762-07 - 4000 cycles

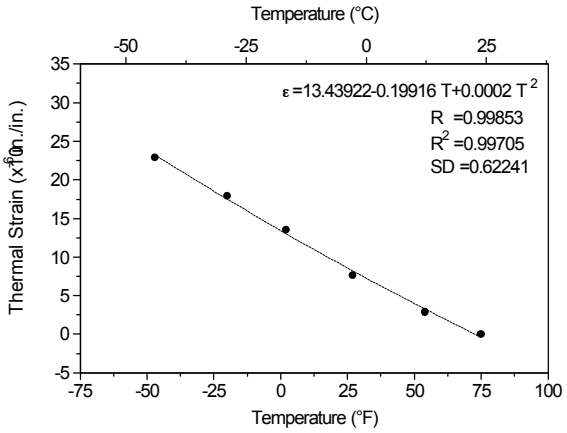

(b) 6762-08 - 4000 cycles

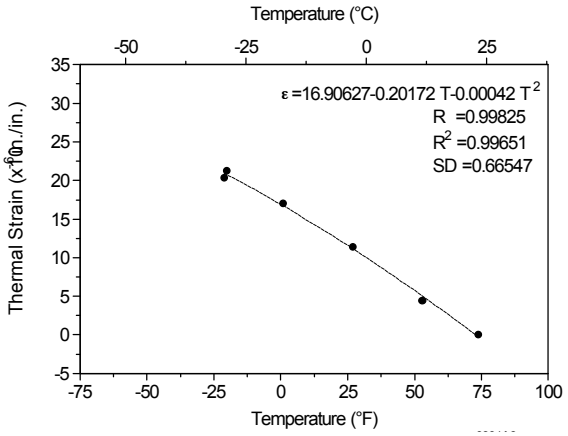

(c) 6762-09 - 4000 cycles

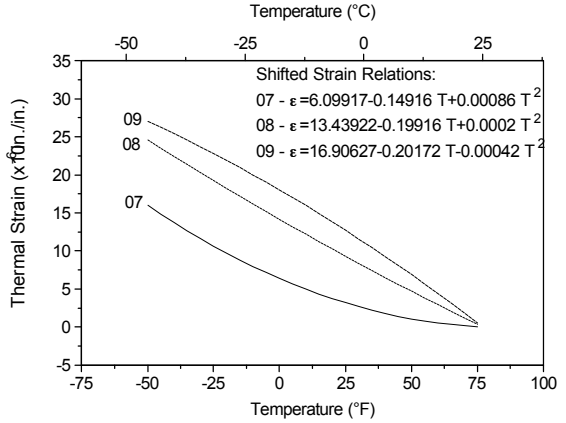

(d) Shifted strain data for 6762-07, 08, 09

Figure D.33. Thermal strain data for specimens 6762-07, 08, and 09 at 4000 cycles.

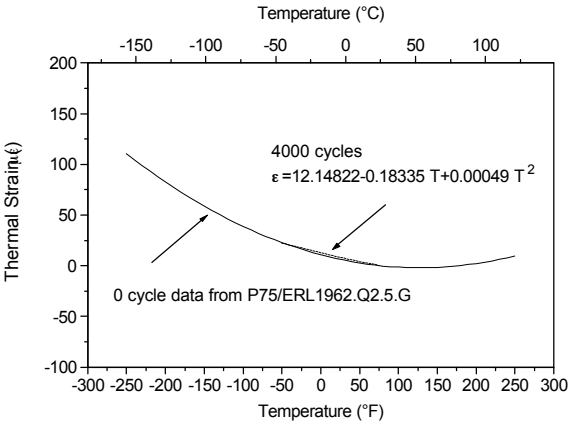

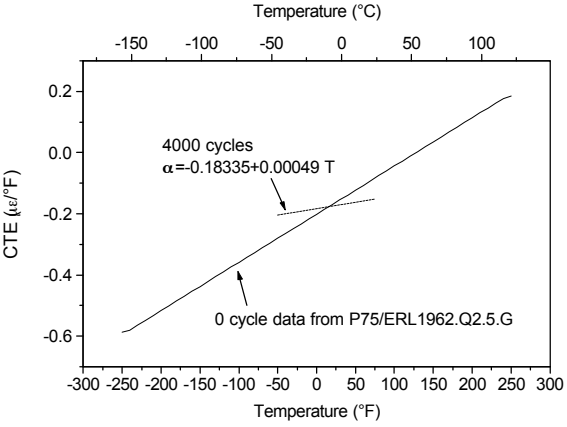

Figure D.34. Average thermal expansion data for specimen series 6762 - P75/ERL1962.Q2.5.C - P75/ERL1962, $[0/+45/90/-45]_S$, 5 mil, ±50°F.

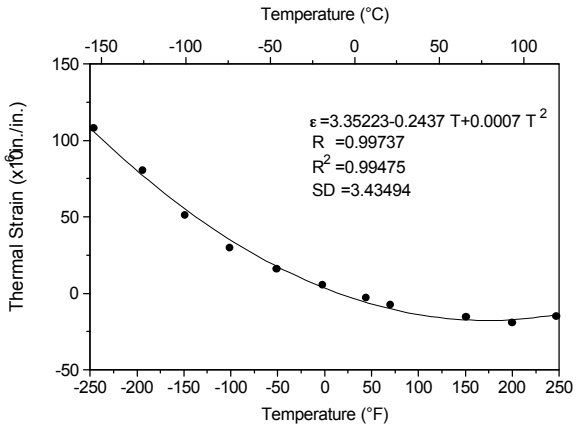

(a) 75RS3-01 - 0 cycles

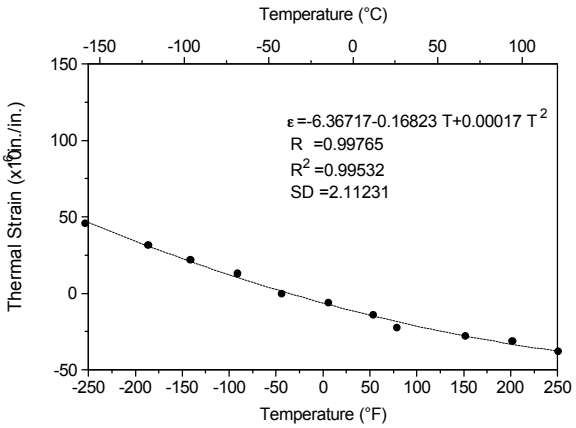

(b) 75RS3-02 - 0 cycles

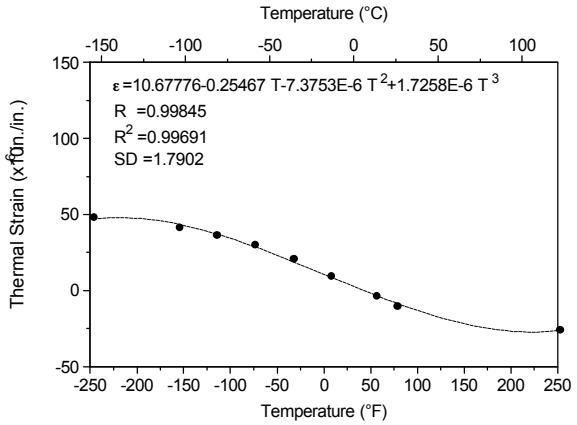

(c) 75RS3-03 - 0 cycles

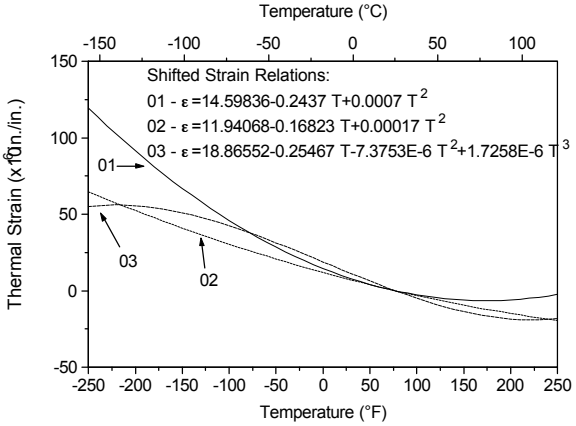

(d) Shifted strain data for 75RS3-01, 02, 03

Figure D.35. Thermal strain data for specimens 75RS3-01, 02, and 03 at 0 cycles.

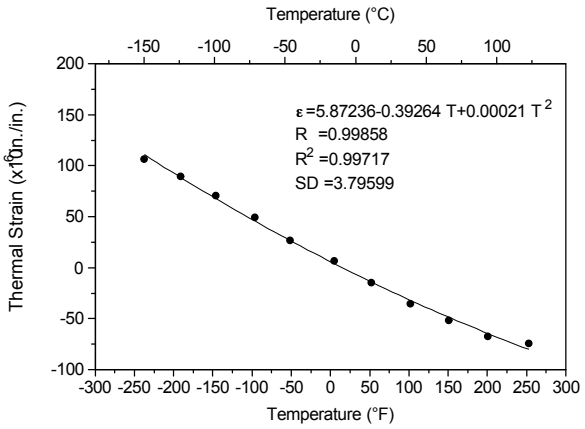

(a) 75RS3-01 - 3000 cycles

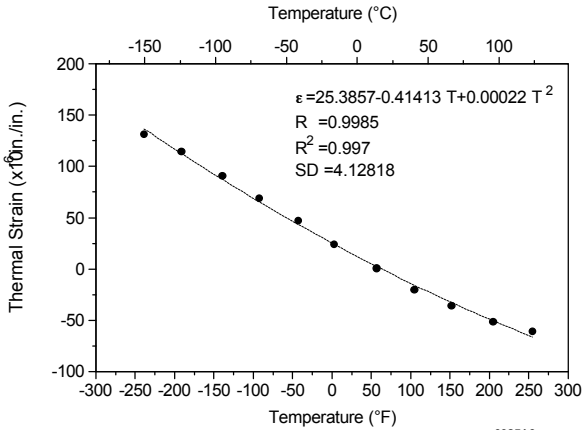

(b) 75RS3-02 - 3000 cycles

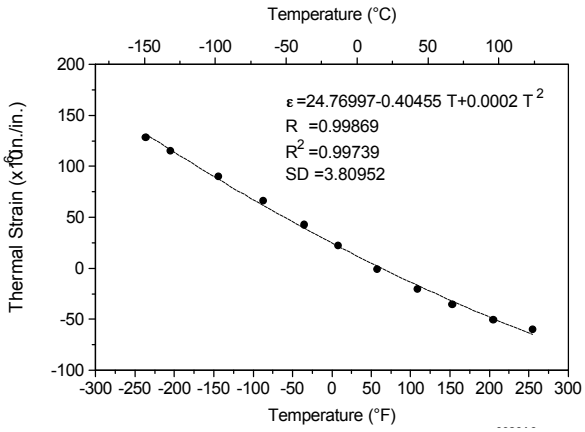

(c) 75RS3-03 - 3000 cycles

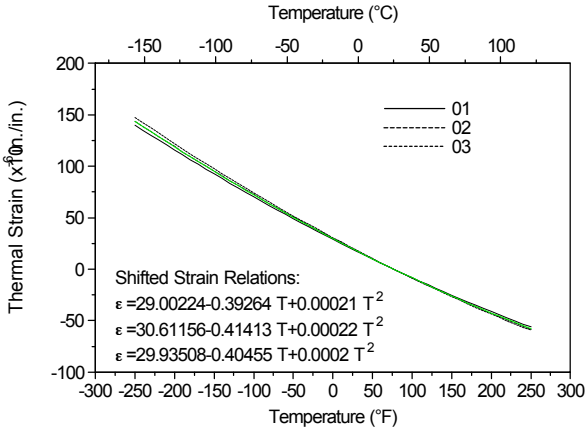

(d) Shifted strain data for 75RS3-01, 02, 03

Figure D.36. Thermal strain data for specimens 75RS3-01, 02, and 03 at 3000 cycles.

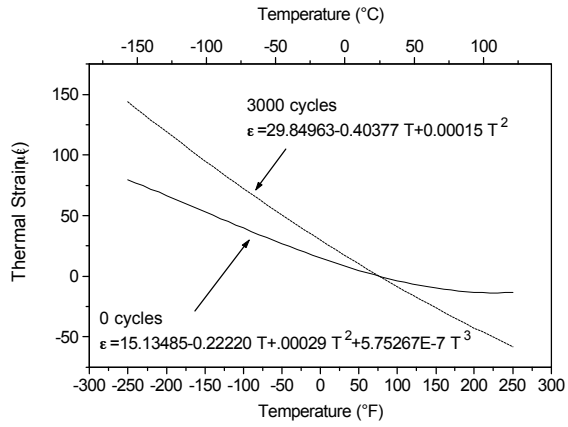

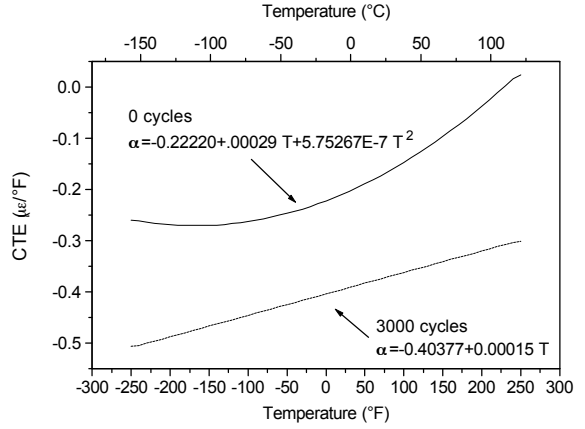

Figure D.37. Average thermal expansion data for specimen series 75RS3 - P75/RS3.Q2.5.G - P75/RS3, $[0/+45/90/-45]_S$, 5 mil, ±250°F.

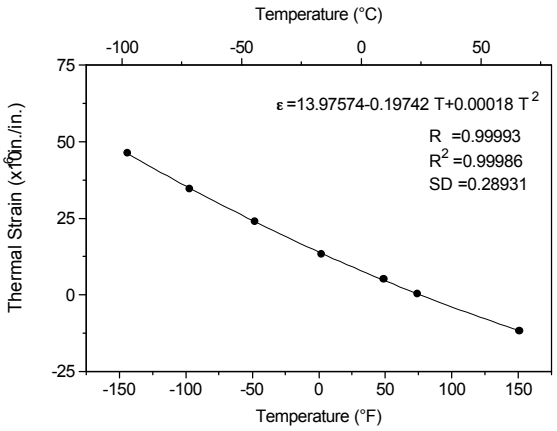

(a) 75RS3-04 - 4000 cycles

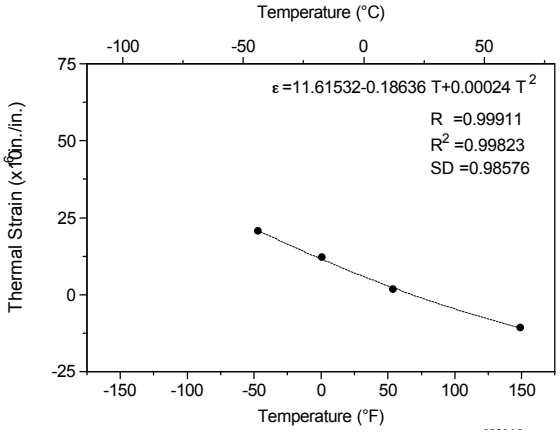

(b) 75RS3-05 - 4000 cycles

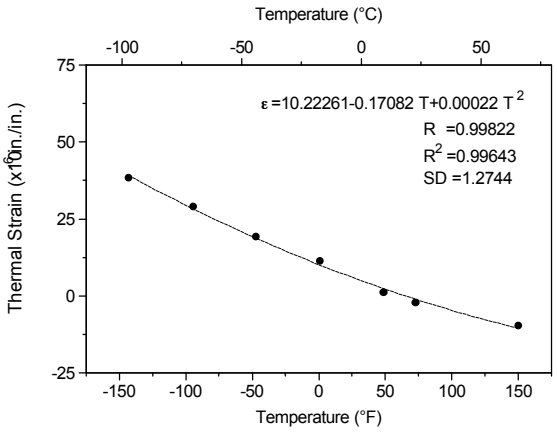

(c) 75RS3-06 - 4000 cycles

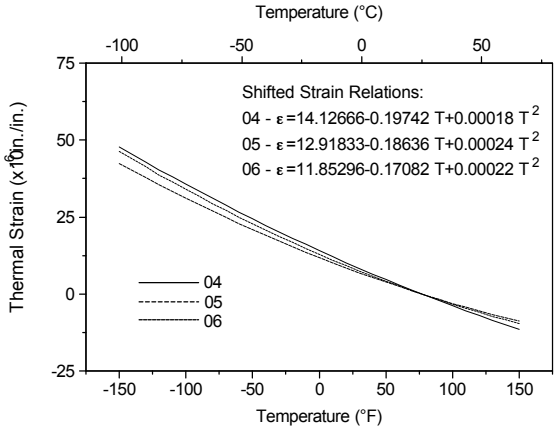

(d) Shifted strain data for 75RS3-04, 05, 06

Figure D.38. Thermal strain data for specimens 75RS3-04, 05, and 06 at 4000 cycles.

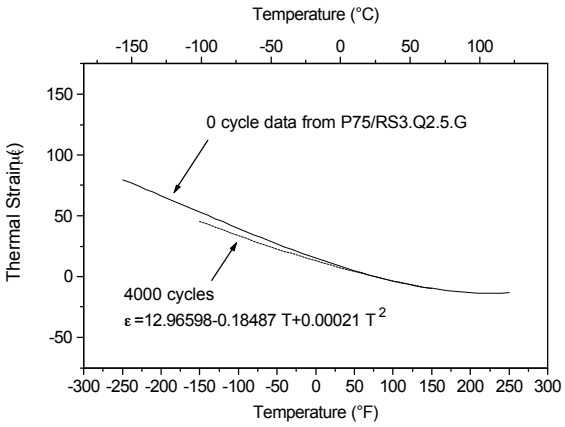

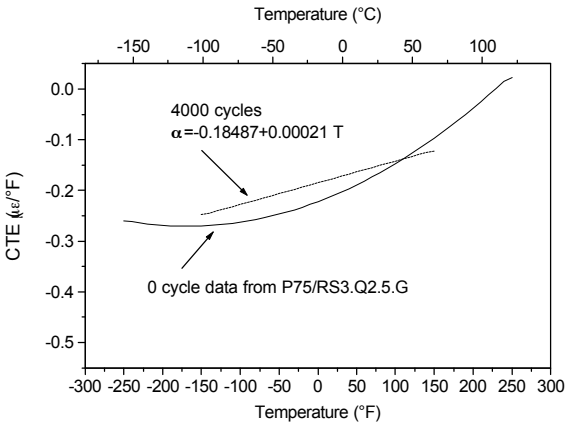

Figure D.39. Average thermal expansion data for specimen series 75RS3 - P75/RS3.Q2.5.L - P75/RS3, $[0/+45/90/-45]_S$, 5 mil, ±150°F.

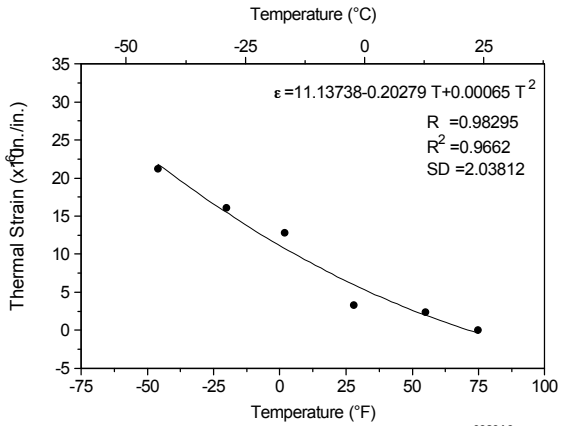

(a) 75RS3-07 - 4000 cycles

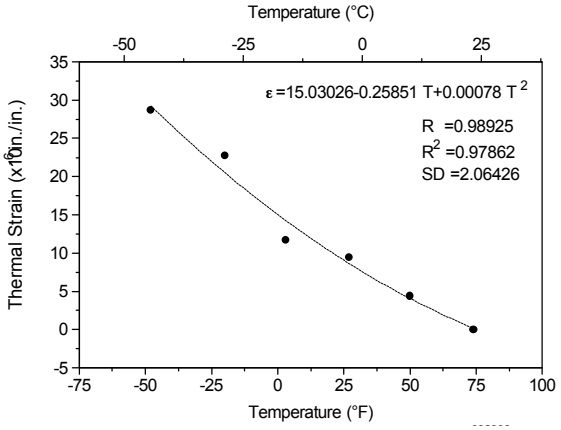

(b) 75RS3-08 - 4000 cycles

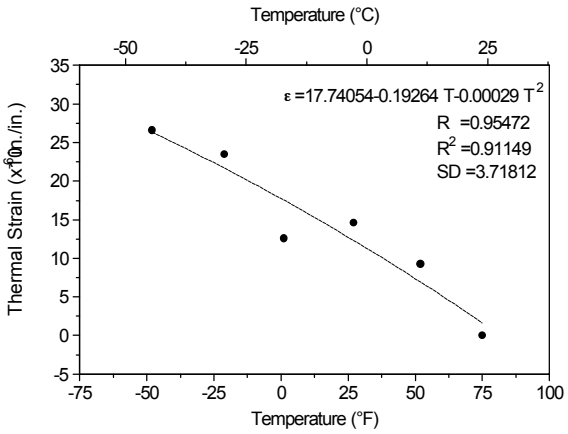

(c) 75RS3-09 - 4000 cycles

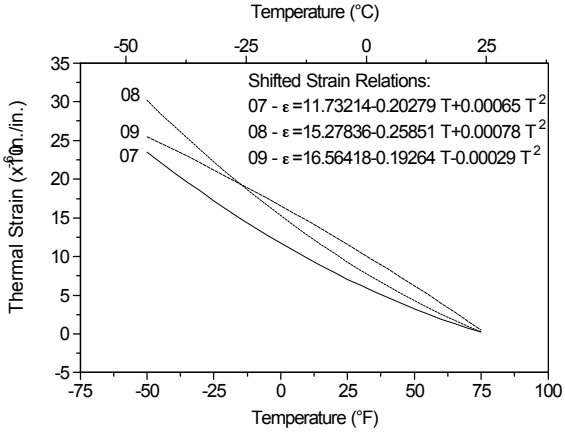

(d) Shifted strain data for 75RS3-07, 08, and 09

Figure D.40. Thermal strain data for specimens 75RS3-07, 08, and 09 at 4000 cycles.

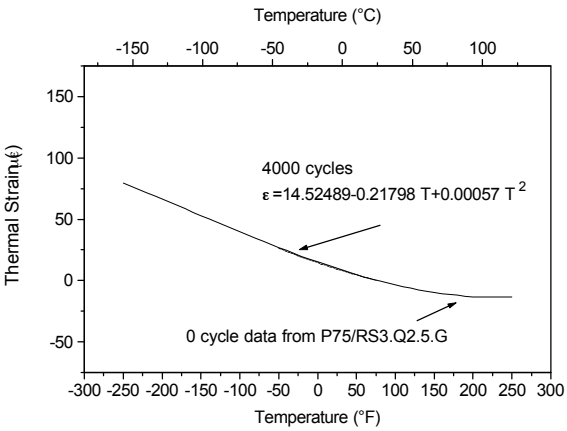

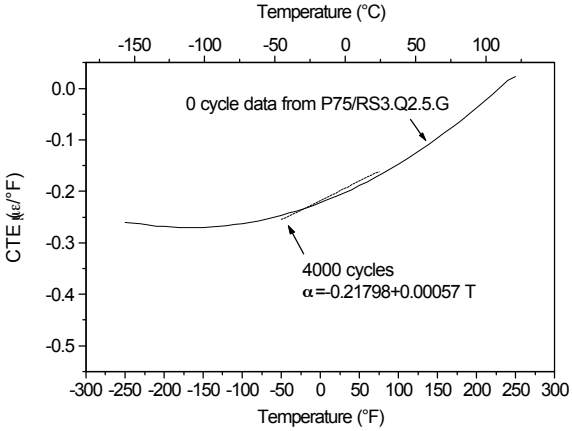

Figure D.41. Average thermal expansion data for specimen series 75RS3 - P75/RS3.Q2.5.C - P75/RS3, $[0/+45/90/-45]_S$, 5 mil, ±50°F.

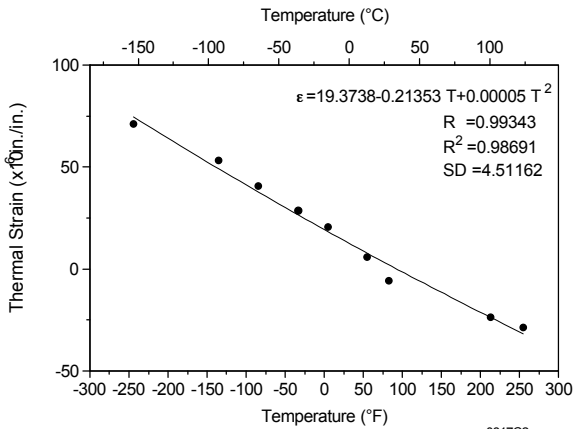

(a) 75R-A-35 - 0 cycles

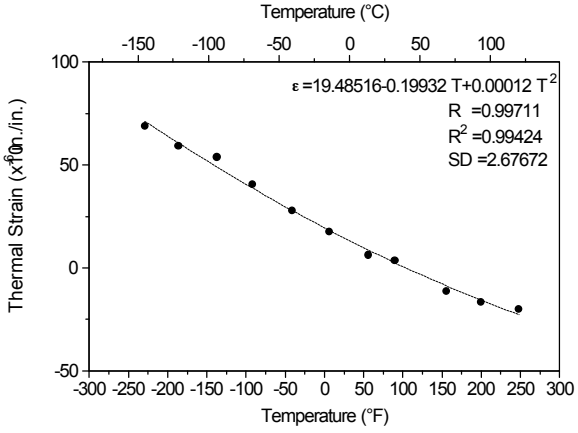

(b) 75R-A-43 - 0 cycles

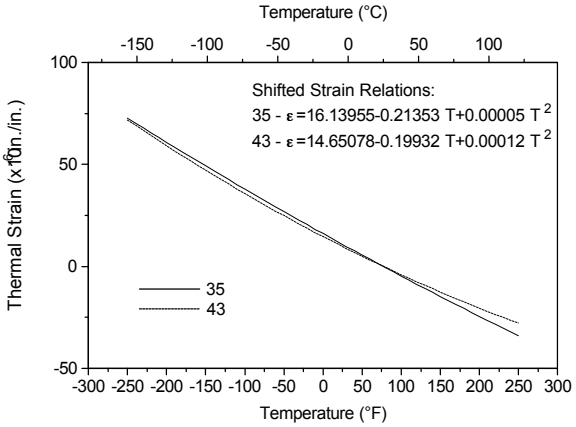

(c) Shifted strain data for 75R-A-35,43

Figure D.42. Thermal strain data for specimens 75R-A-35 and 43 at 0 cycles.

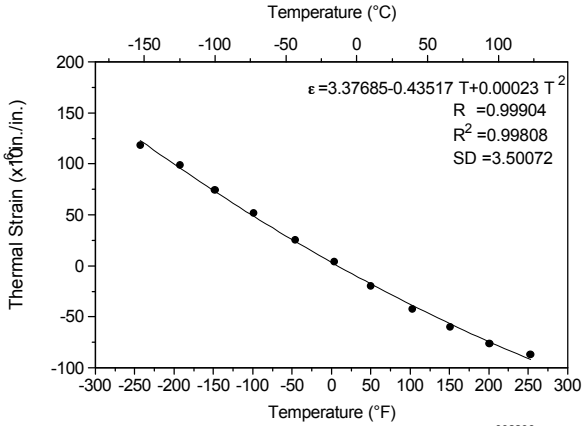

(a) 75R-A-41 - 4000 cycles

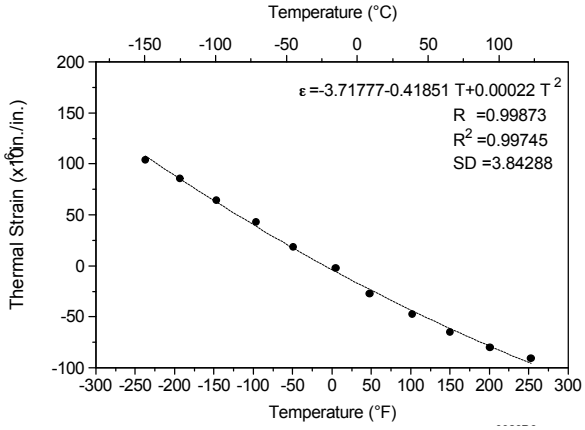

(b) 75R-A-43 - 3500 cycles

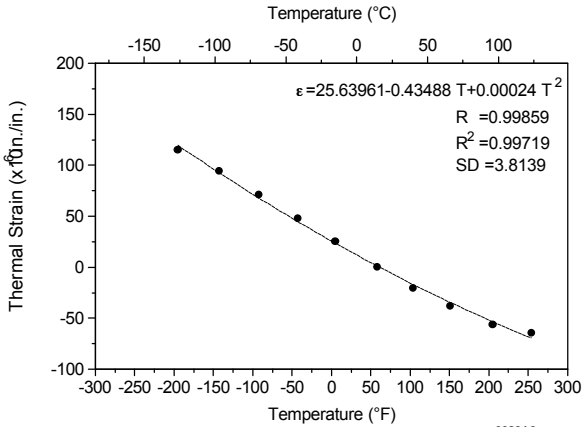

(c)75R-A-44 - 3000 cycles

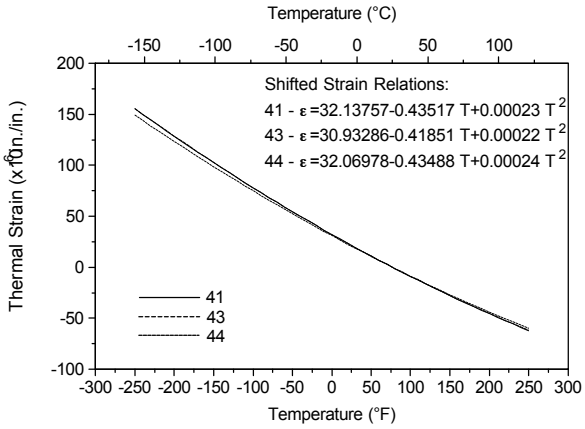

(d) Shifted strain data for 75R-A-41, 43, and 44

Figure D.43. Thermal strain data for specimens 75R-A-41, 43, and 44 at 4000, 3500, and 3000 cycles respectively.

Note that for series 75R-A in Figure D.44, the thermal expansion data are labeled as 3000-4000 cycles. This is because the three specimens from that series were at different stages in cycling (3000, 3500, and 4000 cycles) when thermal expansion data were recorded. Despite this, the behavior was virtually identical for all three specimens and has been included here as a single average.

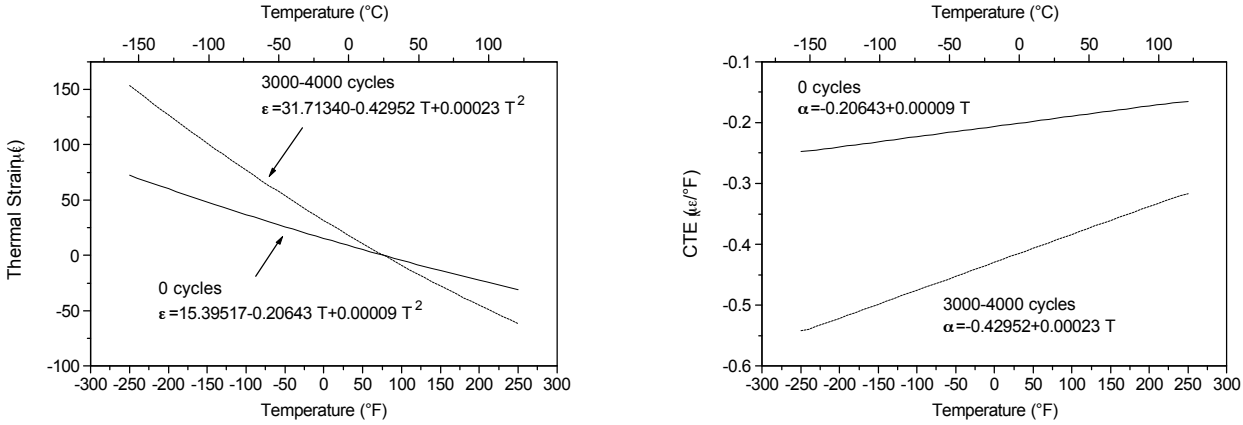

Figure D.44. Average thermal expansion data for specimen series 75R-A - P75/RS3.Q2.5.G - P75/RS3, $[0/+45/90/-45]_S$, 5 mil, ±250°F.

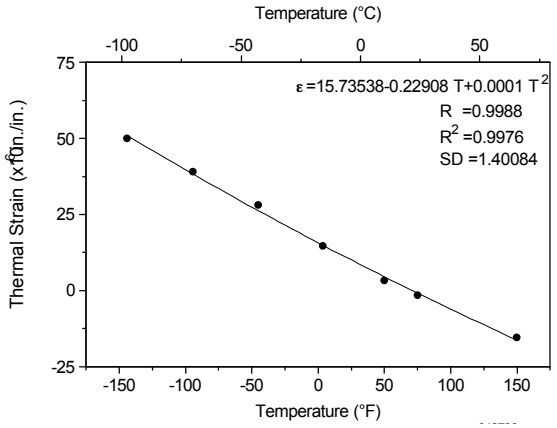

(a) 75R-A-36 - 4000 cycles

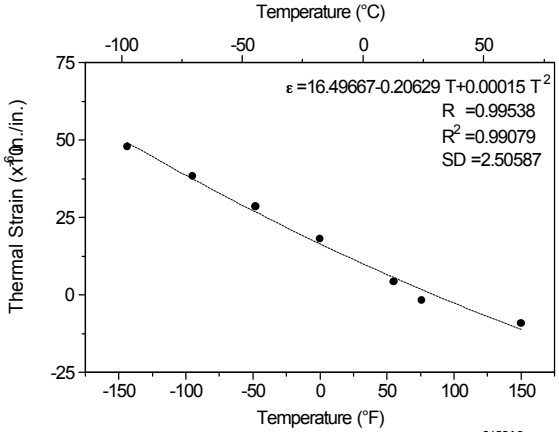

(b) 75R-A-37 - 4000 cycles

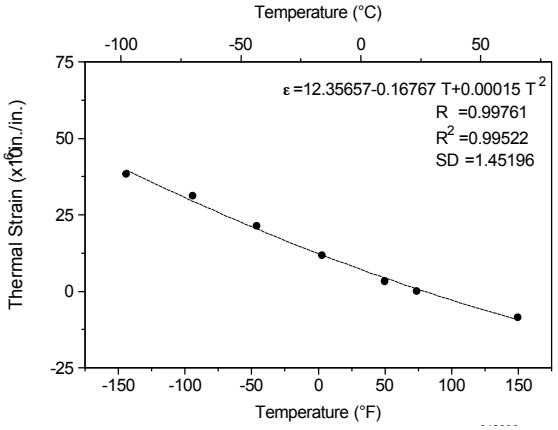

(c) 75R-A-45 - 4000 cycles

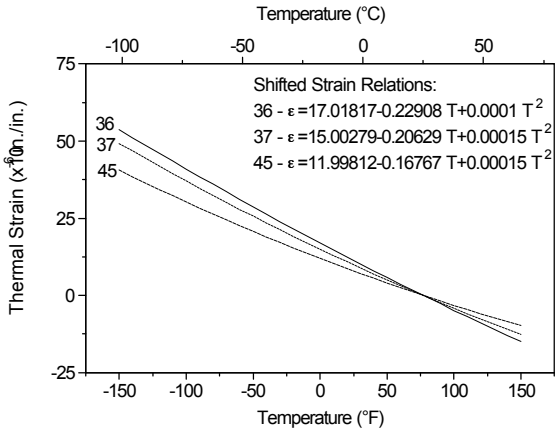

(d) Shifted strain data for 75R-A-36, 37, and 45

Figure D.45. Thermal strain data for specimens 75R-A-36, 37, and 45 at 4000 cycles.

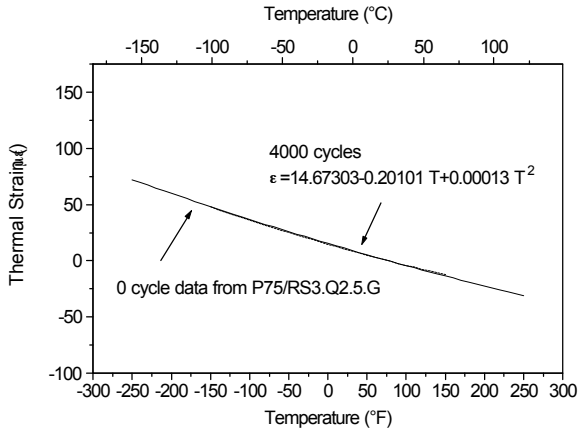

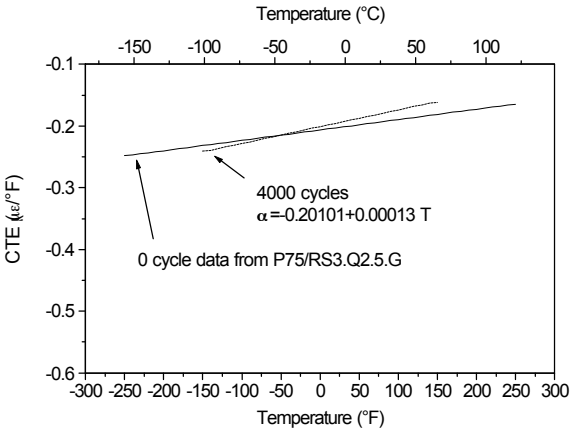

Figure D.46. Average thermal expansion data for specimen series 75R-A - P75/RS3.Q2.5.L - P75/RS3, $[0/+45/90/-45]_S$, 5 mil, ±150°F.

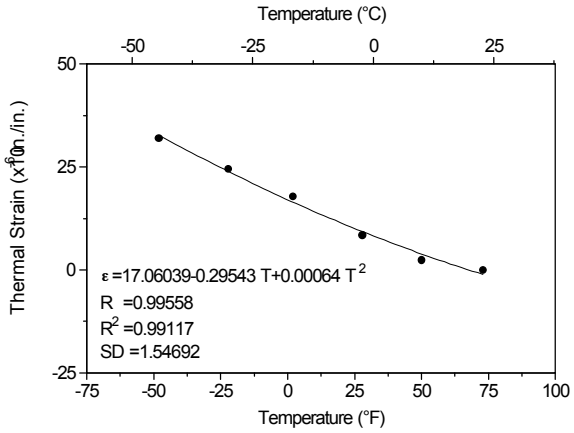

(a) 75R-A-38 - 4000 cycles

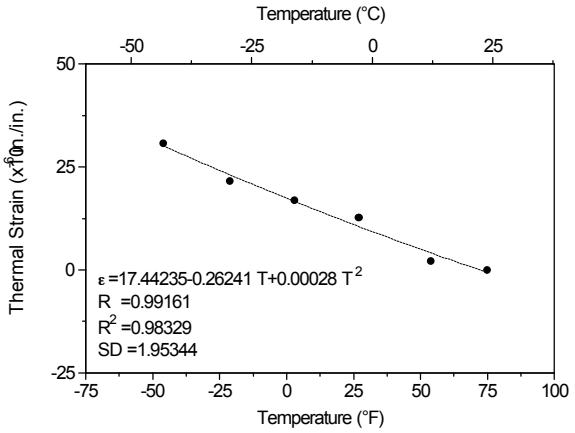

(b) 75R-A-39 - 4000 cycles

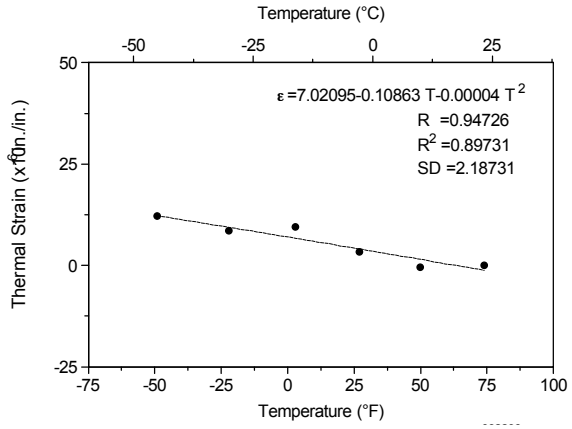

(c) 75R-A-46 - 4000 cycles

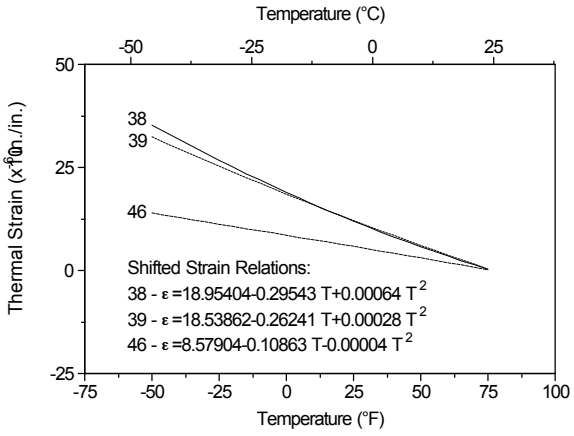

(d) Shifted strain data for 75R-A-38, 39, and 46

Figure D.47. Thermal strain data for specimens 75R-A-38, 39, and 46 at 4000 cycles.

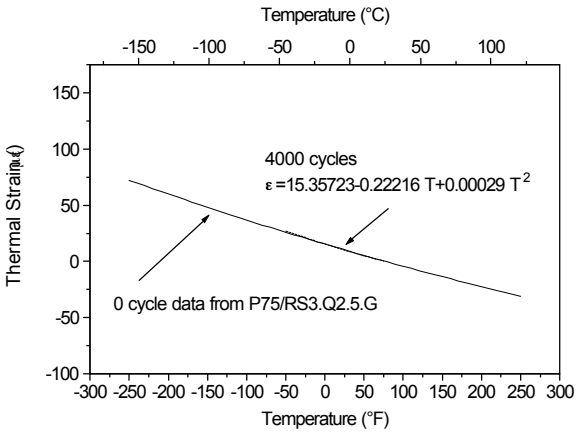

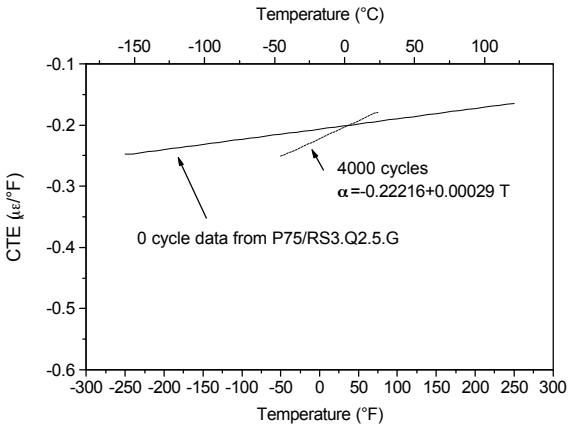

Figure D.48. Average thermal expansion data for specimen series 75RS3 and 75R-A - P75/RS3.Q2.5.C - P75/RS3, $[0/+45/90/-45]_S$, 5 mil, ±50°F.

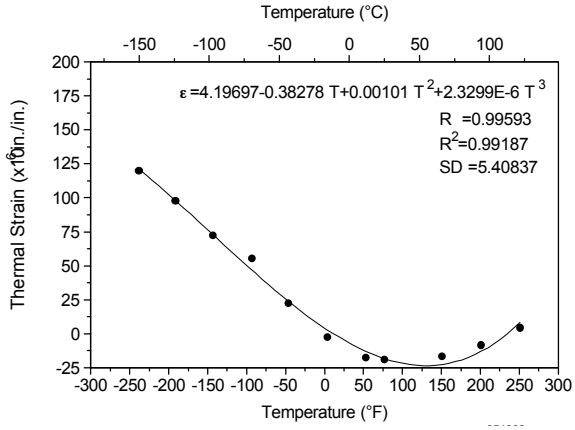

(a) P734Q-2 - 0 cycles

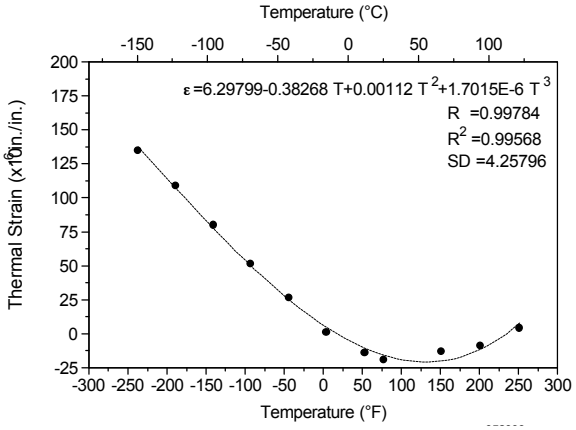

(b) P734Q-3 - 0 cycles

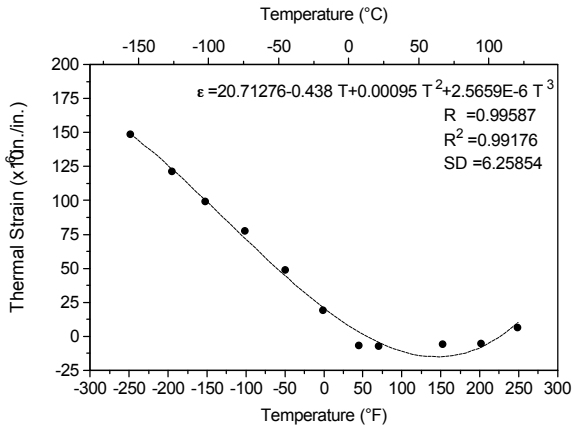

(c) P734Q-4 - 0 cycles

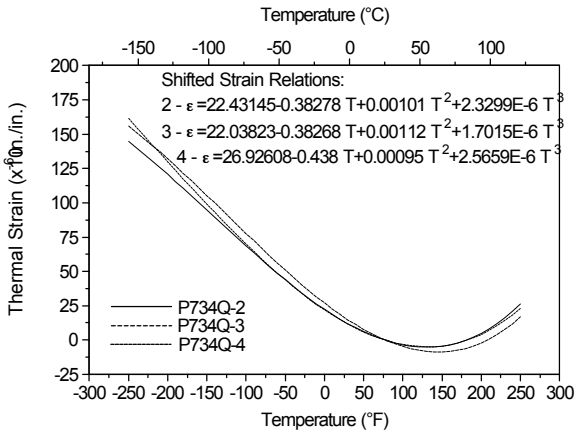

(d) Shifted strain data for P734Q-2, 3, and 4

Figure D.49. Thermal strain data for specimens P734Q-2, 3, and 4 at 0 cycles.

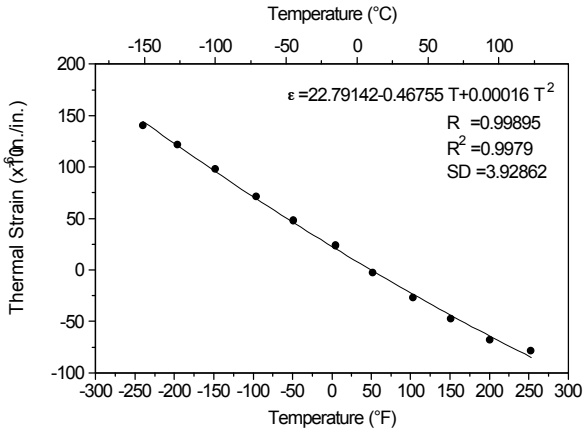

(a) P734Q-2 - 3000 cycles

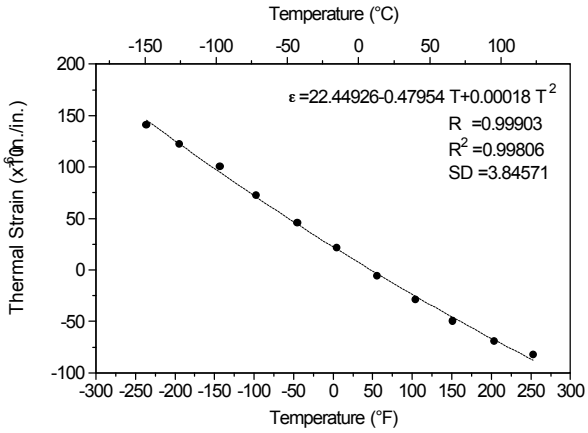

(b) P734Q-3 - 3000 cycles

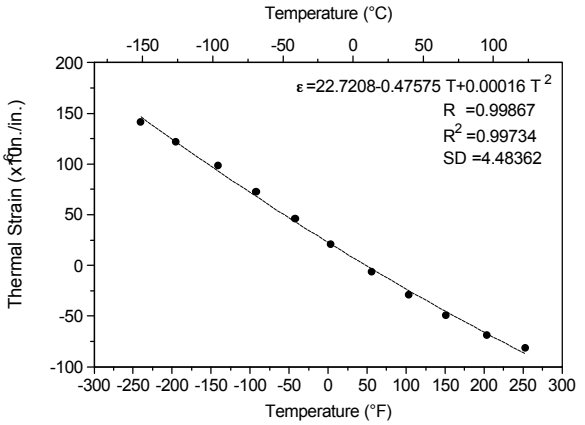

(c) P734Q-4 - 3000 cycles

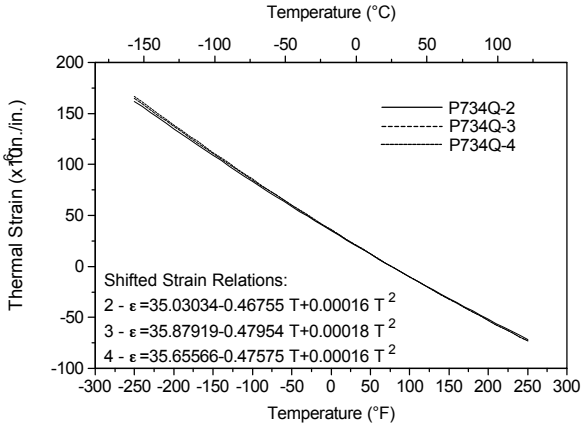

(d) Shifted strain data for P734Q-2, 3, and 4

Figure D.50. Thermal strain data for specimens P734Q-2, 3, and 4 at 3000 cycles.

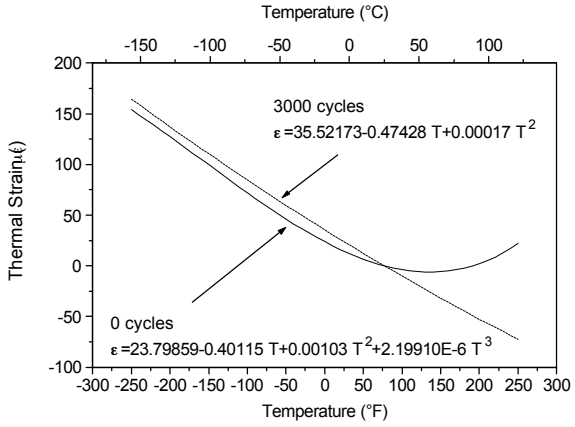

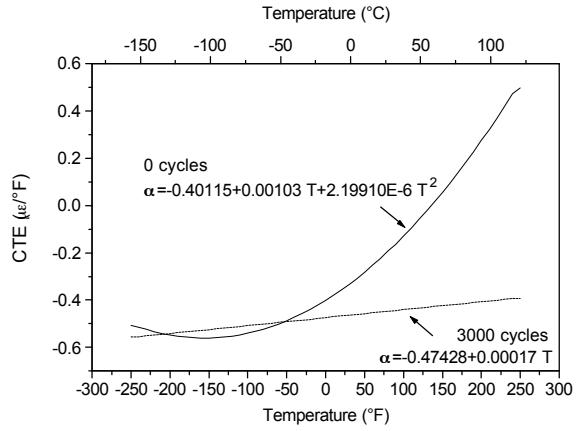

Figure D.51. Average thermal expansion data for specimen series P734Q - P75/934.Q2.5.G - P75/934, $[0/+45/90/-45]_S$, 5 mil, ±250°F.

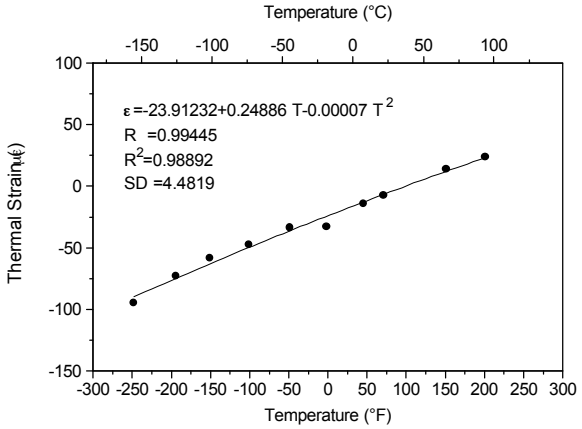

(a) 275RS3-01 - 0 Cycles

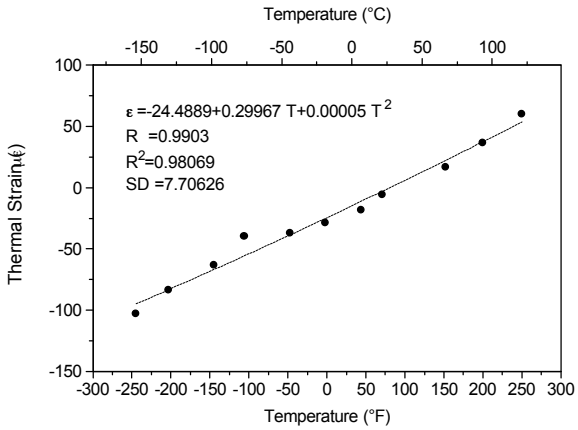

(b) 275RS3-02 - 0 Cycles

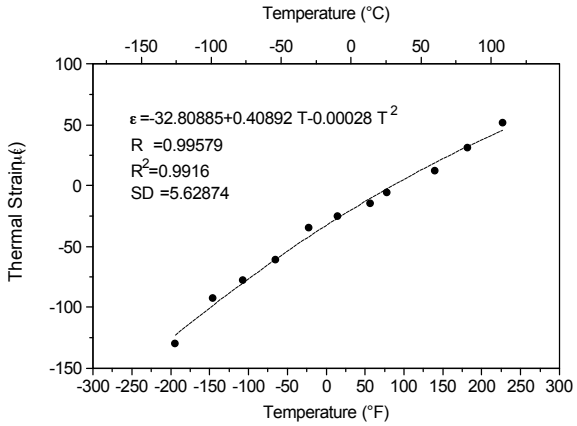

(c) 275RS3-03 - 0 Cycles

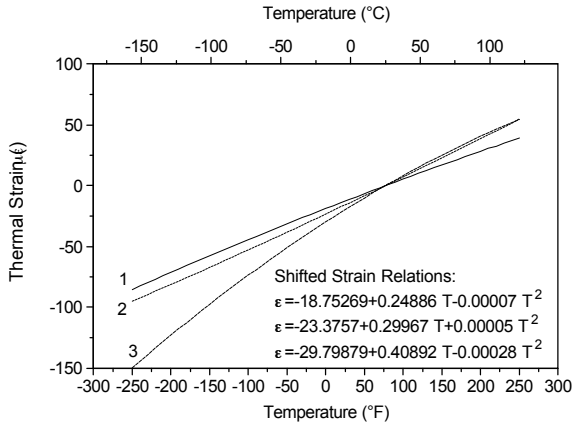

(d) Shifted strain data for 275RS3-01, 02, 03

Figure D.52. Thermal strain data for specimens 275RS3-01, 02, and 03 at 0 cycles.

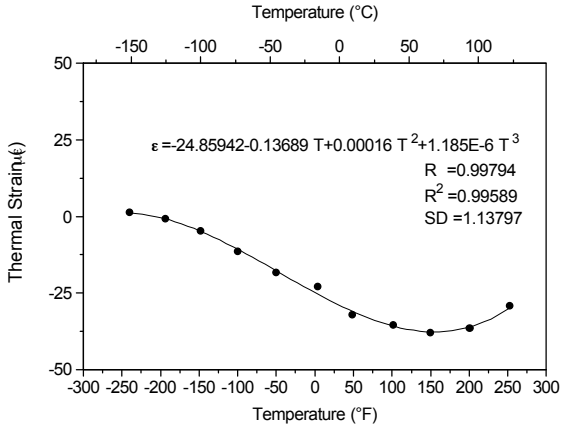

(a) 275RS3-01 - 3000 cycles

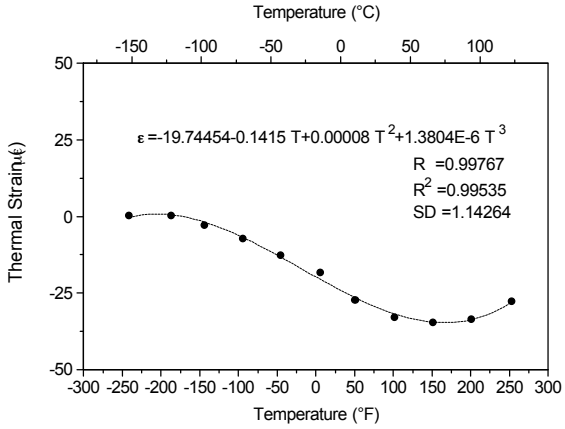

(b) 275RS3-02 - 3000 cycles

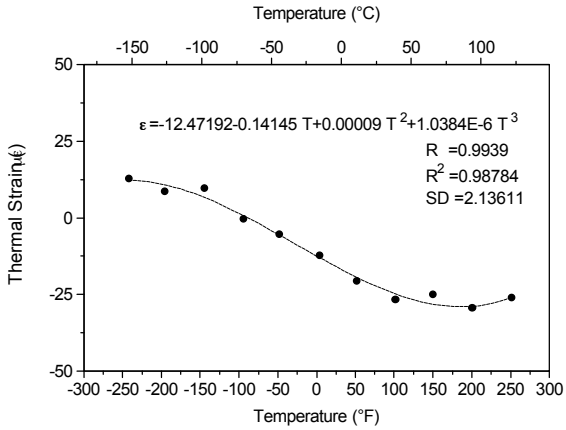

(c) 275RS3-03 - 3000 cycles

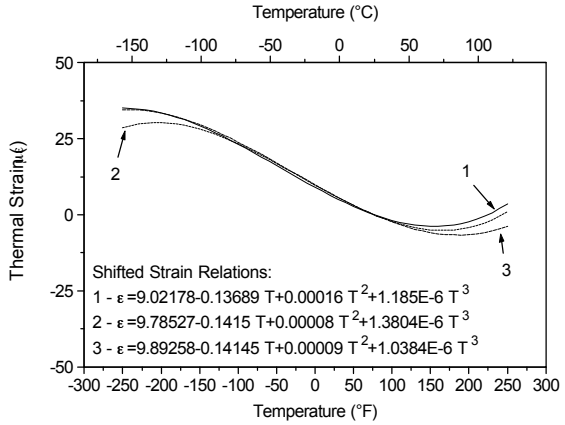

(d) Shifted strain data for 275RS3-01, 02, 03

Figure D.53. Thermal strain data for specimens 275RS3-01, 02, and 03 at 3000 cycles.

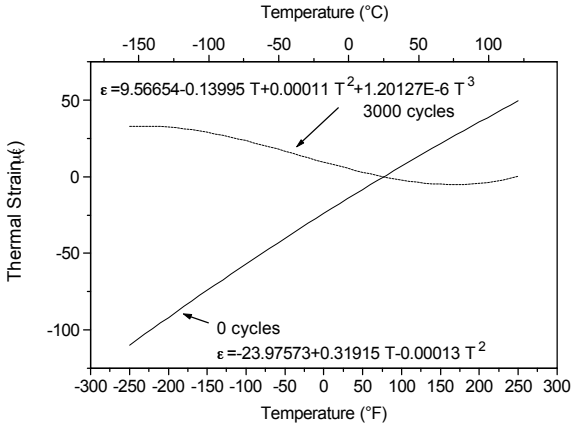

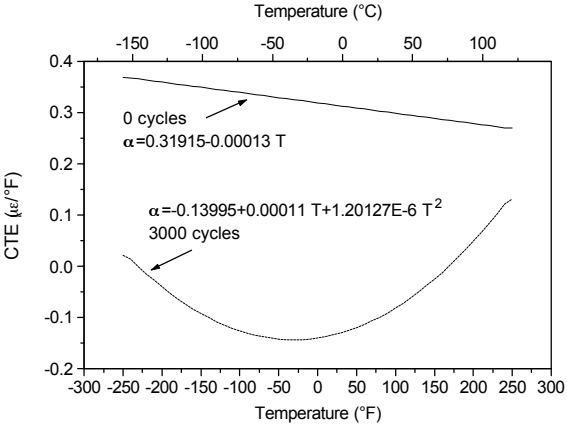

Figure D.54. Average thermal expansion data for specimen series 275RS3 - P75/RS3.Q2.2.G - P75/RS3, $[0/+45/90/-45]_S$, 2 mil, ±250°F.

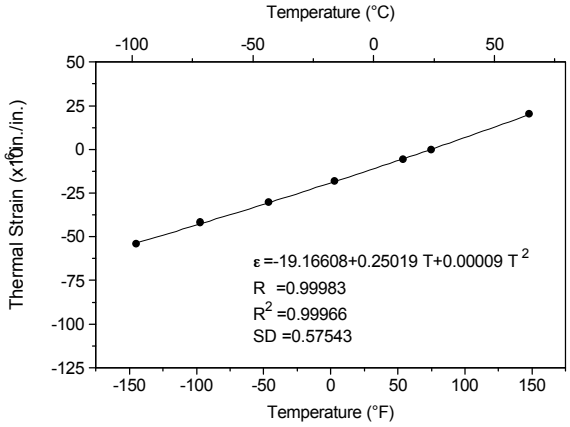

(a) 275RS3-04 - 4000 cycles

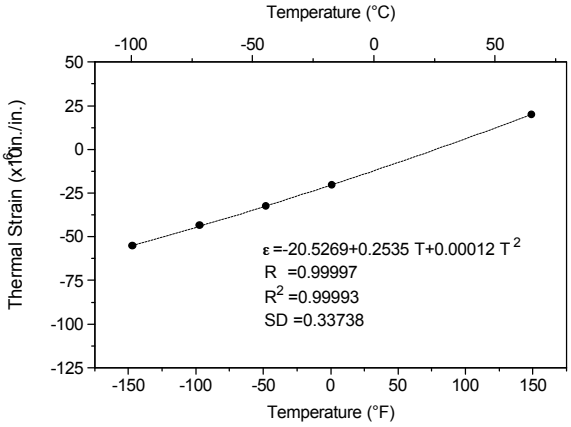

(b) 275RS3-05 - 4000 cycles

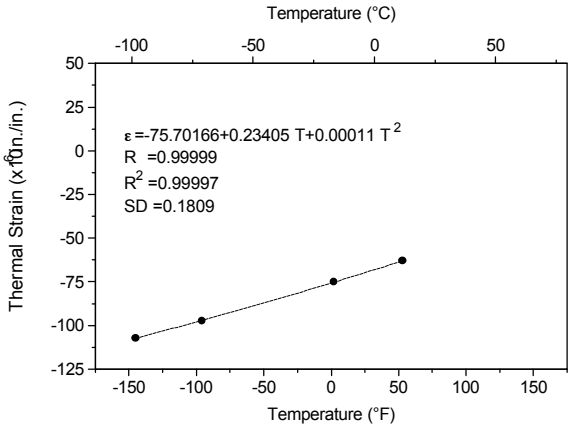

(c) 275RS3-06 - 4000 cycles

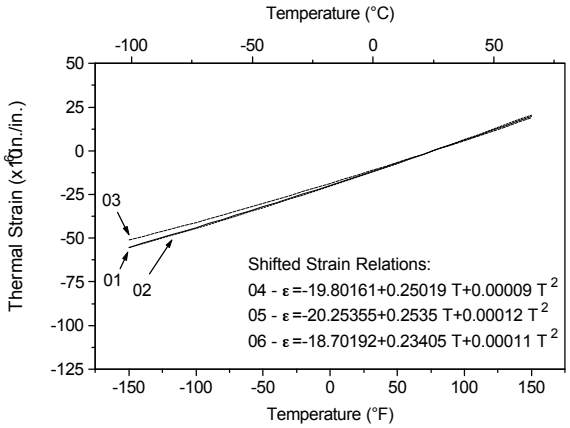

(d) Shifted strain data for 275RS3-04, 05, 06

Figure D.55. Thermal strain data for specimens 275RS3-04, 05, and 06 at 4000 cycles.

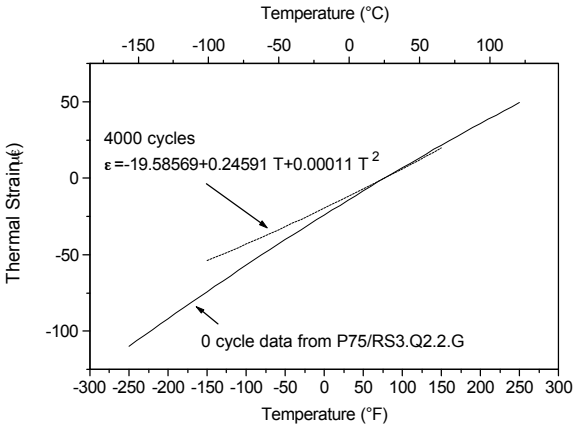

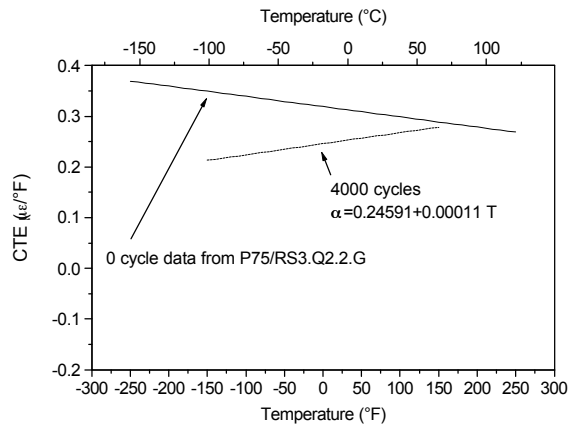

Figure D.56. Average thermal expansion data for specimen series 275RS3 - P75/RS3.Q2.2.L - P75/RS3, $[0/+45/90/-45]_S$, 2 mil, ±150°F.

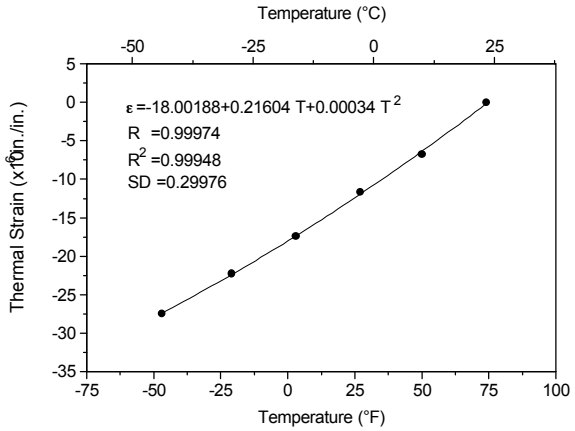

(a) 275RS3-07 - 4000 cycles

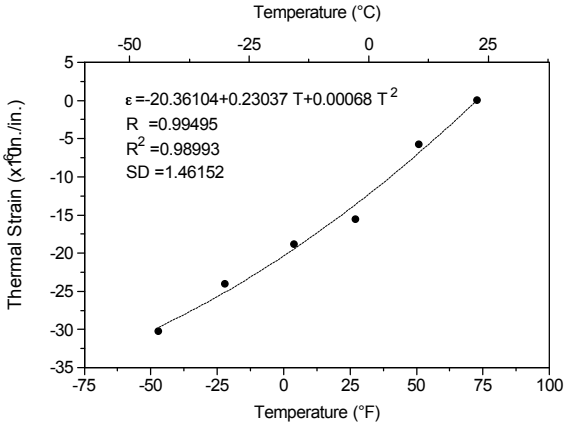

(b) 275RS3-08 - 4000 cycles

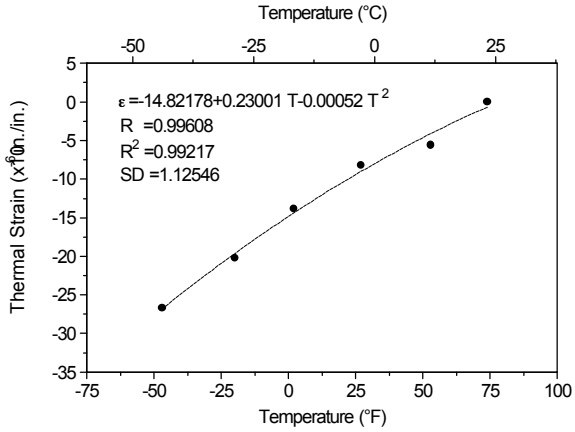

(c) 275RS3-09 - 4000 cycles

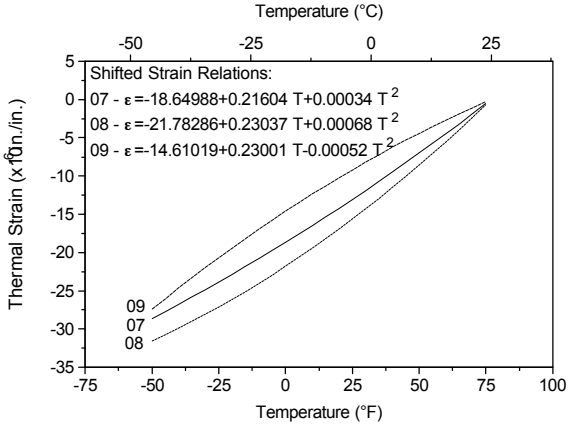

(d) Shifted strain data for 275RS3-07,08,09

Figure D.57. Thermal strain data for specimens 275RS3-07, 08, and 09 at 4000 cycles.

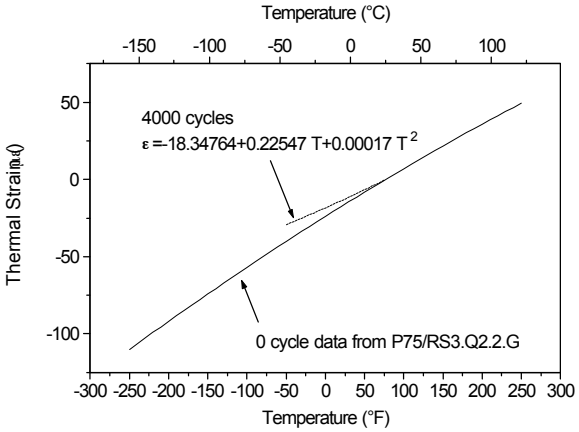

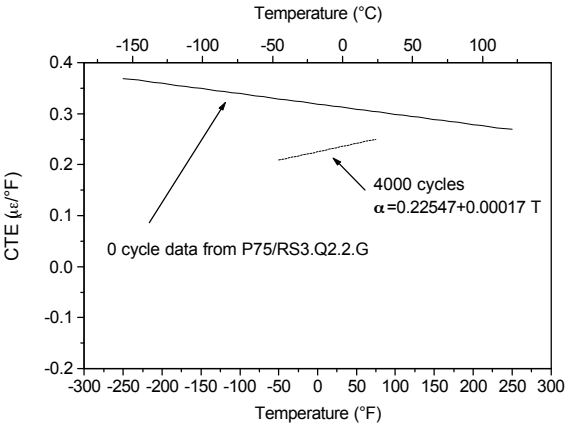

Figure D.58. Average thermal expansion data for specimen series 275RS3 - P75/RS3.Q2.2.C - P75/RS3, $[0/+45/90/-45]_S$, 2 mil, ±50°F.

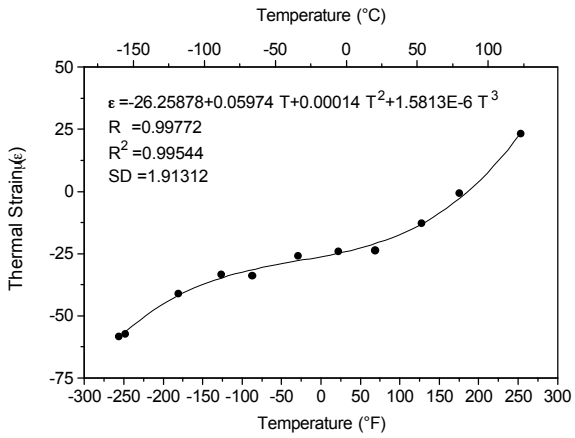

(a) UTQ-1 - 0 cycles

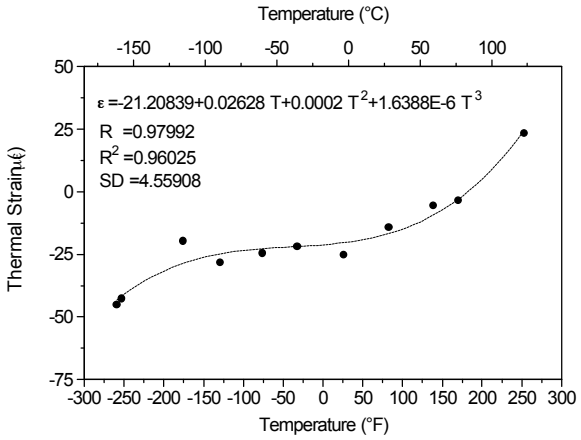

(b) UTQ-2 - 0 cycles

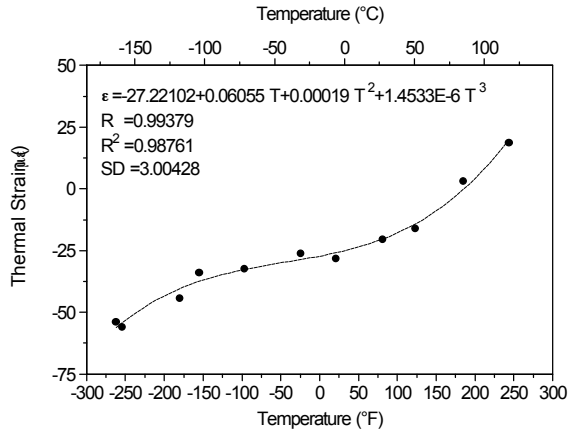

(c) UTQ-3 - 0 cycles

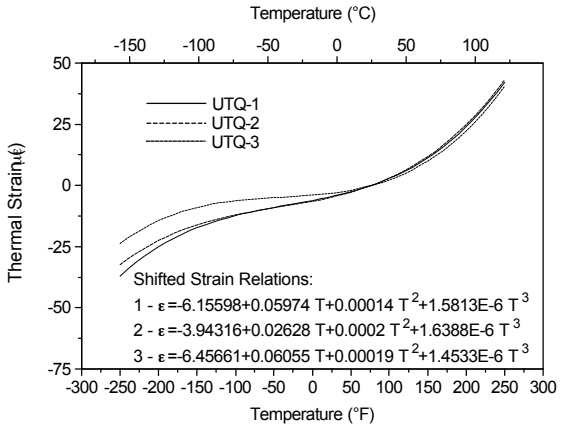

(d) Shifted strain data for UTQ-1, 2, and 3

Figure D.59. Thermal strain data for specimens UTQ-1, 2, and 3 at 0 cycles.

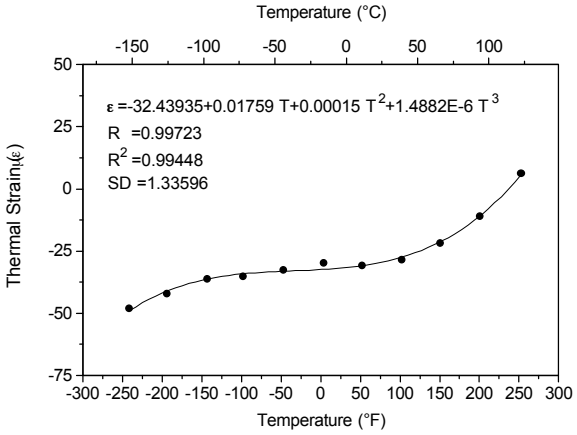

(a) UTQ-1 - 4500 cycles

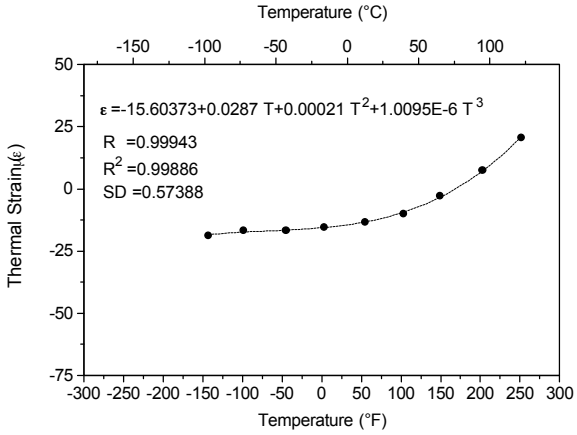

(b) UTQ-2 - 4500 cycles

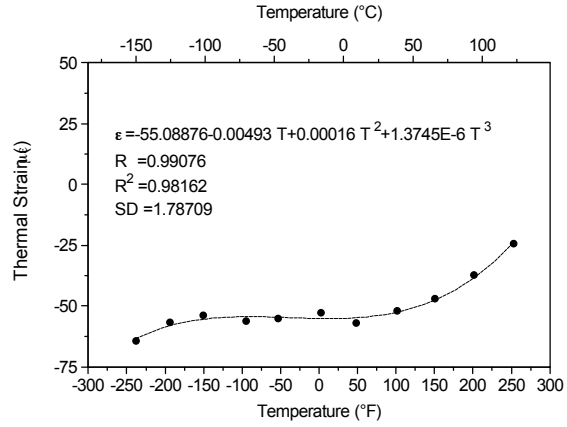

(c) UTQ-3 - 4500 cycles

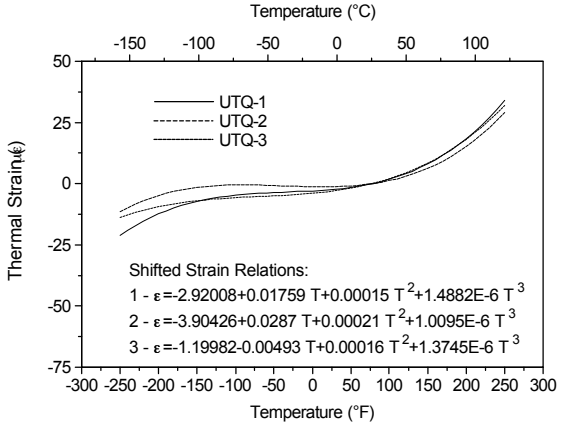

(d) Shifted strain data for UTQ-1, 2, and 3

Figure D.60. Thermal strain data for specimens UTQ-1, 2, and 3 at 4500 cycles.

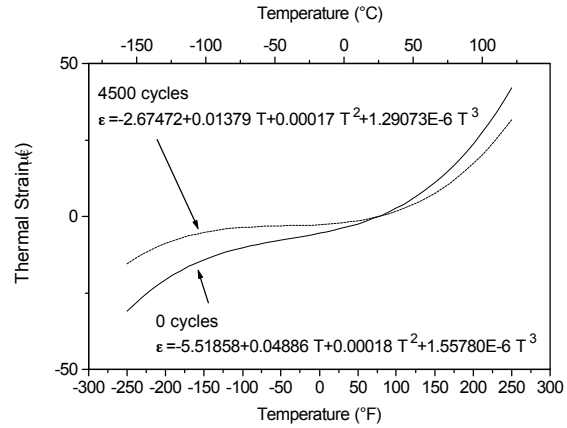

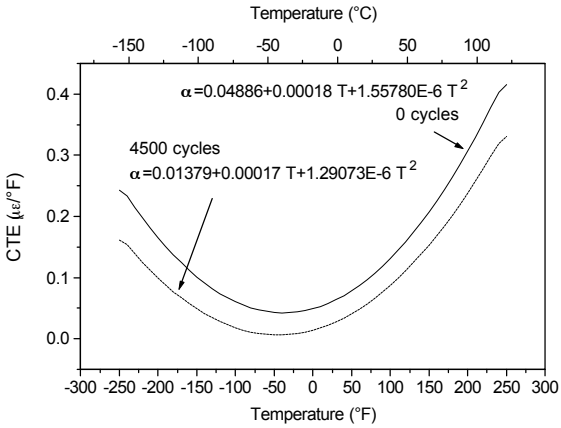

Figure D.61. Average thermal expansion data for specimen series UTQ - P75/ERL1962.Q2.1.G - P75/ERL1962, $[0/+45/90/-45]_S$, 1 mil, ±250°F.

APPENDIX E - NORMALIZED LAMINATE STIFFNESS CALCULATIONS

This appendix provides the rationale for normalizing experimentally measured tensile laminate stiffness by fiber volume fraction in both quasi-isotropic and cross-ply laminate configurations. This normalization was required based on observed scatter in experimentally measured stiffnesses from one specimen to another in a given material series. Also included in this appendix are some typical experimental results showing the linear stress-strain behavior of the specimens and the procedure for calculating average laminate stiffness. Finally, the normalized stiffness for each of the specimens in the test program is summarized in tabular form.

Stress-strain results for the quasi-isotropic specimen 6762-13 are shown in Figure E.1. The front and back stiffness of the specimen are noted as A and B. The stiffness is calculated from a linear regression of the stress-strain behavior from the strain range of 0.10% to the maximum strain for that given test, typically near 0.30%. In this case, the maximum strain is near 0.26% for side A and 0.27% for side B. The stress-strain response for this specimen is observed to be very near linear over this strain range. This is typical of all the specimens in the test program. The front and back stiffness for the specimen are averaged to obtain the average laminate stiffness for the specimen.

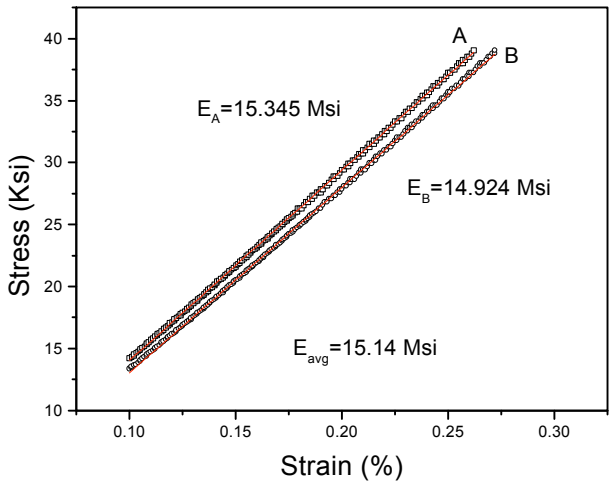

Figure E.1. Experimentally determined laminate stiffness for specimen 6762-13.

After completion of stiffness testing, it was observed that large deviations in laminate stiffness were observed, even for specimens that had undergone similar cycling histories. In fact,

large variations were observed in specimens that had undergone no thermal cycling, i.e., baseline (BSL) specimens. It was suspected that variations in fiber volume fraction due to manufacturing inconsistency were responsible for this variation. As a result, each of the specimens was measured for fiber volume content subsequent to stiffness testing. As an example of the variation, results for the series 6762 baseline specimens, i.e., uncycled, are shown in Table E.1.

Table E.1 Average Measured Stiffness and Fiber Volume Fractions for Series 6762 Baseline Specimens

Specimen	Avg. Measured Stiffness (Msi)	Fiber Volume Fraction
6762-13	15.14	0.592
6762-15	13.45	0.509
6762-1A	13.77	0.546
6762-5A	16.94	0.646
6762-10A	14.20	0.522

As seen in Table E.1, the average measured stiffness for the series 6762 baseline specimens varies significantly. Based on a standard normal distribution, the average stiffness plus or minus one standard deviation for these specimens is given by 14.70±1.41 Msi. It is noted in Table E.1 that the measured stiffness for a given specimen tends to correlate directly with fiber volume fraction, i.e., the higher the fiber volume fraction, the higher the stiffness. This is expected due to the much higher stiffness of the fiber compared to the matrix. For a unidirectional composite, i.e., one with fibers aligned in the same direction in all layers, it makes sense to normalize the unidirectional stiffness by the fiber volume fraction. This is seen by examining a rule of mixtures expression for unidirectional stiffness in the fiber direction, namely,

$$E_1 = E_{1f} v_f + E_m v_m , \tag{E.1}$$

where E_{1f}, E_m, v_f, and v_m are the axial fiber stiffness, the matrix stiffness, fiber volume fraction, and matrix volume fraction, respectively. Considering the range of values for materials considered in this investigation, the matrix contribution to E_1 is negligible compared to that of the fiber. Therefore, the expression for E_1 reduces to

$$E_1 = E_{1f} v_f . \tag{E.2}$$

If we assume that the fiber stiffness is nominally the same for each of the specimens in a given material series, E_1 is directly proportional to fiber volume fraction. Fiber volume fraction is therefore an appropriate normalization parameter for unidirectional laminate stiffness. It is unclear whether the same normalization is appropriate for quasi-isotropic and cross-ply laminate configurations. To determine whether or not quasi-isotropic and cross-ply laminate stiffness should be normalized directly by fiber volume fraction, classical lamination theory (CLT) was used to evaluate the effect of various lamina properties to the overall laminate stiffness for these two lamination sequences. Each of four lamina properties (E_1, E_2, G_{12}, and ν_{12}) were varied from baseline values. The baseline values represent typical properties for the materials in this investigation and are defined as

$$\begin{aligned} E_1 &= 35.0\,Msi \\ E_2 &= 1.0\,Msi \\ G_{12} &= 0.7\,Msi \\ \nu_{12} &= 0.3 \end{aligned} \quad . \tag{E.3}$$

Each of the above material properties was separately varied to 75% and 125% of their baseline values. Laminate stiffness was then calculated using CLT over this range. The stiffness was then normalized by the baseline stiffness and plotted as a function of the variation in material property. The results are shown below in Figure E.2 for the quasi-isotropic laminate in part (a) and the cross-ply laminate in part (b).

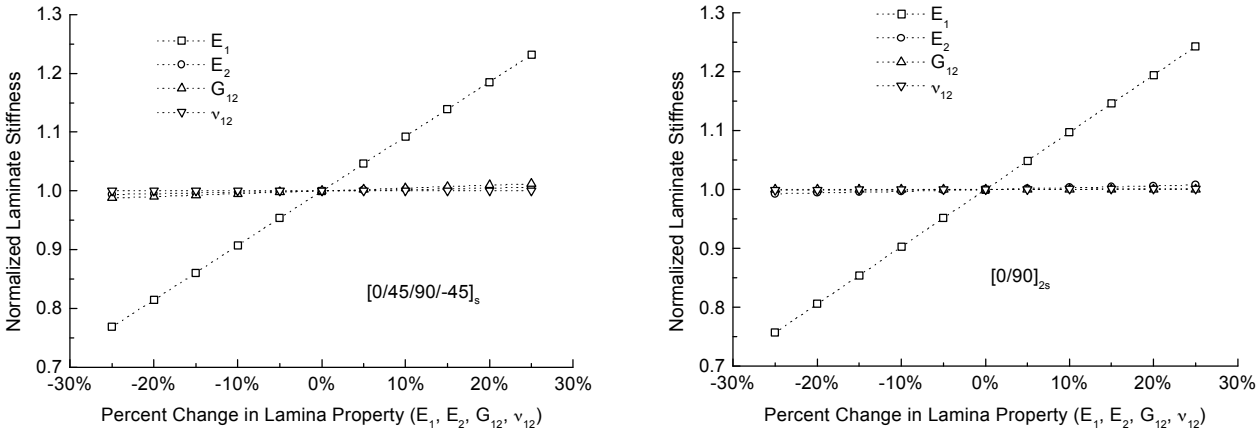

(a) Quasi-isotropic laminate (b) Cross-ply laminate

Figure E.2. Effect of lamina property variation on laminate stiffness for quasi-isotropic and cross-ply laminates.

In both the quasi-isotropic and cross-ply configurations, the laminate stiffness is seen to be affected predominately by E_1, with very little effect from the remaining three lamina properties. Using the same argument regarding fiber volume fraction in unidirectional laminates, it therefore makes sense to normalize the quasi-isotropic and cross-ply stiffness by fiber volume fraction as well. Continuing with the example in Table E.1 and performing this normalization on the series 6762 baseline specimens, the results shown in the last column of Table E.2 are obtained.

Table E.2 Normalized Laminate Stiffness
for Series 6762 Baseline Specimens

Specimen	Avg. Measured Stiffness (Msi)	Fiber Volume Fraction	Normalized Stiffness (Msi)
6762-13	15.14	0.592	25.57
6762-15	13.45	0.509	26.42
6762-1A	13.77	0.546	25.21
6762-5A	16.94	0.646	26.22
6762-10A	14.20	0.522	27.19

The average normalized stiffness plus or minus one standard deviation is given by 26.13±0.77 Msi compared to the earlier measured stiffness of 14.70±1.41 Msi. The scatter in the stiffness is substantially reduced by performing this normalization. The normalized stiffness results for all of the specimens in the test program are summarized in Table E.3. The front and back measured stiffness are shown as E_A and E_B, with the average measured specimen stiffness indicated as E_{avg}. The fiber volume fractions for each specimen are also listed along with the normalized stiffness.

Table E.3 Normalized Laminate Stiffness for All Specimens

Specimen	Temperature Range	E_A (Msi)	E_B (Msi)	E_{avg} (Msi)	Fiber Volume Fraction	Normalized Stiffness (Msi)
J-1	BSL	16.92	15.79	16.36	0.632	25.88
J-2	±250°F	17.16	14.76	15.96	0.617	25.87
J-3	±250°F	16.37	14.70	15.54	0.628	24.74

Specimen	Temperature Range	E_A (Msi)	E_B (Msi)	E_{avg} (Msi)	Fiber Volume Fraction	Normalized Stiffness (Msi)
J-4	±250°F	17.85	15.15	16.50	0.618	26.70
O-1	BSL	15.78	14.50	15.14	0.630	24.03
O-2	±250°F	15.23	13.49	14.36	0.590	24.34
O-3	±250°F	14.84	13.62	14.23	0.595	23.92
O-4	±250°F	14.64	14.15	14.39	0.603	23.87
H-1	BSL	21.71	17.03	19.37	0.513	37.76
H-2	±250°F	23.69	16.75	20.22	0.498	40.60
H-3	±250°F	21.48	16.88	19.18	0.496	38.67
H-4	±250°F	specimen failed prematurely				
Q-1	±250°F	31.40	26.48	28.94	0.560	51.68
Q-2	±250°F	31.33	28.46	29.90	0.556	53.77
Q-3	±250°F	30.43	28.57	29.50	0.559	52.77
Q-4	BSL	30.08	28.77	29.43	0.566	51.99
UT8X-2	±250°F	17.35	14.91	16.13	0.563	28.65
UT8X-4	±250°F	17.80	15.97	16.89	0.562	30.04
UT8X-5	±250°F	17.28	14.37	15.83	0.581	27.24
UT8X-1	BSL	17.09	16.01	16.55	0.571	28.98
UT8X-6	BSL	specimen failed prematurely				
UT8X-2A	BSL	16.65	15.61	16.13	0.572	28.20
UT8X-4A	BSL	17.83	15.68	16.76	0.571	29.34
UT8X-5A	BSL	not tested				
K-2	BSL	11.80	11.33	11.57	0.616	18.77
K-3	±250°F	11.10	10.90	11.00	0.619	17.77
K-4	±250°F	11.68	11.16	11.42	0.619	18.45
P-1	±250°F	9.91	9.51	9.71	0.597	16.26
P-2	±250°F	9.83	9.23	9.53	0.595	16.02
P-3	±250°F	9.65	9.12	9.39	0.599	15.67
P-4	BSL	10.00	9.73	9.87	0.615	16.04
I-1	±250°F	specimen failed prematurely				

Specimen	Temperature Range	E_A (Msi)	E_B (Msi)	E_{avg} (Msi)	Fiber Volume Fraction	Normalized Stiffness (Msi)
I-2	±250°F	12.42	12.17	12.30	0.497	24.74
I-3	±250°F	12.69	12.68	12.69	0.492	25.78
I-4	BSL	12.88	12.41	12.65	0.507	24.94
R-1	±250°F	20.17	18.99	19.58	0.546	35.86
R-3	±250°F	20.24	19.39	19.82	0.529	37.46
R-4	±250°F	19.98	19.26	19.62	0.536	36.60
R-2	BSL	20.02	19.43	19.73	0.540	36.53
6762-1	±250°F	16.37	15.54	15.96	0.644	24.77
6762-3	±250°F	16.38	15.87	16.13	0.653	24.69
6762-5	±250°F	16.83	16.15	16.49	0.648	25.45
6762-2	±150°F	16.26	15.61	15.94	0.646	24.67
6762-4	±150°F	18.28	17.44	17.86	0.673	26.54
6762-6	±150°F	17.82	16.96	17.39	0.668	26.03
6762-7	±50°F	16.97	16.58	16.78	0.654	25.65
6762-8	±50°F	17.56	16.60	17.08	0.602	28.37
6762-9	±50°F	17.54	17.09	17.32	0.633	27.35
6762-13	BSL	15.35	14.93	15.14	0.592	25.57
6762-14	BSL	not tested				
6762-15	BSL	13.66	13.24	13.45	0.509	26.42
6762-1A	BSL	13.99	13.54	13.77	0.546	25.21
6762-5A	BSL	17.02	16.86	16.94	0.646	26.22
6762-10A	BSL	14.57	13.82	14.12	0.522	27.19
75RS3-01	±250°F	15.56	15.50	15.53	0.668	23.25
75RS3-02	±250°F	15.92	15.63	15.78	0.661	23.87
75RS3-03	±250°F	15.76	15.22	15.49	0.717	21.60
75RS3-04	±250°F	16.41	15.68	16.05	0.682	23.53
75RS3-05	±250°F	16.55	15.79	16.17	0.695	23.27
75RS3-06	±250°F	16.69	15.93	16.31	0.665	24.53
75RS3-07	±250°F	16.32	15.76	16.04	0.668	24.01

Specimen	Temperature Range	E_A (Msi)	E_B (Msi)	E_{avg} (Msi)	Fiber Volume Fraction	Normalized Stiffness (Msi)
75RS3-08	±250°F	16.97	16.24	16.61	0.684	24.28
75RS3-09	±250°F	15.79	15.38	15.59	0.672	23.19
75RS3-13	BSL	15.77	15.03	15.40	0.643	23.95
75RS3-14	BSL	16.41	15.65	16.03	0.652	24.59
75RS3-15	BSL	16.22	15.38	15.80	0.651	24.27
75RS3-3A	BSL	16.01	15.52	15.77	0.658	23.96
75RS3-8A	BSL	16.00	15.35	15.68	0.668	23.47
75RS3-11A	BSL	15.52	14.90	15.21	0.656	23.19
75R-A-40	BSL	16.94	16.14	16.54	0.681	24.29
75R-A-38	±50°F	16.76	16.03	16.40	0.665	24.65
75R-A-39	±50°F	16.87	16.26	16.57	0.684	24.22
75R-A-46	±50°F	16.78	16.10	16.44	0.662	24.83
75R-A-36	±150°F	16.59	15.98	16.29	0.676	24.09
75R-A-37	±150°F	16.48	15.88	16.18	0.671	24.11
75R-A-45	±150°F	16.68	16.34	16.51	0.655	25.21
75R-A-41	±250°F	16.40	15.80	16.10	0.666	24.17
75R-A-43	±250°F	16.62	15.90	16.26	0.663	24.52
75R-A-44	±250°F	16.37	16.01	16.19	0.654	24.76
P734Q-2	±250°F	14.26	13.61	13.94	0.516	27.01
P734Q-3	±250°F	14.35	14.11	14.23	0.512	27.79
P734Q-4	±250°F	14.32	13.88	14.10	0.527	26.76
P734Q-5	±250°F	15.14	14.83	14.99	0.558	26.85
P734Q-6	BSL	15.98	15.41	15.70	0.657	23.89
P734Q-3A	BSL	13.59	12.76	13.18	0.495	26.62
P734Q-7A	BSL	15.78	14.84	15.31	0.626	24.46
P734Q-12A	BSL	13.87	13.45	13.66	0.571	23.92
275RS3-1	±250°F	10.42	10.07	10.25	0.547	18.73
275RS3-2	±250°F	10.47	10.46	10.47	0.556	18.82
275RS3-3	±250°F	10.35	10.12	10.24	0.521	19.64

Specimen	Temperature Range	E_A (Msi)	E_B (Msi)	E_{avg} (Msi)	Fiber Volume Fraction	Normalized Stiffness (Msi)
275RS3-4	±150°F	10.80	10.49	10.65	0.532	20.01
275RS3-5	±150°F	10.50	10.37	10.50	0.566	18.55
275RS3-6	±150°F	10.92	10.25	10.59	0.547	19.35
275RS3-7	±50°F	10.47	10.41	10.44	0.523	19.96
275RS3-8	±50°F	10.65	10.58	10.62	0.535	19.84
275RS3-9	±50°F	10.91	10.83	10.87	0.534	20.36
275RS3-13	BSL	10.43	10.45	10.44	0.535	19.51
275RS3-14	BSL	10.26	10.28	10.27	0.536	19.16
275RS3-15	BSL	10.18	10.13	10.16	0.525	19.34
275RS3-1A	BSL	10.20	10.05	10.13	0.543	18.65
275RS3-5A	BSL	10.79	10.48	10.64	0.535	19.88
275RS3-11A	BSL	10.00	10.05	10.03	0.534	18.77
UTQ-1	±250°F	10.39	10.53	10.46	0.615	17.01
UTQ-2	±250°F	10.97	10.72	10.85	0.568	19.09
UTQ-3	±250°F	10.56	10.41	10.49	0.572	18.33
UTQ-3A	BSL	10.27	10.36	10.32	0.609	16.94
UTQ-7A	BSL	9.77	10.13	9.95	0.563	17.67
UTQ-9A	BSL	10.36	10.14	10.25	0.573	17.89

APPENDIX F - LAMINA MATERIAL PROPERTY DERIVATION

This appendix contains the derivation of lamina material properties for the various materials and specimens in the study. Because of variations in fiber volume fraction, material properties varied from specimen to specimen. It is important to know these properties, particularly for any ensuing analysis. Since the analysis used in this study relies on classical lamination theory (CLT), properties important to that theory are presented.

Room temperature (75°F) unidirectional test data for each of the material systems used in this investigation have been obtained experimentally and are summarized below in Table F.1. The average value and standard deviation are shown for each material property along with the number of specimens tested. Note that the average fiber volume fraction (V_f) for each material system is shown in the table as well.

Table F.1 Room Temperature Lamina Properties Measured from Unidirectional Specimens

Material		E_1 (Msi)	E_2 (Msi)	G_{12} (Msi)	ν_{12}	α_1 (με/°F)	α_2 (με/°F)
T50/ERL1962	Average	28.4	1.04	0.630	0.270	-0.305	18.0
(V_f=0.559)	S.D.	0.200	0.089	0.007	0.020	0.032	0.205
	# Spec.	3	3	3	3	3	3
P55/ERL1962	Average	25.1	1.003	0.7*	0.340	-0.385	15.3
(V_f=0.599)	S.D.	0.624	0.229	N/A	0.028	0.018	2.07
	# Spec.	3	3	0	3	3	3
P75/ERL1962	Average	34.3	0.903	0.7*	0.293	-0.501	21.0
(V_f=0.523)	S.D.	0.666	0.006	N/A	0.006	0.016	0.286
	# Spec.	3	3	0	3	3	3
P120/ERL1962	Average	58.5	0.865	0.7*	0.280	-0.675	15.6
(V_f=0.548)	S.D.	2.05	0.007	N/A	0.028	0.006	0.233
	# Spec.	2	2	0	2	2	2
P75/RS3	Average	43.0	0.964	0.7*	0.261	-0.662	15.7
(V_f=0.690)	S.D.	5.36	0.001	N/A	0.086	0.038	0.223
	# Spec.	3	3	0	3	2	2

Material		E_1 (Msi)	E_2 (Msi)	G_{12} (Msi)	ν_{12}	α_1 (με/°F)	α_2 (με/°F)
P75/934	Average	49.4	1.01	0.7*	0.3*	-0.652	16.7
(V_f=0.657)	S.D.	1.84	0.020	N/A	N/A	0.037	N/A
	# Spec.	3	3	0	3	3	1

* This value has been estimated.

The material properties from Table F.1 were used together with CLT to predict as-fabricated laminate stiffness and CTE for each of the laminates considered in this investigation. A range of values equal to plus or minus one standard deviation from the mean value was used for each lamina property to calculate a range of predicted stiffness and CTE. The stiffness results are presented in Table F.2.

The average experimentally measured stiffness values in Table F.2 are shown along with the standard deviation and number of specimens tested. The fiber volume fractions from each stiffness specimen were also measured and averaged. These average values are shown in the table as well, along with their standard deviation. As mentioned above, the one standard deviation range of predicted values is shown in the final column.

Table F.2 Measured and Predicted Laminate Stiffness

Material	Series	Layup	# Spec.	Avg. V_f	S.D. V_f	Avg. Exp. E_x (Msi)	S.D. Exp. E_x (Msi)	Predicted E_x (CLT) (Msi)
T50/ERL1962	J	X	1	0.632	N/A	16.4	N/A	14.6-14.9
	K	Q1	1	0.616	N/A	11.6	N/A	10.2-10.4
P55/ERL1962	O	X	1	0.630	N/A	15.1	N/A	12.7-13.6
	P	Q1	1	0.615	N/A	9.87	N/A	9.00-9.56
P75/ERL1962	H	X	1	0.513	N/A	19.4	N/A	17.3-18.0
	I	Q1	1	0.507	N/A	12.6	N/A	12.1-12.6
	6762	Q2	5	0.563	0.056	14.7	1.406	12.1-12.6
	UTQ	Q2	3	0.582	0.024	10.2	0.195	12.1-12.6
	UT8X	X	3	0.571	0.001	16.5	0.319	17.3-18.0
P120/ERL1962	Q	X	1	0.566	N/A	29.4	N/A	28.7-30.7
	R	Q1	1	0.540	N/A	19.7	N/A	19.7-21.0

Material	Series	Layup	# Spec.	Avg. V_f	S.D. V_f	Avg. Exp. E_x (Msi)	S.D. Exp. E_x (Msi)	Predicted E_x (CLT) (Msi)
P75/RS3	75RS3	Q2	6	0.655	0.008	15.6	0.296	13.5-17.0
	275RS3	Q2	6	0.535	0.006	10.3	0.226	13.5-17.0
	75R-A	Q2	1	0.681	N/A	16.5	N/A	13.5-17.0
P75/934	P734Q	Q2	4	0.587	0.071	14.5	1.23	16.8-18.0

Note that poor agreement is observed between stiffness measured experimentally and stiffness predicted from CLT. This is likely due to the differences in fiber volume fraction between the quasi-isotropic or cross-ply stiffness specimens and the unidirectional stiffness specimens used to measure lamina properties. A parameter study was conducted to examine the effect of fiber volume fraction on the laminate stiffness in quasi-isotropic and cross-ply laminates. Typical lamina material properties were used to represent specimens similar to those in this study. The baseline properties selected are as follows:

$$\begin{aligned} E_1 &= 35.0\,Msi \\ E_2 &= 1.0\,Msi \\ G_{12} &= 0.7\,Msi \\ \nu_{12} &= 0.3 \end{aligned} \quad . \tag{F.1}$$

Each of the four lamina quantities (E_1, E_2, G_{12}, and ν_{12}) was varied independently from their original baseline values by plus and minus twenty five percent. Laminate stiffness was then calculated as a function of these variations. The results are presented in Figure F.1 where normalized laminate stiffness is simply the calculated laminate stiffness divided by the original baseline laminate stiffness. Each of the four lamina material properties is represented by a different symbol in the figure. Note that only E_1 is seen to have a significant effect on laminate stiffness. The correlation between E_1 and laminate stiffness is nearly a one-to-one, with a twenty five percent increase in E_1 resulting in close to a twenty five percent increase in laminate stiffness. This is the true for both the quasi-isotropic laminate (Figure 1(a)) and the cross-ply laminate configuration (Figure 1(b)).

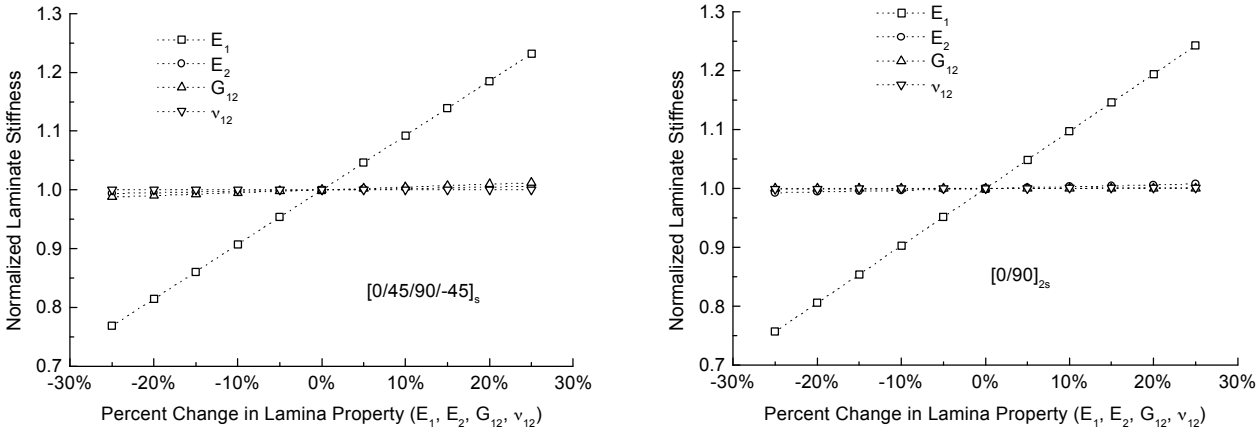

(a) Quasi-isotropic laminate (b) Cross-ply laminate

Figure F.1. Effect of lamina property variation on laminate stiffness for quasi-isotropic and cross-ply laminates.

The correlation between laminate stiffness and fiber volume fraction can be realized by considering a simple rule of mixtures approach to lamina stiffness E_1 given by the following relation:

$$E_1 = E_{1f}V_f + E_mV_m\,, \tag{F.2}$$

where E_{1f}, E_m, V_f, and V_m are the axial fiber stiffness, the matrix stiffness, fiber volume fraction, and matrix volume fraction, respectively. Considering the range of values for materials considered in this investigation, the matrix contribution to E_1 is negligible compared to that of the fiber. Therefore, the expression for E_1 can be realistically simplified to:

$$E_1 = E_{1f}V_f\,. \tag{F.3}$$

Therefore, if we assume that the fiber stiffness is nominally the same for each of the specimens in a given material series, E_1 is directly proportional to fiber volume fraction, and hence fiber volume fraction is directly proportional to laminate stiffness. It is therefore concluded that in order to accurately predict the experimentally measured laminate stiffness in the quasi-isotropic and cross-ply laminate configurations, the lamina property E_1 values from the unidirectional specimen tests must be altered to reflect the fiber volume fraction in the quasi-isotropic and cross-ply stiffness specimens being tested. This calculation has been performed and the revised laminate stiffness predictions are presented in Table F.3 alongside the original predictions from Table F.2, which do not account for variations in fiber volume fraction.

Table F.3 Measured and Revised Predicted Laminate Stiffness Based on Fiber Volume Fraction Measurements

Material	Series	Layup	Avg.±S.D. Exp. E_x (Msi)	Predicted E_x (CLT) (Msi)	Revised Predicted E_x (CLT w/ V_f) (Msi)
T50/ERL1962	J	X	16.4	14.6-14.9	16.4-16.8
	K	Q1	11.6	10.2-10.4	11.2-11.4
P55/ERL1962	O	X	15.1	12.7-13.6	13.3-14.2
	P	Q1	9.87	9.00-9.56	9.22-9.79
P75/ERL1962	H	X	19.4	17.3-18.0	17.0-17.7
	I	Q1	12.6	12.1-12.6	11.8-12.2
	6762	Q2	14.7±1.41	12.1-12.6	13.0-13.4
	UTQ	Q2	10.2±0.195	12.1-12.6	13.4-13.9
	UT8X	X	16.3±0.418	17.3-18.0	18.9-19.6
P120/ERL1962	Q	X	29.4	28.7-30.7	29.6-31.7
	R	Q1	19.7	19.7-21.0	19.4-20.8
P75/RS3	75RS3	Q2	15.6±0.296	13.5-17.0	12.8-16.2
	275RS3	Q2	10.3±0.226	13.5-17.0	10.6-13.4
	75R-A	Q2	16.5	13.5-17.0	13.3-16.8
P75/934	P734Q	Q2	14.5±1.23	16.8-18.0	15.1-16.2

The revised predicted stiffness ranges in the quasi-isotropic and cross-ply laminates more closely match the actual experimental values. Revised E_1 values based on measured fiber volume fractions will therefore be selected to represent the baseline material properties in the crack progression analysis.

The modification to E_1 will also affect the predicted laminate CTE values. To understand what other factors affect the laminate CTE, a second parameter study was performed using CLT. The results from this parameter study are shown in Figure F.2 for the quasi-isotropic and cross-ply laminate configurations. As done previously in the stiffness parameter study, each of the lamina material properties, now including α_1 and α_2, were varied independently plus or minus

twenty five percent of a representative baseline value. The baseline values chosen for α_1 and α_2 are as follows:

$$\begin{aligned} \alpha_1 &= -0.5x10^{-6}/°F \\ \alpha_2 &= 20.0x10^{-6}/°F \end{aligned} . \tag{F.4}$$

Note that for this analysis, an increase in α_1 implies a more negative value of α_1. The effect on laminate CTE was calculated based on the percentage change in lamina property. The normalized CTE shown in the figure is simply the laminate CTE value divided by the baseline laminate CTE value.

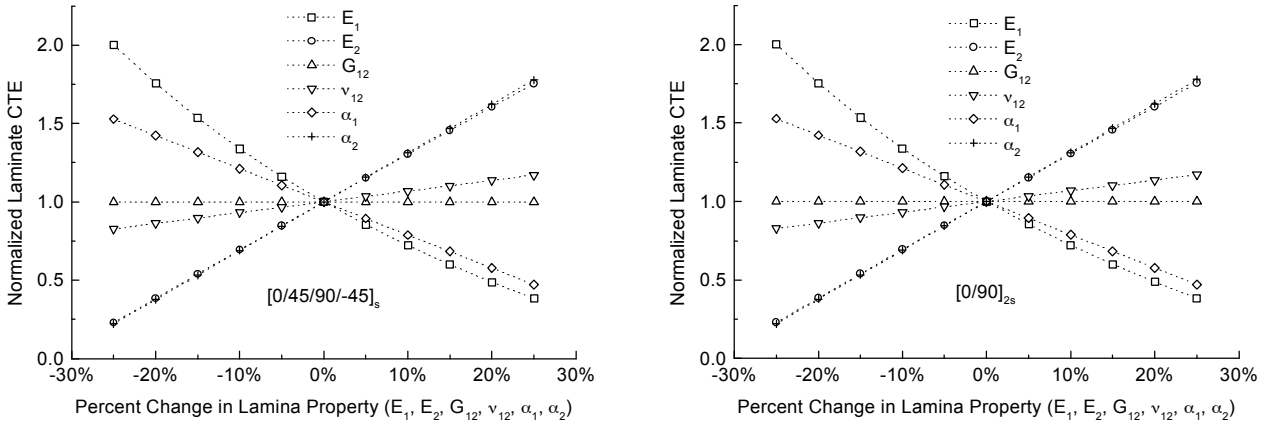

(a) Quasi-isotropic layup (b) Cross-ply layup

Figure F.2. Effect of lamina material property variation on laminate CTE.

In both laminate configurations, it is apparent that all but G_{12} and ν_{12} have a significant effect on laminate CTE. Ideally one would like to relate all of these properties to reflect the changes in fiber volume fraction as was done previously for E_1. Realistically, however, this requires sophisticated micromechanics models which lead to additional material properties that are not accurately known for these materials, i.e., fiber stiffness, matrix stiffness, fiber CTE, matrix CTE, etc. Prior to implementing the more complicated micromechanics approach, a first attempt at using CLT to predict laminate CTE is performed using the known lamina properties from Table F.1, and corrected values of E_1 based on fiber volume fraction measurements.

The average experimentally measured values of baseline laminate CTE, or α_x, are shown in Table F.4 along with the standard deviation and number of specimens tested. It should be noted that the specimens used to measure baseline laminate thermal expansion are different from the specimens used to measure baseline laminate stiffness, and hence the fiber volume fractions have

changed. This, however, will not the case for the post-cycled measurements. The fiber volume fractions from each of the CTE specimens were measured and averaged and are summarized in the table along with their standard deviation. In the case of the CTE predictions from CLT, a range of predicted values is shown based on the range of lamina material properties consisting of plus and minus one standard deviation from the mean measured values. In Table F.4, two columns of predicted CTE are shown. The first column represents the predictions using the original lamina properties from Table F.1. The second column, labeled revised prediction, represents the CTE predictions incorporating the modified E_1 values based on fiber volume fraction measurements.

Table F.4 Measured and Predicted Laminate CTE

Material	Series	Layup	# Spec.	Avg. fiber V_f	S.D. fiber V_f	Avg. Exp. α_x (με/°F)	S.D. Exp. α_x (με /°F)	Predicted α_x (CLT) (με /°F)	Rev. Pred. α_x (CLT w/ V_f) (με /°F)
T50/	J	X	3	0.621	0.006	0.345	0.019	0.380,0.622	0.311,0.538
ERL1962	K	Q1	2	0.619	0.000	0.388	0.016	0.380,0.622	0.313,0.540
P55/	O	X	2	0.599	0.006	0.759	0.060	0.111,0.758	0.111,0.758
ERL1962	P	Q1	2	0.596	0.001	0.683	0.033	0.111,0.758	0.114,0.763
P75/	H	X	2	0.498	0.000	0.310	0.064	0.157,0.246	0.189,0.281
ERL1962	I	Q1	3	0.497	0.005	0.423	0.034	0.157,0.246	0.191,0.283
	6762	Q2	3	0.648	0.005	-0.083	0.060	0.157,0.246	0.031,0.110
	UTQ	Q2	3	0.585	0.026	0.102	0.016	0.157,0.246	0.088,0.172
	UT8X	X	2	0.563	0.001	0.141	0.019	0.157,0.246	0.111,0.197
P120/	Q	X	2	0.560	0.001	-0.278	0.025	-0.401,-0.342	-0.407,-0.348
ERL1962	R	Q1	3	0.537	0.009	-0.231	0.033	-0.401,-0.342	-0.396,-0.335
P75/RS3	75RS3	Q2	3	0.682	0.031	-0.169	0.050	-0.332,-0.077	-0.327,-0.071
	275RS3	Q2	3	0.541	0.018	0.304	0.064	-0.332,-0.077	-0.234,+0.066
	75R-A	Q2	2	0.665	0.003	-0.194	0.017	-0.332,-0.077	-0.318,-0.057
P75/934	P734Q	Q2	3	0.518	0.008	-0.210	0.037	-0.266,-0.144	-0.157,-0.023

The results in Table F.4 indicate that for some of the materials, the experimentally measured CTE falls significantly outside the range of values predicted by CLT, even when including the revised E_1 values. It is therefore apparent that further steps need to be taken to account for fiber

volume fraction variations in regards to how these variations affect the remaining lamina properties. In particular, the three additional lamina material properties which need to be considered, in addition to E_1, are E_2, α_1 and α_2. These four properties affect the laminate CTE most significantly as indicated by the results in Figure F.2.

The rule of mixtures approach to evaluate E_1 will continue to be used, but this time without neglecting the matrix contribution (see Equation F.2). Additional micromechanics relations are needed to evaluate the remaining three lamina properties. The relations chosen are each some form of modified rule of mixtures relations [F1]. The transverse lamina stiffness, E_2, is given by the following relation:

$$\frac{1}{E_2} = \frac{\dfrac{V_f}{E_{2f}} + \dfrac{\eta(1-V_f)}{E_m}}{V_f + \eta(1-V_f)}, \tag{F.5}$$

where V_f is the fiber volume fraction, E_{2f} is the transverse fiber stiffness, E_m is the matrix stiffness, and η is a partitioning factor. The value of η equal to 0.5 appears to work reasonably well when compared to finite-element calculations for either square or hexagonal array fiber packing. The modified rule of mixtures expression for the axial fiber direction lamina expansion, α_1, is given by the following relation:

$$\alpha_1 = \frac{(\alpha_{1f}E_{1f} - \alpha_m E_m)V_f + \alpha_m E_m}{(E_{1f} - E_m)V_f + E_m}, \tag{F.6}$$

where α_{1f} is the CTE of the fiber in the axial direction, α_m is the CTE of the matrix, E_{1f} is the axial fiber stiffness, and E_m is the matrix stiffness. The modified rule of mixtures relation for the transverse fiber direction lamina expansion, α_2, is given by the following relation:

$$\alpha_2 = \alpha_m + (\alpha_{2f} - \alpha_m)V_f + \left(\frac{E_{1f}\nu_m - E_m\nu_{12f}}{E_1}\right)(\alpha_m - \alpha_{1f})(1-V_f)V_f, \tag{F.7}$$

where α_{2f} is the CTE of the fiber in the transverse direction, ν_m is the Poisson's ratio of the matrix, and ν_{12f} is the Poisson's ratio of the fiber.

The four micromechanical relations shown in Equations F.2, F.5, F.6, and F.7 involve several additional material properties which are not well known, specifically eight in total, not including fiber volume fraction. Experimental data are available for each of the four lamina properties E_1, E_2, α_1, and α_2 at known fiber volume fractions. Therefore, if it is reasonable to assume constant values for four of the unknown micromechanical properties, the remaining four

can be uniquely determined. By examining how the various micromechanical properties affect the lamina properties, the validity of this concept can be realized.

To examine how the various micromechanical properties affect the lamina properties, a sensitivity study was performed. Baseline values of micromechanical properties were selected based on reasonable values available from literature and by using the micromechanical relations to derive lamina properties that were on the order of the baseline lamina values in the previous parameter study. The resulting baseline micromechanical properties are as follows:

$$\begin{aligned} E_{1f} &= 54.0\,Msi & \nu_m &= 0.3 \\ E_{2f} &= 1.37\,Msi & \alpha_{1f} &= -0.7x10^{-6}/°F \\ E_m &= 0.5\,Msi & \alpha_{2f} &= 5.0x10^{-6}/°F \\ \nu_{12f} &= 0.2 & \alpha_m &= 37.5x10^{-6}/°F \end{aligned} \quad . \tag{F.8}$$

As in the previous parameter studies, the baseline values for each property were varied to plus and minus twenty five percent of their original values. The effect to each lamina property was then calculated and plotted, normalized by the baseline property value. The results are summarized in Figure F.3. Note that only those micromechanical properties that directly affect the lamina property are included in the figure.

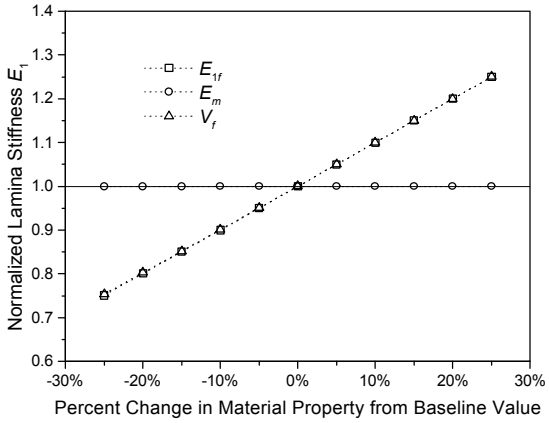

(a) E_1

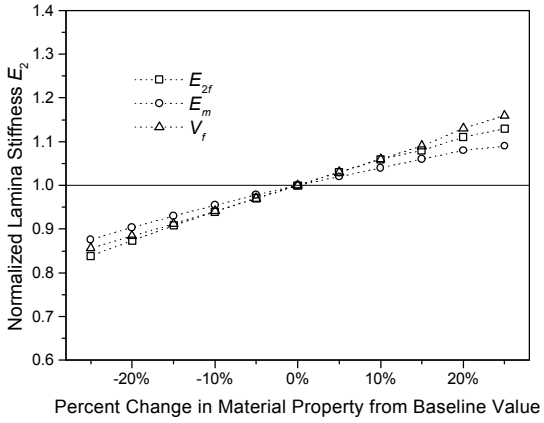

(b) E_2

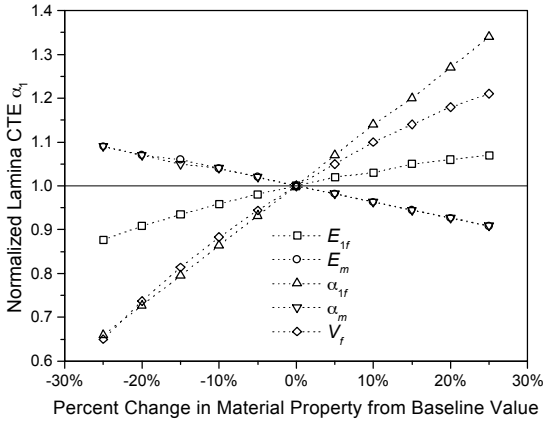

(c) α_1

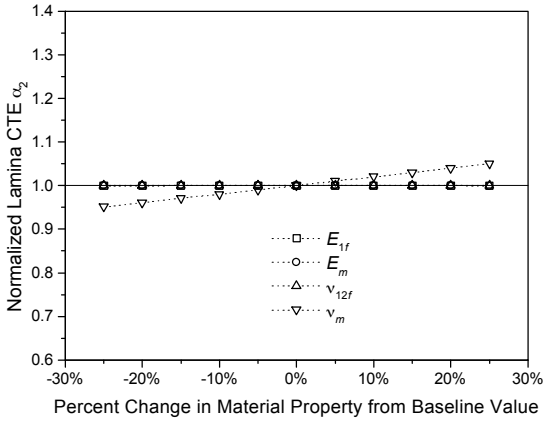

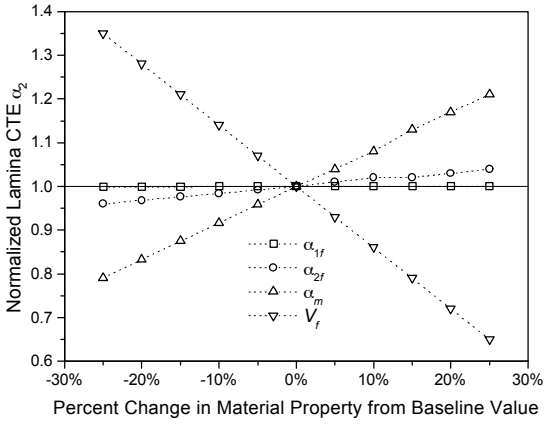

(d) α_2

Figure F.3. Micromechanical parameter study results.

From Figure F.3, it is seen that three of the micromechanical properties have very little effect on any of the lamina properties. These three micromechanical properties are: ν_{12f}, ν_m, and α_{2f}. It is also evident that E_m is a minor factor in E_2 and α_1. Manufacturer information is also available on E_m for one of the resin systems in this investigation. Based on this, E_m will be chosen as the fourth micromechanical property to be held constant. The values of the four fixed micromechanical properties are shown in Table F.5.

Table F.5 Fixed Micromechanical Material Properties

Material	E_m (Msi)	ν_{12f}	ν_m	α_{2f} (με/°F)
T50/ERL1962	0.540	0.200*	0.300*	5.00*
P55/ERL1962	0.540	0.200*	0.300*	5.00*
P75/ERL1962	0.540	0.200*	0.300*	5.00*
P120/ERL1962	0.540	0.200*	0.300*	5.00*
P75/934	0.500*	0.200*	0.300*	5.00*
P75/RS3	0.500*	0.200*	0.300*	5.00*

* Assumed value based on available literature[F2].

The remaining unknown material properties (E_{1f}, E_{2f}, α_{1f}, and α_m) are derived from the micromechanical relations using known data. Specifically, the experimentally measured lamina properties from the unidirectional specimens (Table F.1) were used together with the fiber volume fractions from those specimens and Equations F.2, F.5, F.6, and F.7 to derive the remaining properties. Table F.6 lists the resulting derived properties, including high and low values based on the one standard deviation range of properties from Table F.1.

Table F.6 Derived Micromechanical Material Properties

Material		E_{1f} (Msi)	E_{2f} (Msi)	E_m (Msi)	ν_{12f}	ν_m	α_{1f} (με/°F)	α_{2f} (με/°F)	α_m (με/°F)
T50/ERL1962	high	50.0	1.98	0.540	0.200	0.300	-0.505	5.00	26.8
	low	50.7	1.36	0.540	0.200	0.300	-0.559	5.00	26.1
P55/ERL1962	high	40.5	2.16	0.540	0.200	0.300	-0.616	5.00	27.6
	low	42.6	0.905	0.540	0.200	0.300	-0.572	5.00	19.6
P75/ERL1962	high	63.9	1.32	0.540	0.200	0.300	-0.720	5.00	30.0

Material		E_{1f} (Msi)	E_{2f} (Msi)	E_m (Msi)	ν_{12f}	ν_m	α_{1f} (με/°F)	α_{2f} (με/°F)	α_m (με/°F)
	low	66.4	1.29	0.540	0.200	0.300	-0.736	5.000	29.1
P120/ERL1962	high	102.5	1.17	0.540	0.200	0.300	-0.767	5.000	22.2
	low	110.0	1.13	0.540	0.200	0.300	-0.771	5.000	21.4
P75/934	high	72.1	1.42	0.500	0.200	0.300	-0.726	5.000	30.0
	low	77.7	1.32	0.500	0.200	0.300	-0.792	5.000	30.0
P75/RS3	high	54.4	1.22	0.500	0.200	0.300	-0.754	5.000	30.8
	low	69.9	1.22	0.500	0.200	0.300	-0.798	5.000	29.7

Adjusting the fiber volume fractions to match those of the thermal expansion specimens, and using the four micromechanical relations together with the properties from Table F.6, results in the derived lamina material properties shown in Table F.7 for the thermal expansion specimens in this investigation. Note that each material series has a unique set of material properties due to the variation in fiber volume fraction. Two values are shown in each cell separated by a comma. The first value results in the minimum value of CTE while the second value results in the maximum according to the mean plus and minus one standard deviation for the originally measured lamina properties.

Table F.7 Derived Lamina Material Properties for Thermal Expansion Specimens

Material	Series	Layup	E_1 (Msi)	E_2 (Msi)	G_{12} (Msi)	ν_{12}	α_1 (με/°F)	α_2 (με/°F)
T50/ERL1962	J	X	31.7,31.3	1.0,1.22	.624,.637	.250,.290	-.387,-.326	16.0,16.3
	K	Q1	31.6,31.2	1.0,1.22	.624,.637	.250,.290	-.385,-.324	16.0,16.4
P55/ERL1962	O	X	25.7,24.5	.774,1.23	.700	.312,.368	-.402,-.367	13.2,17.4
	P	Q1	25.6,24.4	.773,1.23	.700	.312,.368	-.400,-.364	13.3,17.5
P75/ERL1962	H	X	33.4,32.1	.879,.890	.700	.288,.299	-.494,-.460	21.5,22.1
	I	Q1	33.3,32.0	.879,.889	.700	.288,.299	-.493,-.459	21.5,22.1
	6762	Q2	43.2,41.6	.994,1.01	.700	.288,.299	-.605,-.580	16.6,17.0
	UTQ	Q2	39.1,37.6	.945,.958	.700	.288,.299	-.565,-.537	18.7,19.2
	UT8X	X	37.6,36.2	.928,.940	.700	.288,.299	-.549,-.520	19.4,19.9
P120/ERL1962	Q	X	61.8,57.6	.865,.880	.700	.252,.308	-.685,-.673	15.1,15.6

Material	Series	Layup	E_1 (Msi)	E_2 (Msi)	G_{12} (Msi)	ν_{12}	α_1 (με/°F)	α_2 (με/°F)
	R	Q1	59.3,55.3	.851,.865	.700	.252,.308	-.677,-.663	15.7,16.1
P75/RS3	75RS3	Q2	47.8,37.2	.957,.959	.700	.175,.347	-.696,-.619	15.746,16.202
	275RS3	Q2	38.0,29.6	.852,.854	.700	.175,.347	-.614,-.509	20.499,21.154
	75R-A	Q2	46.6,36.3	.944,.946	.700	.175,.347	-.688,-.608	16.320,16.800
P75/934	P734Q	Q2	40.5,37.6	.869,.896	.700	.3	-.609,-.529	21.469,21.468

Using the values from Table F.7 together with CLT results in the CTE values summarized in the final column in Table F.8. The previous predictions of CTE are summarized along with the experimentally measured values.

Table F.8 Measured and Predicted Laminate Thermal Expansion

Material	Series	Layup	# Spec.	Avg. Exp. α_x (με/°F)	S.D. Exp. α_x (με /°F)	Predicted α_x (CLT) (με/°F)	Predicted α_x (CLT) E_1 only (με/°F)	Predicted α_x (CLT) $E_1,E_2,\alpha_1,\alpha_2$ (με/°F)
T50/ERL1962	J	X	3	0.345	0.019	.380,.622	.311,.538	.231,.464
	K	Q1	2	0.388	0.016	.380,.622	.313,.540	.236,.469
P55/ERL1962	O	X	2	0.759	0.060	.111,.758	.111,.758	.111,.758
	P	Q1	2	0.683	0.033	.111,.758	.114,.763	.117,.767
P75/ERL1962	H	X	2	0.310	0.064	.157,.246	.189,.281	.223,.318
	I	Q1	3	0.423	0.034	.157,.246	.191,.283	.226,.321
	6762	Q2	3	-0.083	0.060	.157,.246	.031,.110	-.114,-.046
	UTQ	Q2	3	0.102	0.016	.157,.246	.088,.172	.011,.089
	UT8X	X	2	0.141	0.019	.157,.246	.111,.197	.060,.142
P120/ERL1962	Q	X	2	-0.278	0.025	-.401,-.342	-.407,-.348	-.414,-.356
	R	Q1	3	-0.231	0.033	-.401,-.342	-.396,-.335	-.389,-.328
P75/RS3	75RS3	Q2	3	-0.169	0.050	-.332,-.077	-.327,-.071	-.320,-.060
P75/RS3	275RS3	Q2	3	0.304	0.064	-.332,-.077	-.234,+.066	-.074,.292
	75R-A	Q2	2	-0.194	0.017	-.332,-.077	-.318,-.057	-.294,-.023
P75/934	P734Q	Q2	3	-0.210	0.037	-.266,-.144	-.157,-.023	-.013,.128

For clarity, the results shown in Table F.8 are shown graphically in Figure F.4. The shaded columns represent that mean value, with the error bars indicating plus and minus one standard deviation from the mean. From left to right, the four columns represent: 1) experimentally measured values, 2) CLT predictions using lamina properties from Table F.1, 3) CLT predictions using lamina properties from Table F.1 including modified E_1 values based on fiber volume fraction and Equation F.3, and 4) micromechanical predictions accounting for the effect of fiber volume fraction on E_1, E_2, α_1, and α_2.

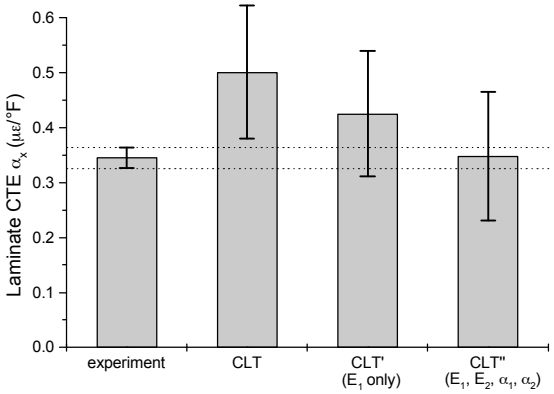

(a) T50/ERL1962.X.5 (Series J)

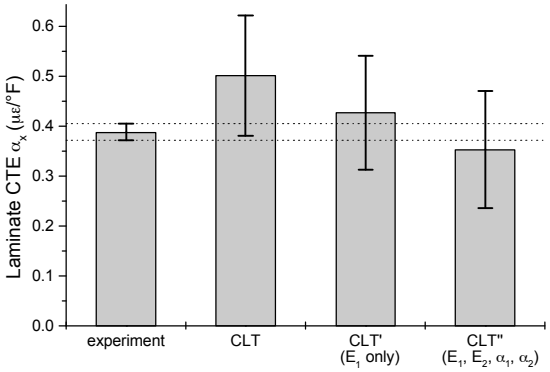

(b) T50/ERL1962.Q1.5 (Series K)

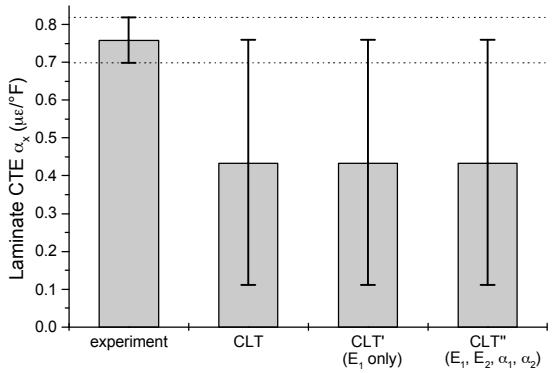

(c) P55/ERL1962.X.5 (Series O)

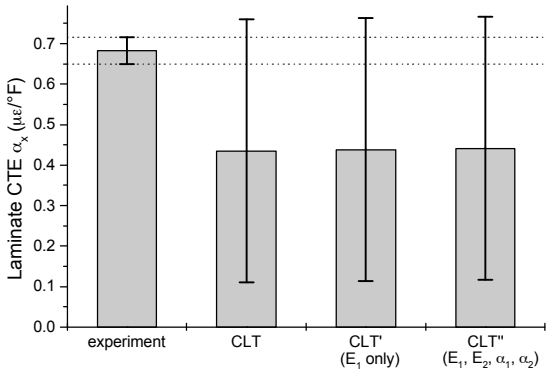

(d) P55/ERL1962.Q1.5 (Series P)

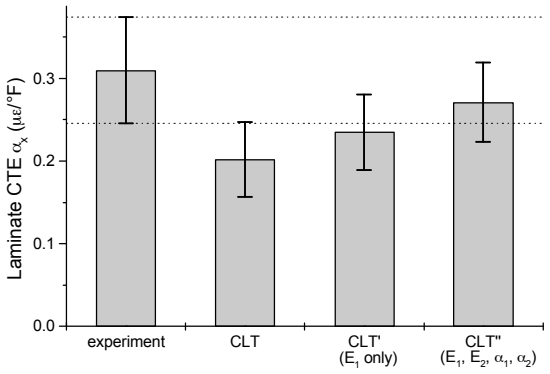

(e) P75/ERL1962.X.5 (Series H)

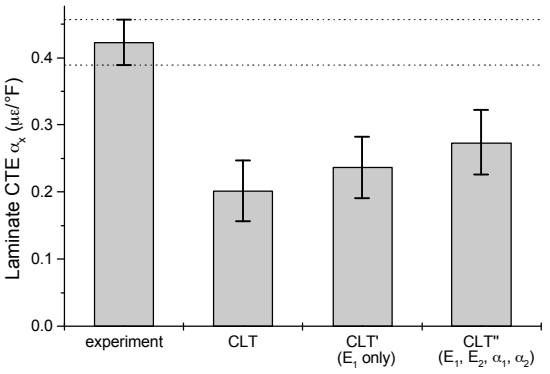

(f) P75/ERL1962.Q1.5 (Series I)

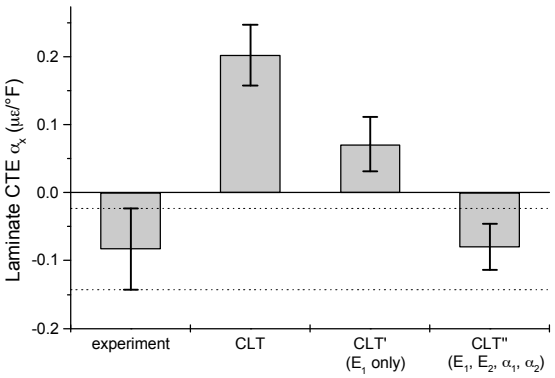

(g) P75/ERL1962.Q2 (Series 6762)

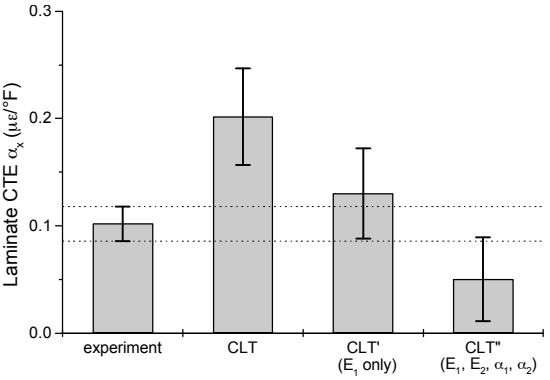

(h) P75/ERL1962.Q2.1 (Series UTQ)

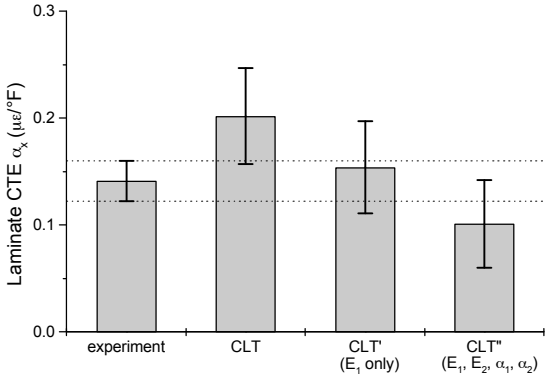

(i) P75/ERL1962.X.1 (Series UT8X)

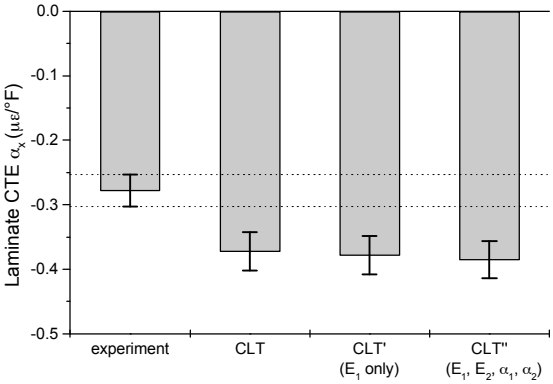

(j) P120/ERL1962.X (Series Q)

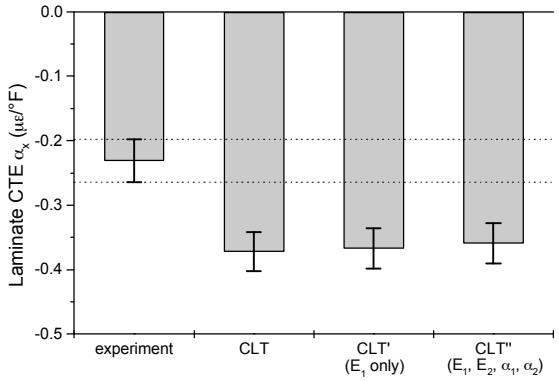

(k) P120/ERL1962.Q1 (Series R)

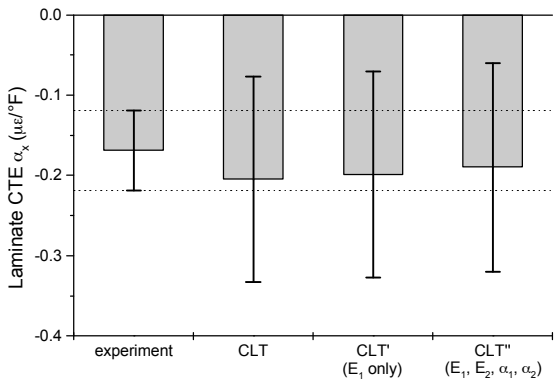

(l) P75/RS3.Q2.5 (Series 75RS3)

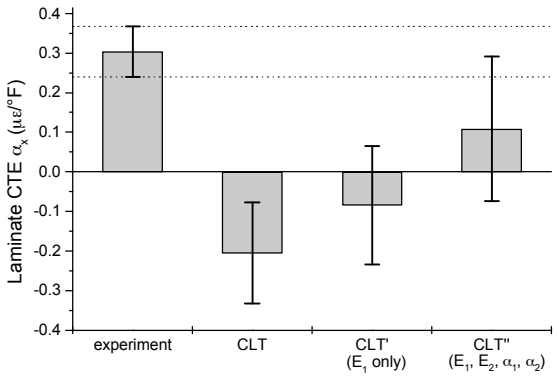

(m) P75/RS3.Q2.2 (Series 275RS3)

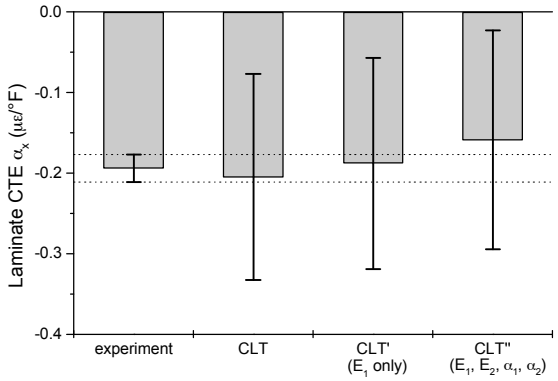

(n) P75/RS3.Q2.5 (Series 75R-A)

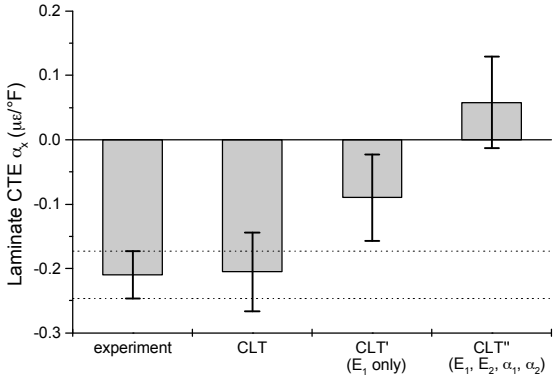

(o) P75/934.Q2 (Series P734Q)

Figure F.4. Comparison of measured and predicted laminate CTE.

Comparing the three predictions, the use of micromechanics in the predictions appears to lead to results that more consistently match experimental measurements. This indicates that in fact, fiber volume fraction effects must be included in more than just the E_1 values. The only

instance in which the micromechanical prediction appears to be, by far, the worst prediction is in the case of the P75/934 laminate. It is unclear why this particular material series behaves this way.

As a final point, the micromechanical property values derived and summarized in Table F.6 can be used along with fiber volume fractions from the baseline quasi-isotropic and cross-ply stiffness specimens to predict baseline laminate stiffness. As a reminder, the previous revised stiffness predictions presented in Table F.3 accounted for fiber volume fraction effects in E_1 only, and in doing so, neglected the effect of E_m in the rule of mixtures relation (Eqn. F.2 and F.3). The stiffness predictions using the micromechanical relations do not neglect E_m in Eqn. F.2 and include fiber volume fraction effects on E_2. These micromechanical predictions have been summarized in Table F.9 in the last column. For convenience, the original predictions neglecting fiber volume fraction and the predictions neglecting E_m and E_2 have been included in this table. To the degree of accuracy shown, there is no change observed by including the matrix contribution, E_m, to E_1 or the effect of fiber volume fraction on E_2. This emphasizes the appropriateness of earlier assumptions on E_1 and the dominant effect of E_1 on quasi-isotropic and cross-ply laminate stiffness.

Table F.9 Measured and Predicted Laminate Stiffness

Material	Series	Layup	Avg. V_f	Avg. Exp. E_x (Msi)	S.D. Exp. E_x (Msi)	Predicted E_x (no V_f effect) (Msi)	Predicted E_x (E_1 only) (Msi)	Predicted E_x (E_1 and E_2) (Msi)
T50/ERL1962	J	X	0.632	16.4	N/A	14.6-14.9	16.4-16.8	16.4-16.8
	K	Q1	0.616	11.6	N/A	10.2-10.4	11.2-11.4	11.2-11.4
P55/ERL1962	O	X	0.630	15.2	N/A	12.7-13.6	13.3-14.2	13.3-14.2
	P	Q1	0.615	9.87	N/A	9.00-9.6	9.22-9.79	9.22-9.79
P75/ERL1962	H	X	0.513	19.4	N/A	17.3-18.0	17.0-17.7	17.0-17.7
	I	Q1	0.507	12.6	N/A	12.1-12.6	11.8-12.2	11.8-12.2
	6762	Q2	0.563	14.7	1.406	12.1-12.6	13.0-13.4	13.0-13.4
	UTQ	Q2	0.582	10.2	0.195	12.1-12.6	13.4-13.9	13.4-13.9
	UT8X	X	0.571	16.3	0.418	17.3-18.0	18.9-19.6	18.9-19.6
P120/ERL1962	Q	X	0.566	29.4	N/A	28.7-30.7	29.6-31.7	29.6-31.7
	R	Q1	0.540	19.7	N/A	19.7-21.0	19.4-20.8	19.4-20.8

Material	Series	Layup	Avg. V_f	Avg. Exp. E_x (Msi)	S.D. Exp. E_x (Msi)	Predicted E_x (no V_f effect) (Msi)	Predicted E_x (E_1 only) (Msi)	Predicted E_x (E_1 and E_2) (Msi)
P75/RS3	75RS3	Q2	0.655	15.6	0.296	13.5-17.0	12.8-16.2	12.8-16.2
	275RS3	Q2	0.535	10.3	0.226	13.5-17.0	10.6-13.4	10.6-13.4
	75R-A	Q2	0.681	16.5	N/A	13.5-17.0	13.3-16.8	13.3-16.8
P75/934	P734Q	Q2	0.587	14.5	1.23	16.8-18.0	15.1-16.2	15.1-16.2

REFERENCES

F1. M.W. Hyer, Stress Analysis of Fiber Reinforced Composite Materials, WCB/McGraw-Hill, New York, 1998, ISBN 0-07-016700-1.

F2. Chamis, C. C., "Simplified Composite Micromechanics Equations for Hygral Thermal and Mechanical Properties," 38th Annual Conference, Reinforced Plastics/Composites Institute, The Society of the Plastics Industry, Inc. February 7-11, 1983, session 21-C, p5.

VITA

Timothy L. Brown was born on January 2, 1968 in Austin, Texas. After graduating from L. C. Anderson High School in 1986, he enrolled at the University of Texas at Austin. He completed his Bachelor of Science degree in Mechanical Engineering in May 1990, and began graduate studies the following fall at Virginia Polytechnic Institute and State University in the Engineering Science and Mechanics Department. His Master's degree research was sponsored by the Office of Naval Research, and included an internship at David Taylor Research Center in Bethesda, Maryland. After completion of his Master of Science degree in Engineering Mechanics in June 1992, he continued graduate studies at Virginia Tech. His doctoral research was supported by the Environmental Interactions Branch at NASA Langley Research Center. Research for the degree was conducted during a three year residency at NASA Langley Research Center. Upon completion of this degree, he will remain at NASA Langley Research Center as a National Research Council post-doctoral fellow in the Nondestructive Evaluation Sciences Branch.